

KINGSTON UNIVERSITY

BAOPENG XU

LARGE EDDY SIMULATION OF EVAPORATING
TWO-PHASE FLOWS

FACULTY OF ENGINEERING

PHD THESIS

KINGSTON UNIVERSITY
FACULTY OF ENGINEERING
PHD THESIS

Academic Year 2002-2006

BAOPENG XU

Large Eddy Simulation of Evaporating Two-Phase
Flows

Supervisors: Prof. Jennifer X Wen, Dr. Siaka Dembele

June 2006

Thesis submitted for the degree of Doctor of Philosophy

© Kingston University 2006. All rights reserved. No part of
this publication may be reproduced without the permission of
the copyright owner

M0034736KP

KINGSTON UNIVERSITY LIBRARY	
Acc. No. 4815138X	PREF
Class No. THESIS, PHD	

Abstract

The objective of this study is to develop a CFD tool for performing reliable large eddy simulation (LES) of the compressible evaporating two-phase turbulent flow in a gas turbine combustor. The KIVA-3V code originally developed by Los Alamos National Laboratory is used as a baseline code. The KIVA-3V code has been modified to facilitate LES calculations. Both the temporal and spatial accuracies of the original KIVA-3V code have been improved to second order. A one-equation subgrid scale (SGS) turbulence model is implemented to describe the unresolved turbulent subgrid effect. To ensure that there are sufficient particle numbers to capture the dynamic droplet dispersion process, the ETAB breakup model coupled with a new hybrid droplet-particle algorithm is also implemented into the code. Furthermore, the effect of the subgrid scale (SGS) velocity on the droplet dispersion is included. The SGS velocity is computed from the subgrid turbulent kinetic energy predicted by the one-equation SGS turbulence model. A new collision model based on the concept of “particle cloud” is proposed and implemented in the code. The new model greatly reduces the grid-dependence of the original O’Rourke model in a Cartesian mesh.

The gas solver of the new LES version of KIVA-3V code, which will be referred as KIVA-LES hereby) is validated against large eddy simulations of natural and forced plane impinging jets. Predictions were carried out for different inflow conditions, which include a natural plane impinging jet with a random perturbation on the inflow plane and a forced plane impinging jet with a Strouhal number of 0.36, locked both in phase and laterally in space. The first simulation was performed to quantitatively study the mean flow and turbulence statistics. The computed field variables and turbulence intensity of streamwise velocity agreed well with the experimental results. The second simulation was performed to study the vortex structures of a forced plane impinging jet. The predictions captured the

typical vortex structures of this kind of flow, such as spanwise rollers, successive ribs, cross ribs and wall ribs were reproduced by the simulation, which were also previously detected by the experiment of Sakakibara et al. [103] with digital particle image velocimetry (DPIV) system, but to our best knowledge never wholly reproduced by numerical simulations to date. Moreover, the study has also led to some new findings related to the formation and evolution of successive ribs, cross ribs and wall ribs.

The new collision model is tested against analytical solutions of simplified realistic collision problems in a box volume. The grid-dependence of the model is also checked against some spray test cases. The new collision scheme is computationally more efficient than the frequently used O'Rourke's [87] scheme since it abandons a sampling procedure to compute the collision number. The new model delivers sufficient accuracy in calculating the collision numbers in cases with uniformly distributed droplets although O'Rourke's model seems to perform better for these scenarios. However, for the prediction of a real spray in Cartesian grid, the new model has delivered much improved results. The predictions of the new model do not show any grid-dependent artefacts.

KIVA-LES with the Lagrangian spray models is used to predict non-evaporating and evaporating diesel fuel sprays. The computed results are compared with the experimental data by Hiroyasu and Kadota [55] and Naber and Siebers [81], as well as the predictions of the original KIVA-3V. The predictions are in good agreement with the data. The large scale vortical structures are reproduced by the LES simulations, which cause "branch-like" spray shape and influence the spray penetration depth. The predictions have also captured the differences between the dense and dilute regions of the sprays. The LES analysis of diesel sprays has also demonstrated that SGS velocity has significant influence on the predicted spray angles. Most importantly, grid-convergent results, which were difficult to obtain with the original KIVA-3V, have been obtained in the present study.

Finally, the validated code is used to study evaporating two-phase spray flow in a coaxial gas turbine model combustor. The predictions were compared with some published experimental data. This is a first step towards a more comprehensive numerical analysis of practical industrial combustors where multiple inlets and more complex combustor geometry are encountered. Good agreement with the data is achieved. The predictions have captured the “ring-like” vortex just downstream the annulus and “worm-like” streamwise vortical structure further downstream. The axial droplet mass flux and Sauter mean radius (SMR) are well predicted.

Overall the present study has demonstrated the capability of KIVA-LES with the newly developed collision model to provide reasonably accurate predictions of evaporating two-phase flows in coaxial gas turbine combustors.

Acknowledgements

Firstly I would like to express my sincere gratitude to my supervisors Prof. J. Wen and Dr. S. Dembele for their guidance and helpful advice throughout the course of this work.

I would like to acknowledge the friends and colleagues in the Fire and Explosion Research Group, who make my daily life more colourful.

I would also like to thank my former colleagues in China for constantly encouraging me to finish my study.

Finally I would like to give my thanks to my wife for her understanding and support.

Contents

Abstract	i
Acknowledgements	IV
Table of Contents	V
List of Abbreviations and Acronyms	VIII
List of Figures	IX
List of Tables	XIII
1 Introduction	1
1.1 Background	1
1.2 Physical processes in a LDI gas turbine combustor	3
1.3 Computational methods	5
1.4 Approaches to spray modeling	9
1.5 Previous studies on LES of gas turbine combustor	12
1.6 KIVA-3V code	17
1.7 Present contributions	23
1.8 Thesis outline	26
2 Mathematical Formulations in the LES Context	28
2.1 What is LES?	29
2.2 Unsteady NS equations	33
2.3 Favre-filtered LES gas phase NS equations	36
2.4 One-equation SGS model	38
2.5 Source terms due to the spray	40
2.6 Spray models	48
2.6.1 TAB breakup model	48
2.6.2 ETAB breakup model with a new hybrid droplet-particle algorithm	50
2.6.3 O'Rourke collision model	54
2.6.4 New collision model	57
2.7 Boundary and initial conditions	60

2.7.1 Solid walls	60
2.7.2 Inflow boundary condition	62
2.7.3 Outflow boundary condition	64
3 Numerical Methods	65
3.1 Temporal discretisation	65
3.2 Spatial discretization	69
3.3 Difference Equations	73
3.3.1 Lagrangian phase	73
3.3.2 Phase C	76
4 LES of Plane Impinging Jets	79
4.1 Introduction	79
4.2 Problem description	82
4.3 Computational results and discussions	86
4.3.1 Natural plane impinging jet	87
4.3.1.1 Numerical accuracy and SGS-model effect	87
4.3.1.2 Main flow	89
4.3.1.3 Turbulence statistics	91
4.3.1.4 Dynamics of the impinging jet	97
4.3.2 Forced plane impinging jet	99
4.3.2.1 Phase-averaging	99
4.3.2.2 Overview of vortex structures	101
4.3.2.3 Formation of successive ribs, cross ribs and wall ribs	111
4.3.2.4 Evolution of organized vortex structures	121
4.4 Summary	127
5 Validation of the New Collision Model	130
5.1 Introduction	130
5.2 Validations	132
5.2.1 Model accuracy	132
5.2.2 Grid-dependency	139

5.2.2.1 Ideal spray test cases	139
5.2.2.2 Realistic spray test cases	142
5.2.2.3 Effect of the parameter of particle cloud radius	149
5.3 Conclusions	150
6 LES of Non-Evaporating and Evaporating Diesel Fuel Sprays	151
6.1 Introduction	151
6.2 Problem description	153
6.3 Computational results and analysis	156
6.3.1 Overview of the predicted spray	156
6.3.2 The predicted spray tip penetration	160
6.3.3 The predicted SMR	165
6.3.4 The predicted results by KIVA-3V with O'Rourke's model	170
6.3.5 The predicted results by KIVA-LES with O'Rourke's model	171
6.3.6 The effect of the fictitious sphere volume	173
6.3.7 The effect of SGS velocity	174
6.3.8 The evaporating case of Naber and Siebers	177
6.4 Summary	179
7 LES of a Coaxial Gas Turbine Model Combustor	180
7.1 Introduction	180
7.2 Problem description	183
7.3 Computational results and discussions	187
7.3.1 Single phase flow	188
7.3.2 Evaporating two phase flow	192
7.4 Summary	208
8 Conclusions and Recommendations for Future Work	209
8.1 Conclusions	209
8.2 Recommendations for future work	211
References	212

List of Abbreviations and Acronyms

ALE	Arbitrary Lagrangian Eulerian
BOFFIN	Boundary Fitted Flow Integrator
CFD	Computational Fluid Dynamics
CPU	Central Processing Unit
CR	Cross Rib
DI	Direct Injection
DNS	Direct Numerical Simulation
DPIV	Digital Particle Image Velocimetry
DSMC	Direct Simulation Monte Carlo
ETAB	Enhanced Taylor Analogy Breakup
LES	Large Eddy Simulation
LDI	Lean Direct Injection
LDV	Laser-Doppler Velocimetry
LEM	Linear Eddy Model
LPC	Lean-Premixed Combustion
NTC	No Time Counter
PDC	Partial Donor cell
QSOU	Quasi Second Order Upwind
RANS	Reynolds Averaging Navier–Stokes
RNG	Renormalization Group
RMS	Root Mean Square
RQL	Rich-burn Quick-quench Lean-burn
SGS	SubGrid Scale
SMR	Sauter Mean Radius
SMD	Sauter Mean Diameter
SR	Successive Rib
TAB	Taylor Analogy Breakup
TVD	Total Variation Diminishing
WR	Wall Rib

List of Figures

Fig. 2.1 Schematic representation of droplet breakup mechanisms: Bag breakup: $6 < We < 80$, stripping (shear) breakup: $80 < We < 350$, catastrophic (surface wave) breakup: $We > 350$.	51
Fig. 3.1 The portion of momentum cell (i, j, k) lying within the regular cell (i, j, k) . Each momentum cell has twenty-four such faces in all.	69
Fig. 3.2 The definition of the gradient of cell-centred quantity Q on cell face α .	71
Fig. 4.1 The computational domain.	82
Fig. 4.2 Mean velocity vectors extracted from the main flow field on different $x=\text{constant}$ and $z=\text{constant}$ planes	86
Fig. 4.3 Vertical velocity component along the centreline.	87
Fig. 4.4 Vertical velocity distributions at different Z positions	88
Fig. 4.5 Vertical turbulent intensity along the centreline.	89
Fig. 4.6 Horizontal turbulent intensity along the centreline.	90
Fig. 4.7 Spanwise turbulent intensity along the centreline.	92
Fig. 4.8 Horizontal distribution of the Reynolds shear stress at $z=5$.	93
Fig. 4.9 Contours of non-dimensional components of turbulence intensity and Reynolds shear stress on the middle plane [x-component (a), y-component (b), z-component (c), and Reynolds shear stress (d)].	94
Fig. 4.10 Iso-surfaces of normalized total vorticity $\omega = 6.3$ (top) and spanwise vorticity component $\omega_y = \pm 3.3$ (bottom).	96
Fig. 4.11 Instantaneous velocity vector on y-z middle plane through the centreline.	97
Fig. 4.12 Schematic of the vertical structure extracted from [103]	98
Fig. 4.13 Iso-surfaces of the total vorticity at different phase angles, $\omega = 1.8$.	102
Fig. 4.14 Iso-surfaces of the spanwise vorticity at different phase angles, $\omega_y = 1.4$ (left roller) and $\omega_y = -1.4$ (right roller).	104

Fig. 4.15 Iso-surfaces of the streamwise vorticity at different phase angles, $\omega_z = 1.2$ (yellow) and $\omega_z = -1.2$ (blue).	107
Fig. 4.16 Iso-surfaces of the lateral vorticity at different phase angle, $\omega_x = 1.2$ (yellow) and $\omega_x = -1.2$ (blue)	109
Fig. 4.17 Instantaneous (a) and relative velocity vectors (b) on the spanwise middle plane; relative velocity vectors on the centre plane (c) at $\phi = 0$, overlapped by amplified amplitude of spatial perturbation at $z=9$.	112
Fig. 4.18 Relative velocity vectors on the middle plane at different phase angles.	113
Fig. 4.19 Instantaneous relative velocity vectors on the spanwise middle plane at different phase angles	116
Fig. 4.20 Relative velocity vectors on the $x=0.25$ plane at different phase angles.	118
Fig. 4.21 Relative velocity vectors on four different x-y plane cutting though the same convergence line at different moments.	120
Fig. 4.22 Contours of the total vorticity (top), spanwise vorticity (bottom left) and lateral vorticity (bottom right) on the spanwise middle plane at different phase angles.	121
Fig. 5.1 The test domain with uniformly distributed droplets. The particles are coloured with the droplet radius in μm . Coordination unit is in cm.	132
Fig. 5.2 The relative error versus the non-dimensional particle cloud radius under different particle numbers.	134
Fig. 5.3 The relative error versus the particle numbers	135
Fig. 5.4 The computational cost versus the particle number.	136
Fig. 5.5 The relative error versus time step in a temporal calculation over a time interval t^*	137
Fig. 5.6 Top view of the predicted spray shapes for the new model (left) and O'Rourke's model (right).	140
Fig. 5.7 Computational mesh.	143
Fig. 5.8 The predicted spray shapes for the new model (left) and O'Rourke's model (right).	144
Fig. 5.9 The curves of predicted penetration depth.	145
Fig. 5.10 The curves of the predicted SMR.	146

Fig. 5.11 Predicted SMR and penetration depth for the cases with the fixed particle number and different particle could radii.	148
Fig. 6.1 Computational mesh (left), vector of cell averaged droplet velocity (middle), and vector of gas velocity (right)	156
Fig. 6.2 The instantaneous velocity vector and the iso-surface of total vorticity of non-evaporating Case 3 of Naber and Siebers at 1.5ms.	157
Fig. 6.3 The front view of the sprays for Naber's non-evaporating cases at different moments.	158
Fig. 6.4 The comparison of predicted angle with the experimental data of Naber's non-evaporating cases	159
Fig. 6.5 Top view of CASE 2 of Hiroyasu and Kadota at $t = 1.0ms$ (CASE 2)	159
Fig. 6.6 Comparison of the predicted and measured spray tip penetration for the cases of Hiroyasu and Kadota	160
Fig. 6.7 Comparison of the predicted and measured spray tip penetration for the non-evaporating cases of Naber and Siebers	163
Fig. 6.8 Comparison of the predicted and measured spray tip penetration for the cases of Hiroyasu and Kadota	165
Fig. 6.9 Comparison of the predicted and measured spray tip penetration for the non-evaporating cases of Naber and Siebers	167
Fig. 6.10 The computed (KIVA-3V) and measured spray tip penetration for Case 3 of Hiroyasu and Kadota	170
Fig. 6.11 LES predictions with the O'Rourke model for Case 3 of Hiroyasu and Kadota	172
Fig. 6.12 The computed spray tip penetrations and SMRs in terms of different volumes of the fictitious parcel cloud for Case 3 of Hiroyasu and Kadota	173
Fig. 6.13 The computed spray tip penetrations and SMR in terms of with and without SGS velocity for Case 3 of Naber and Siebers	174
Fig. 6.14 Front view of the predicted spray with and without SGS velocity for Naber's non-evaporating Case 3 at $t=1.0$ ms	175

Fig. 6.15 Contour of the droplet mass concentration in g/cm^3 for Naber's non-evaporating Case 3 with (left) and without (right) SGS velocity at $t=1.0$ ms	176
Fig. 6.16 Comparison of the predicted and measured spray tip penetration for evaporating cases of Naber and Siebers	177
Fig. 6.17 Grid sensitivity study for evaporating Case 1 of Naber and Siebers	178
Fig. 7.1 Computational geometry overlapped by a snapshot of iso-surface of pressure fluctuation (a) and coloured spray particle distribution according to droplet sizes (b).	183
Fig.7.2 Contours of instantaneous axial velocity (left), mean axial velocity (middle) and axial turbulent intensity (right) (units in m/s).	187
Fig. 7.3 Comparison of the predicted axial mean velocity and the axial turbulent intensity with experiment.	189
Fig. 7.4 Contours of the mean axial gas velocity for the single phase case (left) and the two phase case (right)	192
Fig. 7.5 Instantaneous velocity vectors on the various downstream cross-sections.	193
Fig. 7.6 Distribution of spray droplets on six various cross sections.	194
Fig. 7.7 Comparison of the predicted mean axial droplet velocity and its velocity fluctuation with the experimental data	196
Fig. 7.8 Comparison of the predicted mean axial droplet velocity and its velocity fluctuations with the counterparts of gas phase	198
Fig. 7.9 Comparison of the predicted mean radial droplet velocity with the experimental data	201
Fig. 7.10 Comparison of the predicted Sauter Mean Diameter (SMD) with the experimental data	203
Fig. 7.11 Comparison of the predicted axial droplet mass flux with the experimental data	206

List of Tables

Table 3.1 Computed cases	83
Table 5.1 Computational data of the ideal spray test cases	139
Table 5.2 Computational data of the realistic spray test cases	142
Table 6.1 Computational data for cases of Hiroyasu and Kadota	153
Table 6.2 Computational data for non-evaporating cases of Naber and Siebers	154
Table 6.3 Computational data for evaporating cases of Naber and Siebers	154
Table 6.4 Data for the Computational meshes	155
Table 7.1 Flow conditions of the computed cases	184

Chapter 1

Introduction

1.1 Background

Extensive research has been carried out in the area of gas turbine combustor over the last two decades in order to improve the design of both stationary gas turbines for power generation and aero-propulsion gas turbines. The principal objectives of these investigations are to improve the combustion process in order to achieve higher combustion efficiency with a uniform exit temperature and allowable liner wall temperature distributions and to reduce combustion-generated emissions.

A key characteristic of gas turbine combustor performance is the emission of NO_x . Although the emissions of unburned hydrocarbons and carbon monoxide have been greatly reduced through the design process, the problem of NO_x emission still requires significant improvement in combustor design [64]. Problems like acid rain and stratospheric ozone layer depletion increase the concern about the ill-effects of gaseous pollutants and have singled out NO_x as a potentially hazardous component in this regard. Control of NO_x emission from the combustion process thus becomes an important design criterion in modern gas turbine technology.

Gas turbine combustors have traditionally been operated in the non-premixed mode for safety and stability [28,29,49]. Unfortunately, this mode leads to unacceptable high levels of thermal NO_x , which is produced in the high-temperature, near-stoichiometric regions. As a result, combustor designers have sought non-stoichiometric fuel-air ratios in both rich and lean ranges. Rich-burn combustion reduces NO_x by limiting the amount of oxygen present for high

temperature combustion. Combustors like these are often labelled Rich-burn Quick-quench Lean-burn (RQL). In a RQL combustor, a rich burn primary zone is followed by a quick quench zone where the combustion gases are diluted before combustion is completed in a cooler lean burn zone. This design concept has been the subject of several studies [e.g. 28,29].

An alternative to RQL is Lean-Premixed Combustion (LPC) [61,96] in which a lean combination of fuel and air is premixed and pre-vaporized prior to introduction into the combustor. With LPC, the amount of post-combustion dilution air is reduced, and the combustion zone is operated with excess air to reduce the flame temperature. A combustion zone equivalence ratio of 0.4-0.6 is typical [82,83]. In addition, the fuel and air are premixed to eliminate stoichiometric regions [27]. The flame is cooler and thermal NO_x is virtually eliminated. However, combustion efficiency is reduced at the lower temperatures of LPC. In addition, stability limits are significantly reduced by pre-mixing the fuel and air and by operating at fuel-lean conditions near the lean flammability limit [26,34], and this may sometimes lead to detrimental damage to combustor systems.

A third approach is called Lean Direct Injection (LDI). LDI differs from LPC in that the fuel is injected directly into the flame zone and thus it does not have the potential for auto-ignition or flashback and should have greater stability. NO_x emission from an LDI can approach those from a LPC but since LDI is not premixed and pre-vaporized, it must provide good atomization and mixing of the fuel quickly and uniformly to maintain low flame temperatures and NO_x levels comparable to those of LPC. The operation of the combustor depends on fuel injectors which can produce a spray of very small droplets that quickly atomize and vaporize. Furthermore, the mixing process is also a key issue for the LDI.

1.2 Physical processes in a LDI gas turbine combustor

A LDI gas turbine combustor is a complex combustion device within which there exist a wide ranges of coupled, interacting physical and chemical phenomena. The liquid fuel used as the energy source must be atomized into smaller droplets in order to increase the surface of fuel exposed to the hot gases and to facilitate rapid evaporation and mixing with the oxygen rich ambience. The combustion process and emissions are mainly influenced by the atomization of the liquid fuel, the motion and evaporation of the fuel droplets and mixing of fuel and air. Spray dynamics and combustion studies are extremely important to determine flame stability behavior at widely varying loads and under different operating conditions, to ensure safety and efficient utilization of energy, as well as to better understand the mechanisms of pollutants formation and destruction.

The spray combustion process can be divided into five elements: atomization, transport, vaporization, unmixedness and combustion. In general, liquid fuel is injected through a nozzle system into the combustor chamber and is atomized to form a spray of droplets. In the atomization region, the liquid fuel disintegrates into ligaments and droplets. The dense spray region has significant liquid volume fraction and includes secondary break-up of droplets and ligaments as well as droplet-droplet interactions, such as collisions and coalescence. In the dilute spray region, droplets are well formed and have strong interaction with turbulent airflow. In general, a spray structure depends on the injection pressure difference, injector size, fuel viscosity, fuel density, and ambient gas conditions. With the initial injection velocity, fuel droplets penetrate into the high temperature air. The fuel spray advances with time until droplets are vaporized by the hot air and combustion gas.

In a spray plume, fuel droplets heated by the surrounding hot air and combustion gas start to vaporize when the droplet temperature reaches the boiling point. The rate of vaporization depends mainly on the droplet size, boiling point and latent

heat of fuel liquid, gas temperature, and relative velocity between droplets and gas phase. The fuel vapor mixes with the entrained air in the spray plume. The mixture starts to burn when the gas temperature reaches the ignition point and fuel/air mixture ratio is within the flammability limits. The burning produces heat and combustion products. The combustion products include mainly CO_2 , H_2O , and a small amount of pollutants such as NO_x .

1.3 Computational methods

The hostile combustion environment of a gas turbine combustor makes detailed measurements very difficult. Furthermore, parametric evaluation of design parameters experimentally is economically very expensive and may not provide sufficient insight since detailed measurements are difficult to achieve. Moreover, to characterize the mixing process, details at small scales are needed. Non-intrusive experimental techniques have some inherent limitations in terms of resolving these small-scale details. For example, the near field of a liquid fuel injector has never been properly investigated due to difficulties in carrying out measurements in dense droplet regime. Structure of complex three-dimensional, swirling fuel-air mixing layers is also very difficult to be resolved using current experimental methods.

Recently, it has become apparent that an understanding of the mechanisms relating to fuel vapor formation, subsequent mixing and combustion is the key to the development of non-polluting and high performance combustion systems. An important approach is to use advanced computer models for fundamental studies as well as practical devices. The development of advanced computers with large memories and high speed processors has enabled researchers to numerically solve comprehensive models for the underlying physical and chemical processes involved in spray combustion.

The numerical simulation of flow field in a spray combustor is exceedingly complex and challenging. The turbulent mixing and combustion occur in a three-dimensional, time-dependent system with two-phase turbulent flows, and chemical reactions, which are not yet completely understood. The interactions among the different physical phenomena (turbulence, multi-phase flow and phase change) are highly non-linear. This further increases the complexity of the problem. In the mean time, the combustion characteristics are greatly affected by

the spray characteristics. The formation of NO_x and other pollutants are closely related to the spray combustion process itself. Other contributing factors include turbulence, radiation heat transfer, and fuel-air mixing. These factors are generally interrelated to one another. Computational fluid dynamics (CFD) models have become increasingly important in gaining insight of such complex processes and help supplement experimental verification by providing physical insight into the processes that directly control the combustion processes. Since the physics of the processes of interest is time-dependant, a simulation tool that is capable to capture the spatial-temporal evolution plays an important role in the design cycle of future gas turbine engines, which offers improved combustion performance and reduced emissions while not compromising fuel economy.

The numerical simulation of the unstable turbulent flow in a gas turbine combustor is a complicated task due to the highly nonlinear coupling of several different physical processes such as combustion chemistry, acoustic and turbulent fluid dynamics. The majority of the current numerical methods for a gas turbine combustor flow simulation are based on Reynolds or Favre averaging of the Navier–Stokes equations (RANS) which model all turbulent length-scales (e.g. using the standard $k - \varepsilon$ model). In the Reynolds averaged approaches, all turbulent unsteadiness is averaged out. The non-linear terms in the Navier-Stokes equations give rise to the Reynolds stress term in the Reynolds averaged Navier-Stokes equations. This term must be modeled if the equations are to be closed. The complexity of turbulence makes it unlikely that any single model will be able to represent all turbulent flows. Despite its popularity and low computational cost, the RANS methods such as standard $k - \varepsilon$ suffer from several deficiencies. It is not suitable for modelling swirling flow [111] which is often present and desired in combustors. Therefore, *ad hoc* modifications to the turbulent energy dissipation equation are necessary to provide satisfactory results. It also tends to incorrectly predict recirculation regions [46]. Predictions of these flow structures are important since the location of recirculation regions can influence the residence

time involved in NO_x production [76] and increase the residence time for liquid fuel evaporation. Finally, the RANS methods often under-predict large velocity gradients due to the more diffusive nature of this model [98].

Direct numerical simulation (DNS) is a method in which all of the scales of a turbulent flow are computed. A DNS must solve all scales from the large energy-containing or integral scales to the dissipative scales; the latter is usually taken to be the viscous or Kolmogoroff scales. For any reasonable Reynolds number, this requires a large number of grid points and is very costly. Despite the cost, the ability of DNS to resolve all the turbulent scales has made it a valuable tool for investigating the physics of turbulence in a number of simple flows. The direct calculation of a gas turbine combustor is currently not possible due to the extreme computational cost. Despite the dramatic increase in computational power, this technique will most likely remain as a research tool within the foreseeable future.

Large eddy simulation (LES) represents a potentially powerful and promising method for overcoming many of the limitations of RANS and DNS approaches. LES involves a direct, three-dimensional and time-dependent computation of the large-scale turbulent motions responsible for turbulent mixing whilst those with scales smaller than the computational grid are modeled. Currently, LES appears to be the only feasible simulation methodology which is capable of capturing unsteady turbulent dynamics within the constraint of the existing computational limits. In LES, all turbulent length-scales larger than a specified cut-off (e.g. grid size) are resolved in both space and time while modelling is employed only for those small, unresolved scales (referred to as subgrid scales or SGS). Larger eddies, those on the order of the geometric length-scale, are highly-anisotropic and energetic. Their dynamics is strongly dependent on the geometry of the system; while small eddies are more isotropic and less energetic, they are easy to be modelled. Due to the nature of the turbulent energy cascade, energy transfers from large to small scale. To accurately predict the small-scale property of the

flow, the dynamics of the large, energy-containing eddies must therefore be fully captured in the numerical model.

1.4 Approaches to spray modeling

The gas-spray interactions comprise a number of processes such as atomization, droplet breakup, collision/coalescence and transfer of mass, momentum and energy between different phases. This is achieved by assembling a number of sub-models which describe particular processes.

Two approaches have been used in the literatures to predict the flow properties in situations where a spray of droplets is injected into a turbulent gas field, i.e. Eulerian-Lagrangian and the Eulerian-Eulerian approaches. In the first approach, Eulerian conservation equations are applied to the gas phase with the assumption of insignificant influence of local flow discontinuities induced by the presence of droplets in the gas phase. Lagrangian equations of the droplet motion are written and the thermal balance equations are applied to a finite number of droplet size ranges representing the size distribution within the spray. The trajectory of the droplets is computed through the flow field. This is the liquid droplet spray model and was initially used by Crowe et al. [31] for a spray cooling problem. It has also been employed for diesel engine sprays by Dukowicz [35] and by O'Rourke and Bracco [90]. In the second approach initially used by Williams [134], the spray was modeled through a conservation equation for a statistical distribution function, defined as the number of droplets per unit droplet diameter and velocity and spatial volume. The second approach is fully Eulerian and is quite expensive in terms of computer storage and CPU time unless several simplifications are introduced.

According to Berlemont et al. [14], the Lagrangian approach has the advantage of being able to account for the instantaneous flow properties encountered by the particles. A second cited advantage of the Lagrangian approach is the possibility to readily handle the evolution of the distribution of particle diameters, which is difficult to predict in Eulerian approach. It is also known that the Eulerian approach suffers from numerical diffusion particularly on coarse computational

grids [35]. In a gas turbine combustor, the Lagrangian approach is known to be adequate and generally favored.

When fuel blobs are injected into a combustor, these blobs are subject to break up. The most popular spray break-up models are TAB (Taylor Analogy Breakup) model [89] and wave model [97]. In the TAB model, oscillations of the parent droplet are modelled in the framework of a spring mass system and break up occurs when the oscillations exceed a critical value. In the wave model, new droplets are formed based on growth rate of the fastest wave instability on the surface of the parent blob. Tanner [122] extended the TAB model to an enhanced TAB model (ETAB), where the product droplet size was obtained via a break-up cascade modelled by an exponential law. The parameters of this distribution function were derived from experimental data to achieve better performance of the model.

Droplet collision is important for a dense spray. Most of the current spray collision models follow that of O'Rourke [87], which is based on the proposals for computing collision process in rain clouds by Brazier-Smith et al. [19]. O'Rourke's algorithm is consistent with the stochastic nature of spray simulations, where only a sub-sample of droplets is tracked. The tracked drops represent particles or parcels of varying numbers of drops. This model assumes that droplets in a parcel distribute evenly among the cell in which the parcel lies and a given parcel may collide with another parcel only if these two parcels reside in the same computational cell. The model is, therefore, strongly depends on the adopted computational mesh, as pointed out by Gavaises [41]. The problem of mesh dependency is particularly severe when using a Cartesian mesh [107].

Nordin [85] corrected O'Rourke model by assuming that collisions can only occur if the trajectories of two parcels intersect and the intersection point is reached at the same time within the integration time step. Nordin also abandoned the assumption that parcels distribute uniformly in the cell they reside, by ignoring

the distribution of droplets in a parcel. In stead of using the kinetic theory to determine the collision frequency, the collision frequency is computed from the distance between the two colliding parcels as no grid information is required in this model. The collision model is grid-independent. However, in this model, the collision frequency has no connection with the droplet density. This is physically untrue. In reality, the denser the droplets, the more chances collisions may happen. Moreover, Nordin assumes collision occurs only if two parcels move towards each other. This is also untrue as not all droplets in a parcel cluster on one point.

Schmidt and Rutland [107] proposed a new collision algorithm based on the No Time Counter (NTC) method used in gas dynamics for Direct Simulation Monte Carlo (DSMC) calculations. There are two significant improvements with the NTC algorithm. Firstly, the NTC method involves stochastic sub-sampling of the parcels within each mesh cell instead of sampling all the parcels in the cell, therefore the NTC method is quite efficient. Secondly, a new set of collision mesh is adopted in the NTC method, which is independent of the flow computational mesh. The collision mesh is cylindrical, and can achieve very high spatial resolution without incurring significant CFU cost. By inducing a second set of mesh, the NTC method can reduce the grid dependence. However, the NTC method can only be applied to the case of a single injection due to the limitation of one set of collision mesh. Moreover, the NTC model inherits the assumption that only parcels which reside in the same cell have chances to collide no matter how far/close they are from each other.

1.5 Previous studies on LES of gas turbine combustor

LES of gas turbine combustor has been an active area of research for the last decade. LES techniques are receiving increased interest in the field due to their potential to capture features of the flow field that are currently out of reach of other modeling techniques. However, the complex geometrical aspects of common industrial devices, which drastically increase the cost of performing good-quality LES, together with the issues related to incorporating sufficiently accurate spray and combustion models still impose considerable limitation on the application of LES to practical gas turbine combustor. Major contributions to the LES of gas turbine combustor are summarized in the following.

Mare et al. [71] employed LES to predict temperature and species concentrations in a model can-type gas turbine combustor operating in a non-premixed combustion regime. The subgrid scale stresses have been modelled using the standard Smagorinsky-Lily model, whilst combustion has been accounted for using a conserved scalar approach. The complex flow pattern developing from the interaction of a strongly swirling flow in the primary zone with the impinging primary jets has been captured by the simulations in great detail. The in-house LES code BOFFIN (Boundary Fitted Flow Integrator) was used to solve the filtered LES equations. The code employs Cartesian velocity components and a boundary conforming general curvilinear system with a collocated variable storage arrangement. It was based on a fully implicit low-Mach-number formulation and second order accurate in space and time. For the convection term of the momentum equation, an energy-conserving discretisation scheme was used. All other spatial derivatives were approximated by standard second-order central differences, except for the convective terms in the filtered mixture fraction equation. A centred discretisation of these terms might result in overshoots and undershoots in the mixture fraction for cell Peclet numbers greater than 2. To avoid this, a TVD (Total Variation Diminishing) scheme [118] was used to discretise the convection terms in the mixture fraction transport equation. Time

derivatives were approximated by a three-point backward difference scheme with variable time step. A four-step second-order time-accurate approximate factorisation method was applied to determine the pressure and ensure mass conservation in conjunction with a Rhie and Chow pressure smoothing technique [100] to prevent even-odd node uncoupling of the pressure and velocity field.

Huang et al. [58] conducted a comprehensive LES numerical study of the combustion dynamics in a lean-premixed swirl-stabilized combustor. Finite-rate chemical reactions and variable thermo-physical properties were taken into account. A compressible-flow version of the Smagorinsky model was employed to describe subgrid scale turbulent motions and their effect on large-scale structures. A level-set flamelet library approach was used to simulate premixed turbulent combustion. The governing equations and the associated boundary conditions were solved by means of a four-step Runge-Kutta scheme along with the message passing interface parallel computing architecture. The analysis allowed for a detailed investigation into the interaction between turbulent flow motions and oscillatory combustion of a swirl-stabilized combustor. Several physical processes responsible for driving combustion instabilities in the chamber were also identified and quantified, including the mutual coupling between acoustic wave motions, vortex shedding, and flame oscillations. In particular, the mechanisms of energy transfer from chemical reactions in the flame zone to acoustic motions in the bulk of chamber were carefully studied. The governing equations in the study were solved numerically by means of a density-based, finite-volume methodology. The spatial discretization employed a second order central-differencing scheme in generalized coordinates. A fourth order matrix dissipation with a TVD switch developed by Swanson and Turkel [117] was employed to ensure computational stability and to prevent numerical oscillations in regions with steep gradients. Temporal discretization was obtained using a four-step Runge-Kutta integration scheme.

Caraeni et al. [20] studied the interaction of turbulence, temperature fluctuation, liquid fuel transport, mixing and evaporation using LES. In their study, the gas phase was handled using an Eulerian formulation while the Lagrangian form was employed to capture the spray dynamics. The gas phase velocity field used in the particle equation motion was obtained using only the filtered LES velocity. Models for droplet break-up and coalescence and evaporation were included. Droplets below a predefined cut-off size were assumed to vaporize instantaneously. The spray models were derived from those of KIVA. Dynamic SGS models were used to model the unresolved subgrid scales. The incompressible Navier-Stokes equations for the Euler part of the problem were solved using finite-differences on a stretched grid of fourth-order accuracy. The filtered Navier-Stokes equations were discretized on an analytically stretched staggered Cartesian grid. The derivatives were approximated by a fourth-order central finite difference, except for the convective terms. The convective terms were discretized using a third-order upwind biased scheme. The equations were split in time. The momentum equations are integrated explicitly using a third-order four-step Runge-Kutta method. The pressure was updated by solving a Poisson equation for the pressure correction using a multi-grid solver.

Apte et al. [8] applied LES to a particle-laden, swirling flow in a coaxial-jet combustor. A mixture of air and lightly loaded, spherical, glass-particles with a prescribed size-distribution entered the primary jet, while a swirling stream of air flowed through an annulus. The incompressible, spatially filtered Navier-Stokes equations were solved on unstructured grids to compute the turbulent gas-phase. A Lagrangian formulation and an efficient particle-tracking scheme on unstructured meshes were developed to compute the dispersed phase. The particles were treated as point sources so they influence the gas phase only through momentum-exchange terms. The particle-dispersion characteristics were examined in detail and in particular, the dependence of particle trajectories and residence times upon particle sizes was emphasized. The mean and turbulent

quantities for the gas and particle phases were compared with experimental data and good agreement was obtained.

LES of an industrial gas turbine burner were carried out for both nonreacting and reacting flows using a compressible unstructured solver by Selle et al. [110]. Results were compared with experimental data in terms of axial and azimuthal velocities (mean and RMS), averaged temperature. Combustion was modelled with a reduced two-step mechanism of methane-air combustion and a thickened flame model. The regime of combustion was partially premixed and the computation included part of the swirler vanes. The LES solver AVBP solved the full compressible Navier-Stokes equations on hybrid (structured and unstructured) grids. Subgrid stresses were described by WALE model [84]. The flame/turbulence interaction was modelled by the TF approach [6]. The numerical scheme used third-order spatial accuracy and third-order time accuracy.

Lo and Sung [67] performed a large eddy simulation for turbulent flow around a bluff body inside a sudden expansion cylinder chamber, a configuration which resembles a premixed gas turbine combustor. The Smagorinsky model and the Lagrangian dynamic subgrid scale model were employed. The calculated Reynolds number was 5,000 based on the bulk velocity and the diameter of inlet pipe. The simulation code was constructed by using a general coordinate system based on the physical contravariant velocity components. The predicted turbulent statistics were evaluated by comparing with the LDV (Laser-Doppler Velocimetry) measurement data. The agreement of LES with the experimental data was shown to be satisfactory. Emphasis was placed on the time-dependent evolutions of turbulent vortical structures behind the flame holder. The numerical flow visualizations depicted the behaviour of large scale vortices. The second-order Adams-Bashforth scheme was used for the time discretization. The second-order central difference scheme was employed for the diffusive and convective terms.

Menon et al. [73] performed LES of large-scale combustors. The governing equations of motion for an unsteady, compressible, reacting, multi-species fluid were employed in their study. A non-equilibrium model [74] using a transport equation for the sub-grid kinetic energy was used as a SGS model. This one-equation SGS model allows the use of relatively coarse mesh in a LES calculation. The LEM (Linear Eddy Model) model of Kerstein et al. [62] was used for the subgrid scalar closure. In the LEM method, all the physical processes such as molecular diffusion, small and large scale turbulent convection and chemical reaction are modelled separately, but concurrently at their respective time scale. Moreover, with this LEM method, no LES combustion model is needed. The governing LES equations were solved using a finite-volume formulation in which the integral form was integrated over a discrete control volume. An explicit, second-order accurate in time and fourth-order in space Predictor-corrector scheme was used. In this scheme, two one-sided, second-order accurate differences were combined to give an overall fourth-order accurate formulation.

Reynolds et al. [99] conducted LES of an aircraft gas turbine combustor. Spray combustion was investigated in their study. An unstructured LES solver called CDP had been developed and validated. The code used a novel approach that solves the Navier-Stokes equations in a low-Mach number form on an unstructured mesh, retaining important energy conservation properties. A dynamic procedure was used to compute the subgrid terms. The time advancement was fully implicit. The second-order Crank-Nicholson scheme was used for both convection and viscous terms. The convection terms were linearized prior to solution. The droplets were modelled as point particles which satisfy the Lagrangian equations. A novel stochastic approach [7] for droplet break-up which accounts for a range of droplet sizes was used in the code. A hybrid scheme [7] involving the computation of both individual droplets and particles was also proposed for the LES code.

In summary, most of the previous LES studies of gas turbine combustor were focused on combustion [58, 71, 73, 99, 110] and very rare LES studies [20] were made for fuel air mixing in gas turbine combustors. The work of Caraeni et al. [20] has brought important advance in LES applications to fuel air mixing. But it has involved simplified assumptions on the temperature field and suffers from the lack of validation. Their attempt to combine the simulation of fuel flow in the swirlers, the injection nozzle and the combustion chamber also makes it difficult to judge the accuracy of the individual components of the model. Furthermore, important information on SGS velocity is absent in their study.

1.6 KIVA-3V code

In order to achieve the objective of the present study which is to develop a CFD tool for performing reliable large eddy simulation of the compressible evaporating two-phase turbulent flow in a gas turbine combustor, the KIVA-3V code [2-4] originally developed by Los Alamos National Laboratory is used as a baseline code. KIVA-3V is selected as it is not only well established in the IC engine community but also has applications in the field of gas turbine combustors [25,136,137]. A brief overview about the KIVA-3V code is given below to facilitate the description of the present work. Further details about the code can be found in the original references by Amsden et al. [2-4,25,136,137].

KIVA-3V is the latest version of KIVA family code developed by Amsden et al. [4] at Los Alamos National Laboratory. It is a RANS based CFD code for numerical calculations of transient two- and three-dimensional chemically reactive fluid (mixture of ideal gases) flows, coupled to the equations for a single-component vaporizing fuel spray. KIVA-3V is capable of solving compressible turbulent flows, either subsonic or supersonic with wall heat transfer effects.

The original KIVA code was publicly released in 1985 [5] and was replaced by the improved version KIVA-II in 1989 [2]. The earlier versions were quite inefficient when applied to complex geometries as the entire domain of interest had to be encompassed within a single-tensor-product mesh with fixed index offset in all three directions. This could result in a large number of deactivated cells.

KIVA-3 [3] removed this handicap by the use of a block-structure mesh which entirely eliminated the need to create regions of unused cells. In addition, arrays are sorted, which minimized the length of vector loops and eliminated testing on cell and vertex flags. Furthermore, the boundary condition data was stored in tables that allow KIVA-3 to sweep in shorter vectors over only those vertices or cells involved. KIVA-3V uses the same solution algorithms and solves the same set of equations as KIVA-3 and KIVA-II with the exception of the introduction of an effective valve model.

KIVA code solves the unsteady equations of motion of a turbulent, chemically reactive mixture of ideal gases, coupled to the equations for a single-component vaporizing fuel spray. The gas-phase solution procedure is based on a finite-volume method called the ALE (Arbitrary Lagrangian Eulerian) method. This approach was initially proposed by Hirt [57] to solve a wide-range of moving boundary problems. Spatial differences are formed on a finite-difference mesh that subdivides the computational region into a number of small cells that are hexahedrons. The positions of the vertices may be arbitrarily specified functions of time, thereby allowing a Lagrangian, Eulerian, or mixed description. The arbitrary mesh can conform to curved boundaries and can move to follow changes in combustion chamber geometry. The strength of the method is that the mesh need not be orthogonal. The spatial differencing is made conservative wherever possible. The procedure used is to difference the basic equations in integral form, with the volume of a typical cell used as the control volume, and with divergence terms transformed to surface integrals using the divergence theorem.

The Cartesian components of the velocity vector are stored at cell vertices, and the momentum equations are differenced in a strictly conservative fashion. In contrast to the original ALE method however, cell-faced velocities are used during a portion of the computational cycle. Their use greatly reduces the tendency of the ALE method to parasitic velocity modes, thereby largely eliminating the need for node coupler.

The transient solution is marched out in a sequence of finite time increments called cycles or time steps. On each cycle the values of the dependent variables are calculated from those on the previous cycle. As in the original ALE method each cycle is divided into two phases-a Lagrangian phase and a rezone phase. In the Lagrangian phase the vertices move with the fluid velocity, and there is no convection across cell boundaries. In the rezone phase, the flow field is frozen, the vertices are moved to new user-specified positions, and the flow field is remapped or rezoned onto the new computational mesh. This remapping is accomplished by convecting material across the boundaries of the computational cells, which are regarded as moving relative to the flow field.

Time integration can be explicit, semi-implicit or fully implicit. In certain problems, when time steps are small enough, KIVA automatically uses stable explicit schemes for which no costly iterative solution is required. When time steps are not suitable for explicit marching, a semi-implicit time advancement option is employed. In this partially implicit difference scheme there is some weighting of the old- and new-time values of the solution variable, i.e.,

$$Q^{n+1} = \phi Q^{n+1} + (1 - \phi)Q^n \quad (1.1)$$

Where $n+1$ is the new time level, n is the old time level, Q is a field variable, and ϕ is the associated implicitness factor. Numerical experiments have shown that this approach improves the computational efficiency without degrading the

numerical stability. For this purpose two separate implicitness factors are calculated in KIVA: ϕ_p for terms associated with pressure wave propagation and ϕ_D for diffusion terms. The couple implicit equations are solved by a method similar to the SIMPLE algorithm, with individual equations being solved by the conjugate residual method [88].

Explicit methods are used to calculate convection in the rezone phase, but the convection calculation can be sub-cycled an arbitrary number of times, and thus the main computational time step is not restricted by the Courant stability condition of explicit methods. The convection time step is a sub-multiple of the mean computational time step and does satisfy the Courant condition.

The code gives the user the option of using different convection schemes: A Quasi Second Order Upwind (QSOU) scheme [2] and a Partial Donor cell (PDC) scheme. The QSOU scheme is a flux-limited monotonic scheme which approach second order accurate when convecting smooth profiles. Based on the α and β parameter values, PDC option can give various schemes such as pure donor cell and central differencing etc.

Two kinds of turbulence models are available in KIVA code: (1) standard version of the $k - \varepsilon$ turbulence model modified to include volumetric expansion effects and spray/turbulence interactions, and (2) the Renormalization Group (RNG) theory variant of the $k - \varepsilon$ model proposed by Han and Reitz [51].

Evaporating liquid spray is represented by a discrete-particle technique [35], in which each computational particle represents a number of droplets of identical size, velocity, and temperature. Monte Carlo sampling technique is used to determine the droplet properties. The particles and fluid interact by exchanging mass, momentum, and energy. The momentum exchange is treated by implicit coupling procedures to avoid the prohibitively small time steps that would

otherwise be necessary. Accurate calculation of mass and energy exchange is ensured by automatic reduction in the time step when the exchange rates become large. Turbulence effects on the droplets are accounted for in one of two ways. When the time step is smaller than the droplet turbulence correlation time, a fluctuating component is added to the local mean gas velocity when calculating each particle's mass, momentum, and energy exchange with the gas. When the time step exceeds the turbulence correlation time, turbulent changes in droplet position and velocity are chosen randomly from analytically derived probability distributions for these changes. Droplet breakup, collisions and coalescences are also accounted for.

Several researchers have attempted to modify KIVA for LES calculations. Sone et al. [114] carried out such modification by directly incorporating a one-equation SGS model and a LEM model into the code. Their modified LES version has the following new features: (1) a one-equation model for the subgrid kinetic energy which is used to close the subgrid stresses and heat flux, (2) a subgrid scalar mixing and combustion model that simultaneously takes into account turbulent mixing between species and molecular diffusion at the subgrid scales. The authors made no attempt to improve the numerical accuracy, and the dissipative quasi second-order upwind scheme QSOU is still retained for the advection term in the momentum equation.

Lee et al. [66] also attempted to use KIVA to perform LES calculations of Diesel Engines. In their study, a one-equation LES sub-grid scale model from Menon et al. [75] was used for simulating the diesel combustion process. In addition, based on the one-equation methodology of Menon et al., a new one-equation LES scalar transport model was formulated. These models allowed for the turbulent transfer coefficients for both momentum and scalar flux to be determined independent of each other. A Probability Density Function (PDF) combustion model was used to model the diesel combustion process. The authors made no improvement to the numerical accuracy of the KIVA code.

Huijnen et al. [59] implemented LES into KIVA-3V and validated the code in a fully developed flow through a rectangular duct of square cross section. Three subgrid scale models (Smagorinsky, WALE and Vreman SGS model) were implemented. The adapting local eddy viscosity (WALE) model is based on the traceless symmetric part of the square of the velocity gradient tensor. Vreman SGS model is similar to WALE model and needs only local filter information and first order velocity derivatives. The accuracy of the convective scheme was improved by the non-linear TVD scheme of Hirsch [56]. However, no attempt was made to improve the time accuracy of the original KIVA-3V code.

Gel [43] substantially modified KIVA-3 into a parallel version LES code. In his study, the time accuracy of the code was made fully second-order by implementing a combination of two-stage Runge-Kutta and Adams-Bashforth schemes into the convection phase. Spatial accuracy was also improved substantially by introducing a third convection scheme combination where central differencing and quasi-second order upwinding (QSOU) schemes are used together. However, the author made no improvement to the spray model.

1.7 Present contributions

The present study is concerned with LES of compressible evaporating two-phase flows in gas turbine combustors. In order to achieve this objective, the KIVA-3V code has been substantially modified to facilitate LES calculations. Both the temporal and the spatial accuracy have been improved. A one-equation SGS model and a two-way coupling spray model taking into account the effect of SGS velocity have been also implemented in the code. The modified LES version of the KIVA code, which will be referred as KIVA-LES, has also been validated against experimental results. The following major contributions have been made in this study:

- The spatial and temporal accuracy of the code has been improved to second order to satisfy the accuracy requirement of LES calculations. The temporal accuracy is improved by implementing a combination of a semi-implicit Crank-Nicolson method in Phase B and a two stage MacCormack method [69] in Phase C. Spatial accuracy is improved by using second order central differencing for momentum equations and QSOU for the species density and energy equation to stabilize the numerical solution.
- A non-equilibrium one-equation SGS model has been implemented. This SGS model uses a transport equation to solve the subgrid kinetic energy. As an additional transport equation is solved, the equilibrium requirement between turbulent kinetic energy production and its dissipation in the small scales is relaxed and hence coarser grid LES is possible.
- A two-way coupling spray model which incorporates the effect of SGS velocity on the dispersion of droplets has been implemented. The SGS velocity can be computed from the subgrid kinetic energy computed in the one-equation SGS model.
- To ensure sufficient particle numbers to capture the dynamic droplet dispersion process in LES, the ETAB breakup model coupled with a new hybrid droplet-particle algorithm has also been implemented into the code.

- The pre-processor and post-processor are also intensively modified to accommodate the application of LES.
- KIVA-LES is validated against LES of plane impinging jets. Predictions were carried out for different inflow conditions, which include a natural plane impinging jet with a random perturbation on the inflow plane and a forced plane impinging jet with a Strouhal number of 0.36, locked both in phase and laterally in space. The first simulation was performed to quantitatively study the mean flow and turbulence statistics. The computed field variables and turbulence intensity of streamwise velocity agreed well with the experimental results. The second simulation was performed to study the vortex structures of a forced plane impinging jet. The predictions captured the typical vortex structures of this kind of flow, such as spanwise rollers, successive ribs, cross ribs and wall ribs were reproduced by the simulation, which were also previously detected by the experiment of Sakakibara et al. [103] with digital particle image velocimetry (DPIV) system, but never wholly reproduced in numerical simulations. Moreover, the study has also led to some new findings related to the formation and evolution of successive ribs, cross ribs and wall ribs.
- A new collision model based on the concept of “particle cloud” is proposed and implemented. The new model greatly reduces the grid-dependence of the original O’Rourke model in a Cartesian mesh. The new collision scheme is faster than the O’Rourke’s scheme, as it has abandoned the sampling procedure to compute the collision number.
- The new collision model is validated against analytical solutions of simplified realistic collision problems in a box volume. The grid-independence is checked against spray test cases. The validation has shown that the new model can predict the expected collision numbers of uniformly distributed droplets with good accuracy. It does not show any grid-dependent artefacts.
- KIVA-LES with the new collision model has also been used to predict non-evaporating and evaporating diesel fuel sprays. The computed results are in good agreement with experimental data. The large scale vortical structures are

reproduced by the LES simulations, which cause “branch-like” spray shape and influence the spray penetration depth. The predictions have also captured the differences between the dense and dilute regions. The LES of diesel spray also proves that SGS velocity has a significant influence on the predicted spray angle. Most importantly, grid-convergent results, which were difficult to obtain with the original KIVA-3V, have been readily obtained in the current simulations.

- Finally, KIVA-LES has been used to simulate spray evaporation in a coaxial gas turbine model combustor. The predicted results were compared with some published experimental data. This is a first step towards a more comprehensive numerical analysis of practical industrial combustors where multiple inlets and more complex combustor geometry are encountered. Good agreement with the data is achieved. The predictions have captured the “ring-like” vortex just downstream the annulus and “worm-like” streamwise vortical structure further downstream. The axial droplet mass flux is well predicted. The study has demonstrated the accuracy and reliability of the KIVA-LES and its capability to handle evaporating two-phase flow in the coaxial gas turbine combustor.

1.8 Thesis outline

In Chapter 2, the mathematical formulations for non-reactive two-phase compressible flow are introduced. This chapter starts with a derivation of Favre-Filtered LES gas phase Navier-Stokes Equations followed by the closure of the equations with a one-equation SGS model. Then the sprays models of the dispersed phase are described. Finally, the treatment of boundary conditions and initial condition are described.

Chapter 3 deals with the numerical methods and discretisation of the filtered LES Navier-Stokes equations. The methods of improving temporal and spatial accuracy are detailed in this chapter. The discretization of the governing equations is in the form of Arbitrary Lagrangian-Eulerian (ALE) method. The time solution of the equations is divided into three phases.

Chapter 4 reports on the validation of KIVA-LES for the prediction of plane impinging jets. Simulations were made with different inflow conditions including a natural plane impinging jet with a random perturbation on the inflow plane and a forced plane impinging jet with a Strouhal number of 0.36 locked both in phase and laterally in space. The first simulation was performed to quantitatively study the mean flow and turbulence statistics. The second simulation was performed to study the vortex structures of a forced plane impinging jet detected by the experiment of Sakakibara et al. [103].

In Chapter 5, the accuracy of the new collision model is tested against analytical solutions of simplified realistic collision problems in a box volume. The grid-dependence of the model is also tested against some spray test cases.

In Chapter 6, KIVA-LES is used to predict non-evaporating and evaporating diesel fuel sprays. The computed results are compared with the experimental data

by Hiroyasu and Kadota [55] and Naber and Siebers [81], as well as the predictions of the original KIVA-3V.

In Chapter 7, KIVA-LES is used to simulate spray evaporation in the coaxial gas turbine model combustor. The predicted results are compared with Sommerfeld's experimental results [113].

Chapter 8 summarizes the main findings of the thesis and presents recommendations for future work.

Chapter 2

Mathematical Formulations in the LES Context

This chapter describes the mathematical formulations for non-reactive two-phase compressible flows. The mathematical description is based on the assumption that the fluid is a continuum, in spite of the presence of a liquid phase in the form of droplets, so that all the transport equations arising from the fundamental principles of conservation of mass, momentum and energy can be applied [16,125]. These equations are presented in an Eulerian frame, where the characteristic fluid properties are considered as continuous functions of space and time in an absolute frame of reference. An alternative description is provided for the Lagrangian formulation, in which the dependent variables are the characteristic properties of liquid particles that are followed in their motion. This description will be used later for the dispersed phase.

2.1 What is LES?

The mathematical description of the gas phase takes into account the following features:

- Presence of liquid phase,
- Momentum, heat and mass transfer between the two phases,
- Multi-component composition of gas mixture.

All these features are associated with a turbulent environment, where the field variables fluctuate with a wide range of length and time scales governed by unsteady Navier-Stokes (NS) equations. Among these scales, there are at least one for the energy containing range, and one for the dissipative range. There may be others, but they can be expressed in terms of these. To obtain an exact solution under these circumstances, all the space-time scales of the problem must be taken into account. The discretization has to be fine enough to represent all these scales numerically, i.e. the numerical steps Δx in space and Δt in time must be smaller than the characteristic length and the characteristic time associated with the smallest dynamically active scale of the exact solution. This solution criterion may turn out to be extremely restrictive when the solution to the exact problem contains scales of very different sizes, which is the case for the turbulent flow. For the simplest homogeneous and isotropic turbulent flow, in order to calculate the evolution of the solution in a volume L^3 for a duration equal to the characteristic time of the most energetic scale, we have to solve the NS equations numerically $O(\text{Re}^3)$ times [102]. This would result in an enormous number of discretised equations, whose solution would require computational and storage performances which exceed the limits of existing computers.

In order to reduce the cost of solving unsteady NS equations, a coarser level of description of the fluid system must be introduced. This can be achieved by

picking out certain scales that will be solved directly in the numerical simulation while the others will be modelled. The non-linearity of the NS equation indicates that all the turbulent scales are closely coupled, which implies that these scales cannot be calculated independently of each other. Therefore, the interaction between the resolved and unresolved scale must be considered in a numerical simulation. This is done by introducing additional terms in the equations governing the evolution of the resolved scales to model these interactions.

The above considerations constitute the basic concept of LES. The flow field is decomposed into a resolved scale component, which is solved directly, and a SGS component, which needs to be modelled. This can be regarded as applying DNS to the large resolved scales and RANS to the small unresolved scales. The justification for such a treatment is that the larger scale eddies contain most of the energy, carry most of the transport of conserved properties, and vary most from flow to flow; the smaller scale eddies are believed to be more universal, less dominating and easier to model.

The first task of LES is to distinguish between large and small scales. In order to define these two ranges of scales, a reference or cut-off length has to be determined. Those scales that are of a characteristic size greater than the cut-off length are called resolved large scales, and the others are called unresolved small or subgrid scales. The effect of small scales is included by a statistical model called a subgrid scale (SGS) model.

The scale selection is achieved by a low pass filtering operation. Given a filtering function G , the spatial filtering operation is defined as:

$$\overline{f(x_i, t)} = \int_{\Omega} G(x_i - z_i) f(z_i, t) dz_i, \quad (2.1)$$

where Ω is the filter domain. The filter kernel is a localized function, which is large only when x and z are not far apart. Three kinds of filters are commonly used in LES: Fourier space sharp cut-off filter, Gaussian filter and the Box filter.

- Gaussian filter has the advantage of being smooth and infinitely differentiable in both physical and Fourier space. In fact, its Fourier transform is Gaussian in wave number space.
- Box filter is simply an average over a rectangular region. It is a natural choice when finite difference or finite volume methods are used. Normally, the filter is an average over a grid volume of a finite difference or finite volume mesh, which is tied more closely to the numerical method. According to this definition, \bar{f} is a piecewise constant function.
- Cut-off filter is defined in Fourier space and eliminates all of the Fourier coefficients belonging to wave numbers above a particular cut-off. It is natural to use this filter in conjunction with spectral methods as it leaves more energy in the large scale field than the filters defined above. However, it is difficult to apply to inhomogeneous flow.

Among these filters, the box filter is the most appropriate choice for finite volume method on which KIVA-3V is based. It is, therefore, used in the present study, given by

$$G = \begin{cases} 1/\Delta V, & x_i \in \Delta V \\ 0 & otherwise \end{cases} \quad (2.2)$$

where ΔV stands for cell volume.

As in traditional RANS, it is convenient to use Favre filtering to avoid the introduction of SGS terms in the conservation equation of mass for compressible flows. Usually, Favre-filtering is used for the velocity and temperature, while

normal filtering is applied to the pressure and density [104]. A Favre-filtered (density weighted) variable is defined as

$$\tilde{f} = \overline{\rho f} / \bar{\rho} \quad (2.3)$$

where $\bar{\rho}$ is the spatially averaged density. Flow field f is then decomposed into resolved part \tilde{f} and unresolved subgrid part f' , i.e.

$$f = \tilde{f} + f' \quad (2.4)$$

It should be noted, as stated in Wilcox [133], that Favre averaging eliminates the density fluctuations from the averaged equations. However it does not remove the effect of the density fluctuation on turbulence. Favre filtering is merely a mathematical simplification, not a physical one.

In order to be able to manipulate the Navier-Stokes equations after applying a filter, the following three properties must be satisfied:

➤ Conservation of constants:

$$\bar{a} = a \quad (2.5)$$

➤ Linearity:

$$\overline{\phi + \psi} = \bar{\phi} + \bar{\psi} \quad (2.6)$$

➤ Commutation with derivation:

$$\overline{\frac{\partial \phi}{\partial s}} = \frac{\partial \bar{\phi}}{\partial s}, \quad s = x, t \quad (2.7)$$

Strictly speaking, the properties only apply for the homogeneous and isotropic filter. For non-uniform filters, some commutation error could be introduced [45].

2.2 Unsteady NS equations

Before introducing the LES transport equations, complete unsteady Navier-Stokes equations for compressible turbulent flow with spray are first presented here. For compactness, most of the following equations are written in vector notation with bold symbols representing vector and tensor quantities. The unit vectors in the x -, y - and z - directions are denoted by \mathbf{i} , \mathbf{j} , and \mathbf{k} respectively. The position vector \mathbf{x} is defined by

$$\mathbf{x} = x\mathbf{i} + y\mathbf{j} + z\mathbf{k} \quad (2.8)$$

The vector operator ∇ is given by

$$\nabla = \mathbf{i} \frac{\partial}{\partial x} + \mathbf{j} \frac{\partial}{\partial y} + \mathbf{k} \frac{\partial}{\partial z} \quad (2.9)$$

and the fluid velocity vector \mathbf{u} is given by

$$\mathbf{u} = u(x, y, z, t)\mathbf{i} + v(x, y, z, t)\mathbf{j} + w(x, y, z, t)\mathbf{k} \quad (2.10)$$

where t is time.

In an Eulerian description of a two-phase flow with spray, the complete unsteady transport equations for mass, momentum, and energy are as follows:

Total mass equation:

$$\frac{\partial \rho}{\partial t} + \nabla \cdot (\rho \mathbf{u}) = \dot{\rho}^s \quad (2.11)$$

Mass fraction equation for species m :

$$\frac{\partial \rho Y_m}{\partial t} + \nabla \cdot (\rho Y_m \mathbf{u}) = \nabla \cdot [\rho D \nabla Y_m] + \dot{Y}_m^s \quad (2.12)$$

Momentum equation:

$$\frac{\partial(\rho \mathbf{u})}{\partial t} + \nabla \cdot (\rho \mathbf{u} \mathbf{u}) = -\nabla p + \nabla \cdot \boldsymbol{\sigma} + \mathbf{F}^s + \rho \mathbf{g} \quad (2.13)$$

where

$$\boldsymbol{\sigma} = \mu \left[\nabla \mathbf{u} + (\nabla \mathbf{u})^T \right] - \frac{2}{3} \nabla \cdot \mathbf{u} \mathbf{I} \quad (2.14)$$

Internal energy equation:

$$\frac{\partial(\rho I)}{\partial t} + \nabla \cdot (\rho \mathbf{u} I) = -p \nabla \cdot \mathbf{u} + \boldsymbol{\sigma} : \nabla \mathbf{u} - \nabla \cdot \mathbf{J} + \dot{Q}^s \quad (2.15)$$

Where

$$\mathbf{J} = -K \nabla T - \rho D \sum_m h_m \nabla (\rho_m / \rho) \quad (2.16)$$

State relations:

$$p = R_0 T \sum_m (\rho_m / W_m), \quad (2.17)$$

$$I(T) = \sum_m (\rho_m / \rho) I_m(T), \quad (2.18)$$

$$c_p(T) = \sum_m (\rho_m / \rho) c_{pm}(T), \quad (2.19)$$

$$h_m(T) = I_m(T) + R_0 T / W_m, \quad (2.20)$$

where

ρ_m - mass density of species m

Y_m - mass fraction of species m

ρ - total mass density

\mathbf{u} - fluid velocity

D	- $\frac{\mu}{\rho Sc}$, diffusion coefficient
Sc	- Schmidt number
$\dot{\rho}^s$	- spray source term
p	- fluid pressure
σ	- viscous stress tensor
F^s	- spray source term
g	- gravity
I	- specific internal energy
J	- contributions due to the heat conduction and enthalpy diffusion
T	- temperature
K	- $\mu c_p / Pr$, diffusion/transport coefficient
Pr	- Prandtl number
h_m	- specific enthalpy of species m
\dot{Q}^s	- spray source term
μ	- $\frac{A_1 T^{3/2}}{T + A_2}$, viscosity
A_1, A_2	- constants
I	- unit dyadic.
R_0	- the universal gas constant
W_m	- molecular weight of species m
I_m	- specific internal energy of species m
h_m	- enthalpy of species m
c_{pm}	- specific heat at constant pressure of species m

2.3 Favre-filtered LES gas phase NS equations

Applying the filter in 2.1 to the complete unsteady NS equations in 2.2 and allowing for the above three properties of the filter in 2.1, the unsteady Favre-filtered LES NS equations for compressible flow with sprays can be written as follows:

Total mass equation:

$$\frac{\partial \bar{\rho}}{\partial t} + \nabla \cdot (\bar{\rho} \mathbf{u}) = \bar{\dot{\rho}}^s \Rightarrow \quad (2.21)$$

$$\frac{\partial \bar{\rho}}{\partial t} + \nabla \cdot (\bar{\rho} \tilde{\mathbf{u}}) = \bar{\dot{\rho}}^s \quad (2.22)$$

Mass fraction equation for species m :

$$\frac{\partial \bar{\rho} Y_m}{\partial t} + \nabla \cdot (\bar{\rho} Y_m \mathbf{u}) = \nabla \cdot [\bar{\rho} D \nabla (Y_m)] + \bar{\dot{\rho}}^s \Rightarrow \quad (2.23)$$

$$\frac{\partial \bar{\rho} \tilde{Y}_m}{\partial t} + \nabla \cdot (\bar{\rho} \tilde{Y}_m \tilde{\mathbf{u}}) = \nabla \cdot [\bar{\rho} D \nabla (\tilde{Y}_m) + \phi^{sgs}] + \bar{\dot{\rho}}^s \quad (2.24)$$

Momentum equation:

$$\frac{\partial \bar{\rho} \mathbf{u}}{\partial t} + \nabla \cdot (\bar{\rho} \mathbf{u} \mathbf{u}) = -\nabla \bar{p} + \nabla \cdot \bar{\boldsymbol{\sigma}} + \bar{\mathbf{F}}^s \Rightarrow \quad (2.25)$$

$$\frac{\partial \bar{\rho} \tilde{\mathbf{u}}}{\partial t} + \nabla \cdot (\bar{\rho} \tilde{\mathbf{u}} \tilde{\mathbf{u}}) = -\nabla \bar{p} + \nabla \cdot (\bar{\boldsymbol{\sigma}} + \boldsymbol{\sigma}^{sgs}) + \bar{\mathbf{F}}^s \quad (2.26)$$

Internal energy equation:

$$\frac{\partial \bar{\rho} I}{\partial t} + \nabla \cdot (\bar{\rho} \mathbf{u} I) = -\bar{p} \nabla \cdot \mathbf{u} + \bar{\boldsymbol{\sigma}} : \nabla \mathbf{u} - \nabla \cdot \bar{\mathbf{J}} + \bar{\dot{Q}}^s \Rightarrow \quad (2.27)$$

$$\frac{\partial \bar{\rho} \tilde{I}}{\partial t} + \nabla \cdot (\bar{\rho} \tilde{\mathbf{u}} \tilde{I}) = -\bar{p} \nabla \cdot \tilde{\mathbf{u}} + \bar{\boldsymbol{\sigma}} : \nabla \tilde{\mathbf{u}} - \nabla \cdot (\bar{\mathbf{J}} + \mathbf{H}^{sgs} + \boldsymbol{\psi}^{sgs}) + \dot{Q}^s \quad (2.28)$$

The above filtered equations resemble those of the unfiltered unsteady Navier-Stokes equations in 2.2, except that subgrid terms resulting from the existence of non-linear terms emerge in the equations. The subgrid terms that require closure are:

$$\sigma^{sgs} = \bar{\rho} [\tilde{u}\tilde{u} - \widetilde{uu}] \quad (2.29)$$

$$H^{sgs} = \bar{\rho} [\widetilde{Iu} - \tilde{I}\tilde{u}] + [\overline{pu} - \bar{p}\tilde{u}] \quad (2.30)$$

$$\psi^{sgs} = [\tilde{u}\bar{\sigma} - \overline{u\sigma}] \quad (2.31)$$

$$\phi^{sgs} = \bar{\rho} [\widetilde{Y_m u} - \tilde{Y}_m \tilde{u}] \quad (2.32)$$

These terms represent the subgrid viscous stress tensor, subgrid heat flux, unresolved viscous work and subgrid species mass flux respectively. Their closure will be discussed in the subsequent sections.

2.4 One-equation SGS model

In order to close the filtered equations in 2.3, a one-equation SGS model proposed by Menon et al. [75] is employed to calculate the SGS terms in the filtered equations. Many LES studies adopt the algebraic eddy viscosity model which uses the grid size as the length scale and the resolved rate-of-strain tensor as the time scale. However, the algebraic eddy viscosity model has some serious limitations. For example, this approach requires equilibrium between turbulent kinetic energy production and its dissipation rate in the small scales. This is possible only if a very high resolution LES grid is employed such that only the dissipation scales are unresolved. By using the Menon's approach to solve for the subgrid kinetic energy, the equilibrium requirement can be relaxed and hence coarser grid LES is possible. Furthermore, to model turbulent dispersion of particles, the subgrid kinetic energy provides the required information that is absent in the algebraic model closure. In earlier LES studies by Wang and Squires [131], subgrid kinetic energy equation was explicitly solved to provide additional information to supply velocity variations for the Lagrangian tracking scheme of the particles.

In the one-equation SGS model, the subgrid stress tensor σ^{sgs} is expressed as:

$$\sigma^{sgs} = \bar{\rho} \nu_t \left[\nabla \tilde{u} + (\nabla \tilde{u})^T \right] - \frac{2}{3} \nabla \cdot \tilde{u} I - (2/3) \bar{\rho} k^{sgs} \quad (2.33)$$

Therefore, to complete the closure for subgrid stresses, the subgrid eddy viscosity ν_t and kinetic energy k^{sgs} need to be modelled. The subgrid kinetic energy is defined as:

$$k^{sgs} = [\widetilde{u \cdot u} - \tilde{u} \cdot \tilde{u}] / 2 \quad (2.34)$$

The time evolution equation for the subgrid kinetic energy is given as:

$$\frac{\partial \bar{\rho} k^{sgs}}{\partial t} + \nabla \cdot (\bar{\rho} \tilde{u} k^{sgs}) = P^{sgs} - \bar{\rho} \varepsilon^{sgs} + \nabla \cdot \left(\bar{\rho} \frac{\nu_t}{Pr_t} \nabla k^{sgs} \right) + \dot{w}^s \quad (2.35)$$

where \dot{w}^s is spray source term, P^{sgs} and ε^{sgs} are production and dissipation terms of SGS kinetic energy respectively. According to Chakravarthy and Menon [21],

$$\nu_t = 0.067 \sqrt{k^{sgs}} \Delta, \quad (2.36)$$

$$\varepsilon^{sgs} = 0.916 (k^{sgs})^{3/2} / \Delta, \quad (2.37)$$

and

$$P^{sgs} = -\sigma^{sgs} : \nabla \tilde{u}. \quad (2.38)$$

Δ is a length scale taken to be the cubic root of the cell volume. The coefficient Pr_t is the turbulent Prandtl number and is set to 0.9.

The subgrid heat flux H^{sgs} and the subgrid species mass flux φ^{sgs} are modelled using the eddy viscosity model as follows:

$$H^{sgs} = -[\bar{\rho} \nu_t C_p / Pr_t] \nabla \tilde{T} \quad (2.39)$$

$$\varphi_i^{sgs} = [\bar{\rho} \nu_t / Sc_t] \nabla Y_m \quad (2.40)$$

where C_p is specific heat at constant pressure and Sc_t is the turbulent Schmidt number which is taken to be one.

Another term that requires modelling is the subgrid viscous work term ψ^{sgs} , modelled by SGS turbulent energy dissipation rate $\bar{\rho} \varepsilon^{sgs}$.

2.5 Source terms due to the spray

The following source terms appear due to spray in the filtered Navier-Stokes equation and One-Equation SGS model:

- $\overline{\dot{\rho}^s}$ - mass density source term due to spray species m
- $\overline{F^s}$ - momentum gain rate per unit volume due to the spray
- $\overline{\dot{Q}^s}$ - heat source due to spray interactions
- $\overline{\dot{W}^s}$ - negative rate at which subgrid scales eddies do work to disperse spray droplets.

These source terms are given by:

$$\overline{\dot{\rho}^s} = - \int f \rho_d 4\pi r^2 R dv dr dT_d dy d\dot{y}, \quad (2.41)$$

$$\overline{F^s} = - \int f \rho_d \left(4/3 \pi r^3 F' + 4\pi r^2 R v \right) dv dr dT_d dy d\dot{y}, \quad (2.42)$$

$$\overline{\dot{Q}^s} = - \int f \rho_d \left\{ 4\pi r^2 R \left[I_1(T_d) + \frac{1}{2} (v - \tilde{u})^2 \right] + \frac{4}{3} \pi r^3 \left[c_l \dot{T}_d + F' \cdot (v - \tilde{u} - u') \right] \right\} dv dr dT_d dy d\dot{y} \quad (2.43)$$

$$\overline{\dot{W}^s} = - \int f \rho_d 4/3 \pi r^3 F' \cdot u' dv dr dT_d dy d\dot{y}. \quad (2.44)$$

where $F' = F - g$, F is droplet acceleration and g is gravitational force. The definitions of the variables in the above equation will be defined later. The above source terms are solved by a spray equation [135]. The effects of droplet collision and breakup are included in the equation. Spray droplets are represented by a droplet probability distribution $f(x, v, r, T_d, y, \dot{y}, t)$, which is a function of droplet position x , time t , velocity v , droplet equilibrium radius r , temperature T_d , distortion from a sphere y , and its time rate of change \dot{y} . The droplet distribution

function f is such defined that $f(\mathbf{x}, \mathbf{v}, r, T_d, y, \dot{y}, t) dv dr dT_d dy d\dot{y}$ is the probable number of droplets per unit volume at position \mathbf{x} and time t with velocities in the interval $(\mathbf{v}, \mathbf{v} + d\mathbf{v})$, radii in the interval $(r, r + dr)$, temperatures in the interval $(T_d, T_d + dT_d)$, and displacement parameters in the intervals $(y, y + dy)$, and $(\dot{y}, \dot{y} + d\dot{y})$.

The droplet probability distribution function is governed by the equation:

$$\frac{\partial f}{\partial t} + \nabla_{\mathbf{x}} \cdot (f\mathbf{v}) + \nabla_{\mathbf{x}} \cdot (f\mathbf{F}) + \frac{\partial}{\partial r}(fR) + \frac{\partial}{\partial T_d}(f\dot{T}_d) + \frac{\partial}{\partial y}(f\dot{y}) + \frac{\partial}{\partial \dot{y}}(f\ddot{y}) = \dot{f}_{coll} + \dot{f}_{bu} \quad (2.45)$$

where \mathbf{F}, R, \dot{T}_d , and \ddot{y} are respectively the time change rate of \mathbf{v}, r, T_d , and \dot{y} .

\dot{f}_{coll} and \dot{f}_{bu} are sources due to droplet collisions and breakups.

The collision source term \dot{f}_{coll} is defined by

$$\begin{aligned} \dot{f}_{coll} = & \frac{1}{2} \iint f(\mathbf{x}, \mathbf{v}_1, r_1, T_{d1}, y_1, \dot{y}_1, t) f(\mathbf{x}, \mathbf{v}_2, r_2, T_{d2}, y_2, \dot{y}_2, t) \pi(r_1 + r_2)^2 |\mathbf{v}_1 - \mathbf{v}_2| \\ & \left\{ \sigma(\mathbf{v}, r, T_d, y, \dot{y}, \mathbf{v}_1, r_1, T_{d1}, y_1, \dot{y}_1, \mathbf{v}_2, r_2, T_{d2}, y_2, \dot{y}_2) \right. \\ & - \delta(\mathbf{v} - \mathbf{v}_1) \delta(r - r_1) \delta(T_d - T_{d1}) \delta(y - y_1) \delta(\dot{y} - \dot{y}_1) \} \\ & - \delta(\mathbf{v} - \mathbf{v}_2) \delta(r - r_2) \delta(T_d - T_{d2}) \delta(y - y_2) \delta(\dot{y} - \dot{y}_2) \\ & d\mathbf{v}_1 dr_1 dT_{d1} dy_1 d\dot{y}_1 d\mathbf{v}_2 dr_2 dT_{d2} dy_2 d\dot{y}_2 \end{aligned} \quad (2.46)$$

where collision transition probability function σ is defined so that $\sigma dv dr dT_d dy d\dot{y}$ is the probable number of droplets with properties in the implied intervals that result from a collision between a droplet with subscript 1 properties and one with subscript 2 properties.

Chapter 2 Mathematical Formulations in the LES Context

Two types of collisions are accounted for. If the collision impact parameter $b = \sqrt{YY}(r_1 + r_2)$ (YY is a random number, $0 < YY < 1$) is less than a critical value b_{cr} the droplets coalesce, and if b exceeds b_{cr} the droplets maintain their sizes and temperatures but undergo velocity changes. The critical impact parameter b_{cr} is given by

$$b_{cr}^2 = (r_1 + r_2)^2 \min(1.0, 2.4f(\gamma)/We_L), \quad (2.47)$$

$$f(\gamma) = \gamma^3 - 2.4\gamma^2 + 2.7\gamma, \quad (2.48)$$

$$\gamma = r_2 / r_1 \quad (2.49)$$

where $r_1 \leq r_2$,

$$We_L = \rho_d |v_1 - v_2| r_1 / a(\bar{T}_d), \quad (2.50)$$

and

$$\bar{T}_d = \frac{r_1^3 T_{d1} + r_2^3 T_{d2}}{r_1^3 + r_2^3}. \quad (2.51)$$

The quantity a is the liquid surface tension coefficient. σ is defined by

$$\begin{aligned} \sigma = & \frac{b_{cr}^2}{(r_1 + r_2)^2} \delta \left[r - (r_1^3 + r_2^3)^{1/3} \right] \delta \left[T_d - \frac{r_1^3 T_{d1} + r_2^3 T_{d2}}{r_1^3 + r_2^3} \right] \delta(y - y_2) \delta(\dot{y} - \dot{y}_2) \\ & + \frac{2}{(r_1 + r_2)^2} \int_{b_{cr}}^{r_1 + r_2} [\delta(r - r_1) \delta(v - v_1') \delta(T_d - T_{d1}) \delta(y - y_1) \delta(\dot{y} - \dot{y}_1) \\ & + \delta(r - r_2) \delta(v - v_2') \delta(T_d - T_{d2}) \delta(y - y_2) \delta(\dot{y} - \dot{y}_2)] b db \end{aligned} \quad (2.52)$$

where

$$v_1' = \frac{r_1^3 v_1 + r_2^3 v_2 + r_2^3 (v_1 - v_2) \frac{b - b_{cr}}{r_1 + r_2 - b_{cr}}}{r_1^3 + r_2^3} \quad (2.53)$$

and

$$\dot{v}_2 = \frac{r_1^3 v_1 + r_2^3 v_2 + r_2^3 (v_2 - v_1) \frac{b - b_{cr}}{r_1 + r_2 - b_{cr}}}{r_1^3 + r_2^3} \quad (2.54)$$

The breakup source term \dot{f}_{bu} is given by

$$\dot{f}_{bu} = \int f(x, v_1, r_1, T_{d1}, 1, \dot{y}_1, t) \dot{y}_1 B(v, r, T_d, y, \dot{y}, v_1, r_1, T_{d1}, \dot{y}_1, x, t) dv_1 dr_1 dT_{d1} d\dot{y}_1 \quad (2.55)$$

The breakup transition probability function B is so defined that $B dv dr dT_d dy d\dot{y}$ is the probable number of droplets with properties in the implied intervals that are produced by the breakup of a droplet with subscript 1 properties.

After breakup, the droplet radii are assumed to follow χ^2 distribution:

$$g(r) = \frac{1}{\bar{r}} e^{-r/\bar{r}}, \quad (2.56)$$

where the Sauter mean radius r_{32} is given by

$$r_{32} = 3\bar{r} = \frac{r_1}{\frac{7}{3} + \frac{1}{8} \frac{\rho_d r_1^3}{a(T_{d1})} \dot{y}_1^2} \quad (2.57)$$

The product droplet velocities also differ from that of the parent droplet by a velocity with magnitude w and with direction randomly distributed in a plane normal to the relative velocity vector between the parent drop and gas,

$$w = \frac{1}{2} r_1 \dot{y}_1. \quad (2.58)$$

Then the B takes the form,

$$B = g(r) \delta(T_d - T_{d1}) \delta(y) \delta(\dot{y}) \frac{1}{2\pi} \int \delta[v - (v_1 + wn)] dn, \quad (2.59)$$

where the integral is over normal directions to the relative velocity vector.

The droplet acceleration F has contributions due to aerodynamic drag and gravitational force:

$$F = \frac{3}{8} \frac{\bar{\rho}}{\rho_d} \frac{|\tilde{u} + u' - v|}{r} (\tilde{u} + u' - v) C_D + g. \quad (2.60)$$

The drag coefficient C_D is given by

$$C_D = \begin{cases} \frac{24}{\text{Re}_d} \left(1 + 1/6 \text{Re}_d^{2/3}\right) & \text{Re}_d \leq 1000 \\ 0.424 & \text{Re}_d > 1000 \end{cases} \quad (2.61)$$

where

$$\text{Re}_d = \frac{2\bar{\rho}|\tilde{u} + u' - v|r}{\mu(\hat{T})}, \quad \hat{T} = \frac{\tilde{T} + 2T_d}{3}. \quad (2.62)$$

u' appearing in the above equations is the subgrid velocity. The subgrid velocity is unresolved in LES, which can be derived from the subgrid kinetic energy k^{sgs} in the following way. Since SGS velocity is isotropic, following the original KIVA-3V, each component u' follows a Gaussian distribution with mean square deviation $2/3 k^{sgs}$,

$$G(u') = \left(\frac{4}{3} \pi k^{sgs}\right)^{-3/2} e^{-3|u'|^2 / 4k^{sgs}}. \quad (2.63)$$

The value of u' is chosen once every subgrid correlation time t_{sub} and is otherwise held constant. The droplet correlation time is the minimum of an subgrid eddy breakup time and a time for the droplet to traverse an subgrid eddy, and given by

$$t_{sub} = \min \left(\frac{\Delta}{\sqrt{k_{sgs}}}, c_{ps} \frac{\Delta}{|\tilde{u} + u' - v_p|} \right). \quad (2.64)$$

c_{ps} is an empirical constant set to 0.16 in the current study.

The rate of droplet radius change R follows the Frossling correlation [37],

$$R = -\frac{(\rho D)_{air}(\hat{T})}{2\rho_d r} \frac{Y_1^* - Y_1}{1 - Y_1^*} Sh_d, \quad (2.65)$$

where Sh_d is the Sherwood number for mass transfer, Y_1^* is the fuel vapour mass fraction at the droplet's surface, $Y_1 = \tilde{\rho}_1 / \bar{\rho}$, and $(\rho D)_{air}(\hat{T})$ is the fuel vapour diffusivity in air. The Sherwood number is given by

$$Sh_d = \left(2.0 + 0.6 Re_d^{1/2} Sc_d^{1/3} \right) \frac{\ln(1 + B_d)}{B_d}, \quad (2.66)$$

where

$$Sc_d = \frac{\mu(\hat{T})}{\rho D_{air}(\hat{T})} \quad (2.67)$$

and

$$B_d = \frac{Y_1^* - Y_1}{1 - Y_1^*}. \quad (2.68)$$

The surface mass fraction Y_1^* is obtained from

$$Y_1^*(T_d) = \frac{W_1}{W_1 + W_0 \left(\frac{P}{p_v(T_d)} - 1 \right)}, \quad (2.69)$$

where W_0 is the local average molecular weight of all species exclusive of fuel vapour and $p_v(T_d)$ is the equilibrium fuel vapour pressure at temperature T_d . For the vapour diffusivity in air, the empirical correlation

$$(\rho D)_{air}(T) = D_1 T^{D_2} \quad (2.70)$$

is used, where D_1 and D_2 are constants.

The rate of droplet temperature change is determined by the energy balance equation

$$\rho_d \frac{4}{3} \pi r^3 c_l \dot{T}_d - \rho_d 4 \pi r^2 R L(T_d) = 4 \pi r^2 Q_d, \quad (2.71)$$

where c_l is the liquid specific heat, $L(T_d)$ is the latent heat of vaporization, and Q_d is the rate of heat conduction to the droplet surface per unit area and given by the Ranz-Marshall correlation [37]:

$$Q_d = \frac{K_{air}(\hat{T})(T - T_d)}{2r} Nu_d, \quad (2.72)$$

where

$$Nu_d = \left(2.0 + 0.6 Re_d^{1/2} Pr_d^{1/3} \right) \frac{\ln(1 + B_d)}{B_d}, \quad (2.73)$$

$$Pr_d = \frac{\mu_{air}(\hat{T}) c_p(\hat{T})}{K_{air}(\hat{T})}, \quad (2.74)$$

$$K_{air} = \frac{K_1 \hat{T}^{3/2}}{\hat{T} + K_2}, \quad (2.75)$$

c_p is the local specific heat at constant pressure, and K_1 and K_2 are constants.

Since the latent heat of vaporization L is the energy required to convert a unit mass of liquid to vapour at constant pressure equal to the equilibrium vapour pressure, the liquid and vapour enthalpies and internal energies and L are related by

$$L(T_d) = h_1(T_d) - h_l(T_d, p_v(T_d)) = I_1(T_d) + RT_d/W - I_l(T_d) - p_v(T_d)/\rho_d. \quad (2.76)$$

The equation for the acceleration of the droplet distortion parameter is

$$\ddot{y} = \frac{2}{3} \frac{\rho}{\rho_d} \frac{(u + u' - v)^2}{r^2} - \frac{8a(T_d)}{\rho_d r^3} y - \frac{5\mu_l(T_d)}{\rho_d r^2} \dot{y}, \quad (2.77)$$

where $\mu_l(T_d)$ is the viscosity of the liquid. This equation is based on the analogy between an oscillation droplet and a spring-mass system [123], and it is essentially the equation of a forced, damped harmonic oscillator. The external force is supplied by the gas aerodynamic forces on the droplet. The restoring force is supplied by surface tension forces, and damping is supplied by liquid viscosity.

2.6 Spray models

2.6.1 TAB breakup model

By assuming constant coefficients, the exact solution of Eq. (2.77) is

$$y(t) = \frac{We}{12} + e^{-t/t_d} \left[\left(y(0) - \frac{We}{12} \right) \cos \omega t + \frac{1}{\omega} \left(\dot{y}(0) + \frac{y_0 - \frac{We}{12}}{t_d} \right) \sin \omega t \right], \quad (2.78)$$

Where

$$We = \frac{\rho u^2 r}{a} \quad (2.79)$$

is the Weber number,

$$t_d = \frac{2}{5} \frac{\rho_d r^2}{\mu_l} \quad (2.80)$$

is the viscous damping time, and

$$\omega^2 = 8 \frac{a}{\rho_d r^3} - \frac{1}{t_d^2} \quad (2.81)$$

is the square of the oscillation frequency. A value of $\omega^2 \leq 0$ occurs only for very small droplets for which distortions and oscillations are negligible, so $y_p^{n+1} = \dot{y}_p^{n+1} = 0$ if $\omega^2 \leq 0$.

If $\omega^2 > 0$, the amplitude of the undamped oscillation is calculated by

$$A^2 = \left(y_p^n - \frac{We}{12} \right)^2 + \left(\frac{\dot{y}_p^n}{\omega} \right)^2. \quad (2.82)$$

In the case of $We/12 + A \leq 1.0$, breakup will not happen, since the value of y will never exceed unity. Then y_p and \dot{y}_p is updated by:

$$y_p^{n+1} = \frac{We}{12} + e^{-\Delta t/t_d} \left[\left(y_p^n - \frac{We}{12} \right) \cos \omega t + \frac{1}{\omega} \left(\dot{y}_p^n + \frac{y_p^n - \frac{We}{12}}{t_d} \right) \sin \omega t \right] \quad (2.83)$$

and

$$\dot{y}_p^{n+1} = \left(\frac{We}{12} - y_p^{n+1} \right) / t_d + e^{-\Delta t / t_d} \left[\left(\dot{y}_p^n + \frac{y_p^n - \frac{We}{12}}{t_d} \right) \cos \omega \Delta t - \omega \left(y_p^n - \frac{We}{12} \right) \sin \omega \Delta t \right]. \quad (2.84)$$

If $We/12 + A > 1.0$, then breakup is possible on the current time step. To calculate the breakup time t_{bu} , the drop oscillation is assumed to be undamped for its first period. Then the breakup time is the smallest root greater than t^n of the equation

$$\frac{We}{12} + A \cos[\omega(t - t^n) + \phi] = 1 \quad (2.85)$$

where $\cos \phi = \frac{y_p^n - \frac{We}{12}}{A}$ and $\sin \phi = -\frac{\dot{y}_p^n}{A\omega}$. If t^{n+1} is less than a breakup time t_{bu} ,

then no breakup occurs on the current time step, and Eqs. (2.83) and (2.84) are used to update y_p and \dot{y}_p . Breakup happens only if $t_{bu} \leq t^{n+1}$. The Sauter mean radius r_{32} of the product droplets is calculated from Eq. (2.57), and Eq. (2.58) is used to calculate the velocity w of the product droplets normal to the relative velocity between the parent droplet and gas. The radius r_{bu} of the product droplets is then chosen randomly from χ^2 distribution with Sauter mean radius r_{32} . To conserve mass, the number of droplets N associated with the computational

particle is adjusted according to $N_p^{n+1} = N_p^n \left(\frac{r_p^n}{r_{bu}} \right)^3$. A component with magnitude

w and direction randomly chosen in a plane normal to the relative velocity vector between the parent drop and gas is added to the particle velocity. Following breakup, the product droplets are assumed to be free from distortion and not oscillating, and accordingly $y_p^{n+1} = \dot{y}_p^{n+1} = 0$.

2.6.2 ETAB breakup model with a new hybrid droplet-particle algorithm

Tanner [122] improved the above TAB breakup model by an Enhanced TAB model (ETAB). The ETAB model uses the droplet deformation dynamics from the standard TAB model, but it provides a new strategy for the description of the droplet breakup process. The droplet disintegration is modeled via an exponential law which relates the mean product droplet size to the breakup time of the parent drop. In addition, an energy balance consideration between the parent and product droplets yields an expression for the product droplet velocity components normal to their trajectories.

The main assumption for the modeling of the parent droplet breakup in the ETAB model is that the rate of product droplet generation, $dn(t)/dt$, is proportional to the number of the product droplets, where the proportionality constant, K_{br} , depends on the breakup regime. This assumption leads to

$$\frac{dn(t)}{dt} = 3K_{br}n(t). \quad (2.86)$$

The mass conservation principle between the parent and the product droplets can be expressed as:

$$n(t) = m_0 / \bar{m}(t), \quad (2.87)$$

where m_0 is the mass of the parent droplet and \bar{m} the mean mass of the product droplet distribution. Utilizing the fact that,

$$dn/dt = -m_0 / \bar{m}^2 d\bar{m}/dt, \quad (2.88)$$

the breakup law which relates the product drop size to the breakup time can be derived. The breakup time follows the original TAB's definition.

$$\frac{d\bar{m}}{dt} = -3K_{br}\bar{m}. \quad (2.89)$$

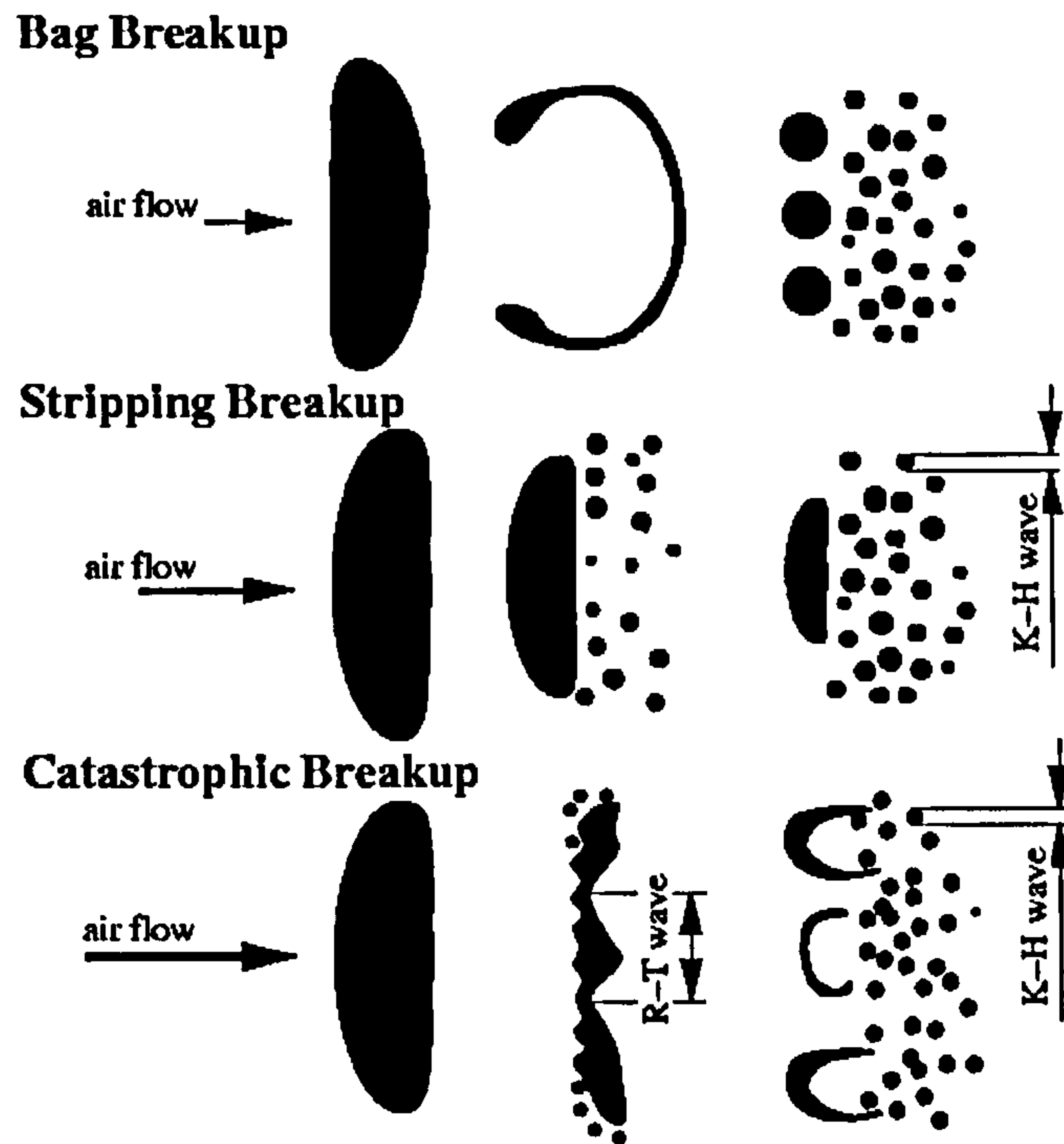


Fig. 2.1 Schematic representation of droplet breakup mechanisms: Bag breakup: $6 < We < 80$, stripping (shear) breakup: $80 < We < 350$, catastrophic (surface wave) breakup: $We > 350$.

The breakup constant K_{br} depends on the breakup regime and is given by parent droplet properties only. According to droplet breakup mechanisms [142], there exist three breakup regimes (see Fig. 2.1). In the ETAB model, stripping breakup and catastrophic breakup are modeled as a single regime. Bag breakup occurs if $We \leq We_c$ and stripping breakup happens if $We > We_c$, with We_c being the regime-dividing Weber number. The breakup constant K_{br} is defined by,

$$K_{br} = \begin{cases} k_1 \omega & \text{if } We \leq We_c \\ k_2 \omega \sqrt{We} & \text{if } We > We_c \end{cases} \quad (2.90)$$

The values of k_1 and k_2 have been determined to match the droplet sizes and velocities from the experimental results of Schneider [109], and have been found to satisfy $k_1 \approx k_2 = 1/4.5$. We_c is set to 80 in the model [142].

In the ETAB model a uniform product droplet size distribution has been assumed. Although this is not true in realistic spray, it is expected to produce good approximations when averaged over many droplet breakups. With this assumption Eq. (2.88) becomes

$$\frac{r}{a} = e^{-K_{br} t}, \quad (2.91)$$

where a and r are the radii of the parent and product droplets, respectively.

As in the standard TAB model, after breakup of a parent droplet, the initial deformation parameters of the product droplets are set to $y_p^{n+1} = \dot{y}_p^{n+1} = 0$. Also the product droplets are initially supplied with a velocity component perpendicular to the path of the parent drop with a value $w = A\dot{y}$, where A is a constant determined from the following energy balance consideration. The energy of the parent droplet is the sum of the surface tension energy and the droplet deformation energy. The second is computed as the product of the aerodynamic drag and the droplet deformation at the stagnation point, estimated to be $5a/9$.

This leads to

$$E_{parent} = 4\pi\sigma a^2 + 5\pi C_D \rho_g a^3 |\mathbf{v}|^2 / 18. \quad (2.92)$$

The energy of the product droplets is given by

$$E_{product} = 4\pi\sigma a^3 / r_{32} + A^2 \pi \rho_l a^5 \dot{y}^2 / 6. \quad (2.93)$$

From Eqs. (2.92) and (2.93), the following relation is obtained,

$$A^2 = 3[1 - a/r_{32} + 5C_D We/72]\omega^2 / \dot{y}^2. \quad (2.94)$$

With approximations this equation becomes

$$A^2 = 5C_D / 4 + 18(1 - a/r_{32})/We. \quad (2.95)$$

With this formulation, only 70% of the parent droplet deformation velocity goes into the normal velocity component of the product droplets. This contrasts with the value $A = 1$ used in the standard TAB model.

The reason to adopt ETAB model in this study is that the original TAB model cannot control the rate of product generation and produce too tiny droplets following the issue of blobs from nozzle exit. Furthermore, the ETAB model can allow adoption of a hybrid droplet-parcel algorithm which is more suitable for LES. In the original spray model in KIVA-3V, only parcels exist in the computational region. The drawback is when the liquid-sheet injected into the computational domain is represented by large blobs, too few parcels can be tracked. The size of droplets are much bigger immediately after injection, therefore they should be tracked separately rather than in the form of parcels. In the proposed new spray model, a critical droplet size is pre-determined. Above the size, droplets are tracked individually. Otherwise they are tracked in the form of parcels. The pre-determined droplet size depends on the computational resources.

2.6.3 O'Rourke collision model

It was shown by Bracco and co-workers [18] that collision processes are important in sprays flow, especially in regions with high droplet number density. Collision is responsible for the growth of the droplets. It also significantly influences the spray penetration due to the exchange of momentum between droplets. In this sense, the collision and breakup processes can be seen as two competing mechanisms which influence the local droplet size distribution.

The collision model in KIVA follows that of O'Rourke [87]. It follows Brazier Smith et al. [19] to compute collision processes in rain clouds, by the statistical discrete-particle method. For each pair of particles, the collision calculation proceeds as follows. The collision calculation is preformed for the pair of particles if, and only if, they are in the same computational cell. To facilitate the description of the collision calculation, the drops of larger radius are called "collectors", and those of smaller radius are called "droplets". For purposes of the collision calculation, the drops associated with each particle are considered to be uniformly distributed throughout the computational cell in which they are located. The collision frequency ν of a collector drop with all droplets is calculated according to

$$\nu = \frac{N_2^n}{V_{ijk}^n} \pi (r_1^n + r_2^n)^2 |\mathbf{v}_1 - \mathbf{v}_2|. \quad (2.96)$$

The subscripts 1 and 2 refer to the properties of the collectors and droplets, N_2^n is the number of droplets in particle 2, and V_{ijk}^n is the volume of the cell in which both particles are located. With this frequency, O'Rourke samples the actual collision number n of a collector with droplets from a Poisson distribution,

$$P_n = e^{-\bar{n}} \frac{\bar{n}^n}{n!}, \quad (2.97)$$

with mean value $\bar{n} = \nu \Delta t$ where Δt is the computational time step. Thus, the probability of no collisions is $P_0 = e^{-\bar{n}}$. A random number XX is chosen in the interval $(0,1)$. If $XX < P_0$, then no collisions are calculated between the drops in particles 1 and 2.

If $XX \geq P_0$, a second random number YY is chosen, $0 < YY < 1$, that determines the outcome of the collision. $\sqrt{YY}(r_1 + r_2)$ is the collision impact parameter b . If $b < b_{cr}$, where b_{cr} is the critical impact parameter below which coalescence occurs, then the result of every collision is coalescence. If $b \geq b_{cr}$, then each collision is a grazing collision. The value of b_{cr} depends on the drop radii, the relative velocity between the drops, and the liquid surface tension coefficient, which is defined in section 2.5.

If the outcome of the collision is coalescence, then the number of coalescences n for each collector is determined by finding the value of n for which

$$\sum_{k=0}^{n-1} P_k \leq XX < \sum_{k=0}^n P_k \quad (2.98)$$

For each collector drop, n droplets are subtracted from their associated particle, and the size, velocity, and temperatures of the collector drops are appropriately modified. If there is an insufficient number of droplets to have n coalesces with each collector, then n is recomputed so that all N_2'' droplets coalesce, and the particle associated with the droplets is removed from the calculation.

There is a time step limitation associated with the above calculation of drop coalescence, and this is that the computational time step Δt must be small compared to the collision time Δt_d for the droplets. That latter is given by

$$\frac{1}{\Delta t_d} = \nu_d = \frac{N_1^n}{V_{ijk}^n} \pi (r_1^n + r_2^n)^2 |v_1 - v_2|, \quad (2.99)$$

where N_1^n is the number of collector drops. When $\Delta t \ll \Delta t_d$, the probable number of droplets that coalesce in a time step, which is $\nu_d \Delta t N_2^n$, will be less than N_2^n . Hence, the number of droplets in particle 2 will not be depleted in one time step due to collisions.

If the outcome of each collision is a grazing collision, only one collision is calculated for each drop. This introduces an additional time step constraint that Δt be small compared to the collision times between drops of nearly equal size, since grazing collisions usually occur between drops of nearly equal size. Grazing collisions are calculated between N pair of drops, where N is the minimum of N_1^n and N_2^n . The N collectors and droplets are then returned to their particles in such a way that mass, momentum, and energy are conserved.

2.6.4 New collision model

The above collision model has well-known weak points, i.e. it is grid-dependant [107]. It is also known to over-predict droplet size [88] and suffers from poor numerical convergence [116], etc. The model performed poorly in Cartesian grid [107], and produced relatively better results in cylindrical grid. Most computational domains of practical interest are complex, in which cylindrical mesh can not be used. A new collision model is proposed to tackle these inherent problems.

The new collision model is based on the assumption of “particle clouds”. The radical reason of grid-dependence of the O’Rourke model is the assumption that the droplets in a particle distribute uniformly in the cell in which they reside and only two particles sharing the same cells have a chance to collide. The newly developed collision model abolishes the above assumption. Droplets are assumed to uniformly occupy a fictitious sphere centred on the particle position. In order to compute the collision frequency, a new variable r_c is introduced, which is the radius of the fictitious sphere. It is determined in the following way. Firstly, the droplet volume density of all particles that lie in a cell is computed, and then the radius of the sphere r_c is defined such that the droplet volume density of the particle occupying the fictitious sphere volume V is the same as that of the cell. For the special case $N_p = 1$, i.e. there is only one droplet in a particle, r_c is set to the droplet radius. An advantage of the definition of r_c lies in that the radius is related to droplet density in a cell and dynamically computed during a simulation. The resulting effect of altering r_c is twofold. Firstly, increasing the radius will decrease the collision frequency, but it also increases the domain in which the particles can meet.

Chapter 2 Mathematical Formulations in the LES Context

Collision between two particles occurs only if the two fictitious spheres in which two particles reside intersect. The intersection volume V_{ol} is used as a collision volume to compute the expected collision frequency. V_{ol} is given by

$$V_{ol} = \begin{cases} \frac{4}{3}\pi r^3 & \text{if } d \leq R-r \\ \frac{\pi(R+r-d)^2(d^2 + 2dr - 3r^2 + 2dR + 6rR - 3R^2)}{12d} & \text{if } R-r \leq d \leq R+r \end{cases} \quad (2.100)$$

where d is the distance between the two particles, R is the radius of the large sphere and r is that of the small one. After V_{ol} is computed, it is assumed that the intersection volume remains unchanged during the current time step and only droplets in the intersection volume participate the collision process. The droplet number of a particle residing in the volume is determined by $N = N_p \times V_{ol} / V_{rs}$, where V_{rs} is the sphere volume. The collision frequency of a collector drop in the intersection volume with all droplets in the same volume from another particle is given by

$$\nu = \frac{N_2}{V_{ol}} \pi (r_1 + r_2)^2 |\mathbf{v}_1 - \mathbf{v}_2| \quad (2.101)$$

where N_2 is the droplet number in the volume from the other particle, r the droplet radius and \mathbf{v} droplet velocity. With this collision frequency, the mean expected number of collision occurring between the two particles during the current time step is defined as

$$\bar{\mu} = \frac{N_1 N_2}{V_{ol}} \pi (r_1 + r_2)^2 |\mathbf{v}_1 - \mathbf{v}_2| dt \quad (2.102)$$

In O'Rourke's collision model, the actual number of collisions is determined by sampling from a Poisson distribution, which is only valid if the sample population is left unchanged, i.e. when collisions do not undergo coalescence. Collision is the most time-consuming spray model. The sampling from the distribution will further worsen its efficiency. In the current collision model, the mean expected collision number $\bar{\mu}$ is used to determine the total number of collision which happens between two particles. It is expected to produce good approximations when averaged over many droplet collisions. When $\bar{\mu} < 1$, there is no collision between the two particles. On the other hand, the outcome of the collision follows the original O'Rourke model.

Since only droplets within the intersection volume V_{oi} participate in the collision process, there are two possible ways to handle the problem that arises from the intersection of particle spheres. One way is to group the droplets in the intersection volume into a new particle with the updated properties. This method would dramatically increase the number of particles in the computational domain. The adopted approach here is, therefore, to return the updated droplets in the intersection volume to their corresponding particles in such a way that mass, momentum and energy are conserved.

2.7 Boundary and initial conditions

The mathematical description of the gas flow is completed by specification of the initial and boundary conditions. The following types of boundaries need special treatment in a large eddy simulation: walls, inflow and outflow surfaces.

2.7.1 Solid walls

Shear flows near solid walls contain alternating thin streaks of high and low speed fluid. If these streaks in boundary layers are not adequately resolved by numerical simulation, the turbulence energy production near the wall is under-predicted, which results in reduction of the Reynolds stress and the skin friction [78]. However, the wall-region turbulence is not tightly coupled with the region far from the wall [22]. Thus, accurate prediction of the flow near the wall does not require accurate simulation of the outer flow, and vice versa. On the other hand, Piomelli et al. [94] have shown that, relatively crude layer boundary conditions can represent the effect of the wall region in a simulation of the central part of a channel flow. Thus, details of the flow in wall region need not to be known in order to simulate the outer region, i.e. either region can be well-simulated if given a reasonable approximation of the conditions at the interface between it and the other zone.

The above information suggests that useful simulations can be done without resolving the entire flow. This is important because a fine grid is required to resolve the wall region. If it can be represented via a model, huge savings are possible. In LES, there are normally two possible ways to handle the solid wall boundary:

A. Resolving the near wall dynamics directly

Since the production mechanisms are beyond the capability of the usual subgrid modeling, a sufficiently fine resolution is needed to capture them. In practice, this is done by setting the solid wall as a no-slip condition and placing the first point in the zone $(0 \leq y^+ \leq 1)$.

B. Modeling the near –wall dynamics

To reduce the number of degrees of freedom and especially avoid having to represent the inner region, a LES wall model is normally used to approximate the near-wall dynamics [33,48,53,94,108,132]. Since the distance from the first grid point to the wall is greater than the characteristic scales of the modes existing in the modeled region, the no-slip condition can no longer be used. The boundary condition will apply to the values of the velocity components and/or their gradients, which will be provided by the wall model. This approach makes it possible to place the first point in the logarithmic layer (in practice, $20 \leq y^+ \leq 200$). The main advantage of this method is that the number of degree of freedom in the simulation can be reduced greatly.

In the KIVA-LES, no-slip boundary condition is applied on solid walls. When the physics of wall boundary layers are important to the interested flow regions, the walls are finely resolved e.g. the impinging wall of plane impinging jets. If the wall boundary layers play little role in the concerned flow regions, the walls are not finely resolved to save computation time.

2.7.2 Inflow boundary condition

LES of spatially inhomogeneous flows requires unsteady inflow boundary conditions with a proper representation of the turbulent fluctuations. The LES results of some cases are highly sensitive to the inflow boundary condition. However, theoretically representing the flow upstream of the computational domain raises difficulties in LES when this flow is not fully known deterministically. Several inflow boundary condition generation techniques appeared in the literature:

A. Stochastic one-point reconstruction

In practice, this is done by superimposing random noises with the same statistical moments as the velocity fluctuations on the mean statistical profile. This can be expressed as

$$u(x_0, t) = U(x_0) + u'(x_0, t) \quad (2.103)$$

Where the mean field U is given by experiment, theory or steady computations, and where the fluctuation u' is generated from random numbers. One drawback of this approach is that the information concerning the phase is lost, which may have very harmful consequences when the consistency of the fluctuation is important. A few ways to generate the random part of the inlet flow are listed in the literature [9,65,112,138].

B. Deterministic computation

A more accurate treatment is to perform a simulation of the upstream flow [40,129], called a precursor simulation. This technique almost completely eliminates the errors, and offers very good results. However, it is hardly practical

in the general case because it requires reproducing the entire history of the flow which, for complex configurations, implies very high computational costs. There is also another drawback of the approach: since the precursor simulation is computed independent of the second one, no feedback information from the second simulation is possible. This is a one-way coupling between two simulations that can become problematic when an acoustic wave is emitted by the second.

C. Semi-deterministic Reconstruction

Bonnet et al. [17] proposed an intermediate approach to recover the two-point correlations of the inflow with no preliminary computations. The signal at the inflow plane is decomposed in the form

$$u(x_0, t) = U(x_0) + U_c(x_0, t) + u'(x_0, t) \quad (2.104)$$

Where $U(x_0)$ is the mean field, $U_c(x_0, t)$ the coherent part of turbulent fluctuations, and $u'(x_0, t)$ the random part of these fluctuations. In practice, this last part is generated by means of random variables and the coherent part is provided by a dynamical system with a low number of degrees of freedom, or by linear stochastic estimation, which gives access to the two-point correlations.

In the KIVA-LES, turbulent inflow boundary condition is applied by superimposing random noises with the same statistical moments as the velocity fluctuations on the mean statistical profile.

2.7.3 Outflow boundary condition

For a simulation with outflow regions, a convective boundary condition is often used to fix each component of the outflow velocity. This non-reflective boundary condition is based on the hyperbolic convection equation:

$$\frac{\partial u}{\partial t} + u_c \nabla u = 0 \quad (2.105)$$

The convective velocity u_c is deduced from the instantaneous integrated mass flux through the outflow sections.

In the current study, a continuative outflow boundary condition is used. Zero gradients of variables are assumed on the boundaries. The outflow boundary condition works well in our validation simulations. Wang et al. [130] concluded that there was little difference between the two kinds of outflow boundary conditions in a LES of a confined turbulent swirling flow.

Finally, since LES solves unsteady NS equations, the simulation should start from still with zero initial velocity.

Chapter 3

Numerical Methods

In the previous chapter, the LES formulations expressing the conservation laws for the non-reactive two-phase flow have been given. All these equations, together with the initial and boundary conditions, define a closed system of mutually coupled non-linear equations. As this system can not be solved by analytical methods, a numerical procedure must be used to solve the closed equations.

3.1 Temporal discretisation

A number of different limitations can be found on the time step. Firstly, as LES formulations are not filtered in time, they should thus be fully resolved in time $\Delta t < \tau$, where τ is Kolmogorov time scale. Secondly, two numerical time step limitations can be found from the balance of the different terms in the discretised NS equations. The balance between the time derivative and the convection terms gives the CFL number:

$$R_{CFL} = \frac{|u|\Delta t}{|\Delta x|}. \quad (3.1)$$

The balance between the time derivative and the viscous terms gives the viscous stability number:

$$R_v = \frac{1}{Re} \frac{D\Delta t}{|\Delta x|^2}. \quad (3.2)$$

D is a constant related to the diagonal term in the numerical scheme. The exact limitations of R_{CFL} and R_v depend on the numerical method. For most explicit

schemes they should both be less than unity. It is possible to avoid these limitations, if an implicit method is used. The influence of the turbulence model can be seen as a change in the effective viscosity and thus in Reynolds number. Larger effective viscosity emphasizes the viscous stability condition. The viscous stability condition is stricter in LES than RANS, since the effective viscosity is much smaller in LES than in RANS. Therefore, it is plausible to adopt an implicit method for the viscous terms in the NS equations to stabilize the solution. The NS equations are normally manipulated to get a Poisson equation for the pressure. This is used in SIMPLE type numerical methods where a Poisson equation is solved for the pressure correction. The physical interpretation of the elliptic pressure equation is that a disturbance in the pressure at some point is instantaneously experienced everywhere. Thus, it can be concluded that an implicit method has to be used to simulate the physical behavior of the pressure.

It should also be required that the truncation error related to the temporal discretisation should be of the same magnitudes as the truncation error related to the spatial discretisation. This suggests that $O(\Delta t^2)$ or higher-order methods should be used for the temporal discretisation to match the $O(h^2)$ or higher-order methods used for the spatial discretisation.

In this study, a time-splitting scheme is used in the temporal discretization. The time-splitting scheme is similar to the one used by Olsson and Fucks [91] in a LES code for an incompressible flow. In the current LES code for a compressible two-phase flow, a time step is split into the following three stages:

Phase A – spray droplet interactions

Phase A consists mainly of calculating the effects of spray droplet interactions due to spray. The terms are explicitly solved in phase A. The overall structure of this phase is as follows:

- Spray effects
 1. droplet injection
 2. calculation of spray droplet transport and SGS velocity
 3. calculation of spray droplet breakup
 4. compute droplet collisions
- Additional spray effects
 1. gravity effects
 2. droplet mass, momentum, and energy couplings.

Phase B – fluid diffusion and droplet velocity calculations

Phase B consists mainly of fluid calculations, with some additional spray effects due to the momentum coupling of the droplets to the fluid. Fluid diffusion is calculated in this phase using a semi-implicit $O(\Delta t^2)$ Crank-Nicolson method. Since computational mesh moves with the flow in the same velocity as u in the Lagrangian phase, no convection occurs across the cell boundaries. The fluid advection will be calculated explicitly in Phase C. The computed terms and effects in this phase are:

- preliminary fluid effects
 1. mass diffusion
 2. viscous stress calculation
 3. predicted pressure
- primary fluid calculation
 1. implicit momentum diffusion
 2. implicit heat diffusion
 3. pressure solution
- additional fluid effects
 1. calculate densities, energy, and Lagrangian coordinates
 2. implicit diffusion of SGS turbulent energy and dissipation
- update of droplet velocities

Phase C – fluid advection and mesh rezoning

The fluid advection is performed in Phase C. A two stage $O(\Delta t^2)$ MacCormack method [69] is used in Phase C. The structure of the computation is:

- grid updating
 1. calculation of grid velocities
 2. rezoning of the grid
 3. new cell volumes and area projections
- fluid advection
 1. explicit advection of mass, energy, and SGS turbulent energy
 2. explicit advection of momentum
- equations of state

3.2 Spatial discretization

The spatial discretization of the governing equations is in the form of Arbitrary Lagrangian-Eulerian (ALE) method [57]. The main characteristic of the method are:

- local and global conservation of physically-conserved properties can be ensured,
- applicable to complex geometries, with stationary and /or moving boundaries,
- easy implementation of boundary conditions,
- clear physical meanings,
- efficient solution methods for the resulting simultaneous algebraic equations.

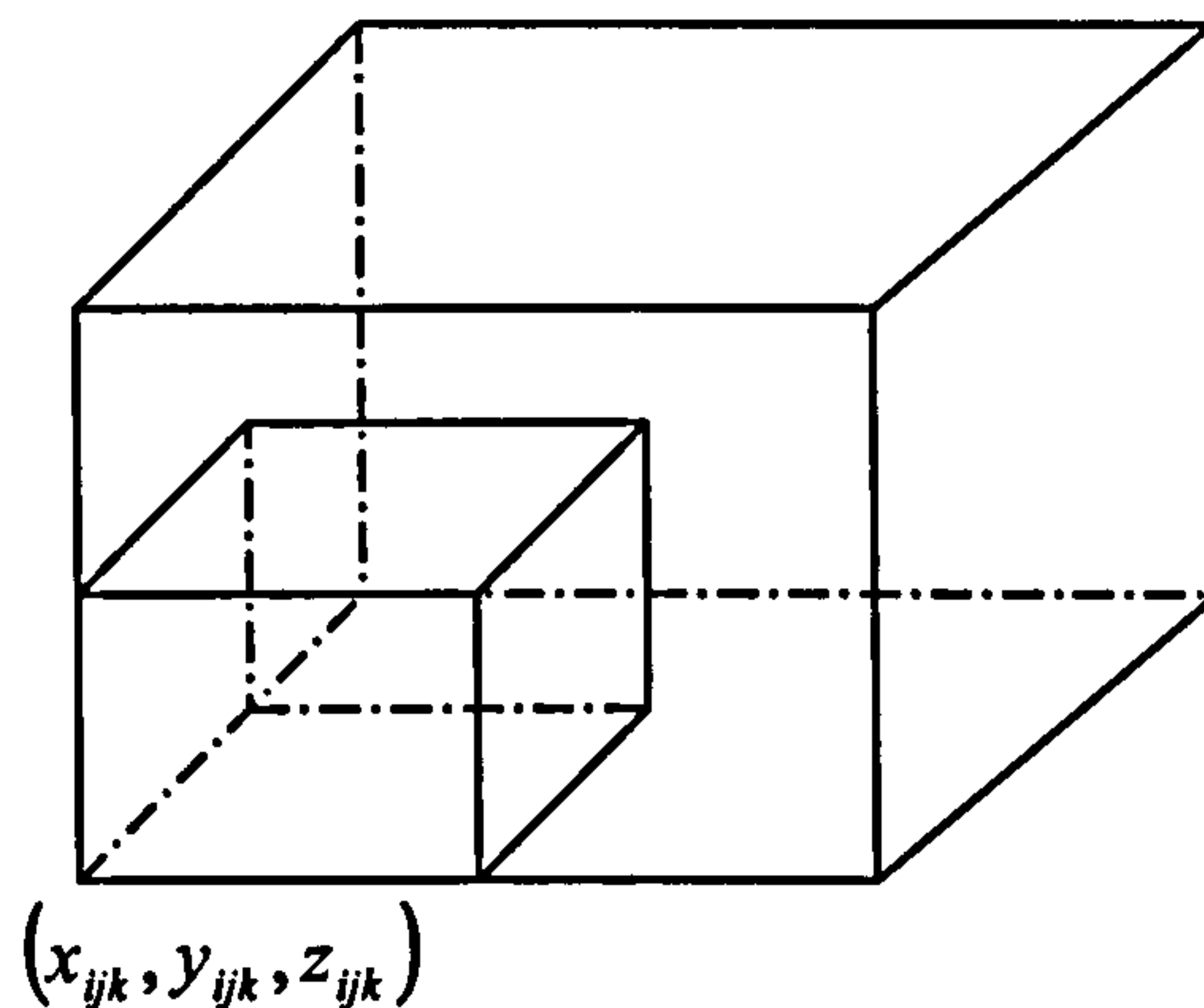


Fig. 3.1 The portion of momentum cell (i, j, k) lying within the regular cell (i, j, k) . Each momentum cell has twenty-four such faces in all.

In the ALE mesh a normal cell is defined as the arbitrary hexahedron in Fig. 3.1 with eight vertices. The cells are indexed by integers (i, j, k) . The cell center is computed as:

$$x_{ijk}^c = \frac{1}{8} \sum_{\alpha=1}^8 x_{\alpha} ,$$

$$y_{ijk}^c = \frac{1}{8} \sum_{\alpha=1}^8 y_{\alpha} , \quad (3.3)$$

$$z_{ijk}^c = \frac{1}{8} \sum_{\alpha=1}^8 z_{\alpha} ,$$

where α ranges over the eight cell vertices. Auxiliary cells, called momentum cells, are defined as surrounding a vertex (i, j, k) , with edges meeting the midpoint of the surrounding regular cell edges. There are then six faces for each normal cell, and twenty-four faces in the case of a momentum cell. By adoption of momentum cells, no interpolation is required in the Lagrangian phase to determine vertex motion. However, this treatment also incurs a major drawback that ALE method solutions are badly susceptible to parasitic modes in the velocity field [86]. The drawback can be alleviated by the introduction of velocities centered on cell faces. The normal velocity components on cell faces are used to compute cell volume changes in Phase B and fluxing volumes in Phase C. The resulting scheme greatly reduces the need for node coupling [57].

Normally, quantities assigned to vertices or mesh points x_{ijk} are $x, y, z, u = (u, v, w)$, and the area of the momentum cells surrounding x_{ijk} . Quantities assigned to cell centers x_{ijk}^c are thermodynamic quantities such as cell volume V , pressure p , internal energy I , mass density ρ etc.

Spatial differences are performed by integrating the differential terms over the volume of a regular or momentum cell. Volume integrals of gradient terms are converted into surface area integrals using the divergence theorem.

$$\int_S \nabla Q \cdot dA = \sum_{\alpha} (\nabla Q)_{\alpha} \cdot A_{\alpha} \quad (3.4)$$

where α represents one of the six cell faces. Evaluating the gradient on the surface is done as follows

$$(\nabla Q)_\alpha \cdot A_\alpha = \alpha_{lr}(Q_l - Q_r) + \alpha_{tb}(Q_t - Q_b) + \alpha_{fd}(Q_f - Q_d) \quad (3.5)$$

where r, l, t, b, f and d indicates right, left, top, bottom, front and back respectively. Here, α_{lr}, α_{tb} and α_{fd} are geometric factors for face α and Q_s are averages computed at mid-points on the surface as shown in Fig. 3.2. Q_s is simply the average of the values of Q in the four cells surrounding the cell edge. The geometric factors are solved according to the equation:

$$A_\alpha = \alpha_{lr}(x_l - x_r) + \alpha_{tb}(x_t - x_b) + \alpha_{fd}(x_f - x_d) \quad (3.6)$$

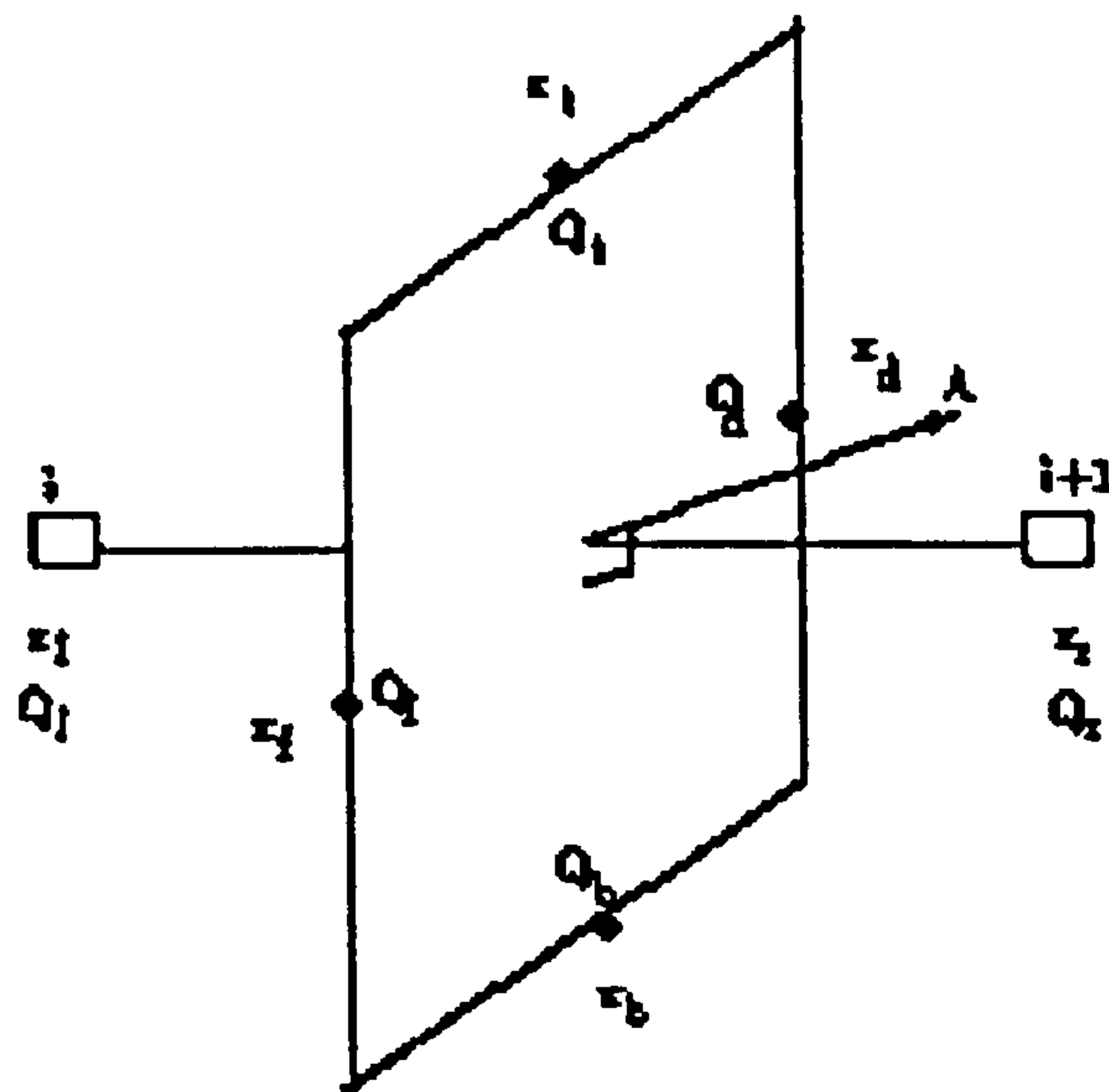


Fig. 3.2 The definition of the gradient of cell-centred quantity Q on cell face α .

Volume integrals over momentum cells are also converted to area integrals. Momentum cells are constructed around vertices and involve 8 regular cells that share a particular vertex. There are a total of 24 faces β , and three of them reside in one of the 8 cells. The area vectors (A') for momentum cell faces are usually

substituted by the regular cell area vectors (A). The integral $\int Q dA$ over the three momentum cell faces in question is represented by

$$\int Q dA = Q_{ijk} (A'_a + A'_b + A'_c) = -\frac{1}{4} Q_{ijk} (A_a + A_b + A_c) \quad (3.7)$$

In the finite volume discretization, several quantities having to do with the mesh must be computed. If the mesh moves in a Lagrangian fashion, then these quantities must be recomputed each time the mesh moves. The main quantities involved are:

V_{ijk} - volume of normal cell (i, j, k) , computed from vertex positions

V'_{ijk} - volume of momentum cell (i, j, k)

M_{ijk} - mass of normal cell (i, j, k) , $M_{ijk} = \rho_{ijk} V_{ijk}$

M'_{ijk} - mass of momentum cell (i, j, k) , $M'_{ijk} = \rho_{ijk} V'_{ijk}$

A_α - outward area vector associated with faces α for a normal cell (i, j, k)

A'_α - outward area vector associated with faces α for a momentum cell (i, j, k)

$(uA)_\alpha = u_\alpha \cdot A_\alpha$; regular cell face normal velocities

$(uA')_\alpha = u_\alpha \cdot A'_\alpha$; momentum cell face normal velocities.

3.3 Difference Equations

To simplify notation, filter operator is omitted in the following equations.

3.3.1 Lagrangian phase

A. Mass Density Equations

$$(\rho_m)_ijk^A - (\rho_m)_ijk^n = (\dot{\rho}_m^s)_{ijk} \quad (3.8)$$

$$M_{ijk}^B \frac{(Y_m)_{ijk}^B - (Y_m)_{ijk}^A}{\Delta t} = \sum_{\alpha} (\rho D_{eff})_{\alpha}^n \nabla \left[\frac{1}{2} (Y_m^B + Y_m^A) \right]_{\alpha} \cdot A_{\alpha}^n \quad (3.9)$$

$$\frac{\rho_{ijk}^B V_{ijk}^B - \rho_{ijk}^n V_{ijk}^n}{\Delta t} = \dot{\rho}_{ijk}^s V_{ijk}^n \quad (3.10)$$

B. Momentum Equations

$$\frac{[(M')_{ijk}^A + S'_{ijk}] u_{ijk}^A - (M')_{ijk}^n u_{ijk}^n}{\Delta t} = -R'_{ijk} / \Delta t + g(M')_{ijk}^n \quad (3.11)$$

$$\begin{aligned} \frac{(M')_{ijk}^B u_{ijk}^B - (M')_{ijk}^A u_{ijk}^A}{\Delta t} &= \sum_{\beta} \left[\frac{1}{2} (p^B + p^n) \right]_{\beta} (A')_{\beta}^n - \sum_{\beta} \frac{2}{3} \rho_{\beta}^A (k^{sgs})_{\beta}^A (A')_{\beta}^n \\ &+ \sum_{\beta} \left[\frac{1}{2} (\sigma_{eff}(u^B) + \sigma_{eff}(u^A)) \right]_{\beta} \cdot (A')_{\beta}^n - S'_{ijk} u_{ijk}^B / \Delta t \end{aligned} \quad (3.12)$$

where

$$S'_{ijk} = \sum_{p \in (ijk)} N'_p \frac{4}{3} \pi \rho_d (r_p^B)^3 \frac{\Delta t D_p}{1 + \Delta t D_p} \quad (3.13)$$

and

$$R'_{ijk} = \sum_{p \in (ijk)} N'_p \frac{4}{3} \pi \rho_d \left[(r_p^B)^3 \frac{v'_p D_p u'_p}{1 + \Delta t D_p} - (r_p^A)^3 v'_p \right] \quad (3.14)$$

The summation is over all particles located in computational cell (ijk) .

C. Cell Face Normal Velocities

In addition to vertex velocities, in Phase B a face-centered normal velocity is used to reduce the susceptibility of computed solutions to the node uncoupling.

$$\left[(M')_{ijk}^B + S'_{ijk} \right] \frac{u_{ijk}^B - u_{ijk}^t}{\Delta t} = \left[\frac{1}{2} (p^B + p^n)_\beta \right] (A')_\beta^n - \sum_\beta \frac{2}{3} \rho_\beta^A (k^{sgs})_\beta^A (A')_\beta^n \quad (3.15)$$

$$\left[(M')_{ijk}^B + S'_{ijk} \right] \frac{u_{ijk}^t - u_{ijk}^A}{\Delta t} = \sum_\beta \left[\frac{1}{2} (\sigma_{eff}(u^B) + \sigma_{eff}(u^n)) \right]_\beta \cdot (A')_\beta^n \quad (3.16)$$

$$(uA)_\alpha^t = \frac{1}{4} (u_a^t + u_b^t + u_c^t + u_d^t) \cdot A_\alpha^n \quad (3.17)$$

Where a, b, c and d label the vertices that form the four corners of cell face α .

$$\begin{aligned} \left[(M'')_\alpha^B + S''_\alpha \right] \frac{(uA)_\alpha^B - (uA)_\alpha^t}{\Delta t} = & - \sum_\gamma \left\{ \left[\frac{1}{2} (p^B + p^A) \right] + \frac{2}{3} \rho^A (k^{sgs})^A \right\} (A'')_\gamma^n \cdot A_\alpha \\ & + \frac{A_\alpha^t - A_\alpha^n}{\Delta t} \cdot \frac{u_a^n + u_b^n + u_c^n + u_d^n}{4} \left[(M'')_\alpha^B + S''_\alpha \right] \end{aligned} \quad (3.18)$$

Where indices γ refer to the faces of cell face control volume α , whose normal area vectors at time t^n are $(A'')_\gamma^n$.

The added mass S''_α associated with the spray droplets in cell face control volume α is given by

$$S''_\alpha = \frac{S'_a + S'_b + S'_c + S'_d}{(M')_a^B + (M')_b^B + (M')_c^B + (M')_d^B} (M'')_\alpha^B \quad (3.19)$$

D. Internal Energy Equations

$$\frac{M_{ijk}^A I_{ijk}^A - M_{ijk}^n I_{ijk}^n}{\Delta t} = \dot{Q}_{ijk}^s V_{ijk}^n \quad (3.20)$$

$$M_{ijk}^B \frac{I_{ijk}' - I_{ijk}^A}{\Delta t} = M_{ijk}^B (\varepsilon^{sgs})_{ijk}^n + \sum_{\alpha} (\rho D_{eff})_{\alpha}^n \left\{ \sum_m h_m (T_{\alpha}^n) \nabla \left[\frac{1}{2} (Y_m^B + Y_m^A) \right]_{\alpha} \right\} \cdot A_{\alpha}^n \quad (3.21)$$

$$M_{ijk}^B \frac{I_{ijk}^B - I_{ijk}'}{\Delta t} = -\frac{P_{ijk}^n + P_{ijk}^B}{2} \frac{V_{ijk}^B - V_{ijk}^n}{\Delta t} + \left[\frac{1}{2} (\sigma_{eff}(\mathbf{u}^B) : \nabla \mathbf{u}^B + \sigma_{eff}(\mathbf{u}^n) : \nabla \mathbf{u}^n) \right] \quad (3.22)$$

$$\sum_{\alpha} (K_{eff})_{\alpha}^n \nabla \left[\frac{1}{2} (T^B + \tilde{T}) \right]_{\alpha} \cdot A_{\alpha}^n$$

where

$$\tilde{T}_{ijk} = T_{ijk}^n + \frac{1}{(c_p)_{ijk}^n} \left[I_{ijk}' - I_{ijk}^n + P_{ijk}^n \left(\frac{1}{\rho_{ijk}^A} - \frac{1}{\rho_{ijk}^n} \right) \right] \quad (3.23)$$

E. One-Equation SGS Equations

$$\frac{M_{ijk}^B (k^{sgs})_{ijk}^A - M_{ijk}^n (k^{sgs})_{ijk}^n}{\Delta t} = (\dot{W}^s)_{ijk} V_{ijk}^n \quad (3.24)$$

$$\frac{M_{ijk}^B (k^{sgs})_{ijk}^B - M_{ijk}^n (k^{sgs})_{ijk}^n}{\Delta t} = \sum_{\alpha} \frac{\rho^n (v_t)_{\alpha}^n}{Pr_t} \nabla \left[\frac{1}{2} ((k^{sgs})^B + (k^{sgs})^A) \right]_{\alpha} \cdot A_{\alpha} \quad (3.25)$$

$$- 0.916 M_{ijk}^B \frac{(\sqrt{k^{sgs}})_{ijk}^n}{(\Delta)_{ijk}^n} (k^{sgs})_{ijk}^B + V_{ijk}^n \left[\frac{1}{2} (\sigma^{sgs}(\mathbf{u}^B) : \nabla \mathbf{u}^B + \sigma^{sgs}(\mathbf{u}^n) : \nabla \mathbf{u}^n) \right]_{ijk}$$

F. Volume Change Equations

$$V_{ijk}^B = V_{ijk}^n + \Delta t \sum_{\alpha} (uA)_{\alpha}^B \quad (3.26)$$

The Phase B values of the flow field variables are found by solving the above implicit equations. The solution procedure is patterned after the SIMPLE method [92], with individual equations solved using the conjugate residual method [88]. Detailed solution procedure can be found in [2].

3.3.2 Phase C

The convective transport associated with moving the mesh relative to the fluid is calculated in Phase C. The time step Δt in the study must satisfy the Courant condition

$$|\mathbf{u}_r| \Delta t / |\Delta \mathbf{x}| < 1, \quad (3.27)$$

where \mathbf{u}_r is the fluid velocity relative to the grid velocity.

Generally, LES requires high-order methods for spatial discretisation. High-order methods are necessary to avoid masking the SGS stress by the truncation error. The Smagorinsky and dynamic SGS models contain Δ^2 in the modeled SGS-stress. This formally makes the modeled SGS-stress an $O(h^2)$ term, since $\Delta \sim h$. While the current one-equation SGS model contains only Δ in the modeled SGS-stress. Thus, the modeled SGS-stress in current study is less likely masked out.

Two convection schemes: central differencing and quasi-second-order upwind (QSOU) are used in the current study. The central differencing scheme is used to discretize the momentum equation; while the QSOU scheme is used for the other transport equation to stabilize the numerical solution. Mittal and Moin [77] have shown that the second-order central differencing provides the energy spectra that are in excellent agreement with its experimental counterpart. QSOU scheme is too dissipative for the momentum equation in LES formulation.

The transport of cell-centred quantities is computed by using a volume δV_α that is swept out by regular cell face α , as it moves from its Lagrangian position to its final position. The volume is computed by

$$\delta V_\alpha = \delta V_\alpha^G - (uA)_\alpha^B \Delta t \quad (3.28)$$

where δV_α^G is the volume swept out by cell face α when the four vertices defining the face are moved from their old position x_{ijk}^n to their new position x_{ijk}^{n+1} . Convective transport of scalars is calculated in the following equations:

A. Species density

$$(\rho_m)_{ijk}^C V_{ijk}^{n+1} = (\rho_m)_{ijk}^B V_{ijk}^B + \sum_\alpha (\rho_m)_\alpha^B \delta V_\alpha \quad (3.29)$$

$$(\rho_m)_{ijk}^{n+1} V_{ijk}^{n+1} = (\rho_m)_{ijk}^B V_{ijk}^B + \frac{1}{2} \left[\sum_\alpha (\rho_m)_\alpha^C \delta V_\alpha + \sum_\alpha (\rho_m)_\alpha^B \delta V_\alpha \right] \quad (3.30)$$

B. Specific internal energy

$$\rho_{ijk}^C V_{ijk}^{n+1} I_{ijk}^C = \rho_{ijk}^B V_{ijk}^B I_{ijk}^B + \sum_\alpha (\rho I)_\alpha^B \delta V_\alpha \quad (3.31)$$

$$\rho_{ijk}^{n+1} V_{ijk}^{n+1} I_{ijk}^{n+1} = \rho_{ijk}^B V_{ijk}^B I_{ijk}^B + \frac{1}{2} \left[\sum_\alpha (\rho I)_\alpha^C \delta V_\alpha + \left[\sum_\alpha (\rho I)_\alpha^B \delta V_\alpha \right] \right] \quad (3.32)$$

C. SGS kinetic energy

$$\rho_{ijk}^C V_{ijk}^{n+1} (k^{sgs})_{ijk}^C = \rho_{ijk}^B V_{ijk}^B (k^{sgs})_{ijk}^B + \sum_\alpha (\rho k^{sgs})_\alpha^B \delta V_\alpha \quad (3.33)$$

$$\rho_{ijk}^{n+1} V_{ijk}^{n+1} (k^{sgs})_{ijk}^{n+1} = \rho_{ijk}^B V_{ijk}^B (k^{sgs})_{ijk}^B + \frac{1}{2} \left[\sum_\alpha (\rho k^{sgs})_\alpha^C \delta V_\alpha + \sum_\alpha (\rho k^{sgs})_\alpha^B \delta V_\alpha \right] \quad (3.34)$$

where $(q)_\alpha^B$, $q = \rho_m, \rho I, \rho k^{sgs}$, are evaluated by the QSOU scheme.

Convective transport of momentum is calculated in terms of the mass increments across momentum cell faces. The mass increment across cell faces α of a particular momentum cell is defined by

$$(\delta M'_\alpha)^B = \frac{1}{8}(\rho_o^B \delta V_o - \rho_i^B \delta V_i) \quad (3.35)$$

where o and i are the regular cell faces on either side of the momentum cell face α , of which i (“inner”) is the one that actually cuts into the momentum cell, while o (“outer”) does not. Before fluxing momentum the mass increments $\delta M'_\alpha$ corresponding to the twenty-four faces of momentum cell (i, j, k) are added in groups to obtain mass fluxes δM_β^c through six composite faces β of the momentum cell. Each composite face is formed from the four cell faces α that touch a common regular cell edge that emanates from vertex (i, j, k) . The momentum fluxing is then computed by

$$(M')_{ijk}^C u_{ijk}^C = (M')_{ijk}^B u_{ijk}^B + \sum_{\beta} (\delta M_\beta^c)^B u_\beta^B \quad (3.36)$$

$$(M')_{ijk}^{n+1} u_{ijk}^{n+1} = (M')_{ijk}^B u_{ijk}^B + \frac{1}{2} \left[\sum_{\beta} (\delta M_\beta^c)^C u_\beta^C + \sum_{\beta} (\delta M_\beta^c)^B u_\beta^B \right] \quad (3.37)$$

where u_β^B is evaluated from the central differencing scheme.

Chapter 4

LES of Plane Impinging Jets

4.1 Introduction

Impinging jets are widely used in industrial applications, because of their high turbulent intensity and heat transfer rate in the impinging region, such as paper drying, cooling of electronic components and turbine blades etc. For plane impinging jets, a pair of spanwise rollers originates from the shear layers just downstream the nozzle exit, due to the shear layer instability of a Kelvin-Helmholtz type, and then the rollers convect downstream towards the impinging wall. The evolution of the rollers is an unstable process susceptible to perturbations on the inlet plane. In a natural jet, the perturbation is random, and the process is less organized. When an artificial periodic perturbation is applied, the process may become periodic and well-organized, i.e. the jet can be locked. The experiment [93,103] has shown that the plane impinging jet could be locked on perturbations of wide frequency range.

Numerous studies of plane impinging jets have been conducted experimentally and numerically over the last decades. Among these, Yokobori et al. [139-140] first discovered the counter-rotating columnar vortices aligning along the impinging wall and through the symmetry plane. Gutmark et al. [50] first reported on measurements of both the mean-flow and turbulence characteristics of such impinging jets. Namer et al. [80] measured the velocity field in a plane turbulent air jet at moderate Reynolds numbers. Sakakibara et al. [105-106] measured the instantaneous velocity field and its time variation using DPIV. They observed a reoccurring presence of concentrations of streamwise vorticity, which advected towards and merged with the wall vortices. Sakakibara et al. [103] extended their study of vortex structures using DPIV by locking the jet both in phase and

laterally in space. They found that the jet shear layers symmetrically evolved into spanwise rollers just downstream the jet nozzle. Accordingly, the rollers on the same side were connected by streamwise successive ribs, while the roller pair was connected by underneath cross ribs across the symmetry plane. The cross ribs intensified themselves through stretching as the rollers advected towards the impingement region. When the cross ribs reached the impinging wall, they merged with the wall ribs, which were composed of vortices of the same sign as the cross ribs, but remained near the wall all the time.

Chuang and Wei [24], Craft et al. [30] and Knowles [63] employed Reynolds averaged turbulence models to study impinging jets. They can be concluded that most standard Reynolds averaged turbulence models can not yield satisfactory results. Over-prediction of the potential core and turbulence kinetic energy near the stagnation point, and under-prediction of the lateral expansion of the jet were found in almost all the RANS simulations. This is partly due to the underlying assumption that turbulent shear stress depends only on the rate of strain tensor, but not on the rotation tensor. While in LES, the problem-dependant large scale eddies are computed directly, only the universal small scale eddies are modelled. This renders LES a more robust choice for numerically simulating the plane impinging jets. Recently, such predictions using LES have been reported by Voke and Gao [128], Cziesla et al. [32], Beaubert and Viazzo [11] and Tsubokura et al. [126].

Voke and Gao [128] studied heat transfer from an impinging jet. Standard Smagorinsky SGS model was used with Van Driest damping factor to reduce SGS eddy viscosity near the wall in their study. They concluded that the dynamics of the turbulence resulted in the temperature variations at the plate surface having very high lateral correlation. Cziesla et al. [32] conducted a LES of flow and heat transfer in an impinging slot jet with a moderate Reynolds number. A dynamic SGS stress model was used for the small scales of turbulence. Their predictions compared favourably with the experimental observations, especially in the

stagnation zone. Beaubert and Viazzo [11] performed a LES of plane turbulent impinging jets at moderate Reynolds numbers to study the mean velocity, the turbulence statistics along the jet axis and at different vertical locations. The simulation was carried out using the dynamic Smagorinsky model. Their results were also in good agreement with experimental data. They also concluded that the effect of the jet Reynolds number is significant between 3000 and 7500 both on the near and far field structure. Tsubokura et al. [126] used LES to study the eddy structures of impinging jets excited at the inlet. An isotropic eddy viscosity model was used as a SGS model in the study. Their study was focused on how spanwise or azimuthal disturbances imposed at the inlet velocity affect the eddy structures in the transition process. They found that the round jet showed definite instability at a fixed wavelength while the plane jet showed almost equivalent sensitivity to all modes. They also observed elongated twin vortices along the impinging wall of the plane jet in the stagnation region and the number of pairs was found to agree exactly with the spanwise wave number imposed at the inlet.

In this chapter, KIVA-LES is applied to plane impinging jets. Simulations are made with different inflow conditions. One is a natural plane impinging jet with a random perturbation on the inflow plane, and another is a forced plane impinging jet with a Strouhal number of 0.36, locked both in phase and laterally in space. The first simulation is performed to quantitatively study the mean flow and turbulence statistics, and the second simulation is performed to study the vortex structures of a forced plane impinging jet.

4.2 Problem description

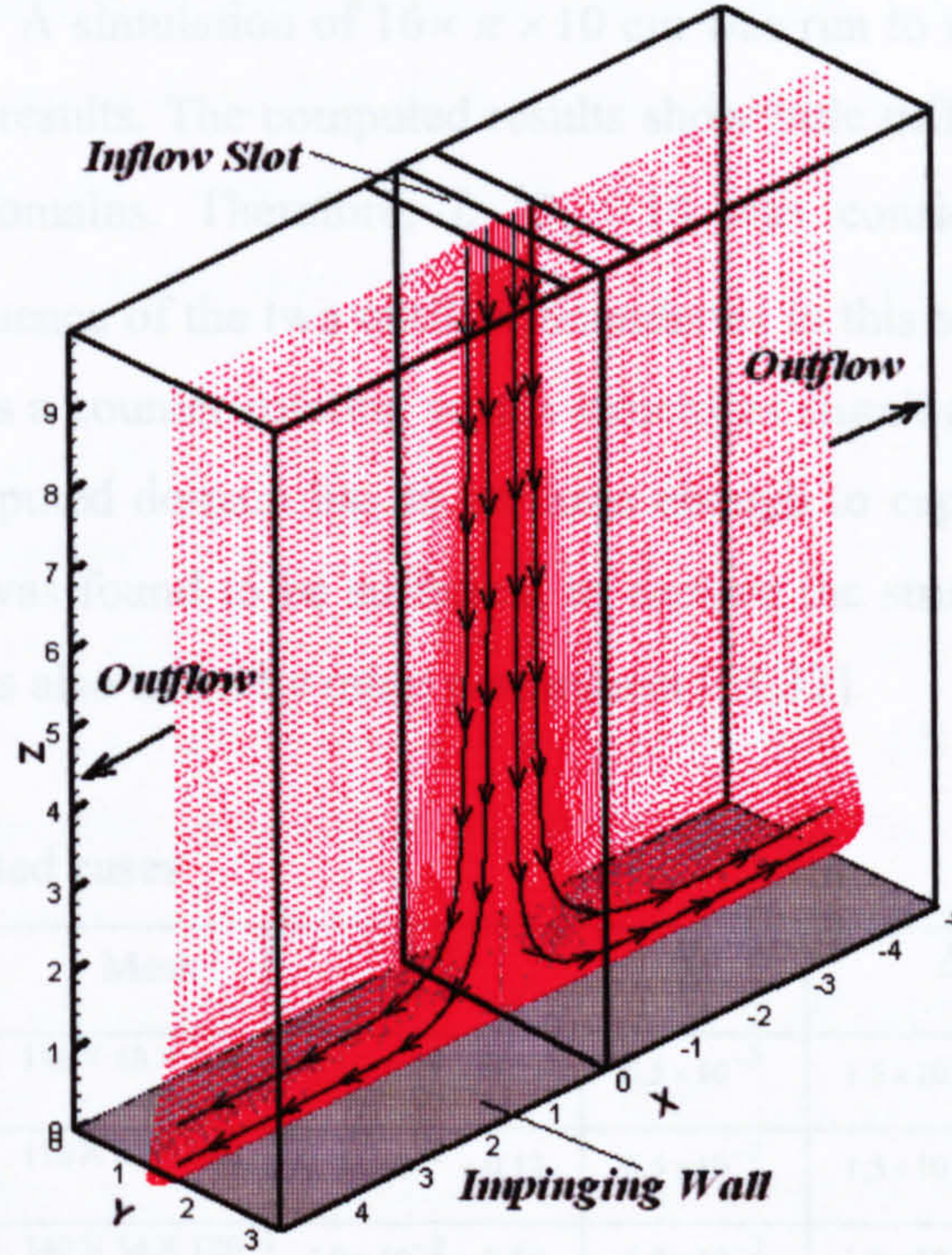


Fig. 4.1 The computational domain.

The computational domain is a semi-confined plane impinging jet, as shown schematically in Fig. 4.1, which is a rectangle box of $10 \times \pi \times 10$ cm in lateral (X-direction), spanwise (Y-direction) and wall-normal (Z-direction) directions, respectively. The separation distance between the nozzle exit and impinging wall is 10 cm, and the width of nozzle B_w is 1 cm. The Reynolds number Re based on the nozzle width and nozzle exit centreline velocity is 5500 and 2000 for natural and forced impinging jet, respectively. A simulation of $Re = 13500$ for the natural impinging jet is also performed to investigate the influence of Reynolds number on the statistical quantities.

The lateral length of the computed domain L_x must be long enough to capture the two large recirculations at each side of the jets and to reduce the influence of the two outflow boundaries. Cziesla et al. [32] used $L_x/B_w = 10$ in their studies,

while Beaubert et al. [11] concluded that a value of $L_x/B_w = 40$ was sufficient in their simulations. A simulation of $16 \times \pi \times 10$ cm was run to test the influence of the length on the results. The computed results show little difference between the two computed domains. Therefore, $L_x/B_w = 10$ was considered sufficient to minimize the influence of the two outflow boundaries in this study. As mentioned above, there exists a counter-rotating vortex structures aligning with the wall. The width of the computed domain has to be large enough to capture these vortices. The width of π was found to be sufficient to capture the structures in this study and this width was also taken by other researchers [11,32].

Table 3.1 Computed cases

Case	Domain	Mesh	Δx	Δy	Δz	R_e	SGS
1	$16 \times \pi \times 10$	$136 \times 48 \times 100$	$6.2 \times 10^{-2} - 0.22$	6.5×10^{-2}	$1.5 \times 10^{-2} - 0.11$	5500	On
2	$10 \times \pi \times 10$	$116 \times 48 \times 100$	$6.2 \times 10^{-2} - 0.12$	6.5×10^{-2}	$1.5 \times 10^{-2} - 0.11$	5500	On
3	$10 \times \pi \times 10$	$140 \times 54 \times 120$	$4.0 \times 10^{-2} - 0.10$	5.8×10^{-2}	$1.0 \times 10^{-2} - 0.10$	5500	On
4	$10 \times \pi \times 10$	$140 \times 54 \times 120$	$4.0 \times 10^{-2} - 0.10$	5.8×10^{-2}	$1.0 \times 10^{-2} - 0.10$	5500	Off
5	$10 \times \pi \times 10$	$140 \times 54 \times 120$	$4.0 \times 10^{-2} - 0.10$	5.8×10^{-2}	$1.0 \times 10^{-2} - 0.10$	13500	On
6	$10 \times \pi \times 10$	$116 \times 48 \times 100$	$6.2 \times 10^{-2} - 0.12$	6.5×10^{-2}	$1.5 \times 10^{-2} - 0.11$	2000	On

The computational meshes are clustered in the wall-normal direction near the impinging wall to resolve the wall boundary layer, and the meshes are also clustered around the two shear layer in the lateral direction in consideration of the strong gradient in the regions. The meshes are uniform in the spanwise direction. To minimize the filter commutation errors arising from the uneven grids, the transition of grid size in the neighbouring grids is limited by less than 10% in the wall boundary layer.

Grid sensitivity is investigated by comparing a high resolution case and a coarser case. Two grid resolutions used for the simulation of natural impinging jet are $116 \times 48 \times 100$ and $140 \times 54 \times 120$ respectively, and the grid resolution of

116×48×100 is used for the forced impinging jet. To ensure that the SGS-model effect of the current LES formulation is not cancelled out by the numerical dissipation, a test case with implicit SGS model, i.e. the one-equation SGS model is turned off, and the numerical dissipative errors act as a SGS model, is performed. All the computed cases and meshes are list in Table 3.1.

Inflow boundary condition is applied on the inlet plane. Two kinds of inflow condition are employed here. One is a natural inflow condition with a superimposed average steady profile and a random noise, and another is a forced inflow condition with a streamwise time-dependant sinusoidal disturbance and a spatial periodic disturbance imposed on the steady profile. The application of inflow boundary condition is an important factor for LES as discussed in Chapter 3. In the study of impinging jet [128], Voke et al. performed a separate LES to compute the inflow condition. While Cziesla et al. [32] and Beaubert et al. [11] employed a constant inlet velocity profile with no turbulent effect. Beaubert et al [12] concluded that LES of impinging jets with either a turbulent intensity of 10% at the nozzle exit or a constant inlet velocity profile showed negligible effect on the turbulent statistics. As will be seen in the following section, the two shear boundary layers dominate the turbulence production, so the inflow turbulent has little effect on the turbulent statistics of the natural impinging jet. In our study, a random noise with a turbulent intensity of 3% is imposed on the inflow boundary to mimic the turbulent inflow condition.

A continuative outflow boundary condition is applied on the outlet planes. In the literature, most LES predictions of impinging jets were performed with a mass-conserving “convective flow” outflow condition. The continuative outflow boundary condition used in this study is a kind of “zero gradient” outflow condition. Wang et al. [130] used both conditions in their simulation of a confined swirling flow and concluded that there was little difference between the two kinds of outflow boundary conditions. Periodic boundary condition is applied on spanwise boundaries, while no-slip wall condition is applied on the solid walls.

Chapter 4 LES of Plane Impinging Jets

The upper wall is not resolved in the study, since its influence is minor. The working fluid is air at 298K and 1 atmosphere. The simulation starts from still.

4.3 Computational results and discussions

The solution of a LES is transient. To compare with experimental data, the predicted results have to be averaged. The averaging is done during the running of the simulations by sampling every ten time steps after the solution reaches a statistically steady condition. The averaged values start to be calculated from the 100th sample, and turbulent variances are computed from the 200th sample. These values are calculated every sampling time step and monitored at a fixed time interval. As the sample number increases, the values will converge to the final results. Finally, the converged values are space averaged in the spanwise direction to compare with experimental results. This sampling method can save huge hard disk space on the computer and also significantly reduce the computing time. Since only the sum of these values is needed to be saved during the sampling process, the memory usage is affordable. The following results are made non-dimensional with the jet inlet centreline velocity w_{in} and the slot width B_w , and \diamond stands for time average.

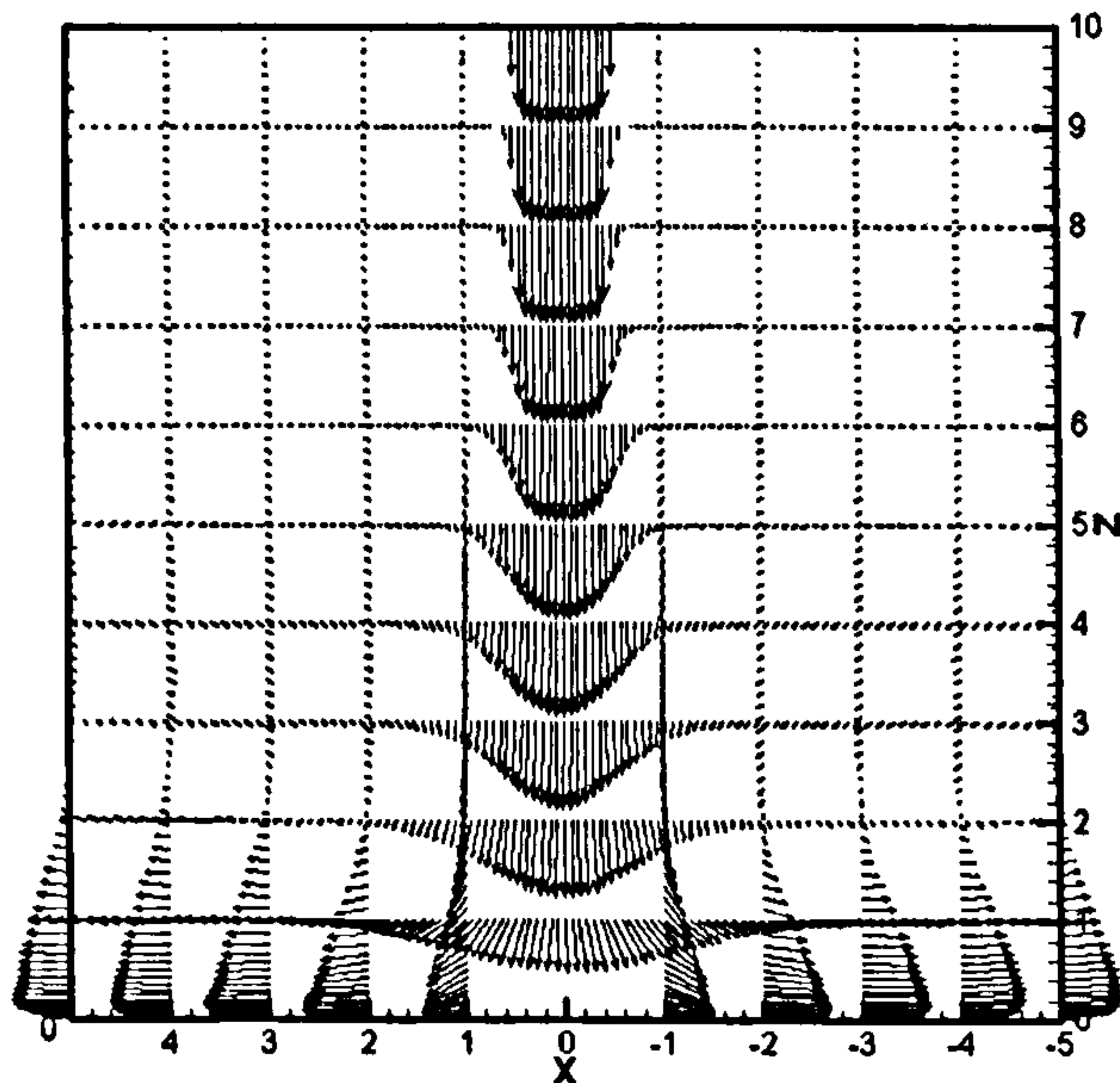


Fig. 4.2 Mean velocity vectors extracted from the main flow field on different $x=\text{constant}$ and $z=\text{constant}$ planes

4.3.1 Natural plane impinging jet

4.3.1.1 Numerical accuracy and SGS-model effect

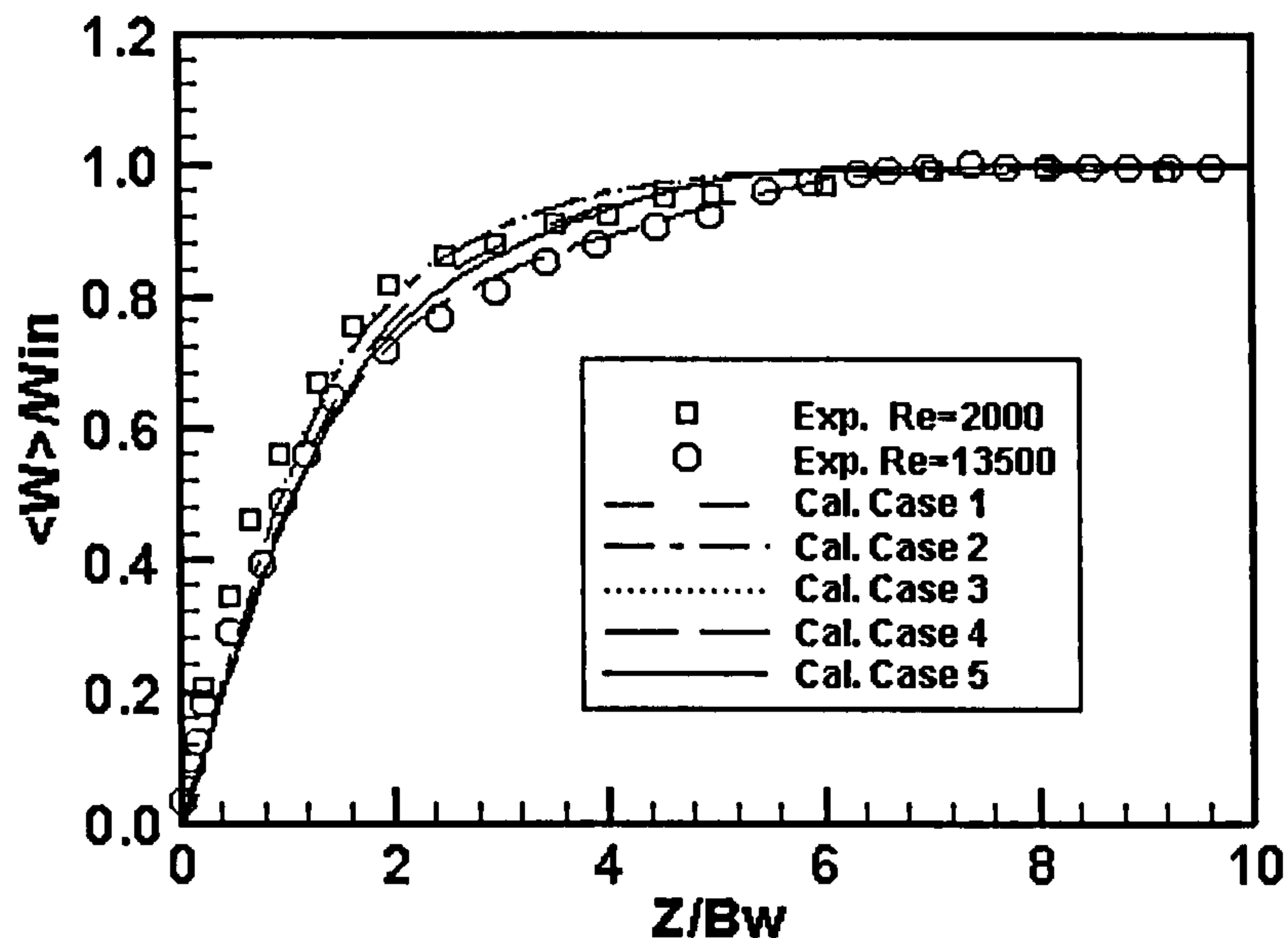


Fig. 4.3 Vertical velocity component along the centreline.

The quality of the LES results is strongly influenced by the spatial resolution. A sufficient resolution is required to avoid excessive damping of the instabilities and the transition to turbulence. In the current implementation of LES, the filter size is equal to the grid size. This results in more small scales being resolved with increase in the grid resolution. The LES will converge to a DNS when all scales of motion are resolved. Hence, there is no concept of traditional grid independence in the implementation of LES [44]. However, to make a LES trustable, the grid resolution must be fine enough to resolve those eddies that are large enough to contain information about the geometry and dynamics of the specific problem under investigation. The grid effect is investigated by comparison between the coarse resolution Case 2 and the high resolution Case 3 for $Re = 5500$. The results in Fig. 4.3 and Fig. 4.5-4.7 indicate that the adopted resolution is sufficient and numerical errors are at an acceptable level. The results of Case 1 shown in these

figures also demonstrate that the influence of the extent of the computed domain is within an acceptable level.

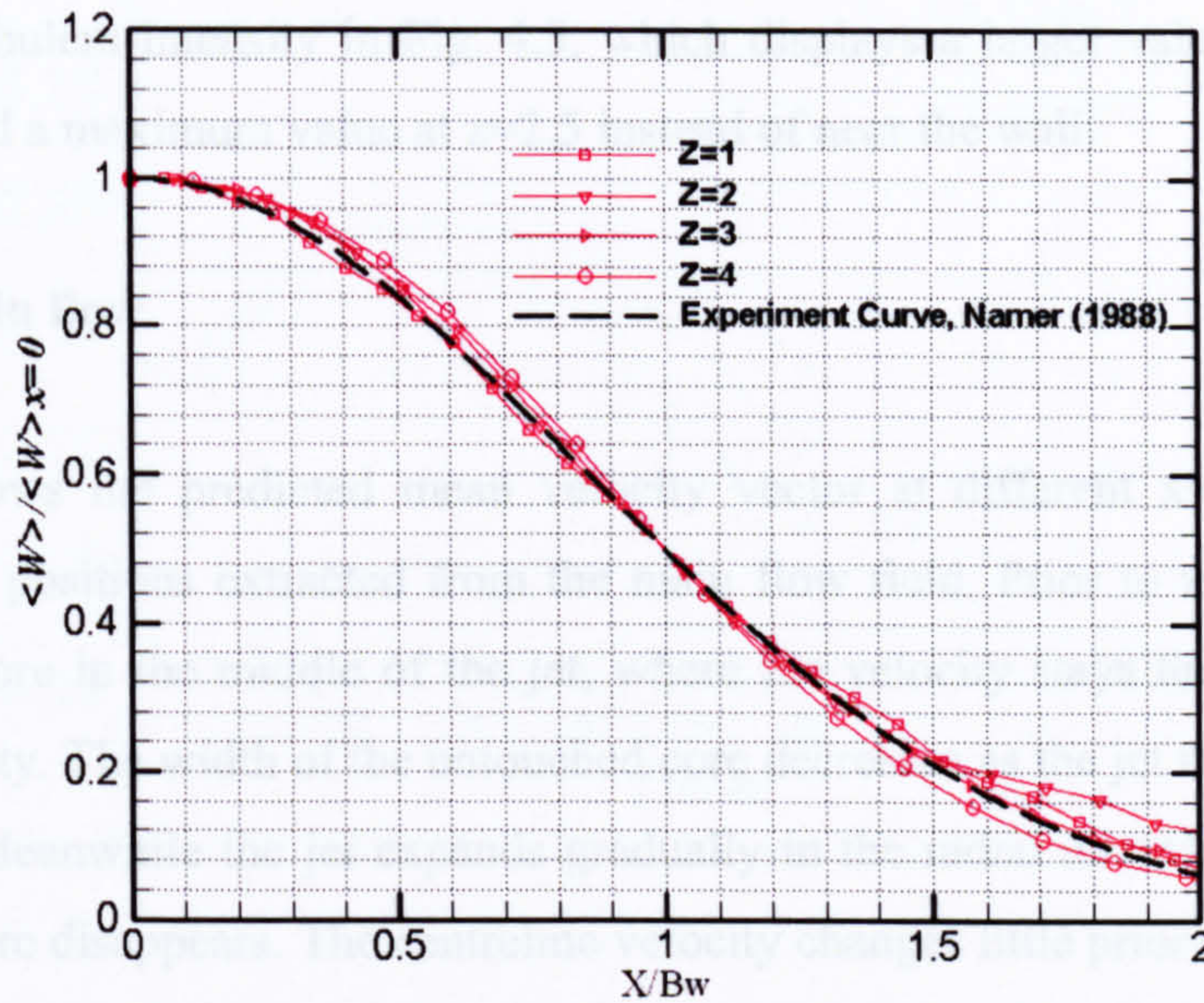


Fig. 4.4 Vertical velocity distributions at different Z positions.

SGS models will cause errors if they fail to properly represent the energy transfer between the resolved scales and the unresolved scales. The current one-equation SGS model does not allow for backscatter of energy from the small scales to the large scales. Therefore, the SGS model acts as an additional viscosity in the filtered NS equations. The additional viscosity stabilizes the numerical solution. Some dissipative numerical schemes also play a role in the stabilization of numerical oscillations. If the adopted numerical schemes are too dissipative, the SGS effect would be masked out. To examine the effect of the one-equation SGS model, comparison between Case 3 with explicit SGS model and Case 4 with implicit SGS model are made. The results in Fig. 4.3 and Figs. 4.5-4.7 show that the SGS model successfully models the effect of the small scales on the resolved large scales and plays a significant role to stabilize the numerical solutions. The results with explicit SGS model are much closer to the experimental data, especially for the turbulent intensities. Without the explicit SGS model, the small

scales are not sufficiently modelled by the implicit numerical errors in the current simulations, and the predicted flow field shows more violent turbulence due to the lack of the additional viscosity. This can be proved by the changing pattern of the vertical turbulent intensity in Fig. 4.5, which displays a larger value away from the wall and a maximum value at $z=2.5$ instead of near the wall.

4.3.1.2 Main flow

Fig.4.2 shows the predicted mean velocity vector at different $x=\text{constant}$ and $z=\text{constant}$ positions extracted from the main flow field. Prior to $z=5$, there is a potential core in the middle of the jet, where the velocity stays the same as the inlet velocity. The width of the untouched core decreases as the jet moves towards the wall. Meanwhile the jet expands gradually in the radial direction. At around $z=5$, the core disappears. The centreline velocity changes little prior to $z=3$, then it rapidly decelerates to zero at the stagnation point. After the impingement, accelerating wall jets develop along the wall surface. But the wall jet flow decelerates gradually with increasing distance from the wall due to the spread of momentum in the wall normal direction.

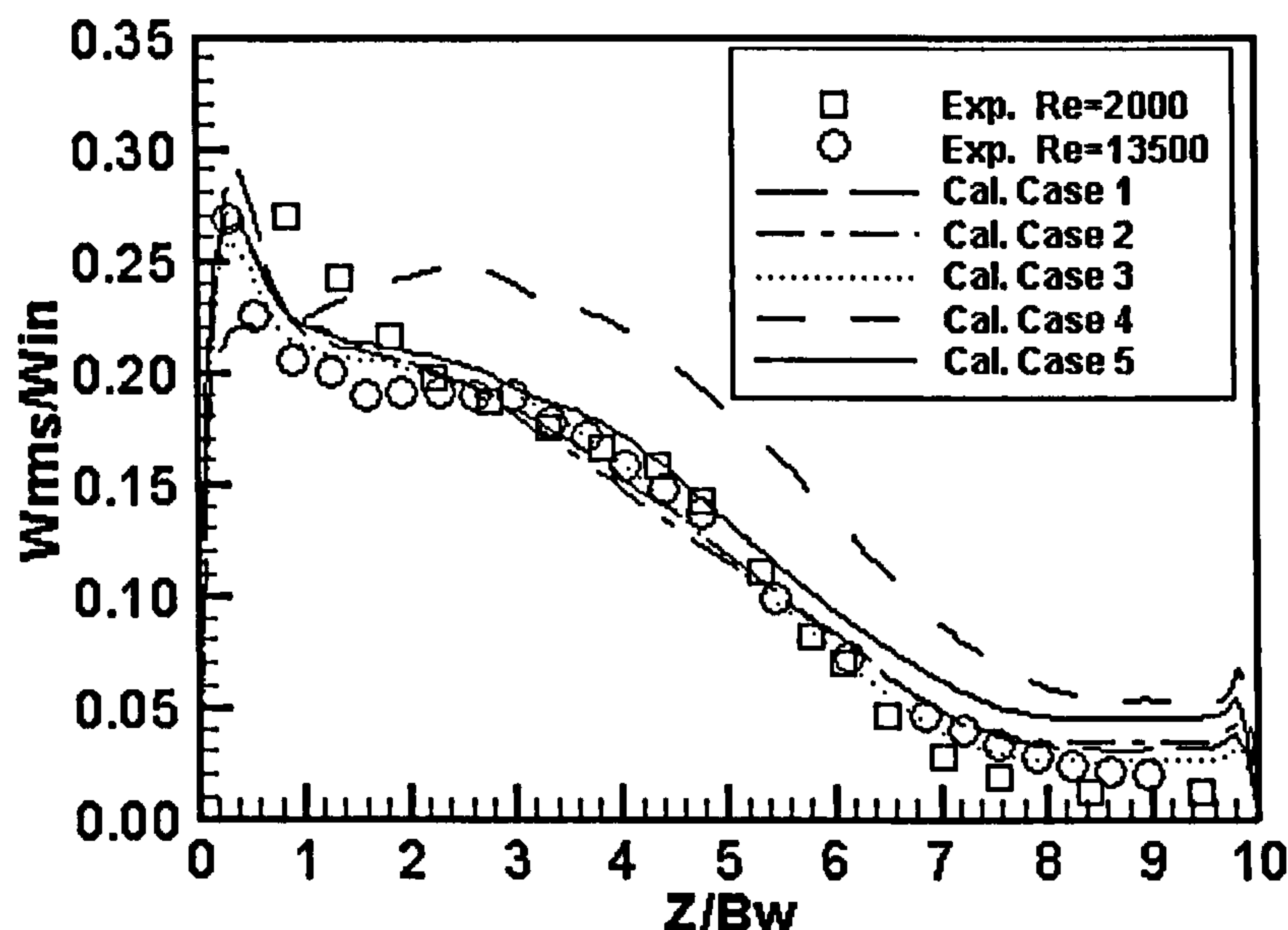


Fig. 4.5 Vertical turbulent intensity along the centreline.

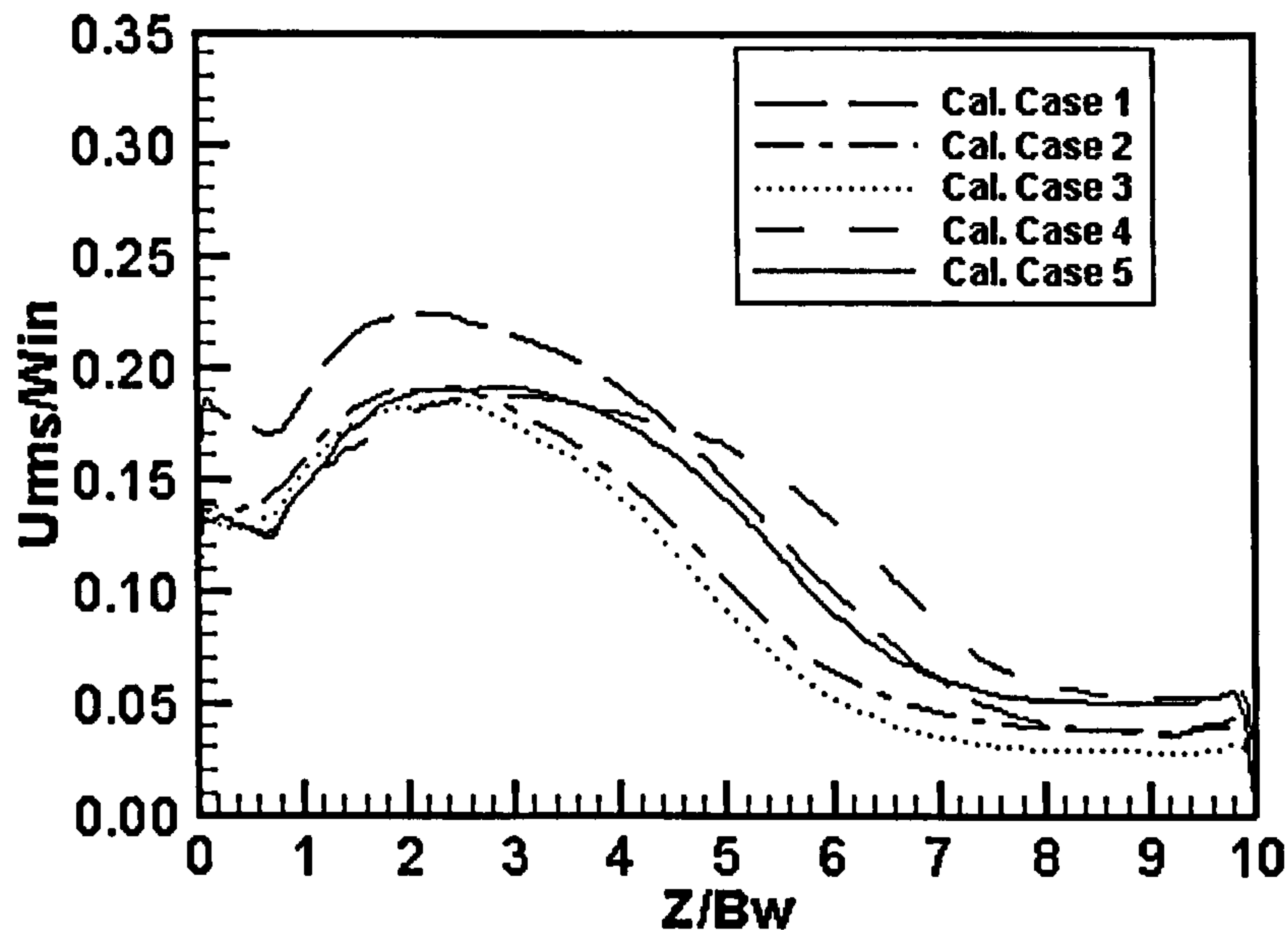


Fig. 4.6 Horizontal turbulent intensity along the centreline.

The vertical velocity distribution on the centreline is given in Fig. 4.3. The predictions are in good agreement with the experimental data [72,103]. The vertical velocity shows a slight dependence on the Reynolds numbers with a large value for $Re = 2000$. The velocity remains nearly constant between $z=5$ and $z=10$. Then it begins to decrease and the decreasing rate changes steeply at $z=2.5$ due to the resistance from the downstream impinging wall, implying that the impingement region occupies about a quarter of the distance between the impinging wall and nozzle exit. This result is consistent with the analysis and experimental observations of Beltoas [13], Gutmark et al. [50] and Sakakbara et al. [103].

Fig. 4.4 presents the self-similar development of the axial velocity in four different planes normal to the jet axis for Case 3. The computed curves compare well with the experimentally obtained Gaussian-like curve of Namer and Otugen [80], demonstrating that the jet expansion is accurately predicted by the present simulations. The parameter B_w in Fig. 4.4 is the half-width of the jet, the distance

from the jet axis to the point where the axial velocity has dropped to half of its centreline value.

4.3.1. 3 Turbulence statistics

Fig. 4.5 shows the distribution of the vertical turbulence intensity on the centreline (along the jet axis). The predictions agree well with the experimental data of Maurel [72] for Reynolds number of 13500, except that there are discrepancies in the region close to the jet exit. The discrepancies may be related to the imposed random turbulent intensity. It can be clearly seen that the predicted value of the fine resolution case is closer to the experiment. The relatively larger discrepancy in the Case 5 for $Re = 13500$ is probably due to the insufficient grid resolution for the high Reynolds number. The predicted results show little dependence on the Reynolds numbers. Just downstream the nozzle exit, the turbulent intensity is small, about only 3% of the inflow random turbulent intensity. The value remains constant between $z=8$ and $z=10$ because the spanwise vortex pairs just start to develop in this region and the turbulent intensity is small. Then the spanwise vortex pairs gain energy from the main flow. Their intensities augment and the RMS (Root Mean Square) value almost increases linearly to 0.2 before the jet move into the impingement region, i.e. prior to $z=2.5$. The turbulence intensity remains almost constant between $z=1$ and $z=2.5$, then increases sharply again to a maximum value of 0.275 near the wall (at $z=0.4$). After the peak, the turbulence intensity decreases quickly to zero at the wall. At the peak, the RMS value is almost the same as the normal component of the main velocity, so there must exists an “up-wash” velocity in the vicinity of the impinging wall. The “up-wash” velocity is induced by the counter rotating vortex pairs near the wall.

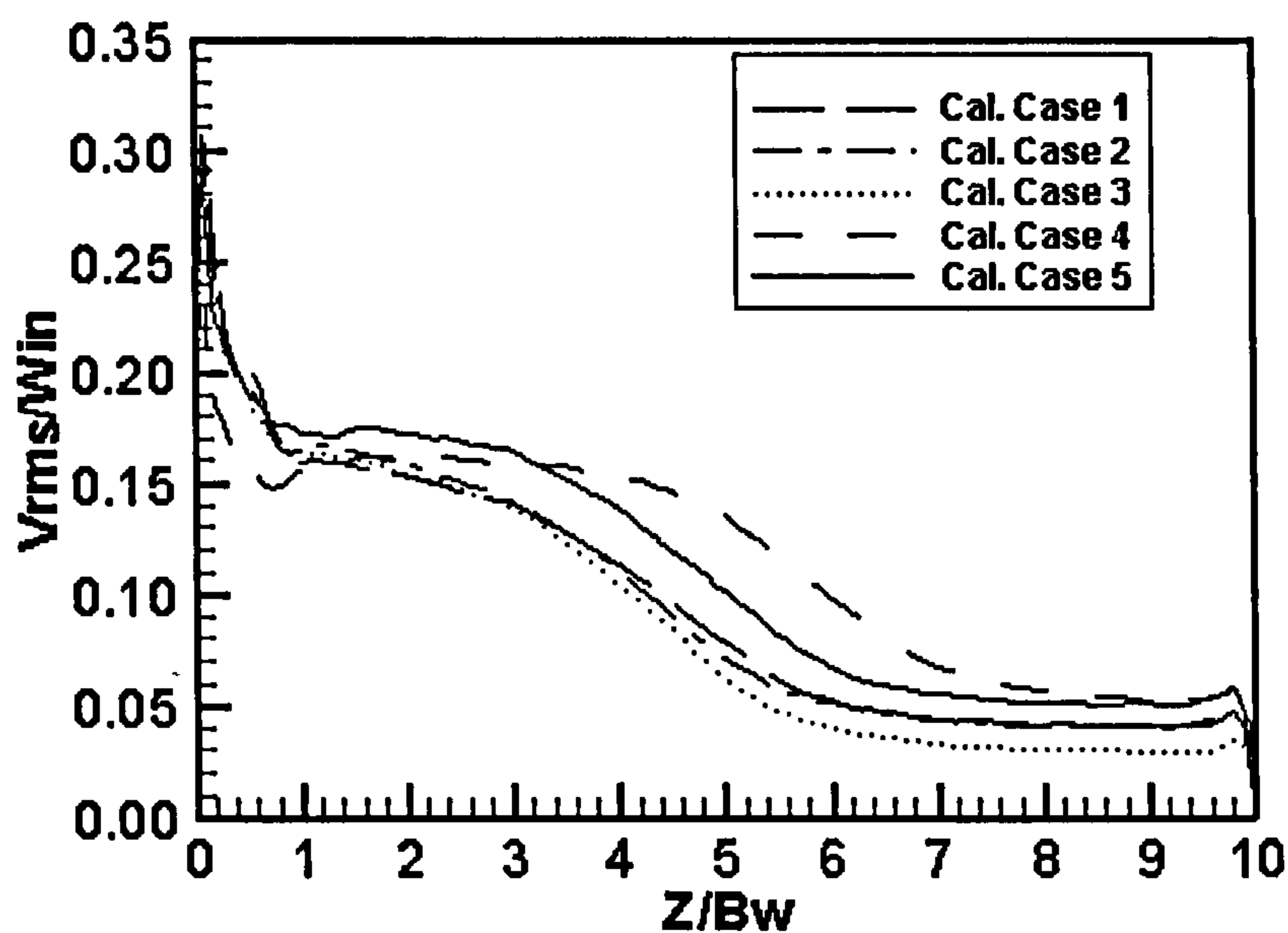


Fig. 4.7 Spanwise turbulent intensity along the centreline.

The distributions of the horizontal and spanwise turbulence intensities on the centreline (along the jet axis) are shown in Figs. 4.6 and 4.7 respectively. The changing pattern of the spanwise turbulence intensity is quite similar to the vertical one. Nearly the same maximum value is found close to the wall, but its position is closer to the wall than the vertical component. This high velocity variance in the spanwise direction is caused by the movement of the counter-rotating vortex pair on the wall. The altering pattern of the horizontal turbulence variance follow that of the vertical one as well before the jet moves into the impingement zone, and the variance reaches a maximum value of 0.2 at $z = 2.5$. After the jet moves into the impingement zone, the value is decreased to 0.15 close to the wall. Fig. 4.8 plots the Reynolds shear stress distribution along the x-direction at $z = 5$. The computed curve is in good agreement with the experimental data. The maximum value is 0.015 and located around the shear layer. The results also display little Reynolds number dependence.

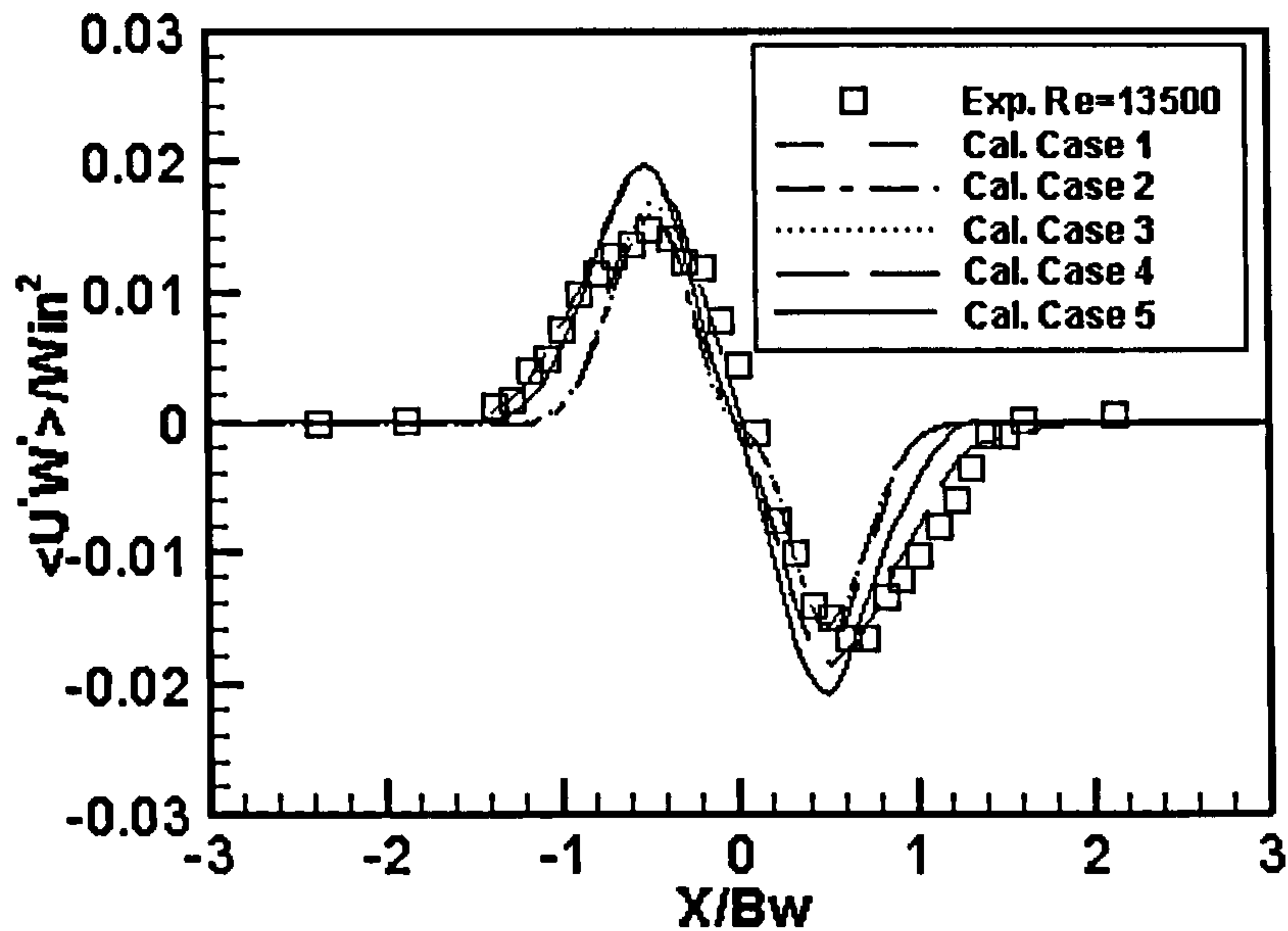
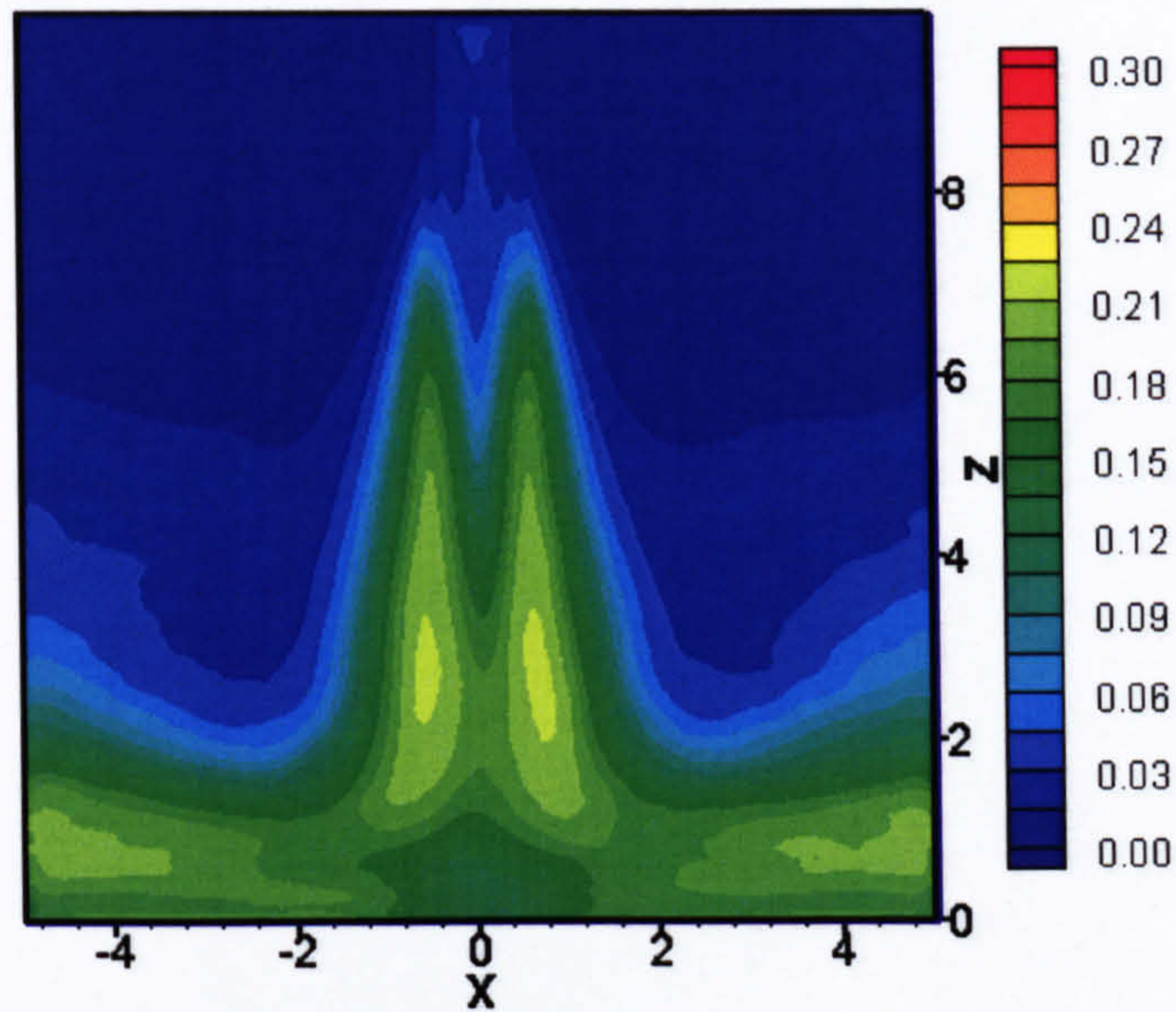


Fig. 4.8 Horizontal distribution of the Reynolds shear stress at $z=5$.

The contour plots of non-dimensional components of turbulence intensities and Reynolds shear stress are also presented in Fig. 4.9. All variances show a high value in the jet shear layer and a lateral spread pattern with increasing distance downstream from the nozzle exit, due to the perturbation of rolling vortices and the flapping of the jet. The variances have a small value close to nozzle exit prior to the emergence of vortex rollers at both shear layers. The rollers induce a high disturbance along the two shear layers. The vertical and spanwise components also exhibit a highest value near the impinging wall around stagnation point, which is related to the counter rotating vortex aligning with the wall. This also verifies that the direction of the vortex pair is along the wall. The lateral component and the Reynolds shear stress show a high value in the outer mixing region of the wall-bounded flow after impingement, but demonstrate a relatively low value in the impingement region.

(a)



(b)

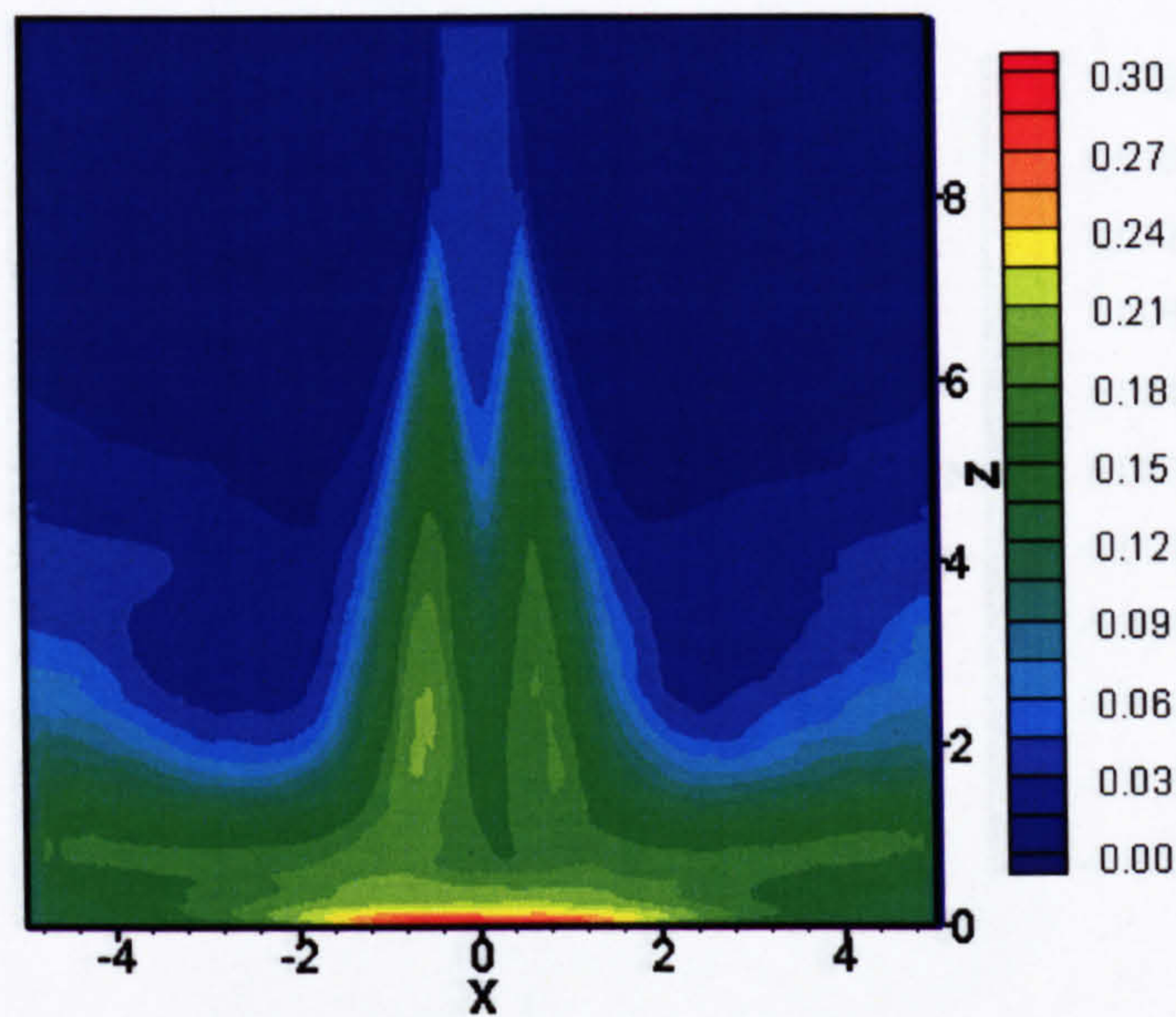
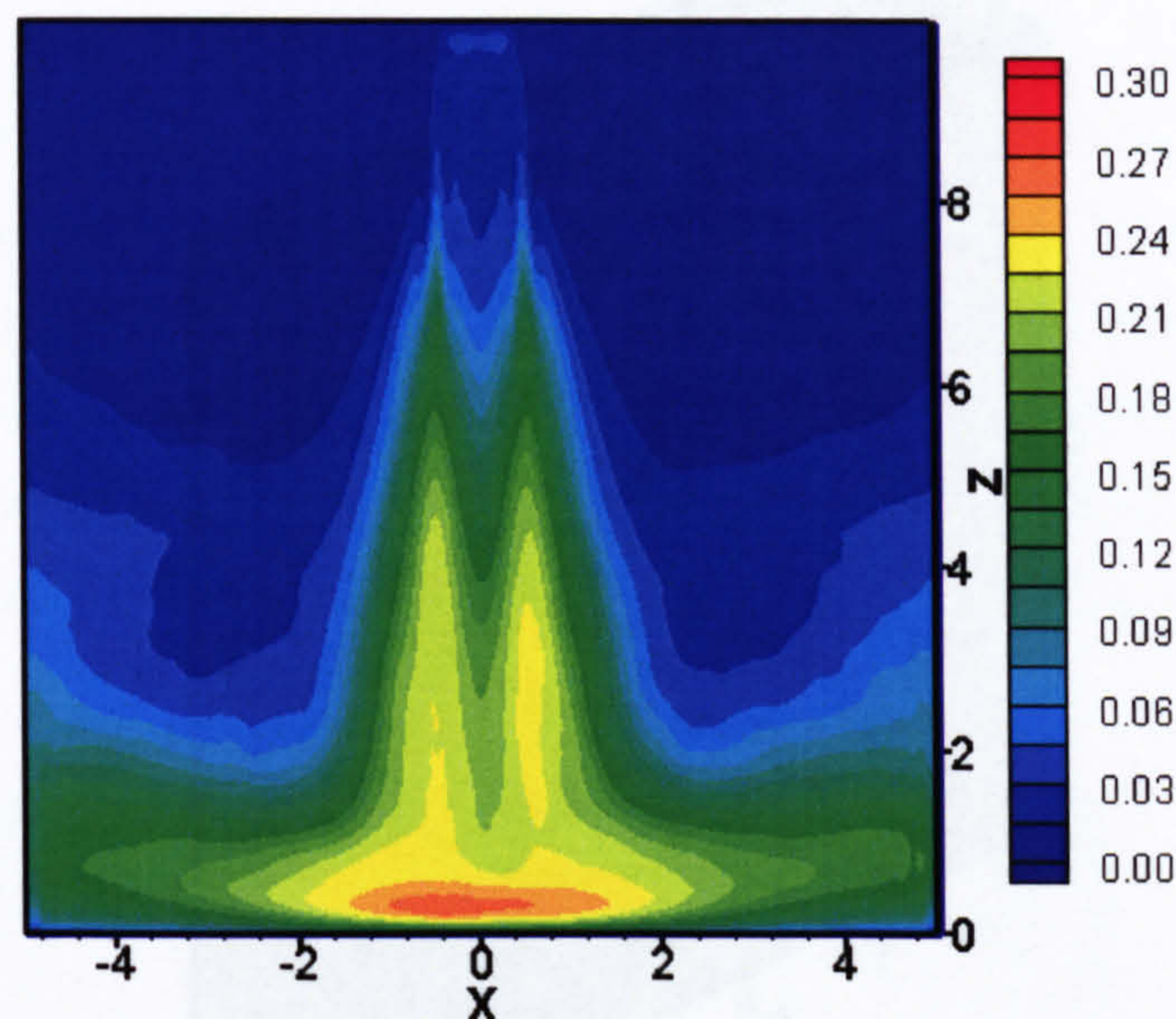


Fig. 4.9 Contours of non-dimensional components of turbulence intensity and Reynolds shear stress on the middle plane [x-component (a), y-component (b), z-component (c), and Reynolds shear stress (d)]. (To be continued)

(c)



(d)

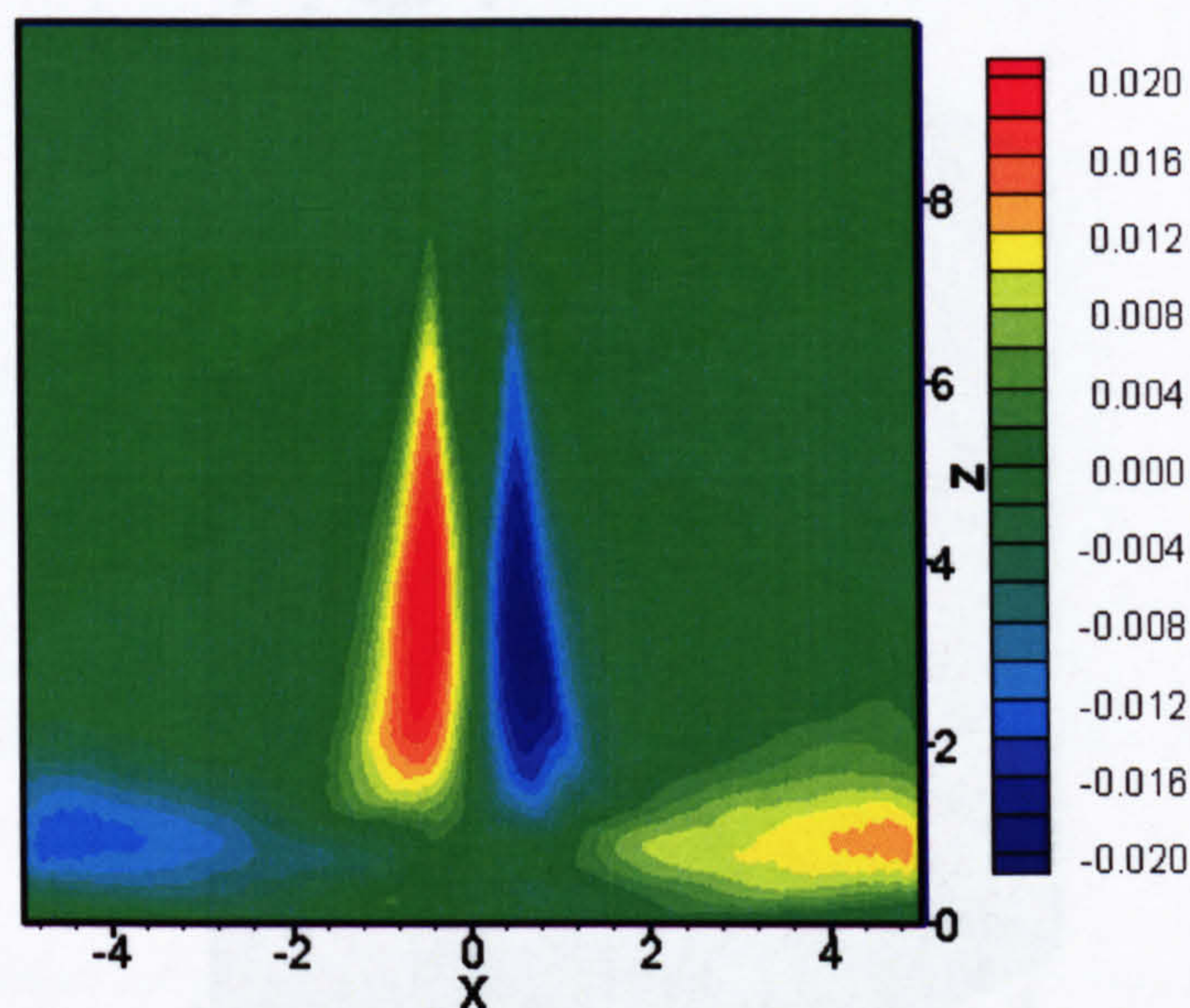


Fig. 4.9 (continued) Contours of non-dimensional components of turbulence intensity and Reynolds shear stress on the middle plane [x-component (a), y-component (b), z-component (c), and Reynolds shear stress (d)].

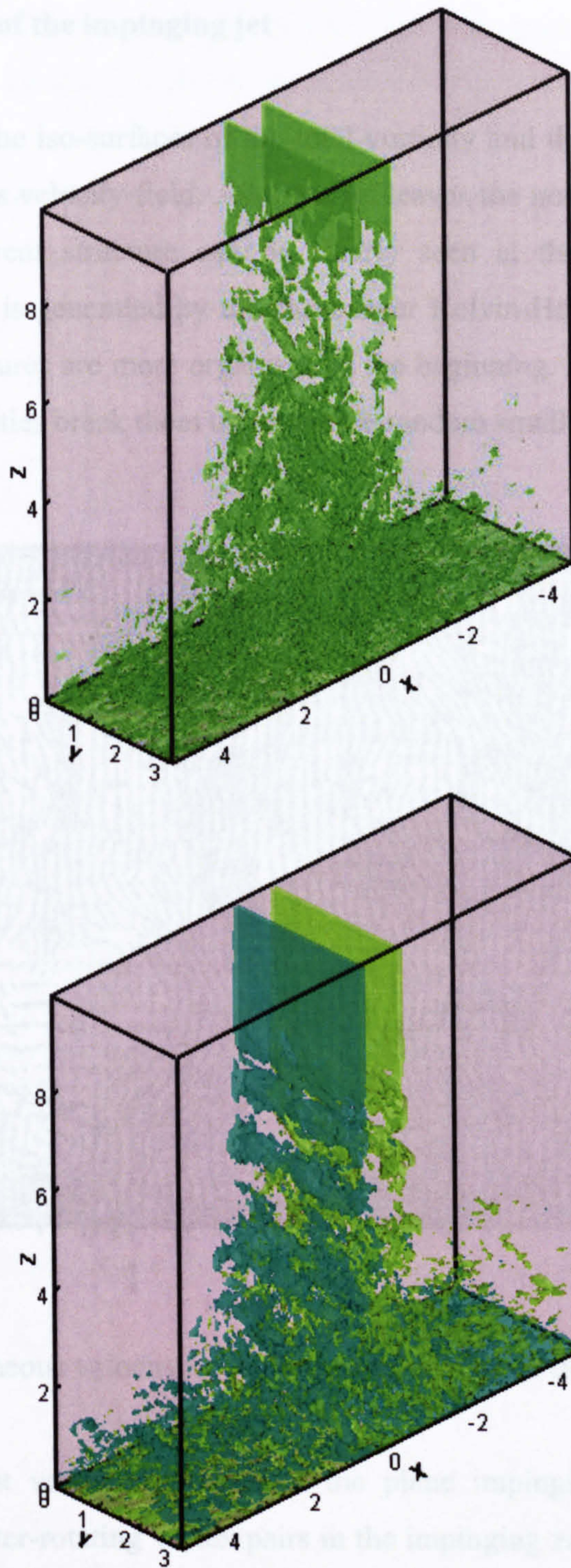


Fig. 4.10 Iso-surfaces of normalized total vorticity $\omega = 6.3$ (top) and spanwise vorticity component $\omega_y = \pm 3.3$ (bottom).

4.3.1.4 Dynamics of the impinging jet

Fig. 4.10 depicts the iso-surfaces of the total vorticity and the spanwise vorticity of an instantaneous velocity field. After the jet leaves the nozzle exit, a highly 3-dimensional coherent structure can be clearly seen at the shear layers. The coherent structure is generated by the shear-layer Kelvin-Helmholtz instabilities. The vortical structures are more organized in the beginning. Further downstream, secondary instabilities break them up into more random smaller scales turbulence.

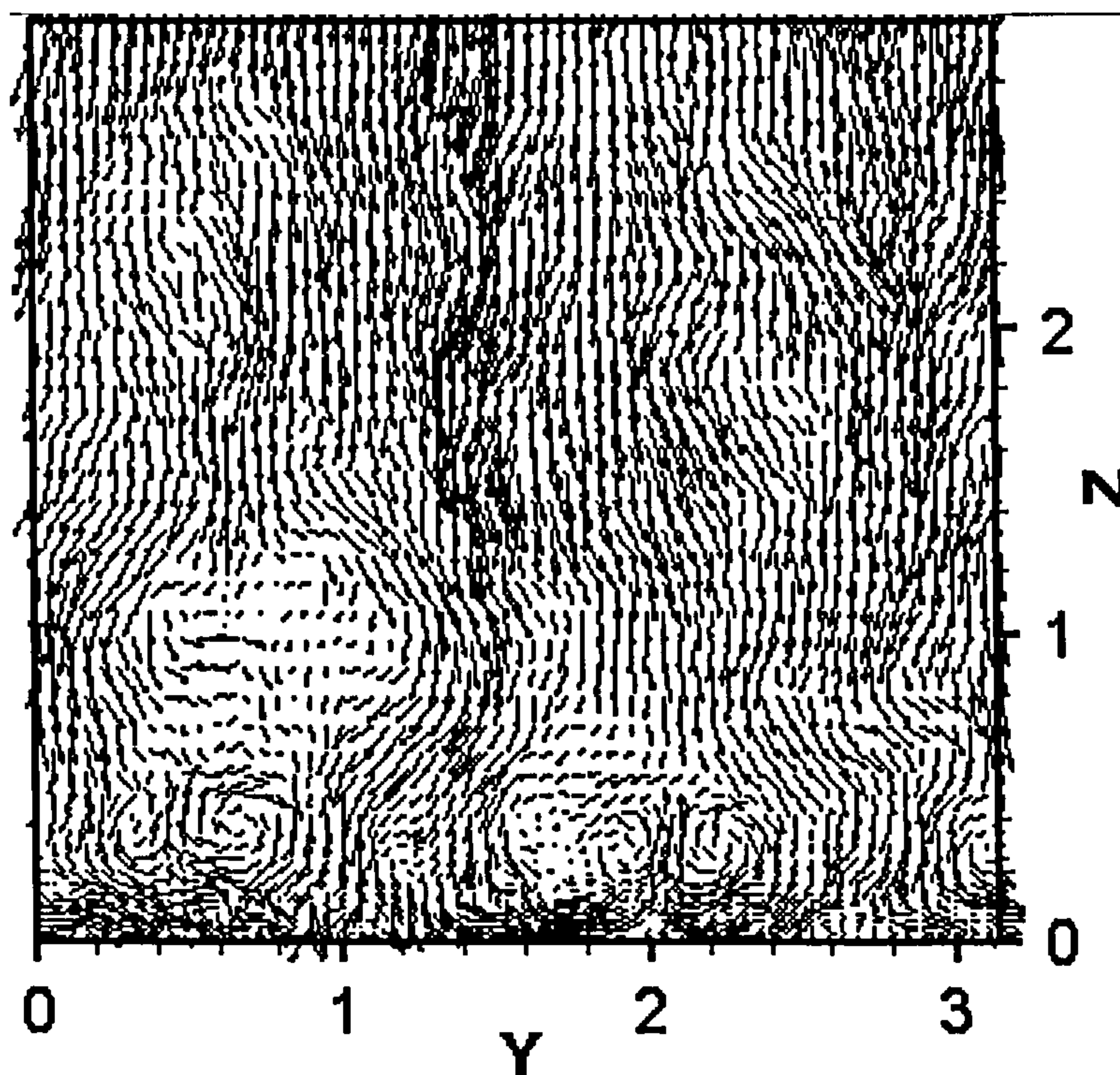


Fig. 4.11 Instantaneous velocity vector on y-z middle plane through the centreline.

Another important vortical structure of the plane impinging jet is the three-dimensional counter-rotating vortex pairs in the impinging zone. The vortex pairs lie on the wall along the direction of wall jets extending from both sides of the symmetry jet plane. Their positions are not fixed on the wall but move in the spanwise direction. The existence of these counter-rotating vortices induces a very

high turbulent intensity in the vicinity of wall. The important vortical structure is reproduced by the current simulation as shown in Fig. 4.11. Two pairs of the vortices can be clearly seen in the figure. There exists a region with “up-wash” velocity close to wall. This “up-wash” velocity is induced by the counter-rotating vortex pair.

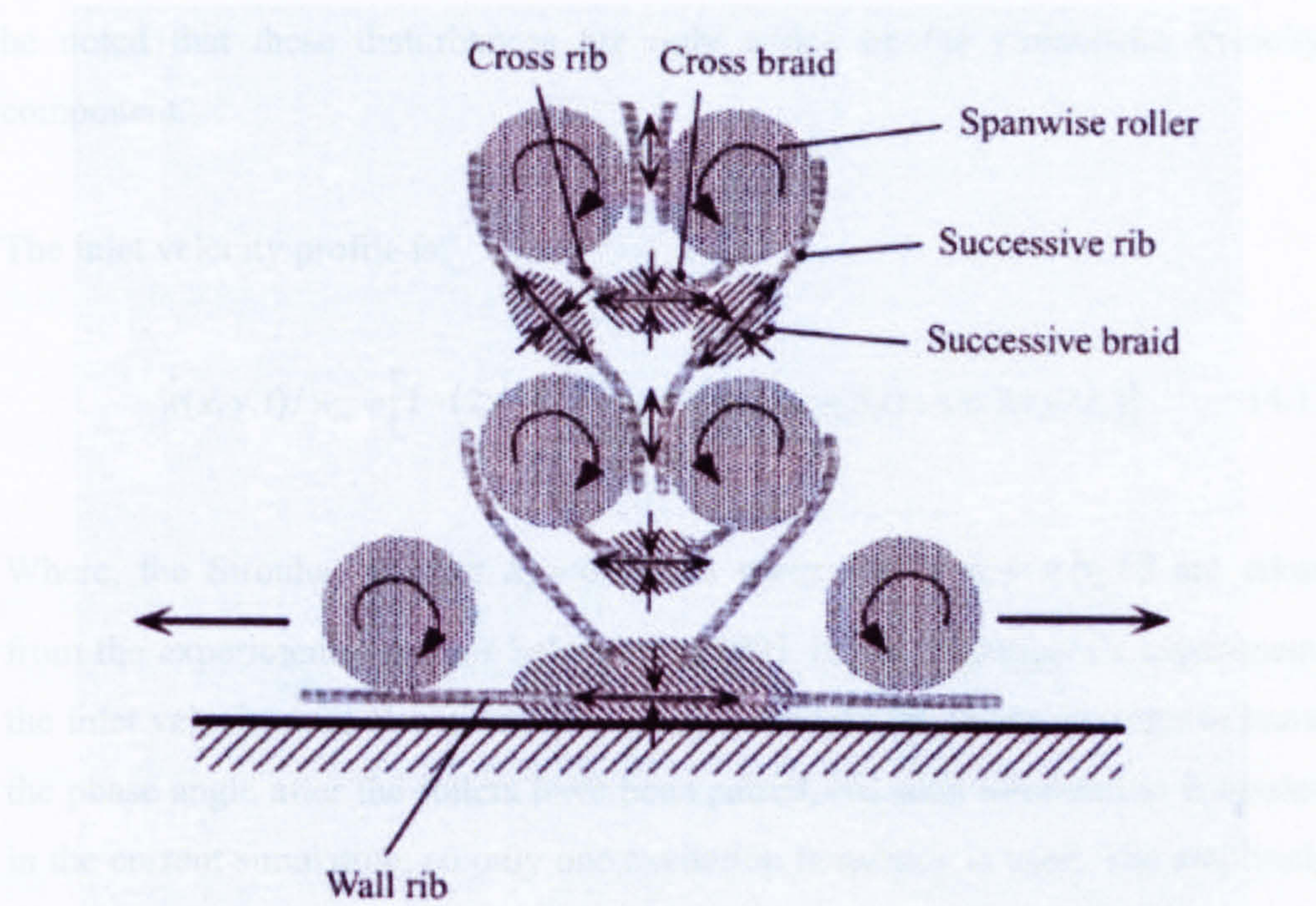


Fig. 4.12 Schematic of the vertical structure extracted from [103]

4.3.2 Forced plane impinging jet

The roll-up of the vortices of plane impinging jet is susceptible to inlet perturbations, and can be locked by the perturbations. The roll-up process of the locked jet become periodic and regular, and the vortex structures are quite organized and coherent. In the present study, the jet was locked both in phase and laterally in space by imposing a streamwise sinusoidal disturbance and a spatially periodic disturbance in spanwise direction as defined by equation (4.1). It should be noted that these disturbances are only added on the streamwise velocity component.

The inlet velocity profile is:

$$w(x, y, t) / w_{in} = \left[1 - (2x / B_w)^8 \right] + A \times [\sin(2\pi w_{in} S_t t) + \sin(2\pi y / \lambda_z)] \quad (4.1)$$

Where, the Strouhal number $S_t = 0.36$ and wave length $\lambda_z = \pi B_w / 3$ are taken from the experimental data of Sakakibara [103]. In the Sakakibara's experiment, the inlet velocity was also excited by a sub-harmonic frequency in order to know the phase angle after the rollers have been paired. No such information is needed in the current simulation, so only one excitation frequency is used. The amplitude of fluctuations A is taken to be 0.012. This takes into account the fact that the initial roll-up of the shear layers would be locked when the RMS turbulence intensity at the nozzle exit reaches $0.009 w_{in}$ [103].

4.3.2.1 Phase-averaging

The organized eddy structures corresponding to the forced inlet condition can be extracted by the phase-averaging technique. In the study of turbulence structure, the time-varying velocity signal $u(x, t)$ can be decomposed into a global mean

component $\bar{u}(x)$, a periodic mean component $\tilde{u}(x,t)$ and a residual random component $u'(x,t)$. This triple decomposition used by Hussain [60] can be written as follows:

$$u(x,t) = \bar{u}(x) + \tilde{u}(x,t) + u'(x,t) = \langle u(x,t) \rangle + u'(x,t) \quad (4.2)$$

$$\bar{u}(x) = \lim_{T \rightarrow \infty} \frac{1}{T} \int_0^T u(x,t) dt \quad (4.3)$$

$$\langle u(x,t) \rangle = \lim_{N \rightarrow \infty} \frac{1}{N} \sum_{n=0}^{N-1} u(x, t + n\tau) \quad (4.4)$$

Where τ is the vortex shedding period and

$$\langle u(x,t) \rangle = \bar{u}(x) + \tilde{u}(x,t) \quad (4.5)$$

is the phase average associated with coherent structures. The phase average is realized by taking an average over the conditional samples at a given phase. In the present study, the phase-averaging period is taken as $\frac{2}{f}$, but not $\frac{1}{f}$, $f = w_{in} \frac{S_t}{B_w}$ is the forcing frequency. This is because the dominant frequency of the forced jet is $\frac{f}{2}$ as will be explained later. The phase averaging is taken at: $\pi w_{in} S_t t = 0 + 2n\pi, \pi/4 + 2n\pi, \dots, 7\pi/4 + 2n\pi$, where n is a natural number. Since no random fluctuation is added on the inlet plane and the jet is locked by the artificial periodic perturbation, the phase averaged flow field is quite similar to the instantaneous flow field, except for slight differences in the near wall region. Moreover, as will be seen, the phase averaged flow field of the jet is symmetrical about the middle plane of the jet, and the vortex structures are quite organized and consist of several coherent structures. From now on, all quantities will be phase-averaged ones.

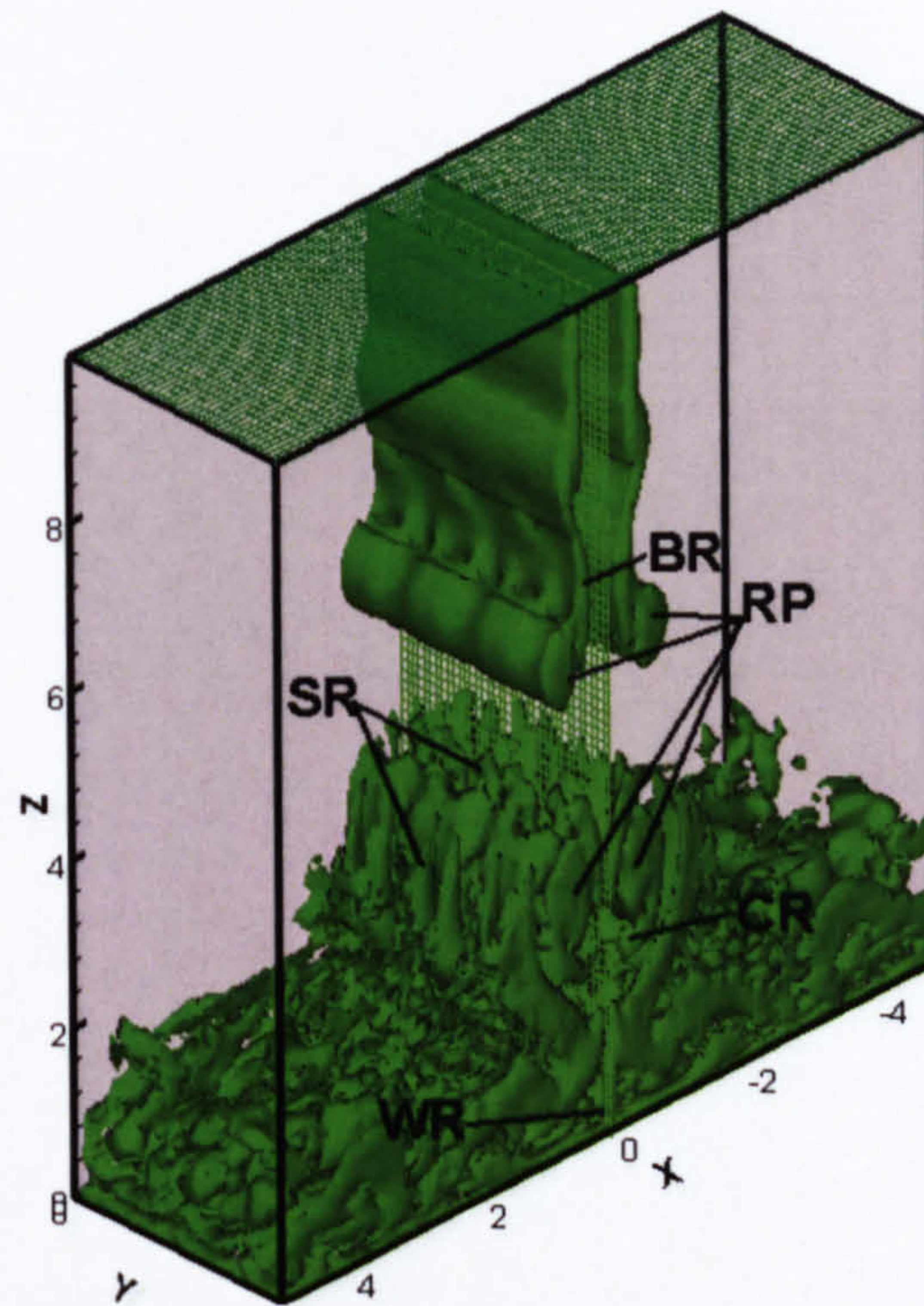
4.3.2.2 Overview of the vortex structures

To facilitate understanding of the vortical introduced in the following sections, a schematic drawing of the vertical structure extracted from [103] is shown in Fig. 4.12. Fig. 4.13 gives an overview of the vortex structures of the forced plane impinging jet using iso-surface of total vorticity at different phase angles. All vorticities are non-dimensionized by $\frac{w_{in}}{B_w}$. Just downstream the nozzle, the shear

layers begin to evolve into two symmetrical spanwise vortices, due to the Kelvin-Helmholtz instability of the shear layer. The positions of the vortices are locked by inlet conditions (their production frequencies is the same as the inlet perturbation frequency), and their intensities are rather weak at the beginning. However, not all these vortices can roll up into the dominant vortex structure, the spanwise rollers. Alternatively, one pair of the vortices above the rollers are stretched, by the rollers, into the so-called braid-region (labelled as BR). Therefore, the dominant frequency of the impinging jet, i.e. the roll-up frequency of the roller, is only half of the perturbation frequency. This is the reason why the phase-averaging period is taken to be $\frac{2}{f}$. Accordingly, the rollers begin to

replicate the spanwise spatial perturbation of the inlet condition, and the distortion and intensity level of the rollers grow larger as the rollers move towards the impinging wall. After impinging the wall, the roller pair moves apart from each other following the wall jets. The above process can be seen more clearly in Fig. 4.14 by iso-surfaces of the spanwise vorticity component. The convection velocity of the rollers is not constant. There is an acceleration stage after the shear layers evolve into the rollers and a deceleration stage while rollers move into the impingement region. The computed main convection velocity of the roller is $0.51w_{in}$, which is quite close to the corresponding measured value of $0.52w_{in}$ [103].

(a) $\phi = 0$



b) $\phi = \pi/2$

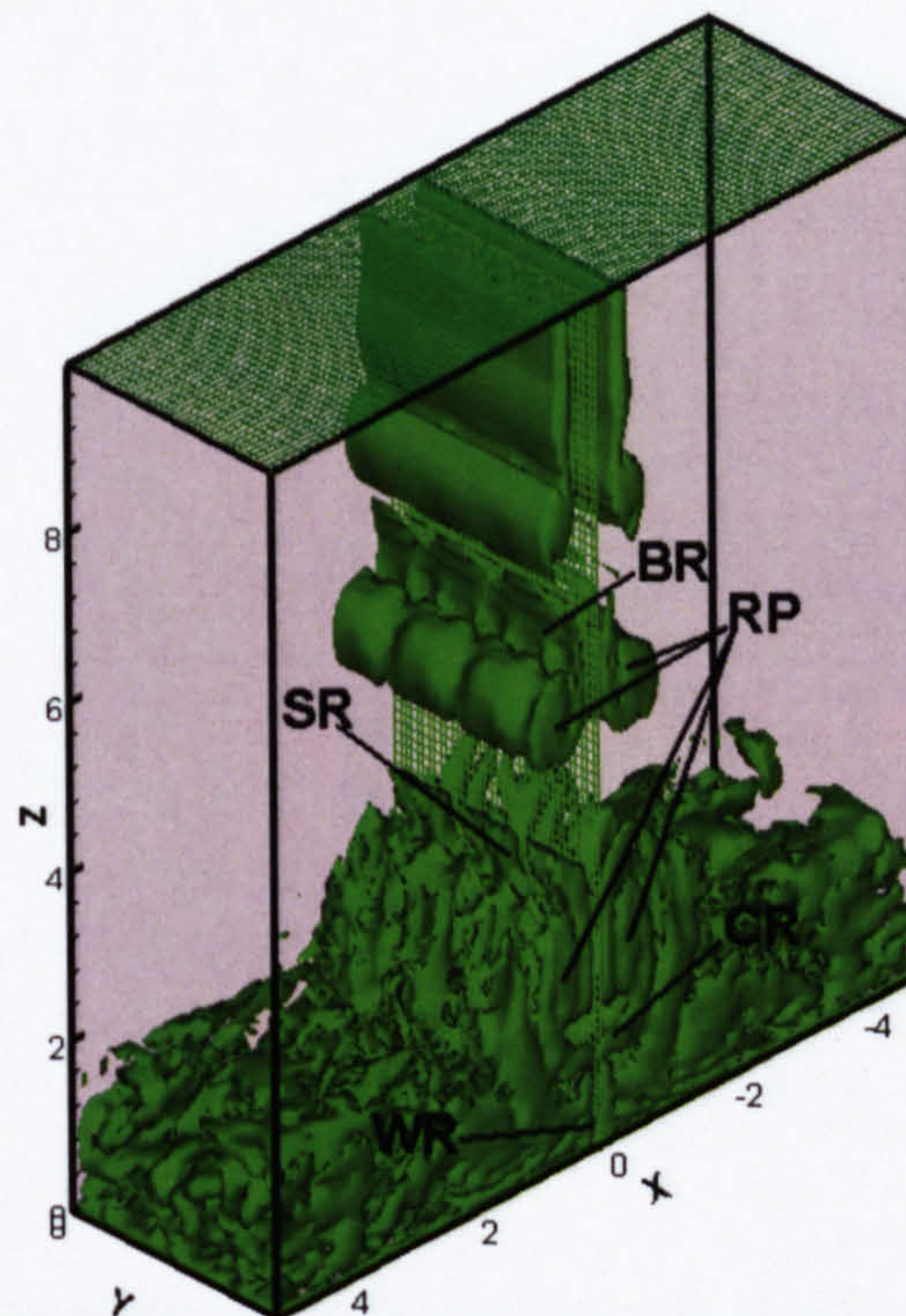
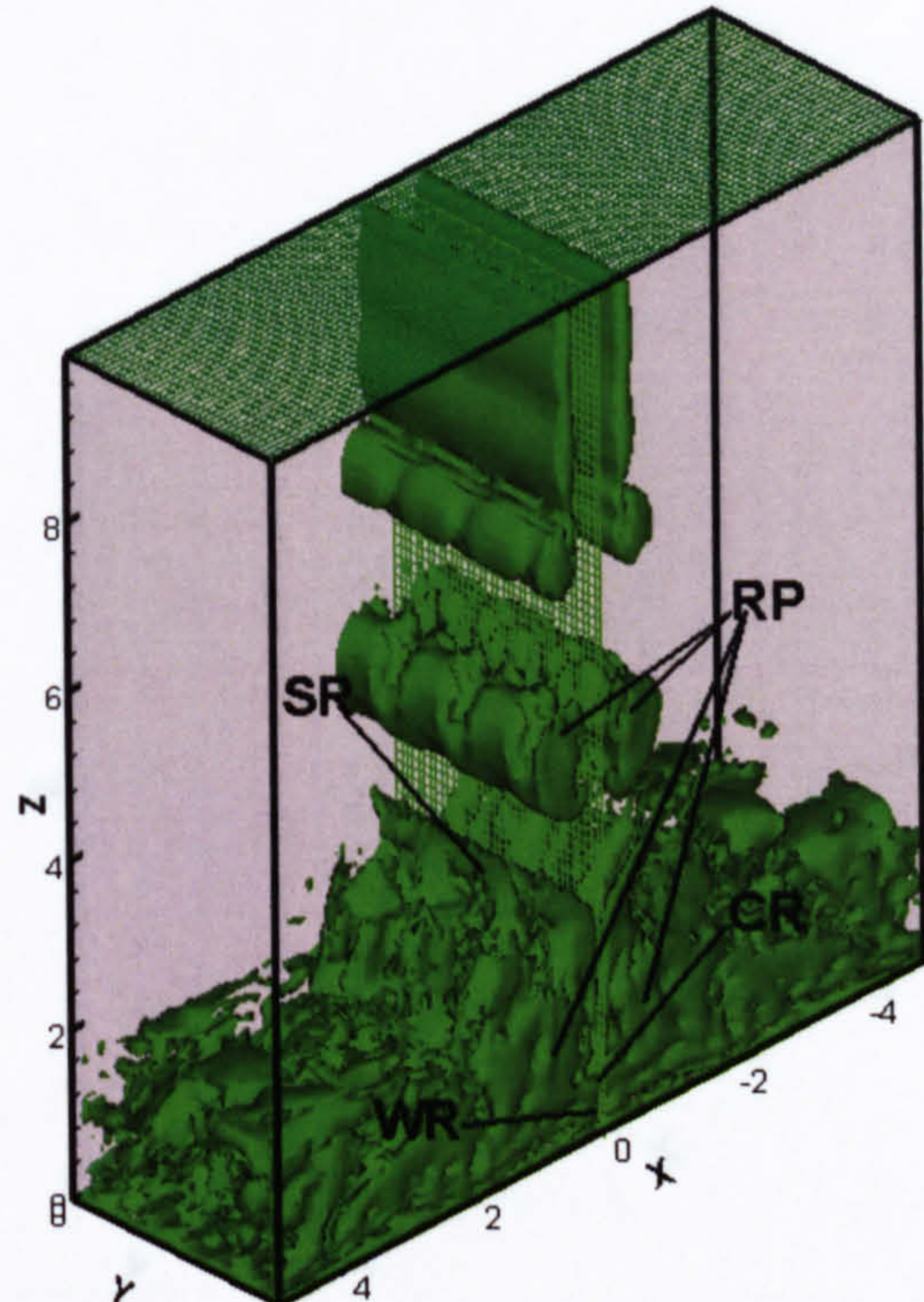


Fig. 4.13 Iso-surfaces of the total vorticity at different phase angles, $\omega = 1.8$. (To be continued)

(c) $\phi = \pi$



(d) $\phi = 3\pi/2$

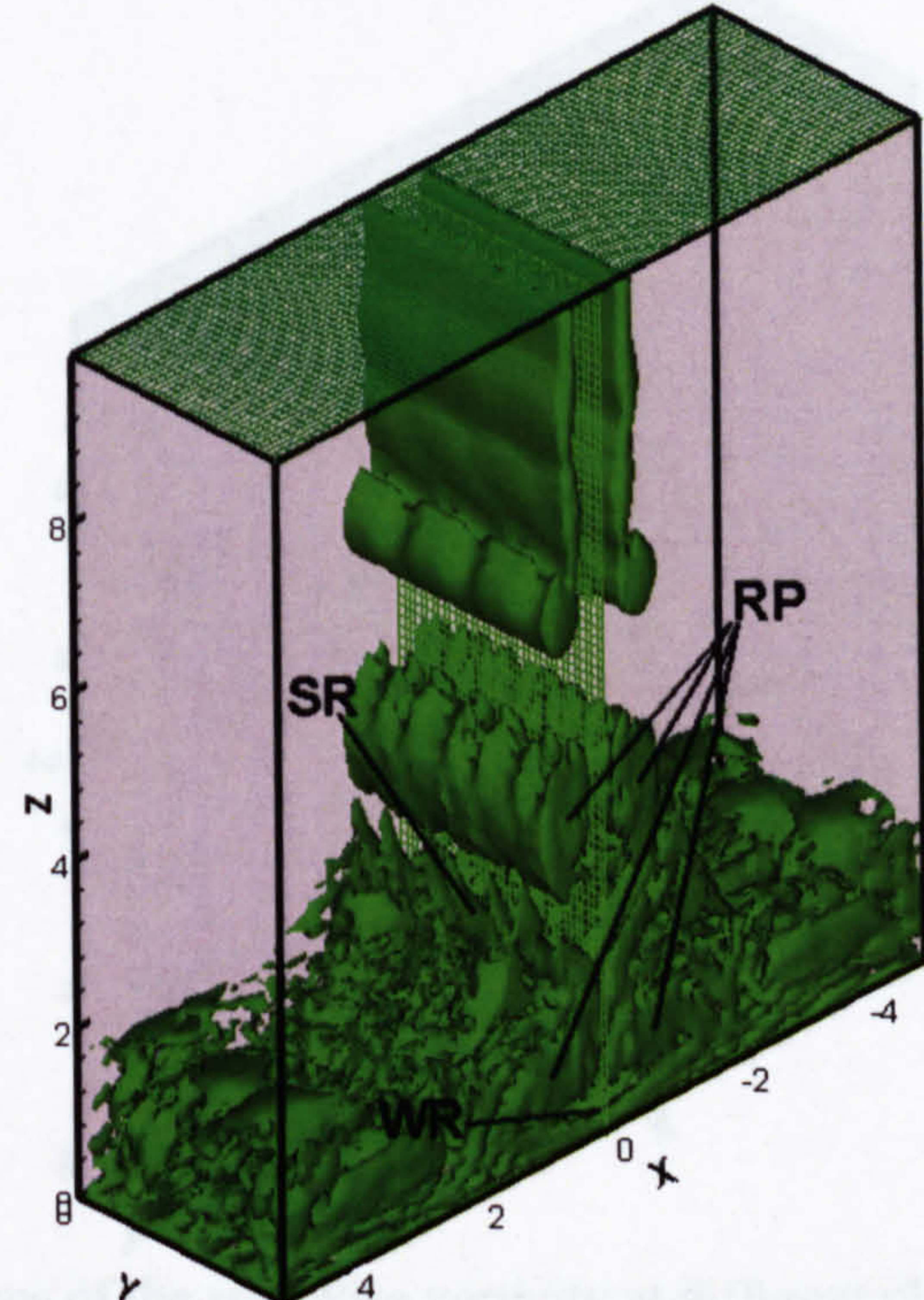
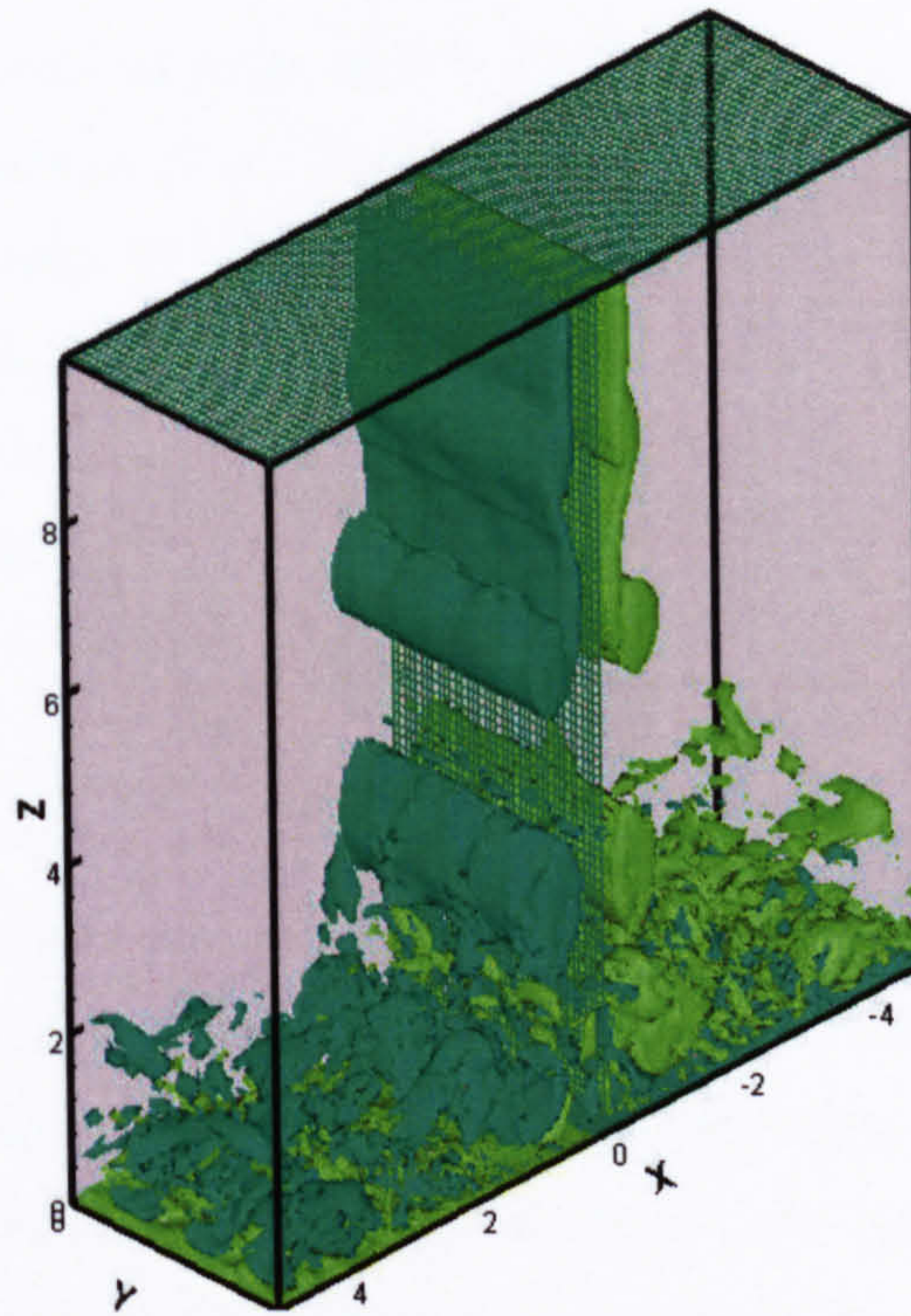


Fig. 4.13 (Continued) Iso-surfaces of the total vorticity at different phase angles, $\omega = 1.8$.

(a) $\phi = 0$



(b) $\phi = \pi/2$

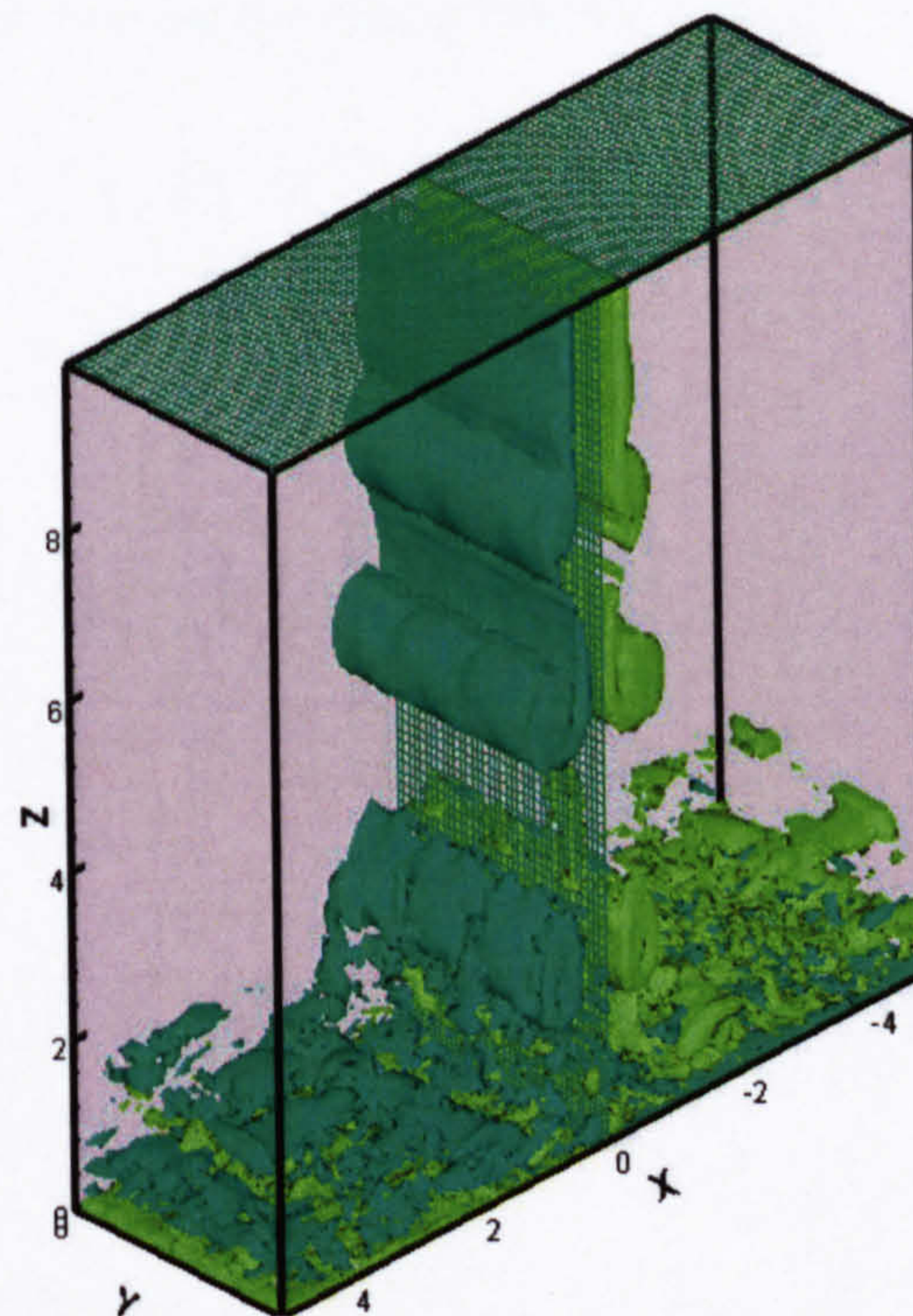
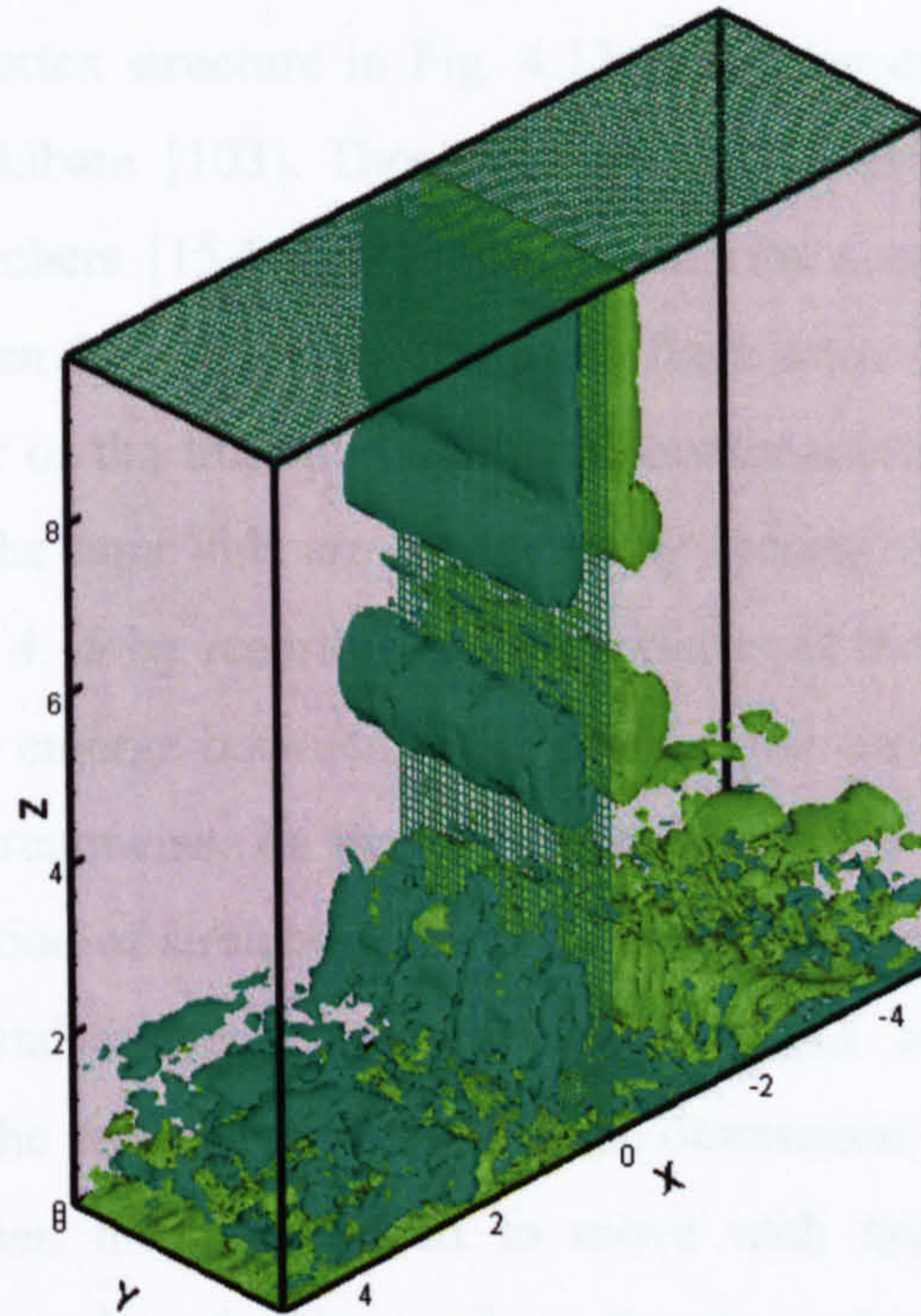


Fig. 4.14 Iso-surfaces of the spanwise vorticity at different phase angles, $\omega_y = 1.4$ (left roller) and $\omega_y = -1.4$ (right roller). (To be continued)

(c) $\phi = \pi$



(d) $\phi = 3\pi/2$

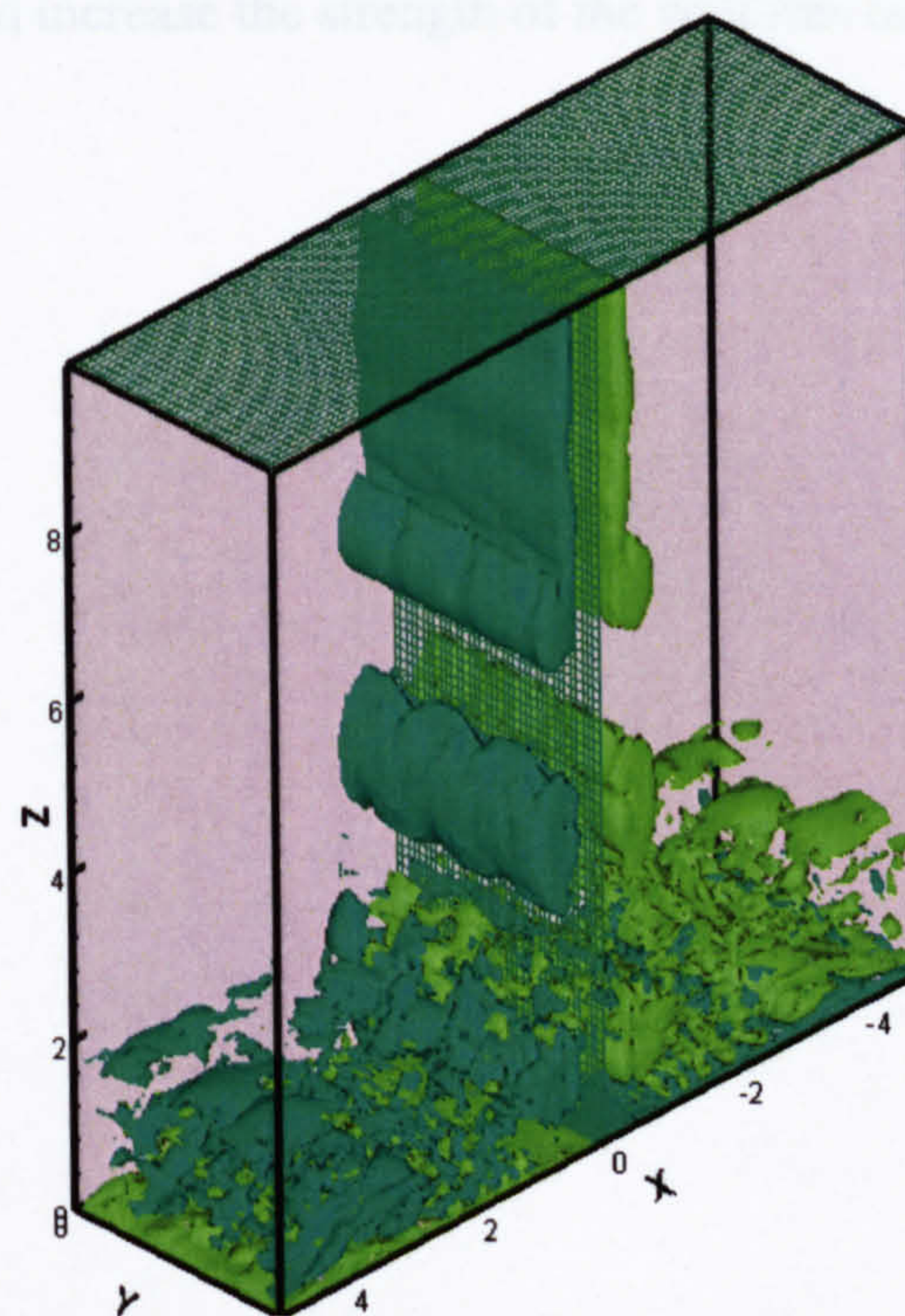
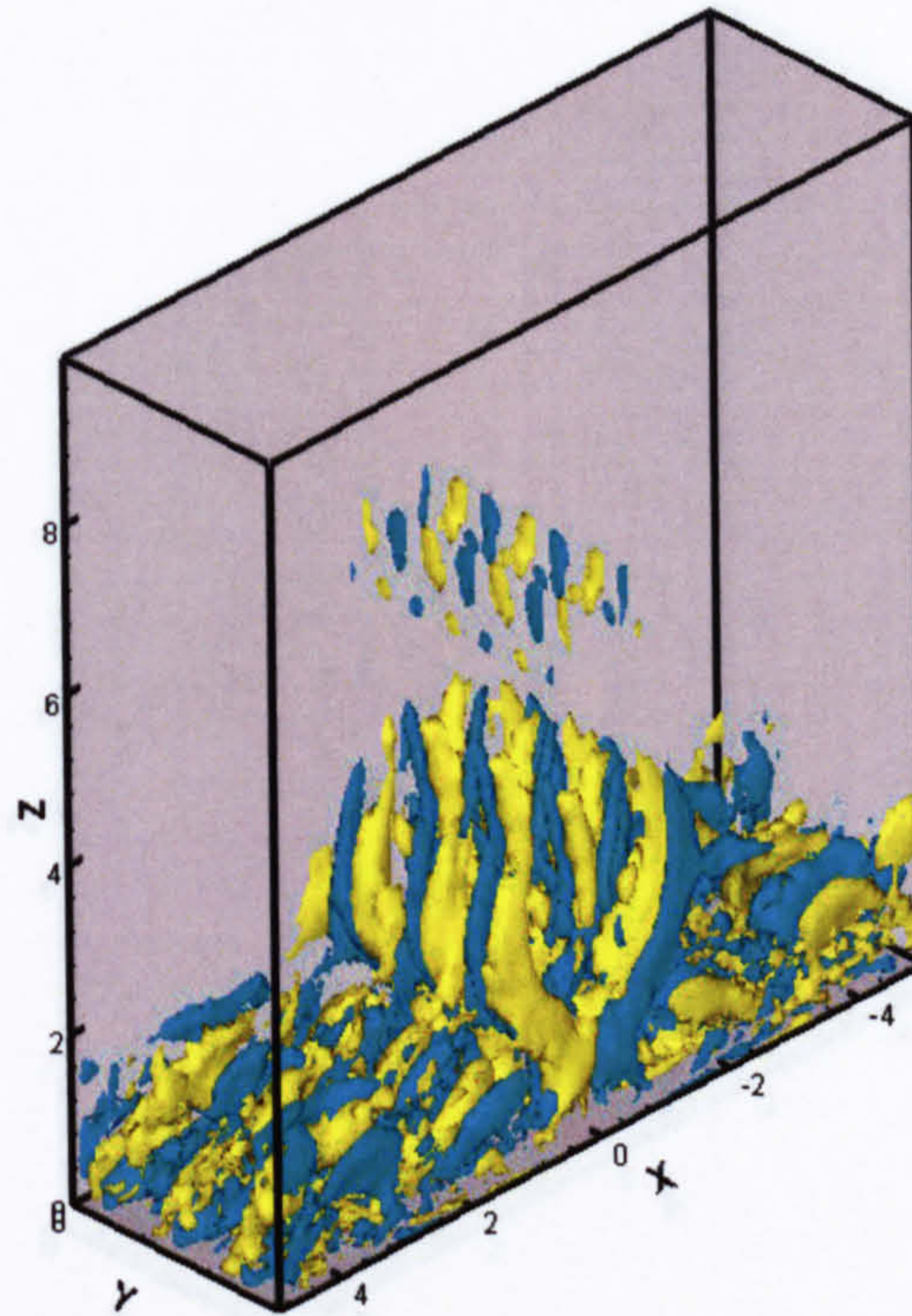


Fig. 4.14 (continued) Iso-surfaces of the spanwise vorticity at different phase angles, $\omega_y = 1.4$ (left roller) and $\omega_y = -1.4$ (right roller).

Another apparent vortex structure in Fig. 4.13 is the successive ribs, labelled as SR following Sakakibara [103]. These ribs were also previously observed by several other researchers [15,60,103]. Successive ribs consist of two separated arrays of ribs between two adjacent roller pairs. Each array of ribs is composed of three (wave number of the inlet perturbation) counter-rotating vortex pairs. Two adjacent rollers on the same side are connected by successive ribs. These ribs can also be seen in Fig. 4.15 by resorting to iso- surfaces of the streamwise vorticity. The successive ribs emerge between roller pairs in the early stage of the rollers. Their direction is streamwise. As they advect toward the wall, their strengths are amplified by the action of stretching. Near the impingement region, they begin to change directions and connect with the two same side adjacent rollers. Upon touching the wall, the successive ribs retain the orientation until the upper rollers reach the wall. Then they are forced to move with and fall on the rollers. Meanwhile, the successive ribs change their directions along the wall and merge with the wall ribs and increase the strength of the wall ribs on the same side.

(a) $\phi = 0$



(b) $\phi = \pi/2$

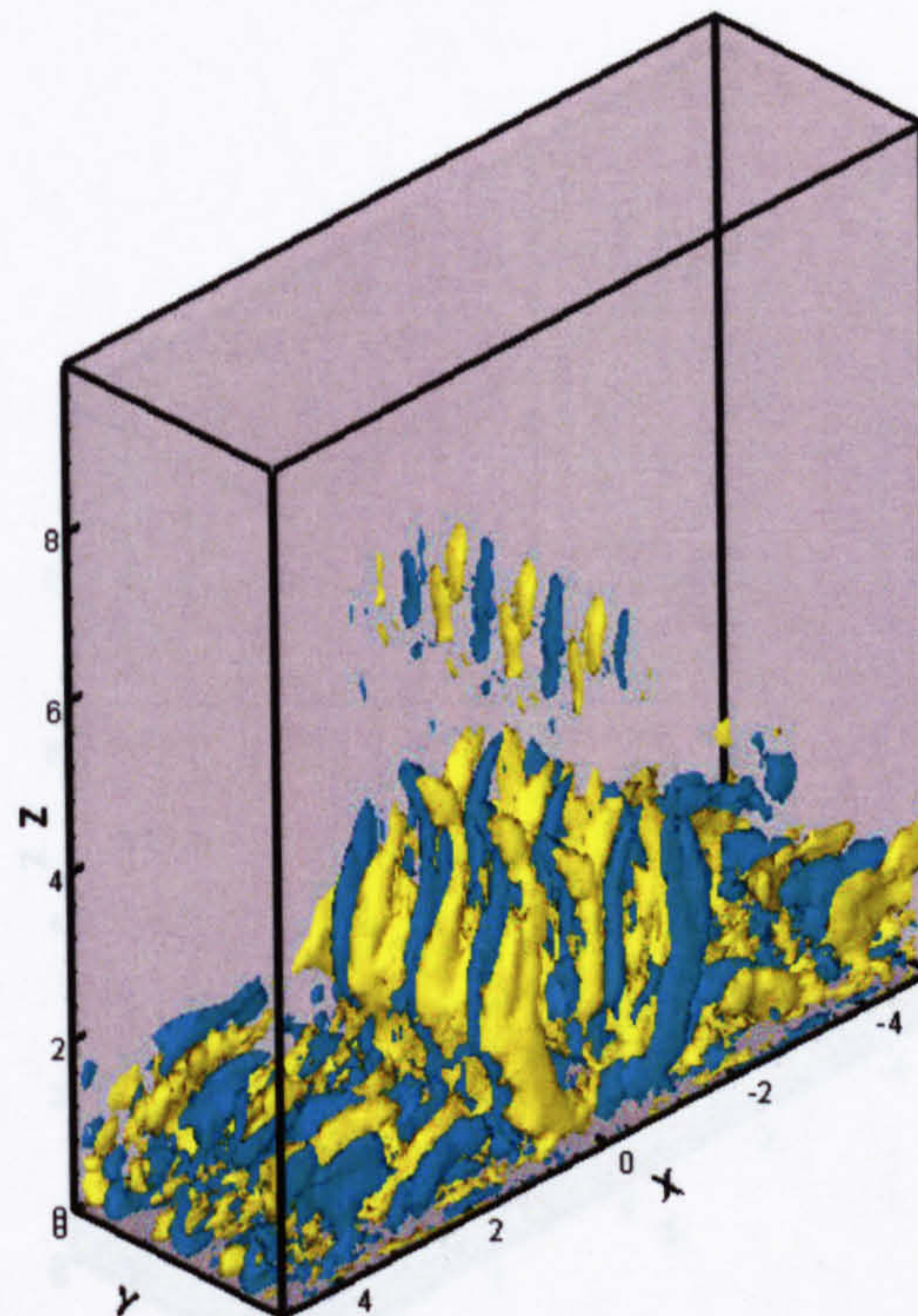
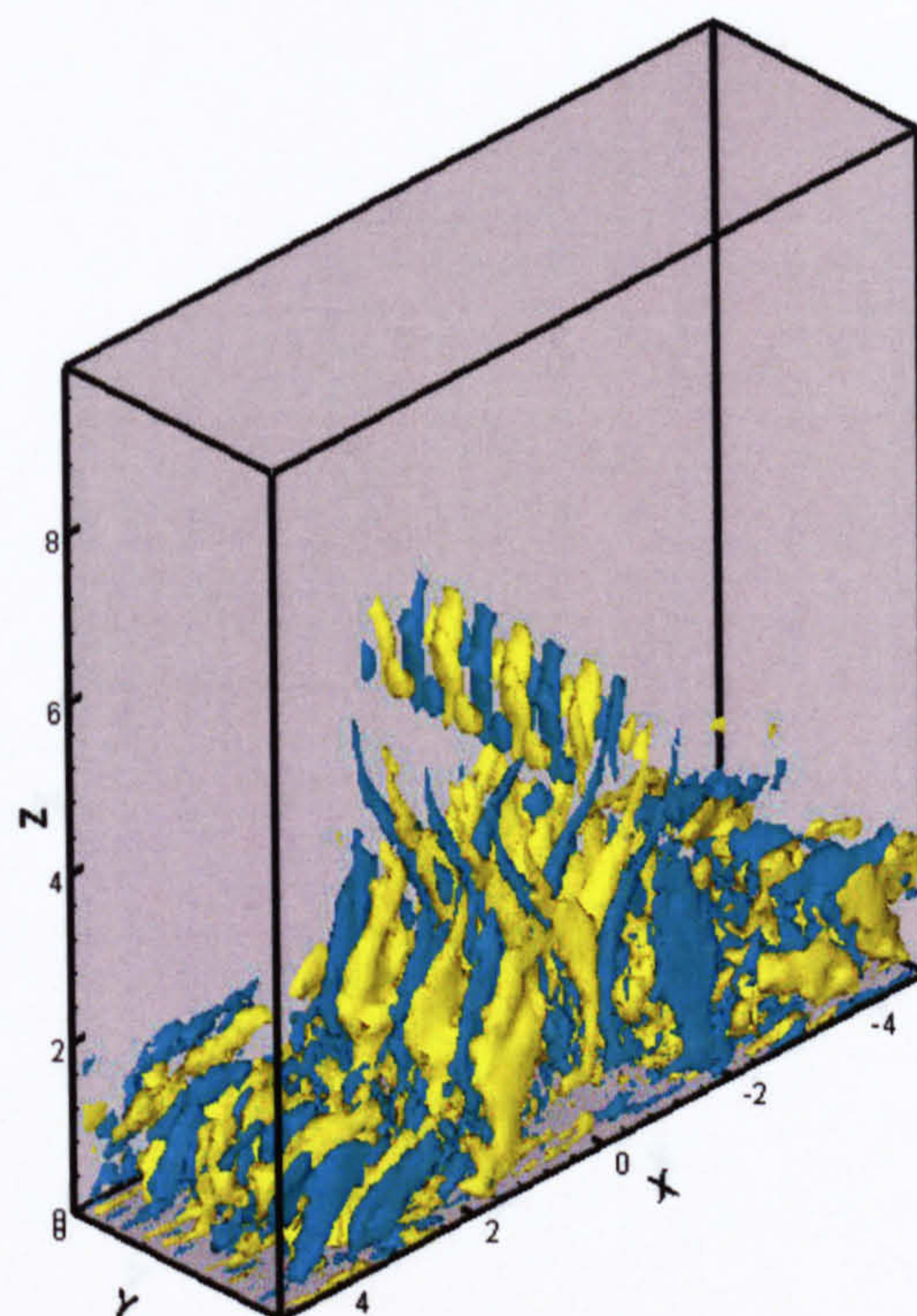


Fig. 4.15 Iso-surfaces of the streamwise vorticity at different phase angles, $\omega_z = 1.2$ (yellow) and $\omega_z = -1.2$ (blue). (To be continued)

(c) $\phi = \pi$



(d) $\phi = 3\pi/2$

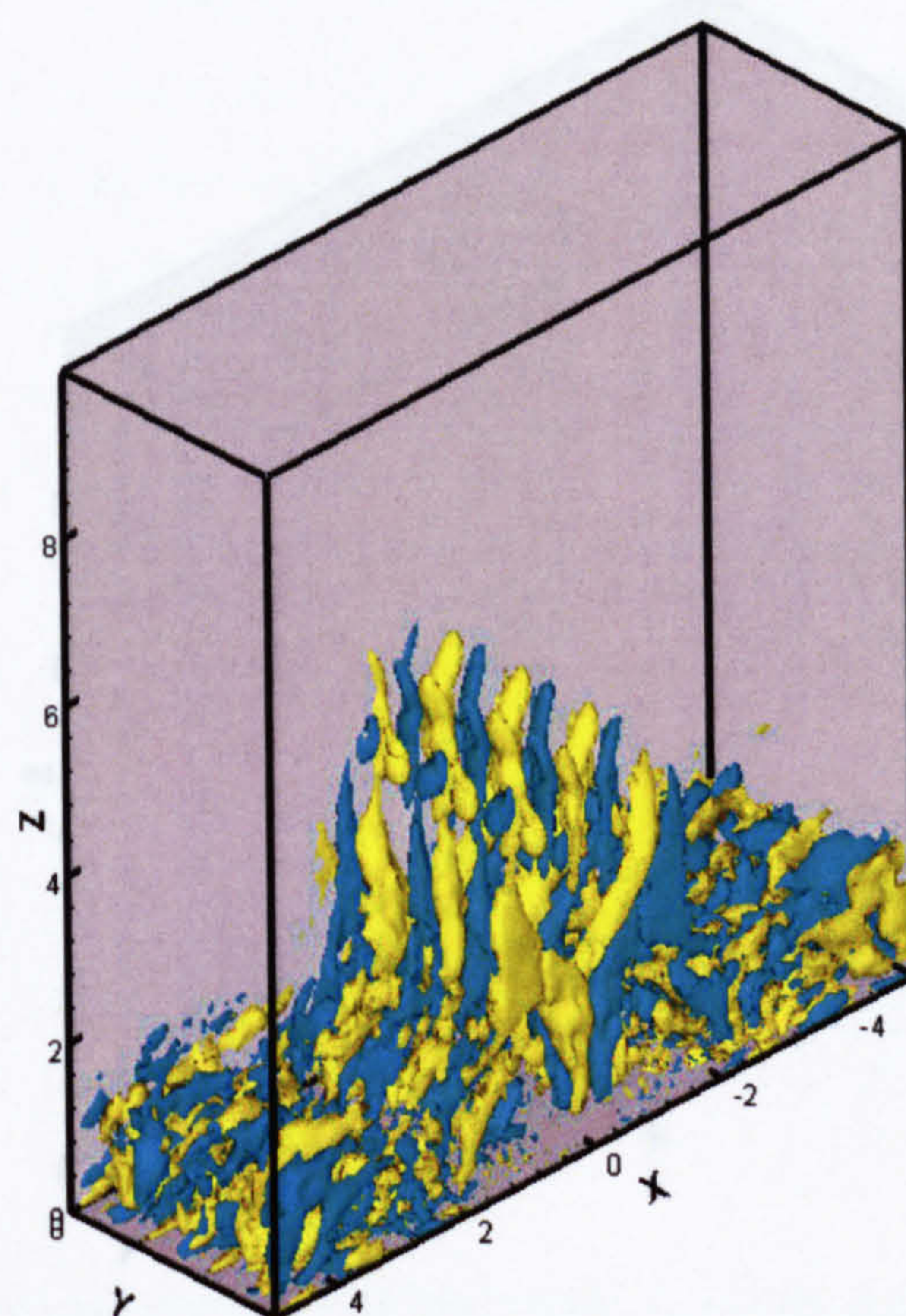
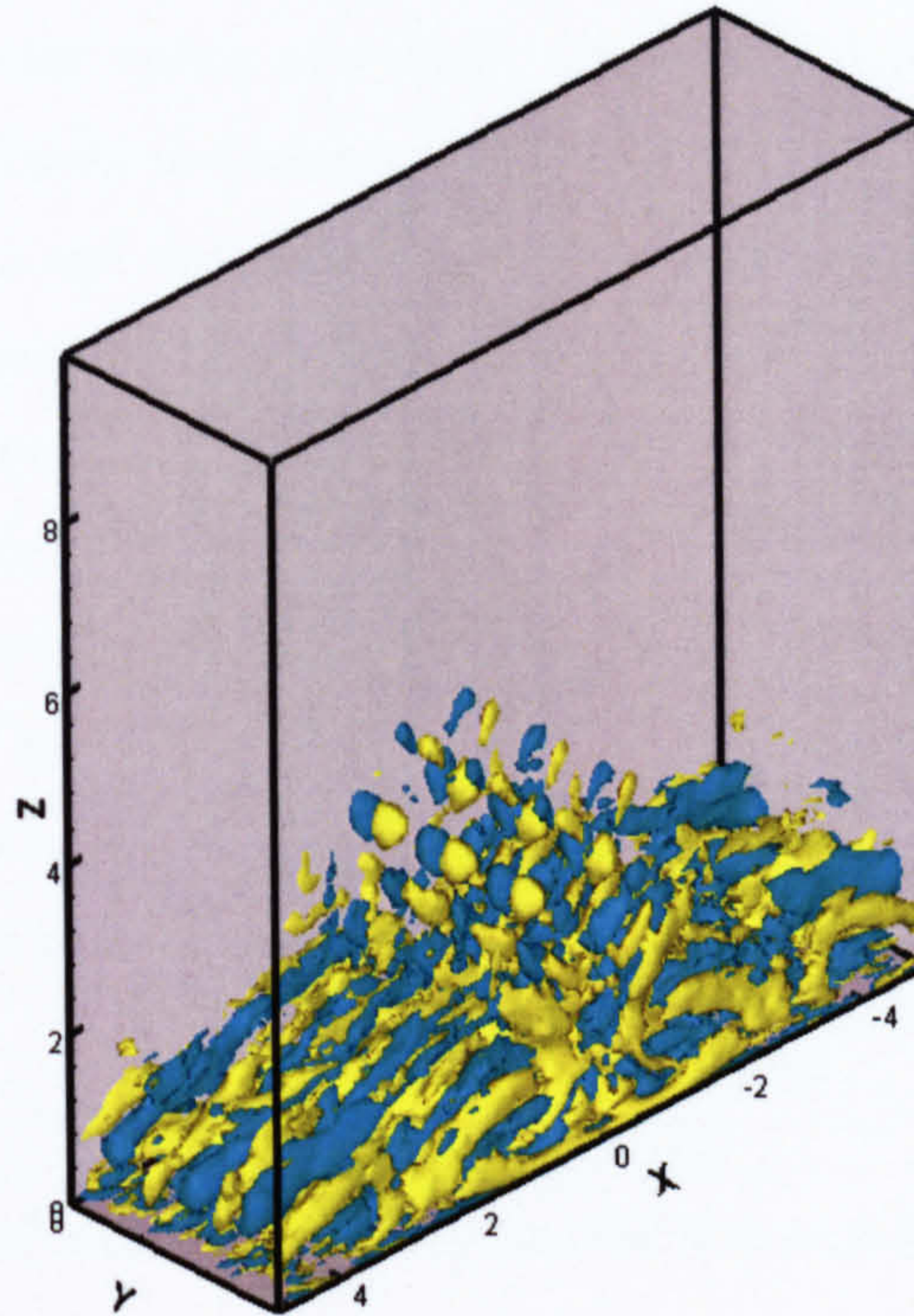


Fig. 4.15 (continued) Iso-surfaces of the streamwise vorticity at different phase angles, $\omega_z = 1.2$ (yellow) and $\omega_z = -1.2$ (blue).

(a) $\phi = 0$



(b) $\phi = \pi/2$

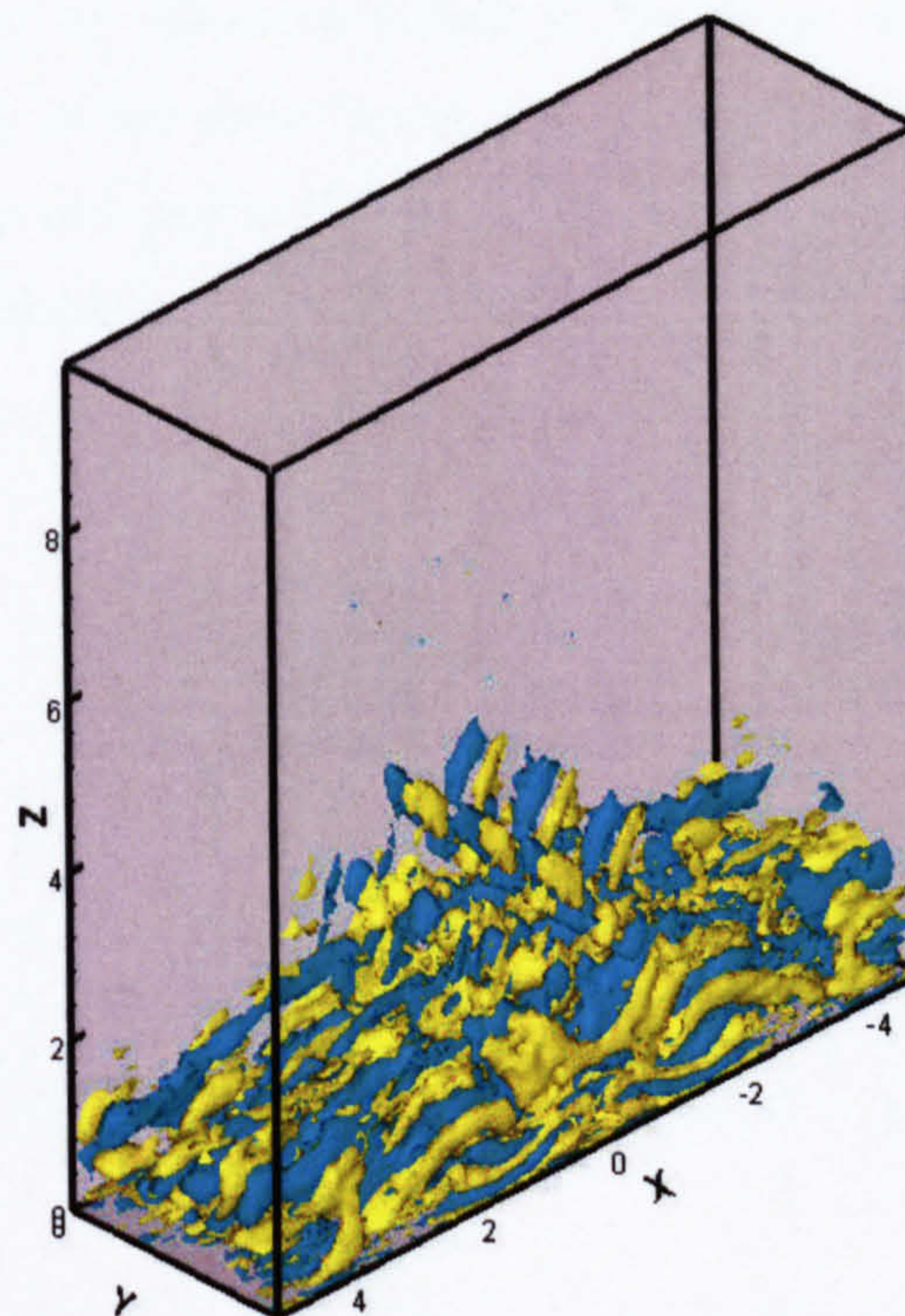
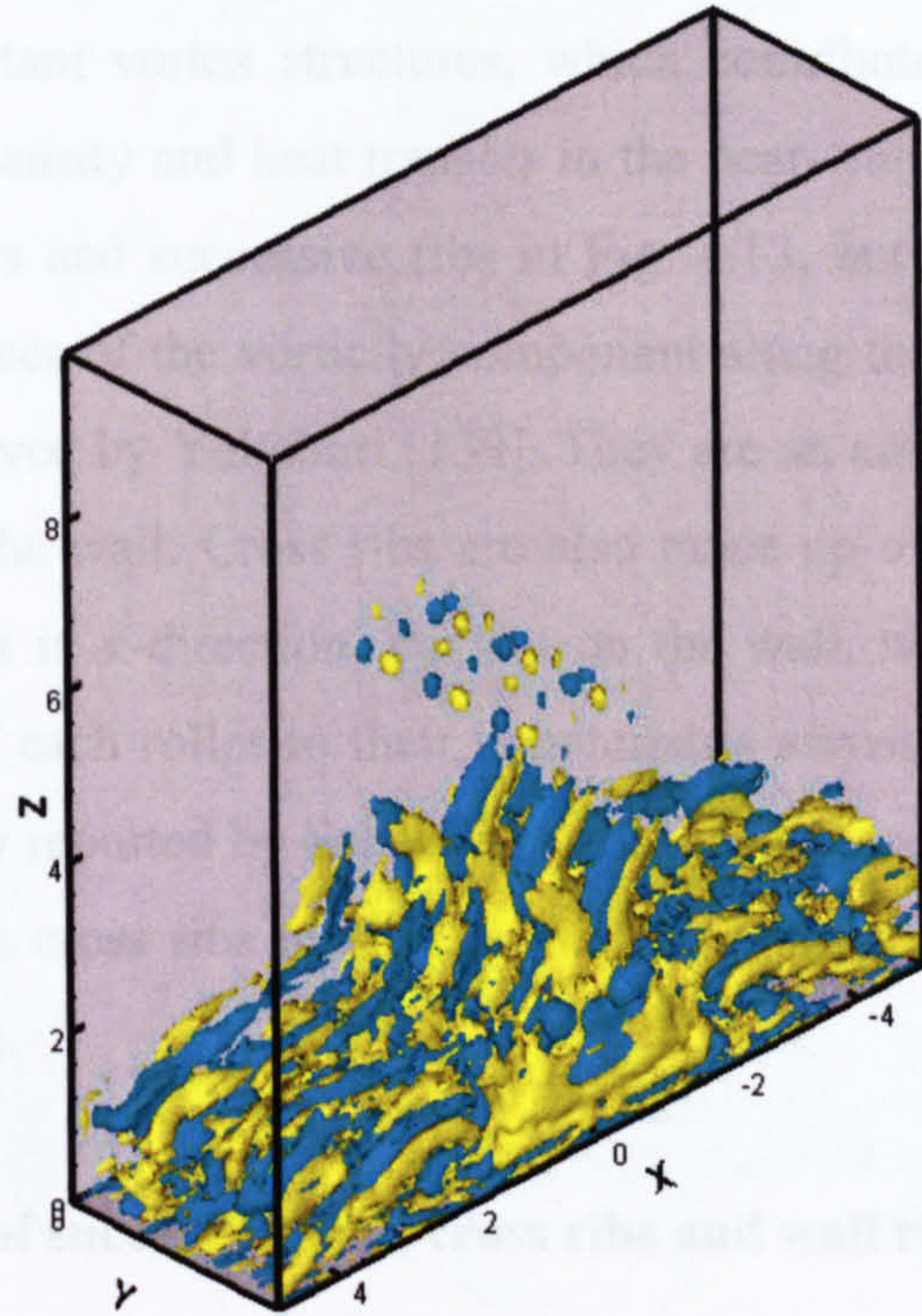


Fig. 4.16 Iso-surfaces of the lateral vorticity at different phase angle, $\omega_x = 1.2$ (yellow) and $\omega_x = -1.2$ (blue). (To be continued)

(c) $\phi = \pi$



(d) $\phi = 3\pi/2$

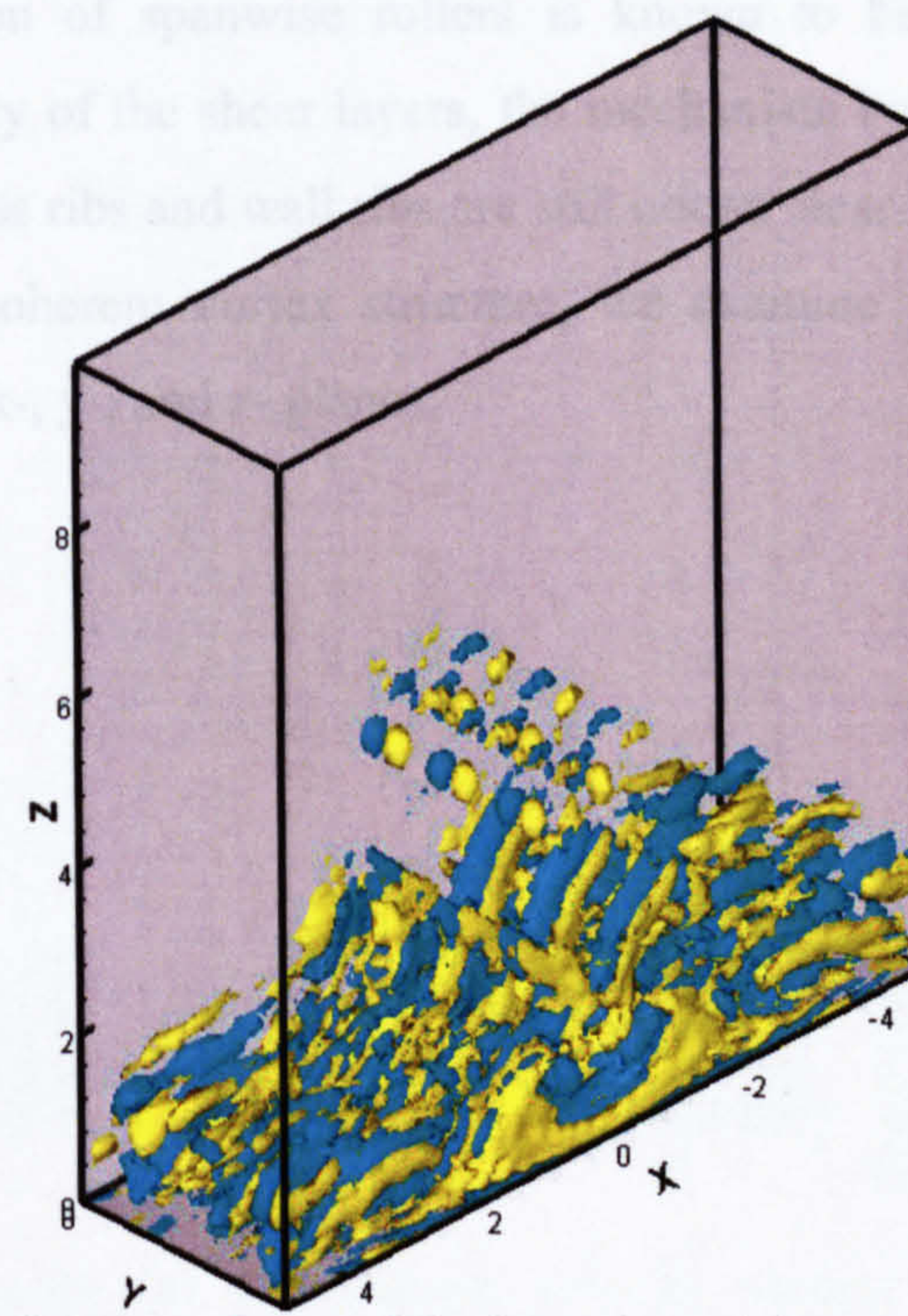


Fig. 4.16 (continued) Iso-surfaces of the lateral vorticity at different phase angle, $\omega_x = 1.2$ (yellow) and $\omega_x = -1.2$ (blue)

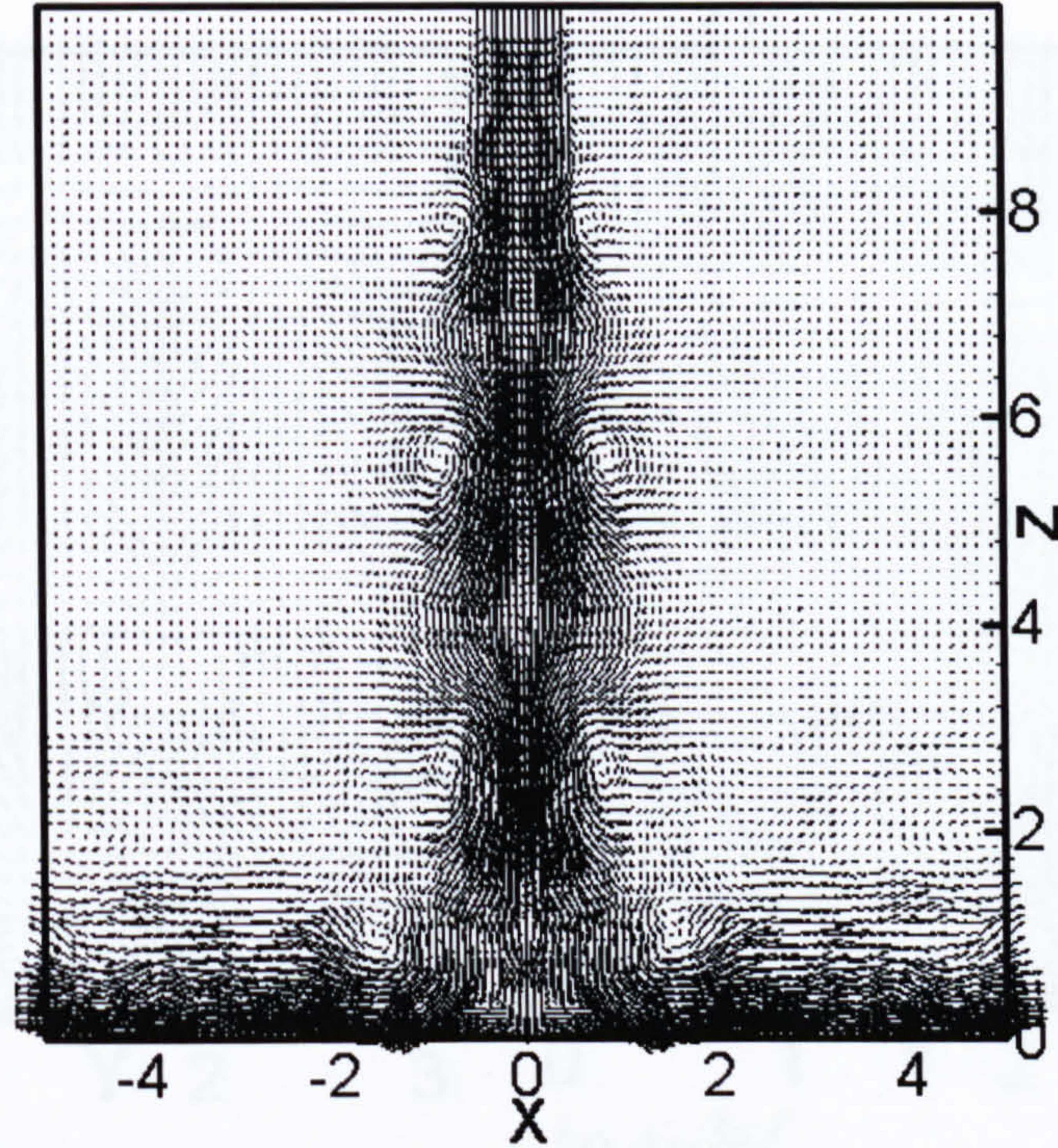
Wall ribs and cross ribs (respectively labelled by WR and CR in Fig. 4.13) are two kinds of important vortex structures, which contribute significantly to the highest turbulent intensity and heat transfer in the near-wall region. They are not so obvious as rollers and successive ribs in Fig. 4.13, but more evident in Fig. 4.16 using iso-surfaces of the vorticity component along the wall direction. Wall ribs were first observed by Yokobori [139]. They are an array of counter-rotating vortex pairs along the wall. Cross ribs are also made up of an array of counter-rotating vortex pairs in x-direction, but not on the wall, which extend from the downstream side of each roller to their counterparts across the symmetry plane. Cross ribs were only reported by Sakakibara [103]. They seem to only exist in the phase-locked jet. As cross ribs reach the wall, they merge with and enhance the wall ribs underneath.

4.3.2.3 Formation of successive ribs, cross ribs and wall ribs

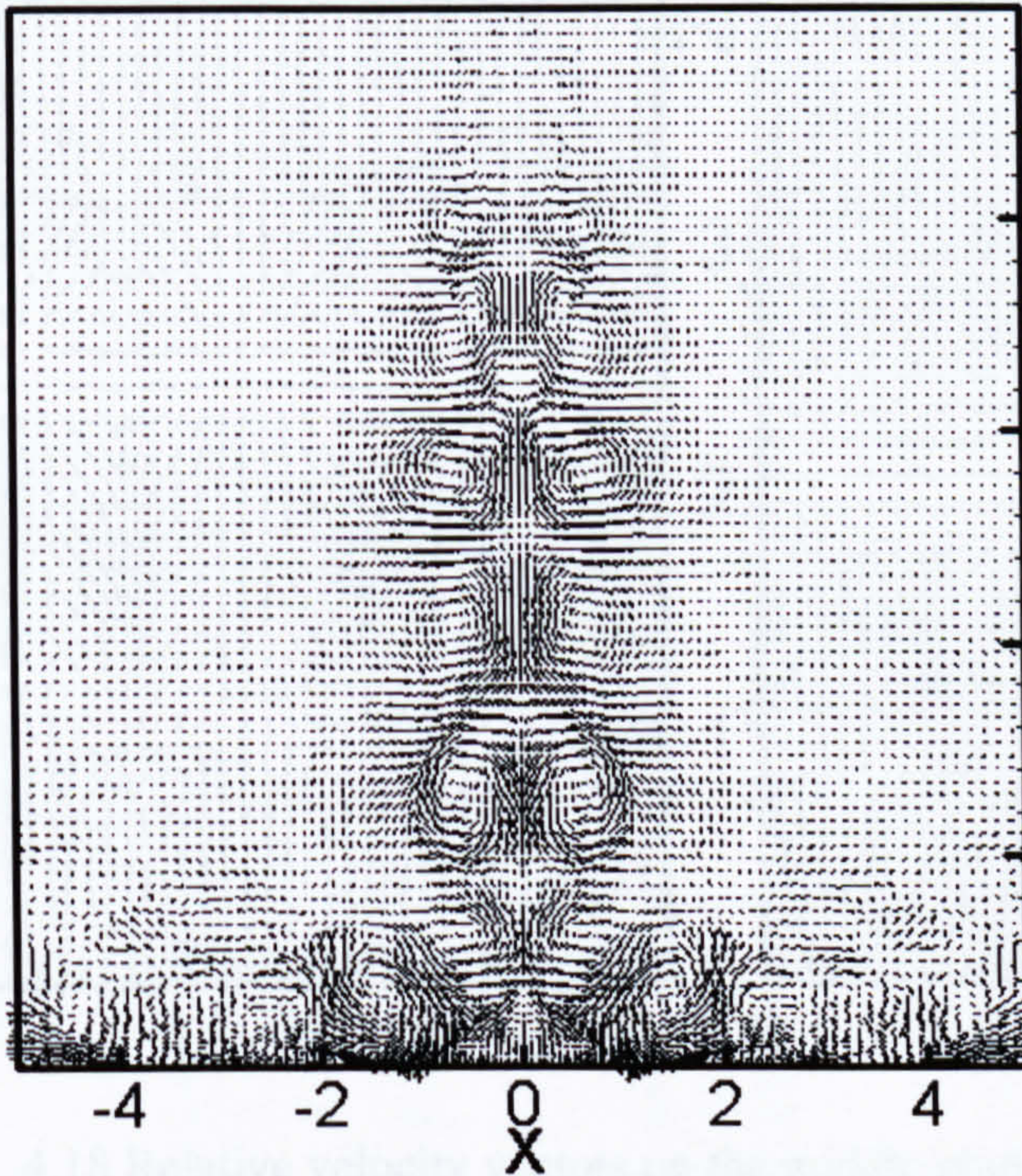
While the formation of spanwise rollers is known to be due to the Kelvin-Helmholtz instability of the shear layers, the mechanism behind the formation of successive ribs, cross ribs and wall ribs are still not so clear. In order to gain more insight into such coherent vortex structure, we examine in detail the velocity vectors at constant x-, y-, and z- planes.

Fig. 4.17 Instantaneous (a) and relative velocity vectors (b) on the spanwise middle plane; relative velocity vectors on the centre plane (c) at $z=0$, overlapped by amplified amplitude of spatial perturbation at 20%.

(a)



(b)



(c)

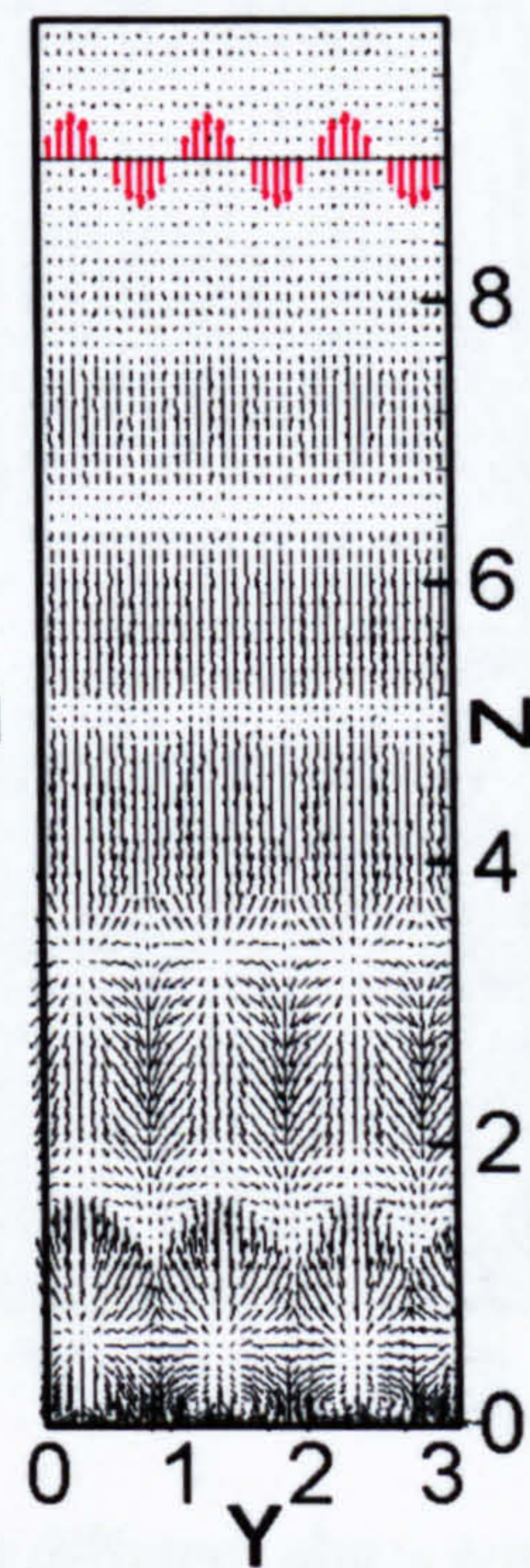


Fig. 4.17 Instantaneous (a) and relative velocity vectors (b) on the spanwise middle plane; relative velocity vectors on the centre plane (c) at $\phi=0$, overlapped by amplified amplitude of spatial perturbation at $z=9$.

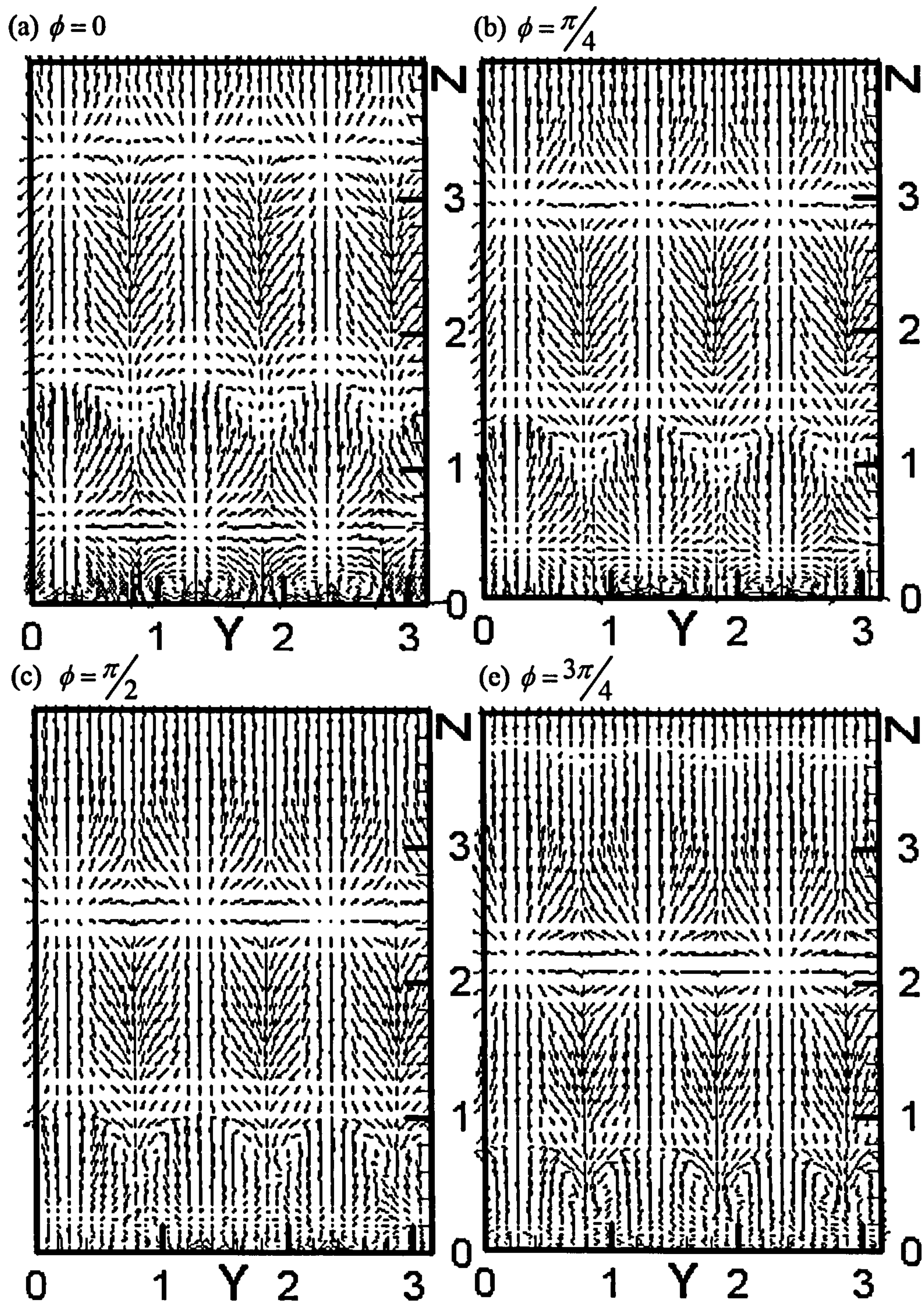


Fig. 4.18 Relative velocity vectors on the middle plane at different phase angles.
(To be continued)

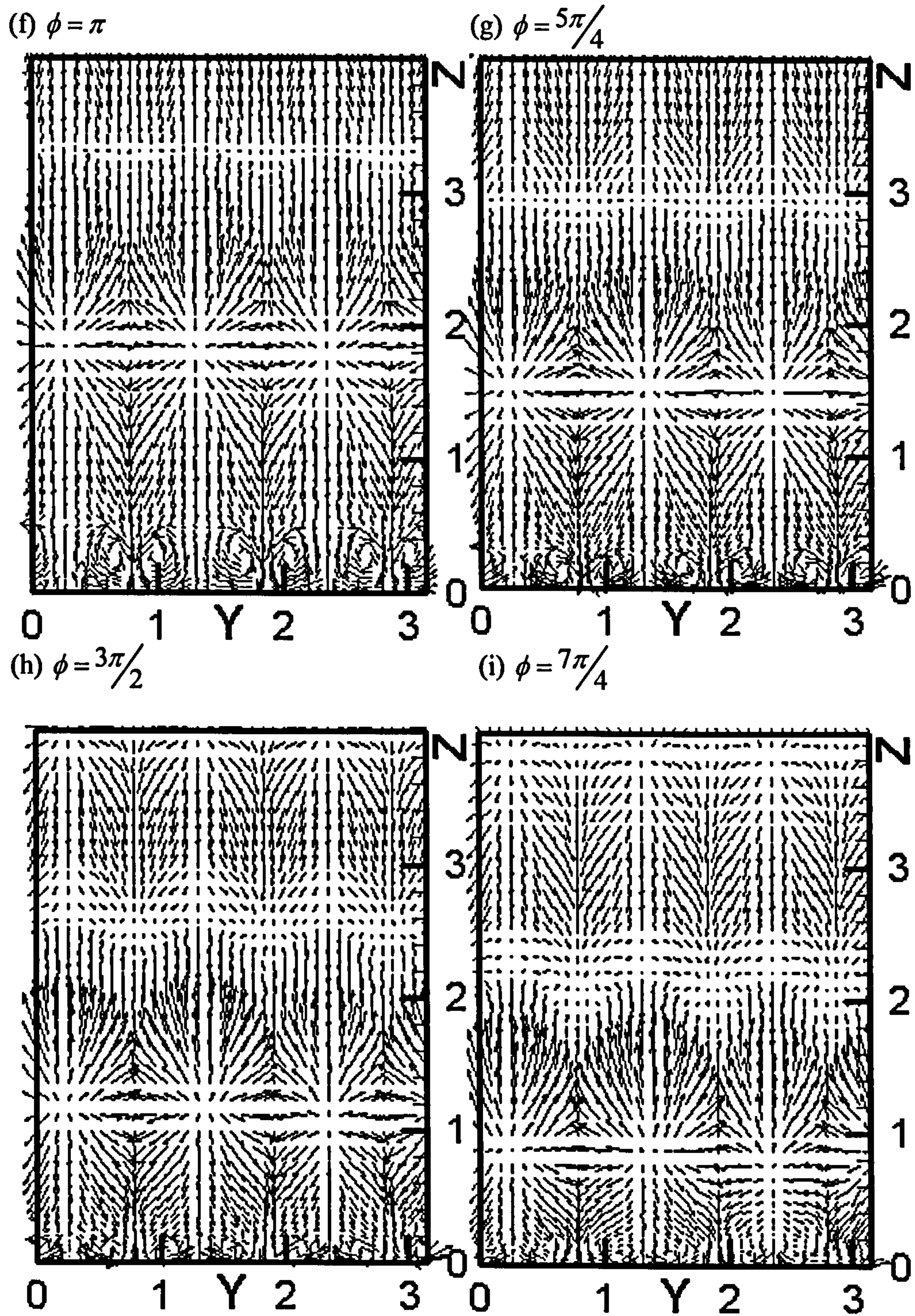


Fig. 4.18 (continued) Relative velocity vectors on the middle plane at different phase angles.

Vortex structures in the form of vectors are sensitive to the velocity of the observer. According to the secondary instability theory of Herbert [54], vortex structures are three dimensional perturbations about a mean structureless flow. A relative velocity (u', v', w') is, therefore, used to identify the vortex structures. The reference mean velocity is taken to be the spanwise averaged value (U', V', W') of the time averaged velocity (U, V, W) .

Fig. 4.17 shows the instantaneous and relative velocity vectors in the middle planes of x- and y- directions. The aforementioned dominant spanwise rollers can be clearly seen in the instantaneous velocity vectors. In the vector plot of relative velocity, the rollers are still there, but an opposite-signed counter-rotating pair emerges between two adjacent dominant roller pairs. The new roller pair is induced by the dominant roller, so we call it secondary rollers. The roll-up frequency of the roller is exactly the same as the inlet perturbation frequency. In the vector plot of the relative velocity in the x-direction middle plane, due to the existence of the alternative opposite-signed roller pairs, the flow field is divided into several sections by two kinds of relatively static lines, on which the relative velocities are zero. The flow directions on each side of the lines are opposite. According to the flow direction, these lines can be classified as convergence and divergence lines. Closer to the wall, these lines tend to be curlier due to the amplification of the spatial perturbation. Accordingly, there are three (the same as wave number of the inlet spatial perturbation) sink points and three source points on each convergence and divergence line, respectively. The corresponding sink and source points are staggered and locked by the maximum and minimum points of the inlet spatial perturbation, as shown in Fig. 4.17 overlapped at $z=9$ with the amplified amplitude.

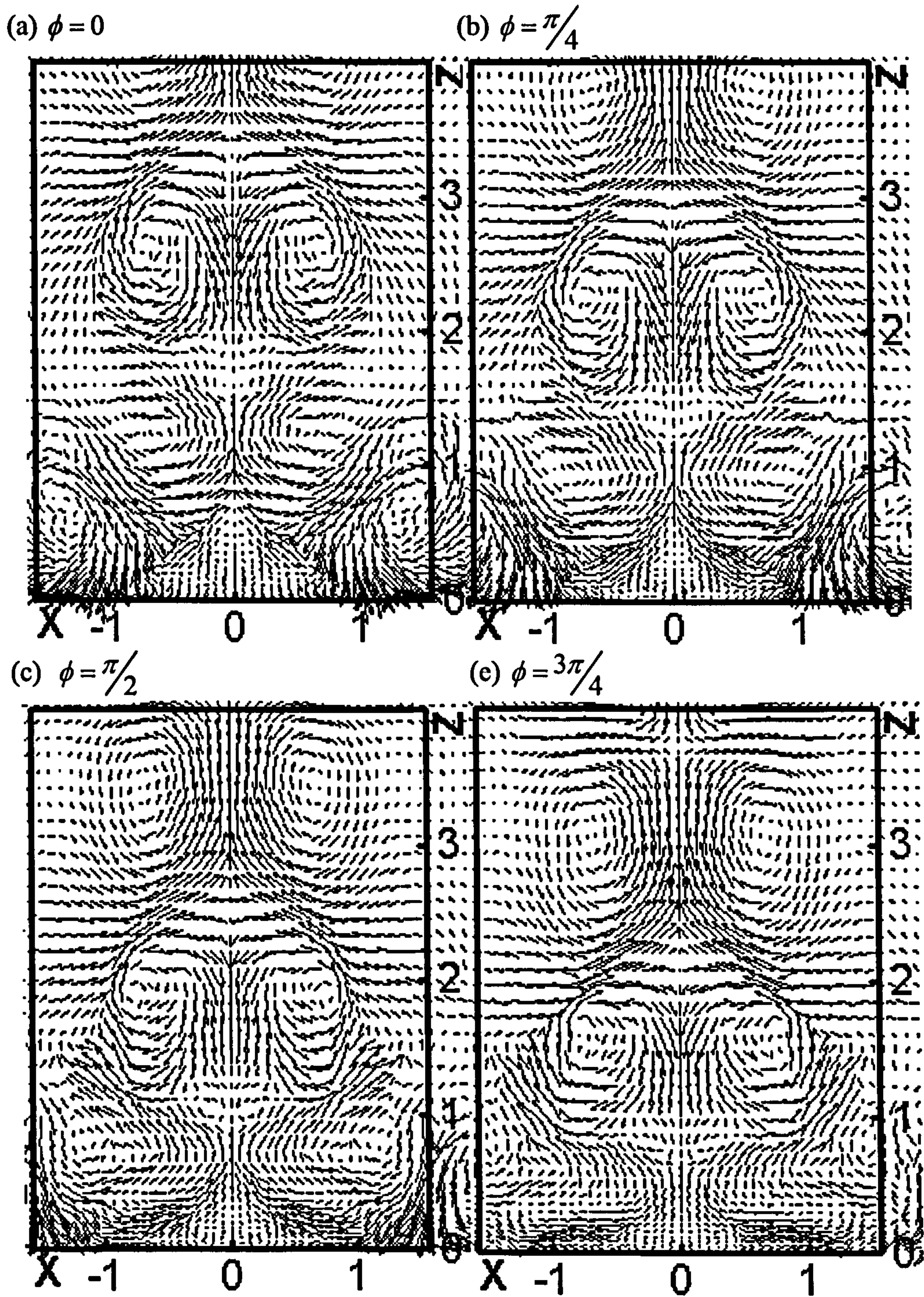


Fig. 4.19 Instantaneous relative velocity vectors on the spanwise middle plane at different phase angles. (To be continued)

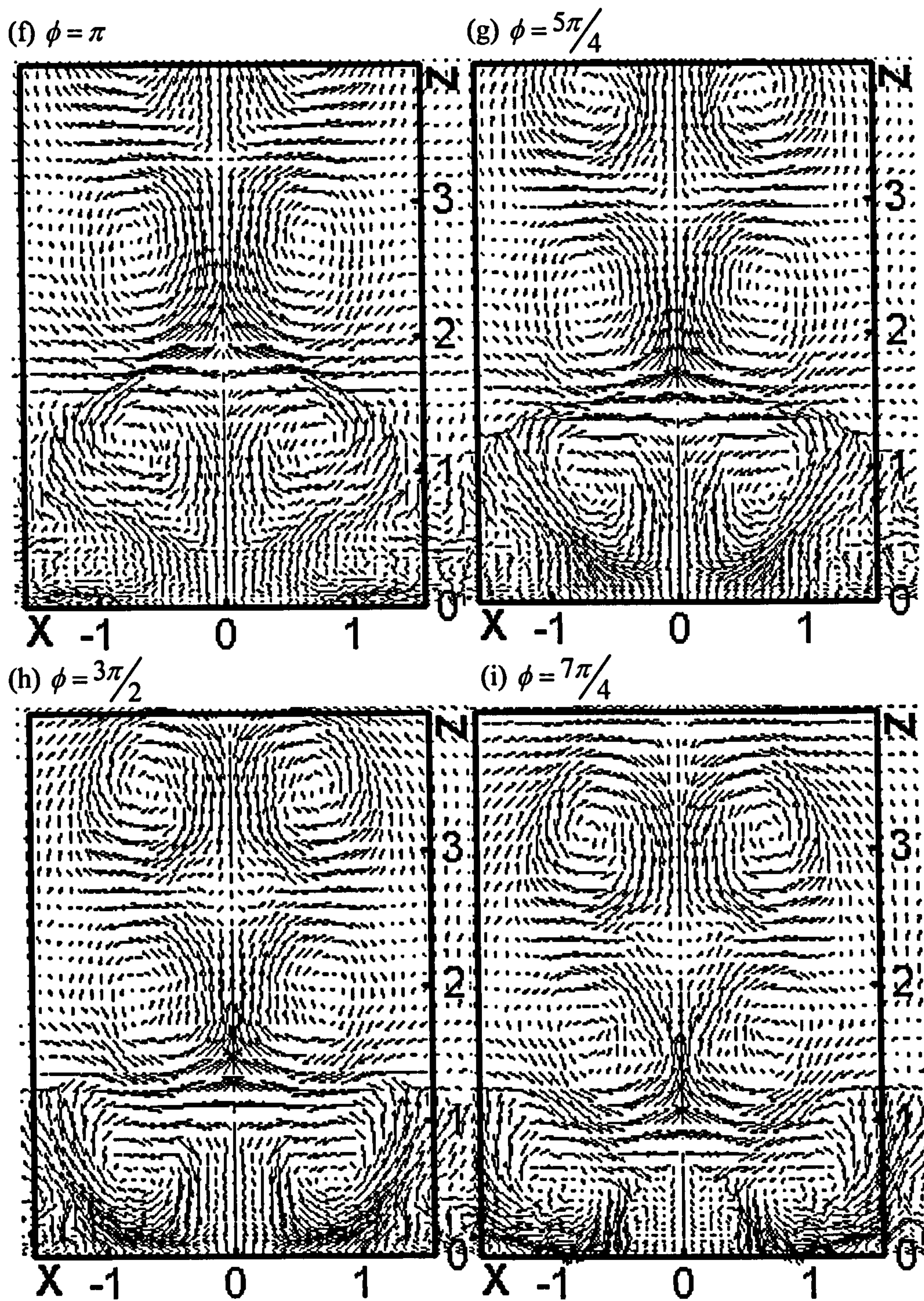


Fig. 4.19 (continued) Instantaneous relative velocity vectors on the spanwise middle plane at different phase angles

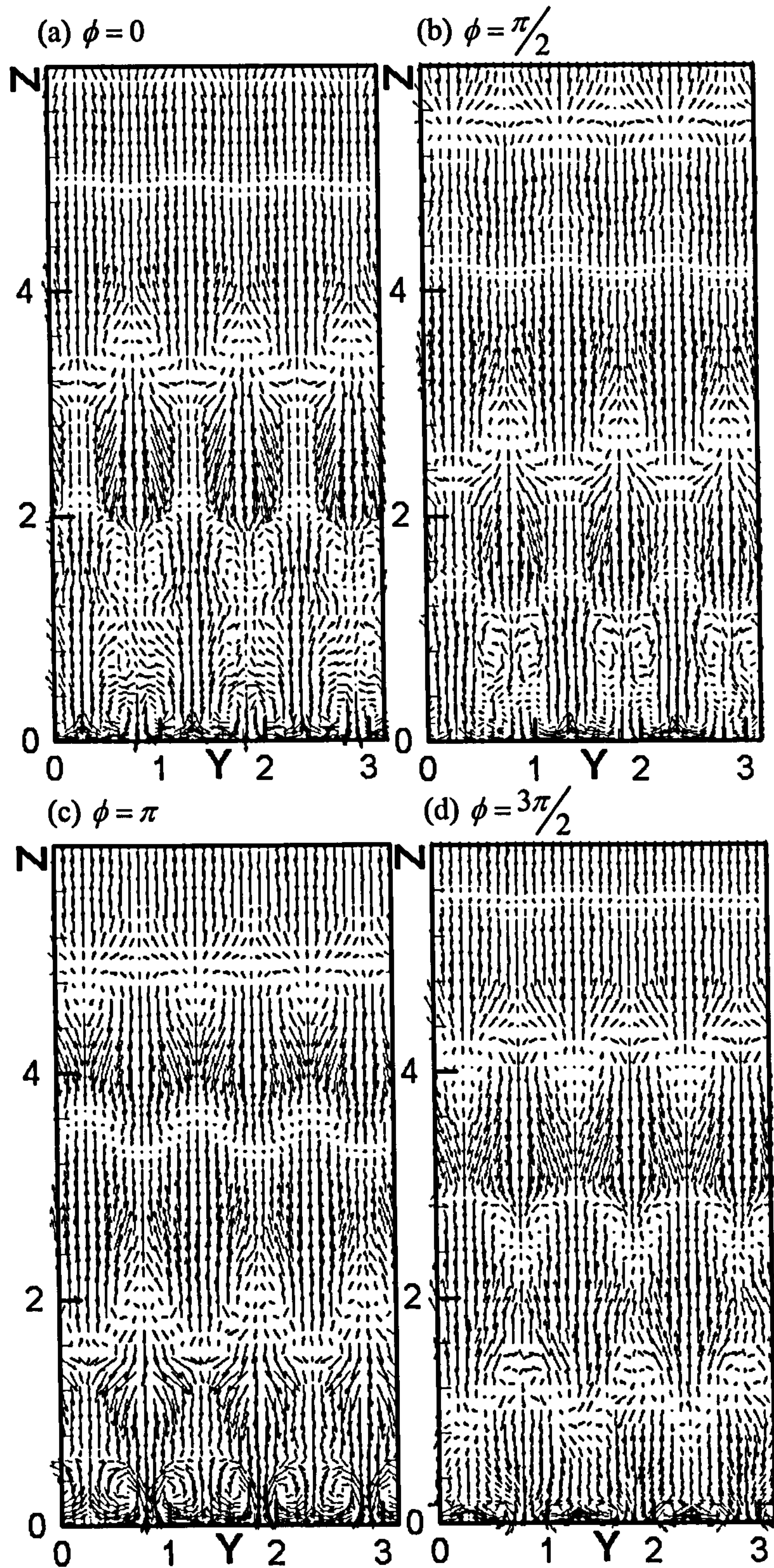


Fig. 4.20 Relative velocity vectors on the $x=0.25$ plane at different phase angles.

With the above knowledge, we now examine the formation of cross ribs and successive ribs. Plots of relative velocity vector in the middle planes at phase intervals of $\pi/4$ are presented in Figs. 4.18 and 4.19. In Fig. 4.18, wall ribs can be clearly seen near the wall almost at every phase angle, but their intensity is periodical. As the divergence line approaches the wall, the intensity decreases. As the convergence line moves towards the wall, the velocities at different side of the line tend to be more unbalanced and unstable. This unbalance leads the cross ribs to produce near sink points at around $z=1.0$. When they reach the wall, they merge with the wall ribs beneath and increase the intensity. The merged wall ribs are centred about the vertical line through the sink points. As the divergence line approaches the wall, the vortex pairs in the wall ribs are forced apart and then they re-pair themselves. Finally, they are centred about the vertical line through the source point. This kind of re-pairing causes wall ribs to move in the spanwise direction periodically and increases the overall turbulent intensity in the near-wall region.

We now know that the curly unbalanced convergence line is the position where cross ribs start to evolve into vortices, but we also know that the middle plane is less disturbed by the rollers. Therefore, the cross ribs should not first form in the middle plane, they should form first somewhere away from this plane. In other words, the cross ribs should start to form in the position where the convergence line tend to be curliest and most unbalanced. This is evident in Fig. 4.20 by vector plots of relative velocities in the $x=0.25$ plane at a phase interval of $\pi/2$. Cross ribs begin to form at around $z=2.8$ and $\phi = 3\pi/2$. This is much earlier than in the middle plane. Furthermore, it is more apparent in Fig. 4.20 that the wall ribs remain attached to the wall all the time.

We now know that cross ribs form on the convergence lines, so the same formation mechanism can apply to successive ribs. Successive ribs are in streamwise direction, so we should look at the plots in the x - y plane. Because of mass conservation, the divergence lines on the x - z plane should turn into

convergence ones on the x-y plane. As cross ribs are known to form on the convergence lines, we trace the above-mentioned divergence lines on the x-y plane using a Lagrangian method. Fig. 4.21 shows plots of relative velocity vectors on different x-y planes cutting through four different positions of the same divergence line at a time interval of $\frac{1}{2f}$. As anticipated, the divergence line turns

into a convergence line in the x-y plane. As the convergence line moves towards the wall, the spanwise perturbation in the vicinity of the convergence line is amplified. Three sink points start to form on the line and subsequently successive ribs begin to form in the immediate vicinity of these sink points.

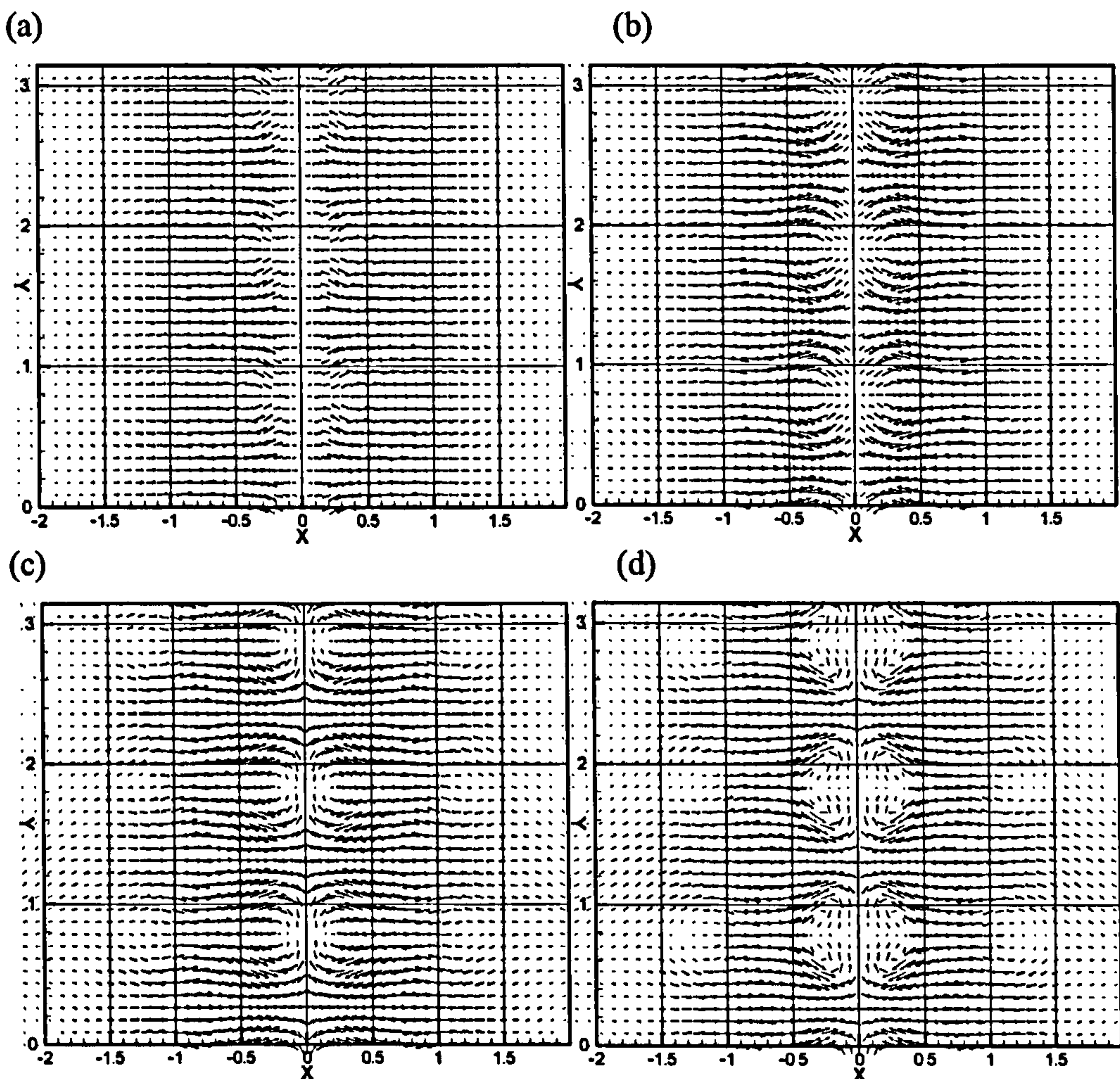


Fig. 4.21 Relative velocity vectors on four different x-y plane cutting though the same convergence line at different moments.

4.3.2.4 Evolution of the organized vortex structures

(a) $\phi = 0$

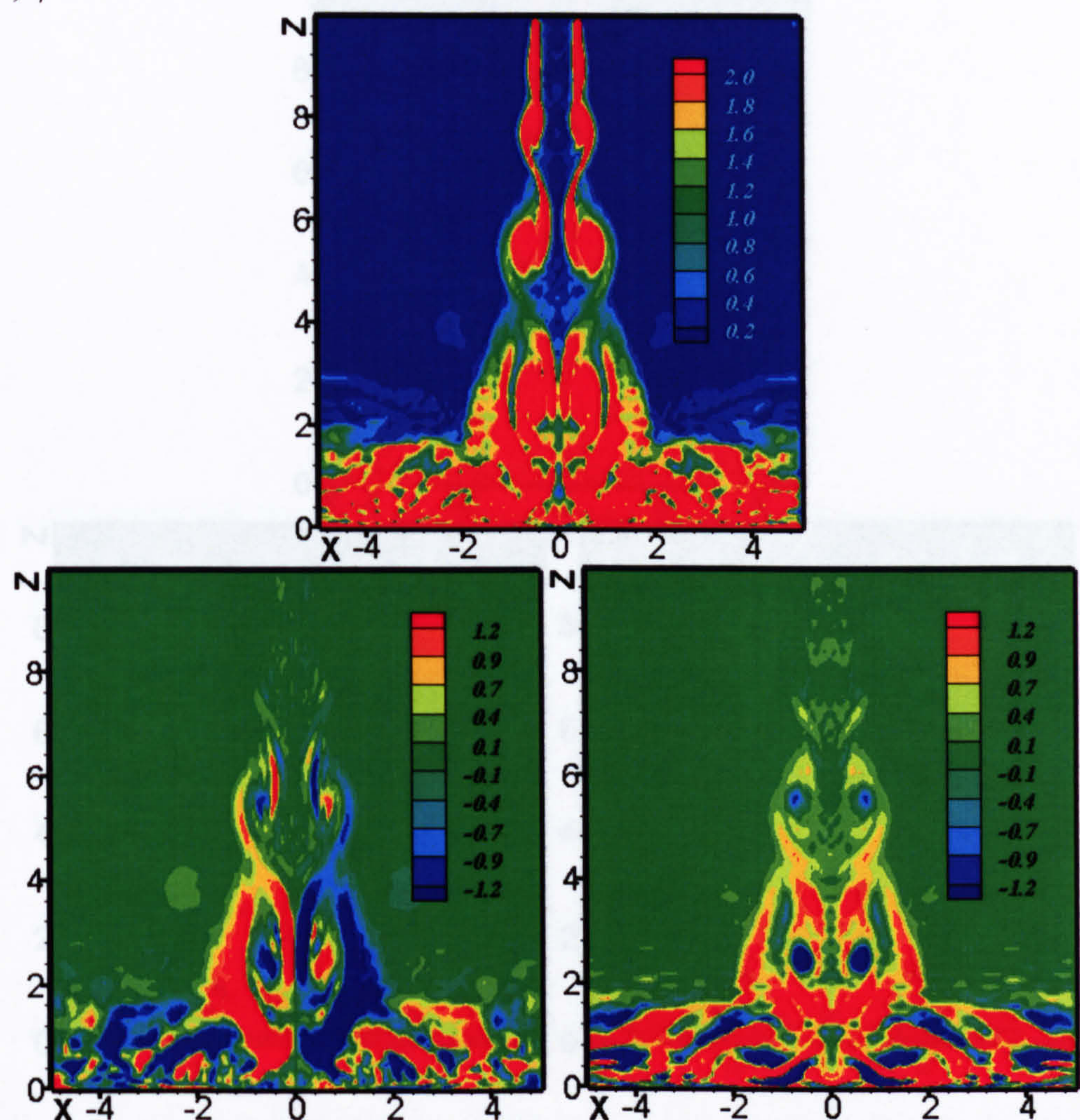


Fig. 4.22 Contours of the total vorticity (top), spanwise vorticity (bottom left) and lateral vorticity (bottom right) on the spanwise middle plane at different phase angles. (To be continued)

(b) $\phi = \pi/2$

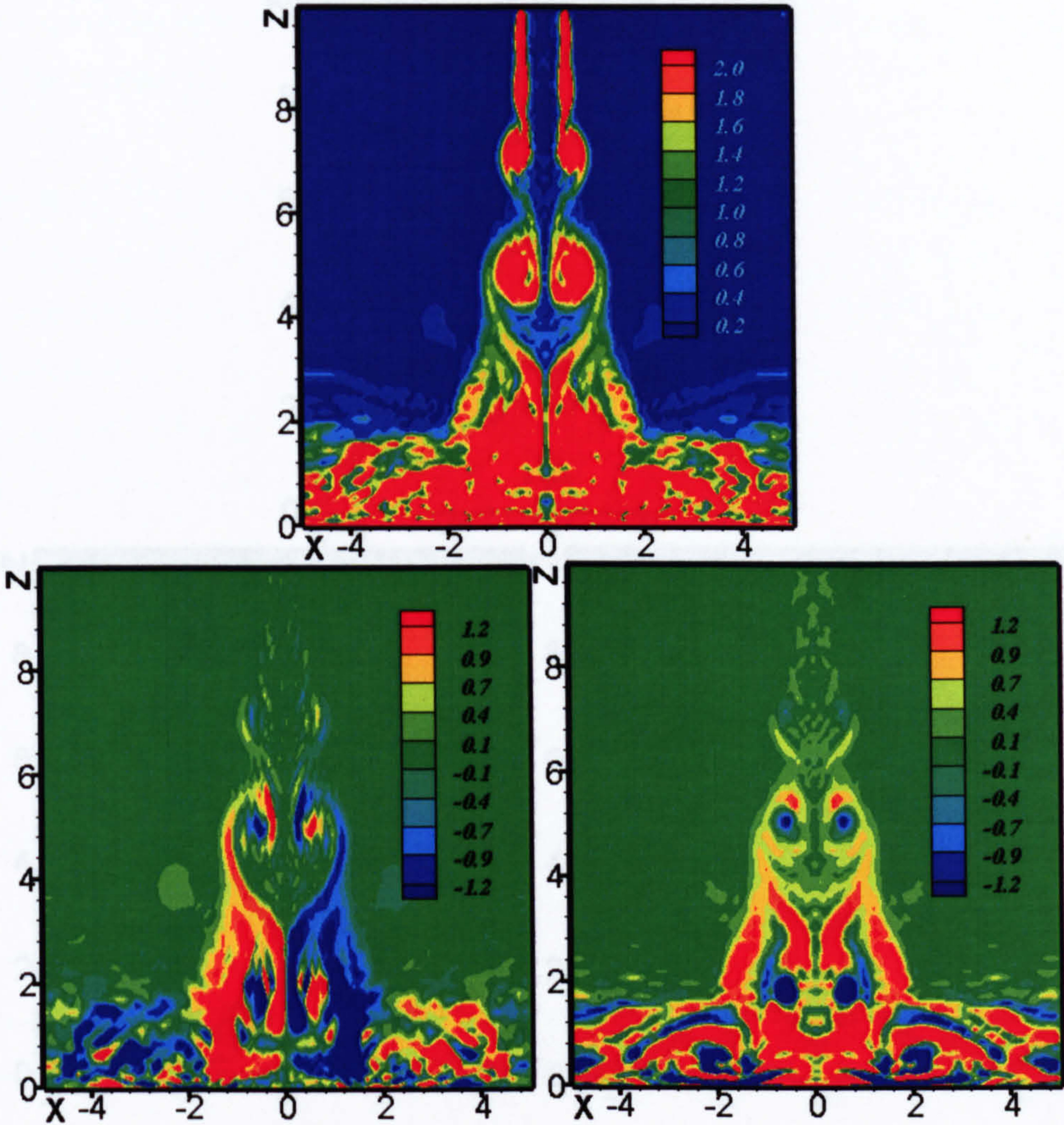


Fig. 4.22 (continued) Contours of the total vorticity (top), spanwise vorticity (bottom left) and lateral vorticity (bottom right) on the spanwise middle plane at different phase angles. (To be continued)

(c) $\phi = \pi$

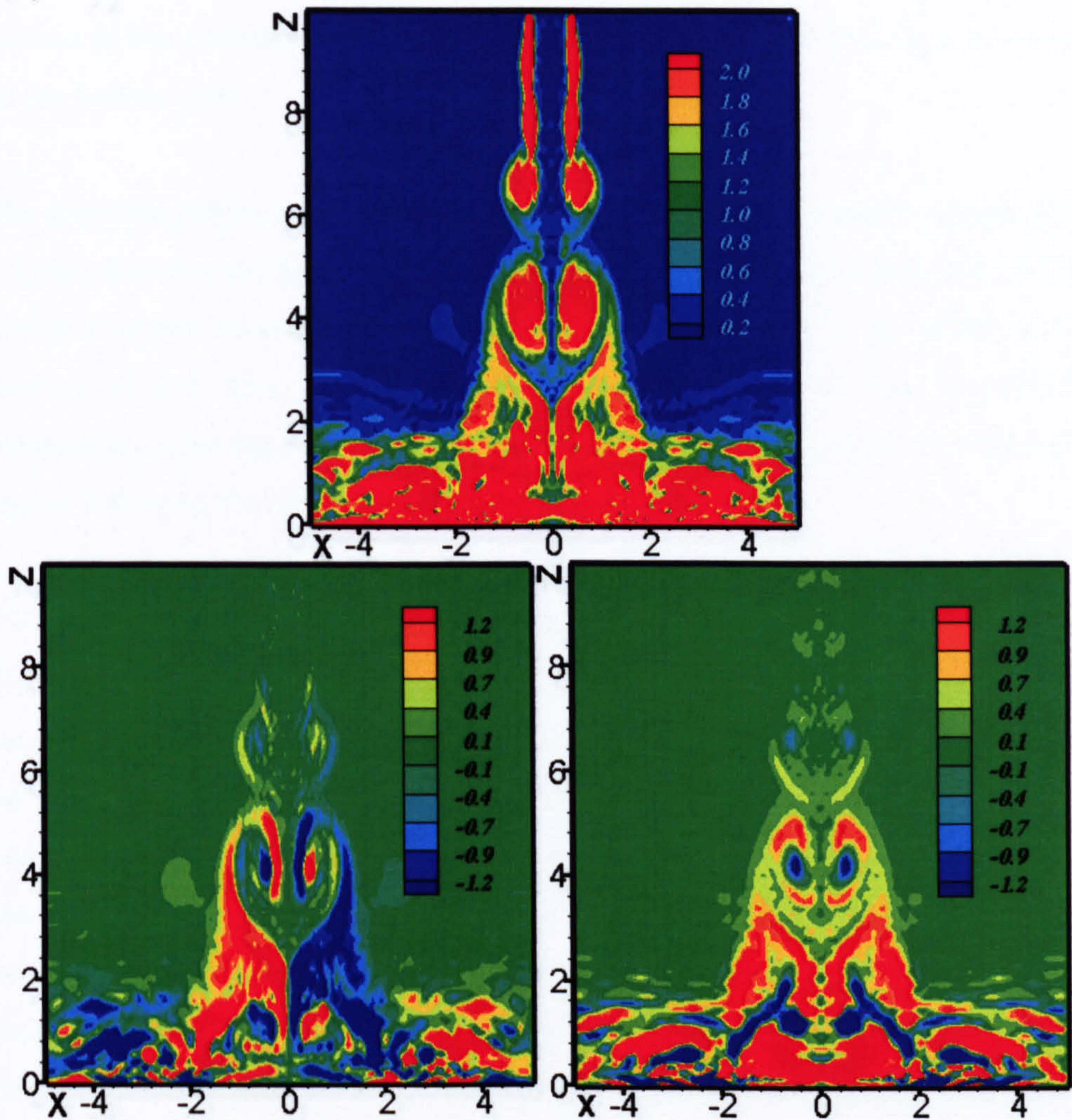


Fig. 4.22 (continued) Contours of the total vorticity (top), spanwise vorticity (bottom left) and lateral vorticity (bottom right) on the spanwise middle plane at different phase angles. (To be continued)

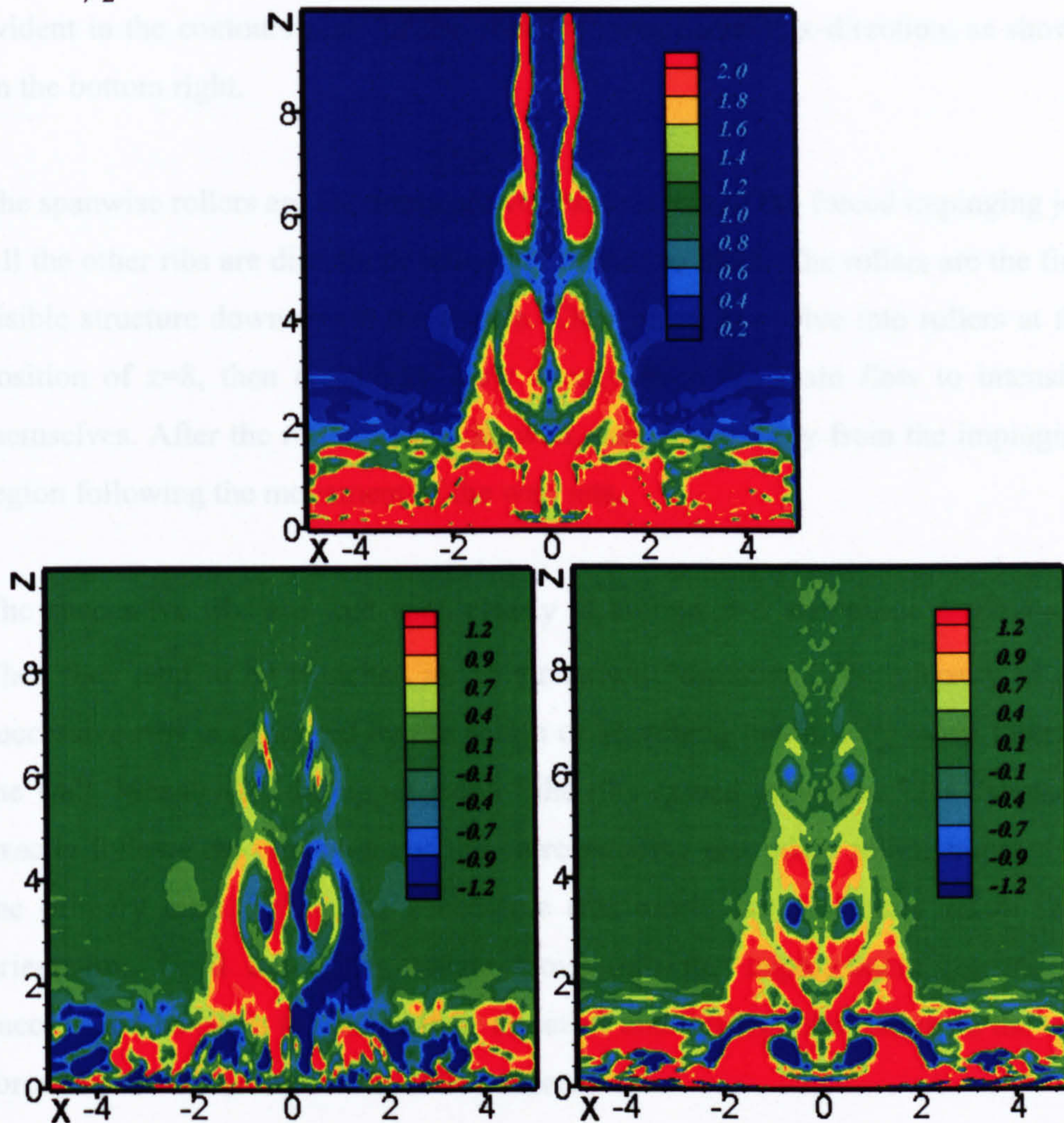
(d) $\phi = 3\pi/2$ 

Fig. 4.22 (continued) Contours of the total vorticity (top), spanwise vorticity (bottom left) and lateral vorticity (bottom right) on the spanwise middle plane at different phase angles.

Contour plots of vorticities on the spanwise middle plane at a phase interval of $\frac{\pi}{2}$ are presented in Fig. 4.22. This plane cuts through the successive and cross ribs.

As the wall ribs are not fixed, they are only visible at the moment when the merge of the wall and cross ribs happens. Three kinds of contours are plotted in Fig. 4.22. The top plots are contours of the total vorticity where almost all vortex structures can be seen. The contours of the streamwise vorticity are plotted

on the bottom left, where successive ribs are seen to be present. The cross ribs are evident in the contours plots of the vorticity component in x-direction, as shown on the bottom right.

The spanwise rollers are the dominant vortex structure of the forced impinging jet. All the other ribs are directly or indirectly related to them. The rollers are the first visible structure downstream the nozzle. They begin to evolve into rollers at the position of $z=8$, then constantly draw energy from the main flow to intensify themselves. After the rollers reach the wall, they move away from the impinging region following the movement of the wall jets.

The successive ribs are first seen clearly at around $z=6$ and phase angle $\phi = 0$. Then they tend to be stretched in the streamwise direction. The intensity of the successive ribs is enhanced by the action of stretching, while they move towards the wall. Meanwhile, the upper side of the ribs extend outwards. This extension exactly follows the movement of the corresponding secondary rollers induced by the primary ones. When the successive ribs touch the wall, they retain their orientation. Until the upper rollers move into the impingement region, the successive ribs begin to change their direction and fall onto the rollers on the wall forced by the movement of the rollers there.

The cross ribs first present themselves near $z=5$, just under the rollers at phase angle $\phi = 0$, then they begin to extend towards the jet axis. At the position of $z=1.8$ and phase angle $\phi = 0$, the two-side ribs are connected into an array of integral cross ribs. When the ribs reach the wall, they merge with the wall ribs underneath. The signs of the successive, cross and wall ribs are identical. When the successive and cross ribs merge with wall ribs, they enhance the intensity of the wall ribs. Around the stagnation point, the wall ribs are sustained only by the cross ribs, the successive ribs play little role in the sustenance of the wall ribs here. Away from the stagnation point, the successive ribs have more influence on the

wall ribs. There also exist opposite sign vortices in the wall jets. When these vortices merge with the wall ribs, the intensity of the wall ribs is reduced.

4.4 Summary

Large eddy simulations have been conducted to study natural and forced plane impinging jets. The predictions for the natural impinging jet agree well with the experimental data. It was found that the dissipative error of the numerical methods is minor and the effect of the SGS model is not masked out by the numerical methods. The SGS model successfully describes the small scales and plays a significant role to stabilize the numerical solutions. The results with the explicit SGS model are much more close to the experimental data than the one without SGS model. This serves to demonstrate the accuracy and the capability of KIVA-LES for modelling such complex turbulent flows.

Downstream of the natural impinging jet, coherent structures are generated by the shear-layer Kelvin-Helmholtz instabilities. The vortical structures are more organized in the beginning. Further downstream, secondary instabilities break them up into more random smaller scales turbulence. In the impinging zone, there exist three-dimensional counter-rotating vortex pairs. The vortex pairs lie on the wall along the direction of wall jets extending from both sides of the symmetry jet plane. Their positions are not fixed on the wall but move in the spanwise direction. The existence of these counter-rotating vortices induces “up-wash” velocity close to the wall hence the high turbulent intensity in the vicinity of wall.

The main focus of this chapter is on the detailed vortex structures of the forced impinging jet. The typical vortex structures such as the spanwise rollers, the successive, cross and wall ribs reported by Sakakibara et al. [103], have been captured in the current simulation. To the best of our knowledge, this is the first time numerical predictions of these detailed structures are reported. The present predictions have resulted in valuable findings about the formation and evolution of the three types of ribs. It would, however, be prudent for such findings to be backed by some new experiments.

The spanwise vortex pairs are seen to symmetrically appear at the two shear layers of the jet just downstream the nozzle exit. Their positions are locked by the inlet condition. However, not all these vortex pairs can survive into the dominant structure, i.e. the spanwise rollers. The vortex pair just above the rollers is stretched into braid regions. Therefore, the dominant frequency of the jet is only half of the forced frequency. This finding is consistent with that of Sakakibara et al. [103]. As the spanwise rollers advect towards the wall, they begin to depict and amplify the spatial disturbance of the inlet.

The successive ribs emerge as two arrays of streamwise counter-rotating vortex pairs between a pair of spanwise roller. The number of the pairs is exactly the same as the wave number of the spanwise disturbance. Accordingly, the ribs extend themselves by the action of stretching with the upper side extending towards the outside of the upper roller. Finally, the two adjacent rollers of the same side are connected by the ribs. When the ribs reach the wall, they retain their orientations. After the upper rollers reach the wall, the ribs are forced to change their directions and fall onto the rollers attached to the wall.

The cross ribs form under each of the roller pair, but they do not come into contact with each other until they move into the impingement region. When the cross ribs reach the wall, they merge with the wall ribs underneath and enhance the intensity of the wall ribs with the same signs. The wall ribs remain attached to the wall almost all the time. However, their positions are not fixed and their intensities are periodic.

The wall ribs can induce high turbulent intensity in the impinging region. They are sustained by merging with the successive and cross ribs. In the stagnation region, the cross ribs contribute much more to the sustenance of the wall ribs than the successive ribs. After the cross ribs merge with the wall ribs, the intensity of the wall ribs reaches a maximum value, implying that the heat transfer in the stagnation region should be controlled by regulating cross ribs through the inlet

perturbations. This finding has important implication on the design of practical systems involving the use of impinging jets.

Chapter 5

Validation of the New Collision Model

5.1 Introduction

The modelling of liquid droplet collision/coalescence is important in analyzing Diesel sprays. Droplet collisions in a dense spray have a significant impact on the droplet size [48] and also on the dispersion and velocities of the droplets [74].

Most existing spray collision models were derived from the original model of O'Rourke [108] which followed the method of computing collision process in rain clouds by Brazier-Smith et al. [90]. O'Rourke's algorithm is consistent with the stochastic nature of spray simulations, where only a sub-sample of droplets is tracked. The tracked droplets represent parcels or particles of varying numbers of droplets with identical size, velocity, and temperature. This model assumes that droplets in a particle distribute evenly within the cell in which the particle lies and a given particle may collide with another particle only if these two particles reside in the same computational cell.

O'Rourke's collision model has well-known weak points, i.e. it is grid-dependant [117]. It is also known to over-predict droplet size [56] and suffers from poor numerical convergence [16], etc. The model performed poorly in Cartesian grids [117], and produced relatively better results in cylindrical grids. However, most computational domains of practical interest are complex, in which cylindrical mesh can not be used. The root of the incompetence of the original O'Rourke's model is the assumption that the droplets in a particle distribute uniformly in the cell which they reside and only two particles sharing the same cells have a chance to collide. This assumption not only produces grid-dependent results but also "clover-effect" artefact.

Chapter 5 Validation of the New Collision Model

In this chapter, the newly developed collision model described in chapter 2 is validated against analytical solutions of simplified realistic collision problems in a box volume. The grid-dependence is checked against some spray test cases.

5.2 Validations

5.2.1 Model accuracy

To verify the accuracy of the new collision model, validations against analytical solutions and O'Rourke's model have been made for a simplification of realistic problems. The test cases in this section are taken from Schmidt and Rutland [107]. In the test cases, the outcome of collisions is omitted, only the number of collisions is considered. The consideration of realistic collision outcomes would make it much more difficult to obtain an analytical solution. Furthermore, the improvement of the new collision model is mainly related to prediction of the incidence of collision.

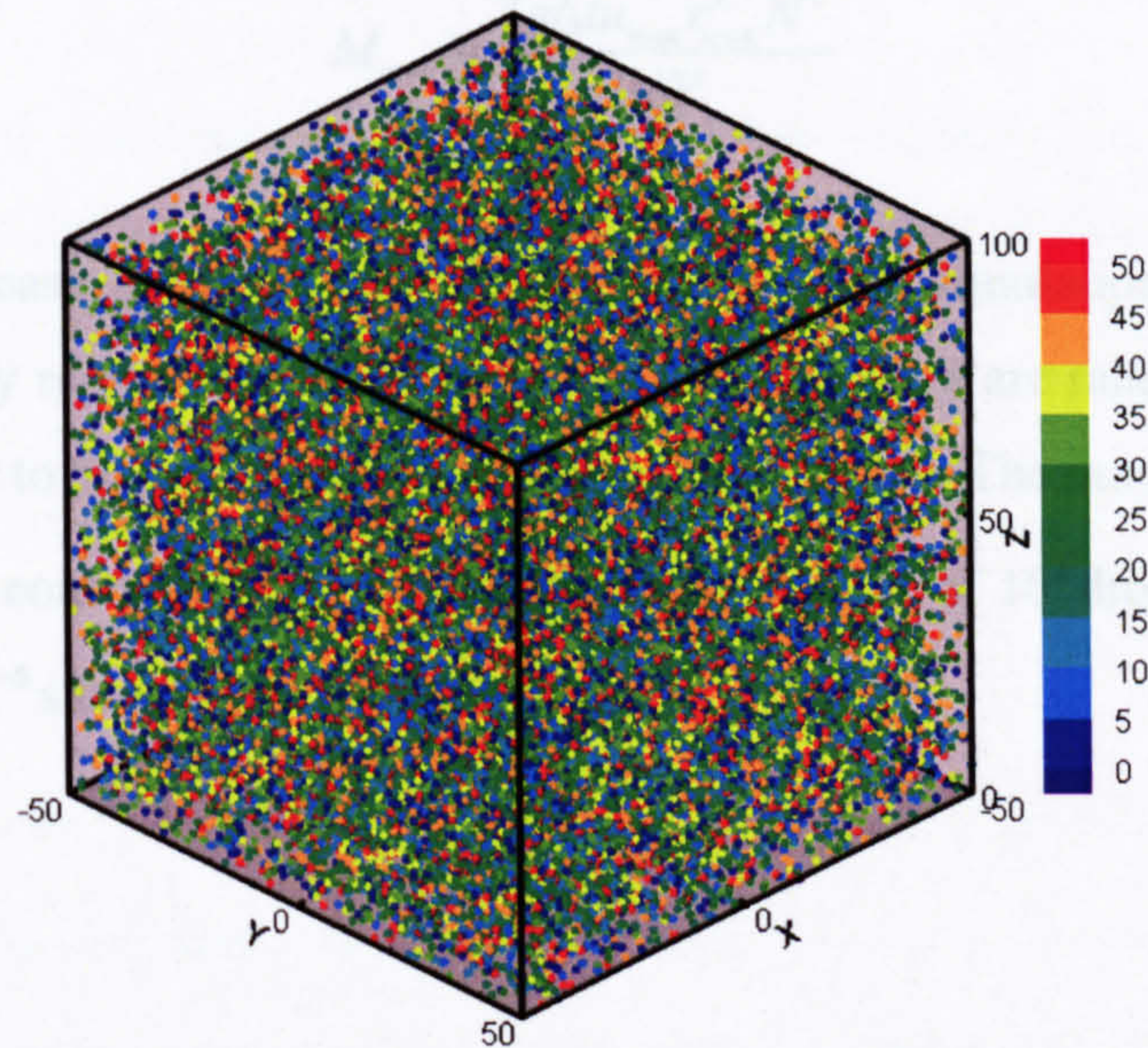


Fig. 5.1 The test domain with uniformly distributed droplets. The particles are coloured with the droplet radius in μm . Coordination unit is in cm.

The first test case is spatially uniformly distributed droplets in a box volume V shown in Fig. 5.1. The parameters of the droplets are given as radius $[0, r_{\max}]$ and velocity in the x direction $[0, u_{\max}]$. The sizes and velocities of droplets follow a uniform distribution in the box.

The expected number of collisions can be calculated from the integral of the collision probability over the size and velocities, given as following,

$$M_{coll} = \frac{N^2 \Delta t}{2V} \int_0^{r_{max}} \int_0^{r_{max}} \int_0^{u_{max}} \int_0^{u_{max}} f_u(u_1) f_u(u_2) f_r(r_1) f_r(r_2) |u_1 - u_2| \pi(r_1 + r_2)^2 du_1 du_2 dr_1 dr_2 \quad (5.1)$$

where functions f are the probability distribution functions, which are simply uniform distributions in this case. The evaluation of this integral gives the following expected number of collisions:

$$M_{coll} = \frac{7\pi \Delta t u_{max} r_{max}^2 N^2}{36V} \quad (5.2)$$

Since the test case is a spatially uniform problem, the simulation is run with a volume of unity represented by a single cell. The particles are randomly assigned a radius from 0 to 50 μm and a velocity from 0 to 100m/s. The number of droplets per particle is constant. The particles represent a total of 10^9 droplets. A single time step of 10^{-5} s is run for the simulation.

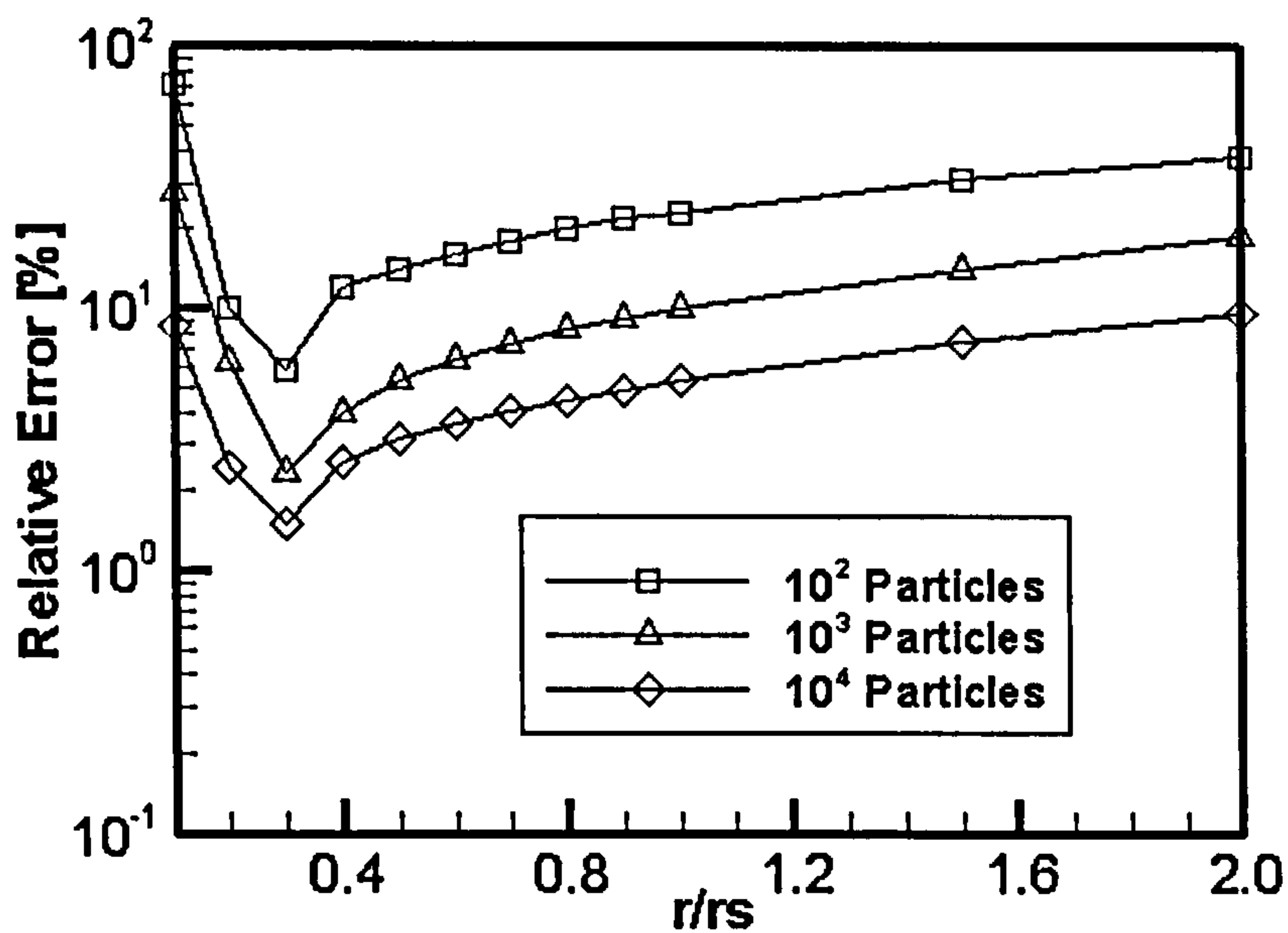


Fig. 5.2 The relative error versus the non-dimensional particle cloud radius under different particle numbers.

The effect of the fictitious particle radius is first investigated. Fig. 5.2 shows the radius effect on the relative error of predicted number of collisions for the new method under varied particle numbers. The relative error is defined by

$$\varepsilon = \frac{|M_{theo} - M_{predi}|}{M_{theo}} \quad (5.3)$$

M_{theo} is the theoretic value of Equation (5.2), M_{predi} is the predicted value of the new model. To eliminate the random effect, M_{predi} is averaged over 100 simulations to obtain a mean value. The results demonstrate that the relative error is connected to both particle number and the sphere radius. Under a certain sphere radius, the relative error decreases with an increase in particle number. With a fixed particle number, there exists an optimum radius at the position $r/r_s = 0.3$. The relative error increases steadily with the sphere radii when $r/r_s > 0.4$.

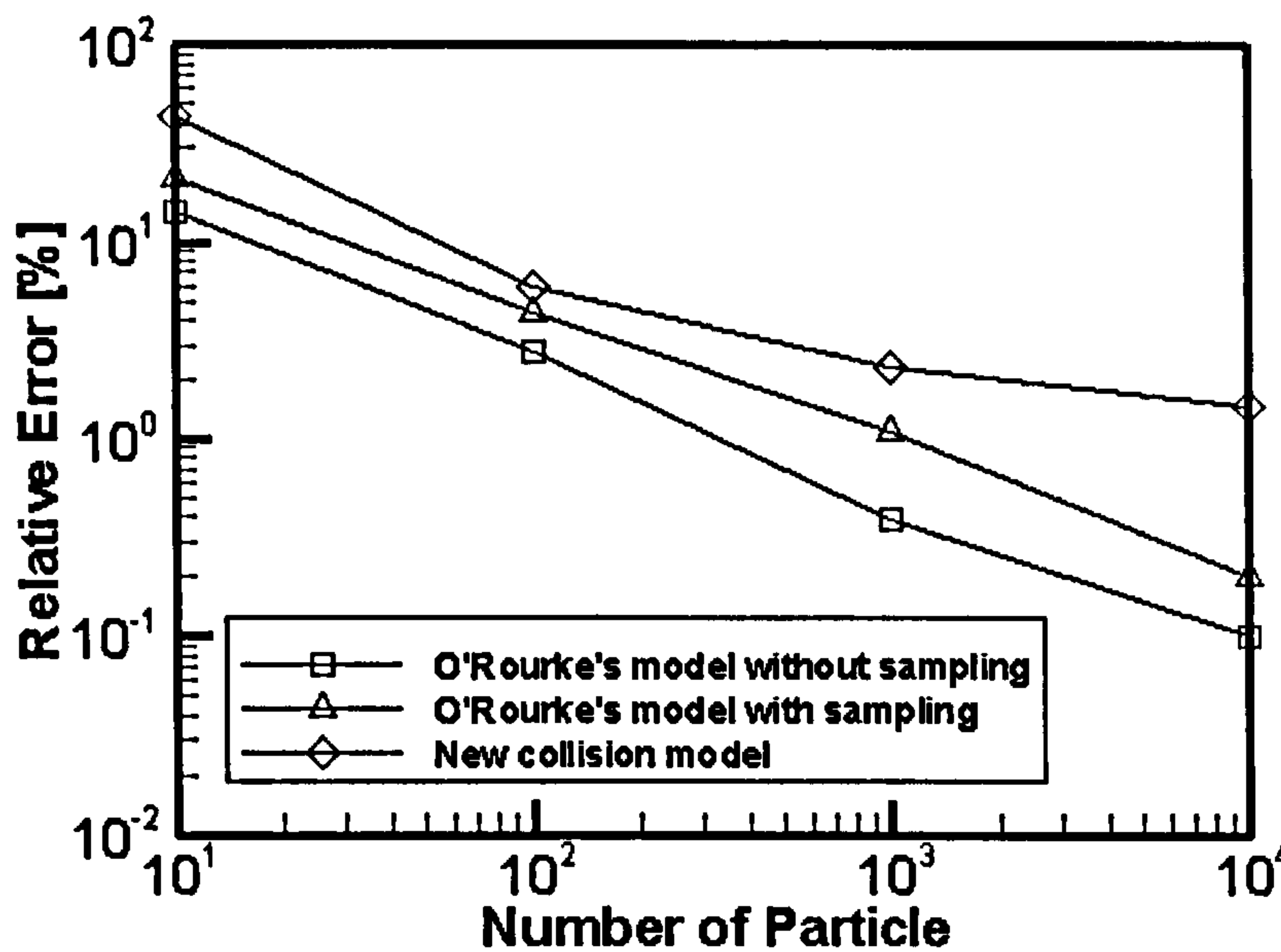


Fig. 5.3 The relative error versus the particle numbers

Fig. 5.3 shows the relative error of the predicted number of collisions by the new model and the O'Rourke model. Two cases are computed for the O'Rourke model with and without the sampling. All the results show a trend that relative errors decrease with increase in particle number. The result of the O'Rourke's scheme without Poisson distribution is most accurate. The sampling procedure does not improve the accuracy. The new model is a little bit less accurate in predicting the number of collisions than O'Rourke's scheme for the present test case of uniformly distributed droplets without consideration of the outcome velocities. However, it will be seen in the following section that the new model is more accurate in predicting a realistic spray in which the outcome of collision velocities is taken into account. This is because the new model is less grid-dependant than O'Rourke's mode and there are no artefacts in the new model.

Fig. 5.4 shows a comparison of the cost of the two collision models using a single-processor 2GHz computer. Since no sampling procedure is used in the new model, the cost of the new model is nearly the same as that of the O'Rourke's scheme without sampling. The sampling procedure is very expensive, and the cost of O'Rourke's scheme with Poisson distribution is almost ten times slower than

without Poisson distribution. In general, the cost of the models is quadratically dependent on the particle number.

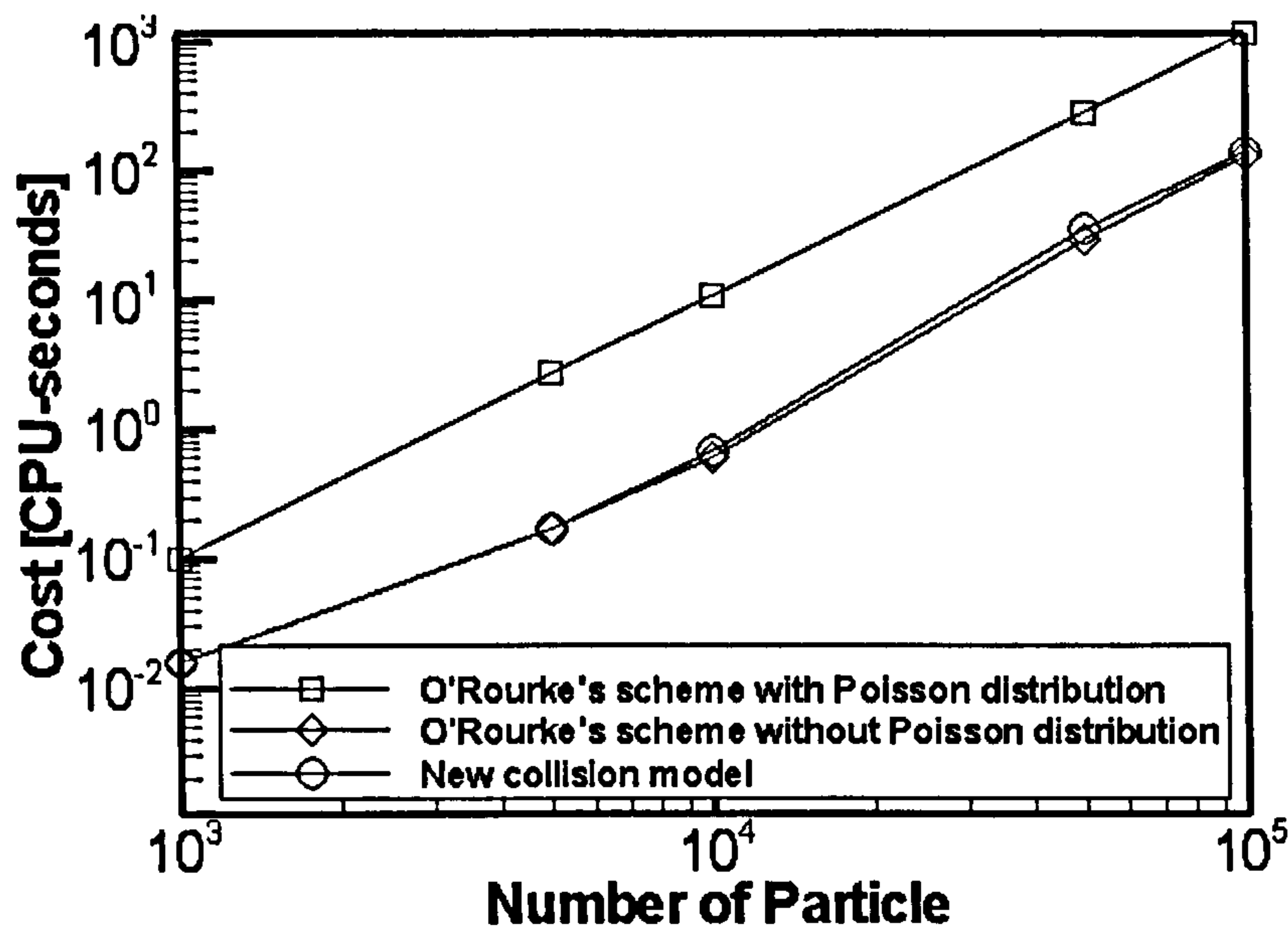


Fig. 5.4 The computational cost versus the particle number.

Another transient test is used to determine the order of temporal accuracy. The test case is also spatially uniformly distributed droplets in a box volume V shown in Fig. 5.1. The initial droplet size is a constant of r_0 . The velocity of the droplets is bimodal, given by the following probability density function:

$$f_u(u) = \frac{1}{2}\delta(u - u_0) + \frac{1}{2}\delta(u + u_0), \quad (5.4)$$

where δ is the Dirac delta function. Only the velocity component in the x -direction follows the function, and the other two components were set to zero. The droplet number of a particle is also constant. Every incidence of collision results in a removal of one particle randomly selected from the colliding particle pair. Allowing for the homogeneity of the problem, the positions of particles are not updated during the simulation. The expected number of droplets remaining in the box at time t can be analytically solved to be

$$N(t) = \frac{N_0}{1+t/t^*} \quad (5.5)$$

Where N_0 is the initial number of droplets, and t^* is a time scale defined by

$$t^* = \frac{V}{2\pi r_0^2 N_0 u_0} \quad (5.6)$$

The simulation is run with a volume of unity represented by a single cell. The droplet radius r_0 is taken to $20 \mu m$ and velocity component u is set to $\pm 100 m/s$. The total particle number is 10,000, and the particles represent a total of 10^9 droplets. Three time steps of $0.01 t^*$, $0.1 t^*$ and t^* are used in the simulations. The running time of the simulations is set to t^* .

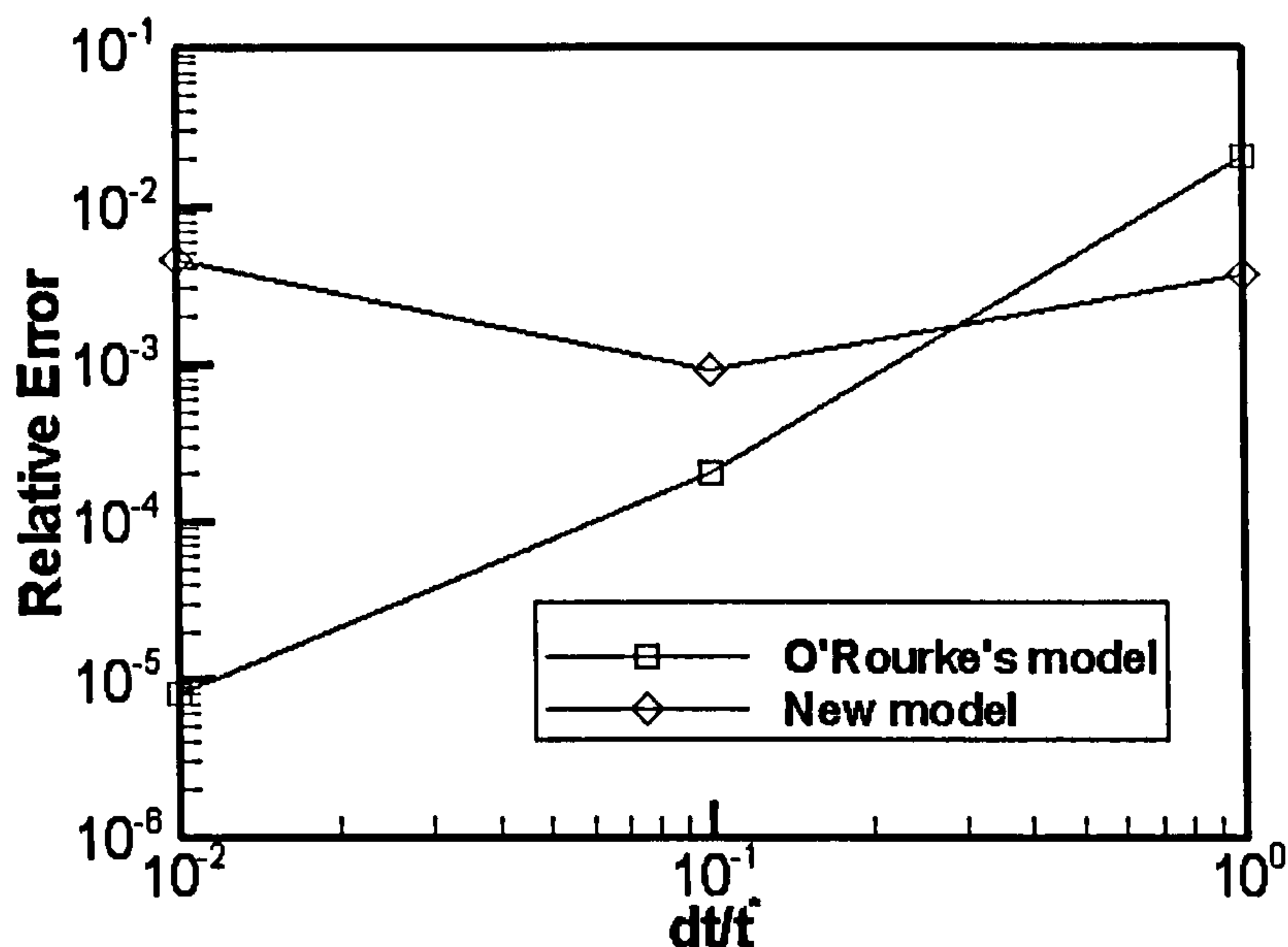


Fig. 5.5 The relative error versus time step in a temporal calculation over a time interval t^*

The computed results are shown in Fig. 5.5. The time accuracy of O'Rourke's model is nearly first-order, which is the best accuracy order that is normally

Chapter 5 Validation of the New Collision Model

obtained for most stochastic collision models, as the complicated nature of the problem prohibits the use of high order methods. The predicted relative error of the new model shows less dependence on the time step than that of O'Rourke's model. In general, O'Rourke's model is more accurate than the new model. However, the new model gives more accurate results, when the time step is close to t^* . Both models produce accepted errors for the computed time steps.

In the test cases of this section, the outcome of collisions is omitted. The accuracy of O'Rourke's model is a little bit more accurate than the new collision model. In the next section, realistic collision outcomes will be considered. As will be seen, with the consideration of collision outcomes, O'Rourke's model will produce severe artefacts in Cartesian meshes. The accuracy of O'Rourke's model will deteriorate due to the artefacts.

5.2.2 Grid-dependency

In this section, the grid-dependency of the new collision model and O'Rourke's collision model is investigated. Since O'Rourke's model is especially grid-dependant in the frame of Cartesian mesh, all the test cases in this section are computed in Cartesian meshes. The predicted spray shape, penetration depth and SMR are used to evaluate the grid-dependency of the two collision models.

5.2.2.1 Ideal spray test cases

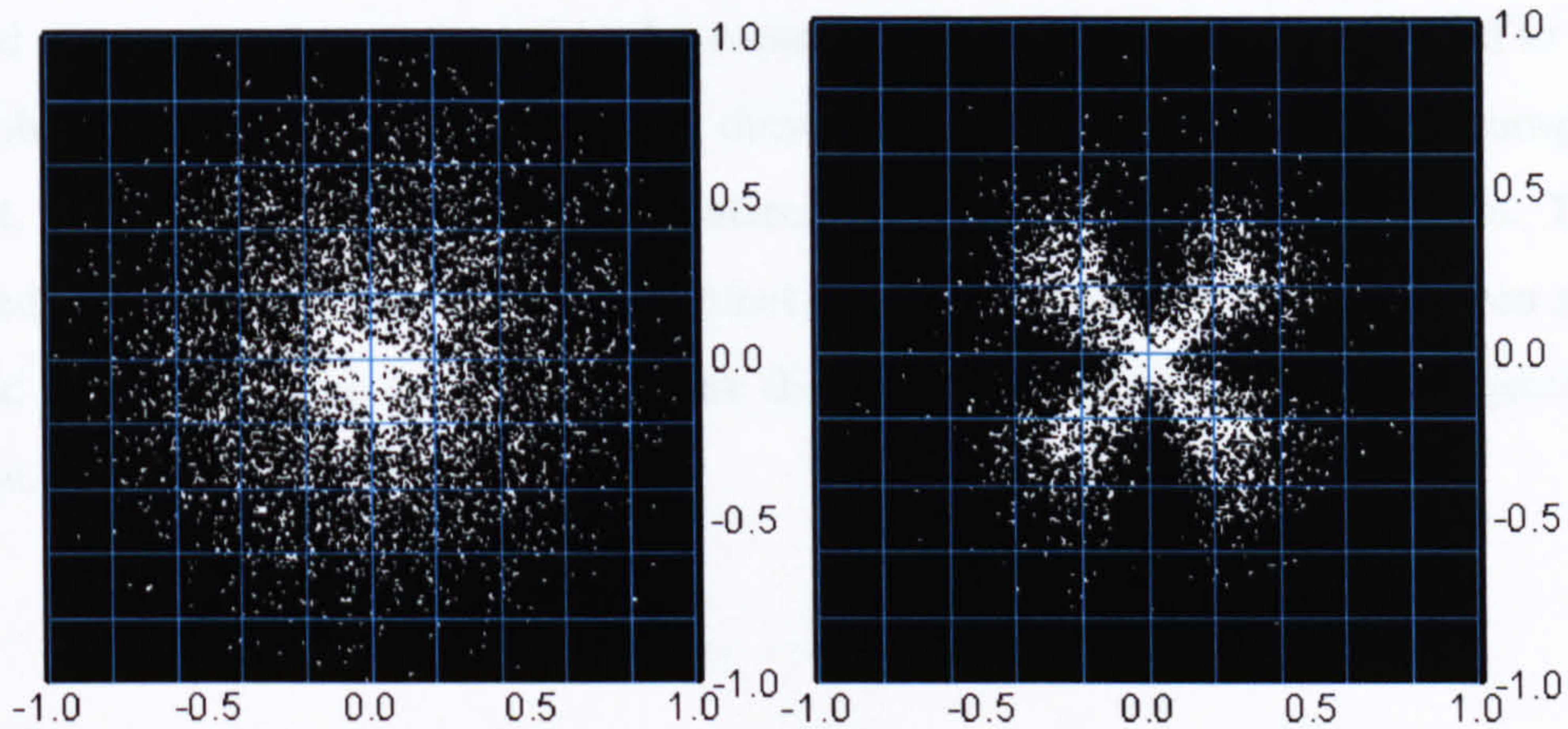
Table 5.1 Computational data of the ideal spray test cases

Cases	Case 1	Case 2	Case 3	Case 4
Computed domain	$2 \times 2 \times 4 \text{ cm}$			
Mesh	Uniform $10 \times 10 \times 20$		Uniform $11 \times 11 \times 20$	
Collision model	O'Rourke	New	O'Rourke	New
Breakup model	Switched off			
Drag	Switched off			
Inject flow rate	5g/s			
Initial size distribution	χ^2 -distribution; SMR=10 μm			
Initial inject velocity	50 m/s			
Particle number rate	$1 \times 10^7 \text{ s}^{-1}$			
Spray angle	Solid 25 degree			
Ambient pressure	5 MPa			
Ambient temperature	293 K			

It is well-known that O'Rourke's model produces artifacts of spray in Cartesian meshes. The predicted spray of O'Rourke's model behaves differently in even and odd Cartesian meshes. As seen in Fig. 5.6, the spray injection point locates on a vertex for the even mesh and in the center of a cell for the odd mesh. Ideal spray tests are constructed to investigate the predicted spray shape from the two models.

The parameters of the test cases are listed in Table 5.1. In the test cases, the spray shape is used to evaluate the grid-dependency.

(a) Even mesh



(b) Odd mesh

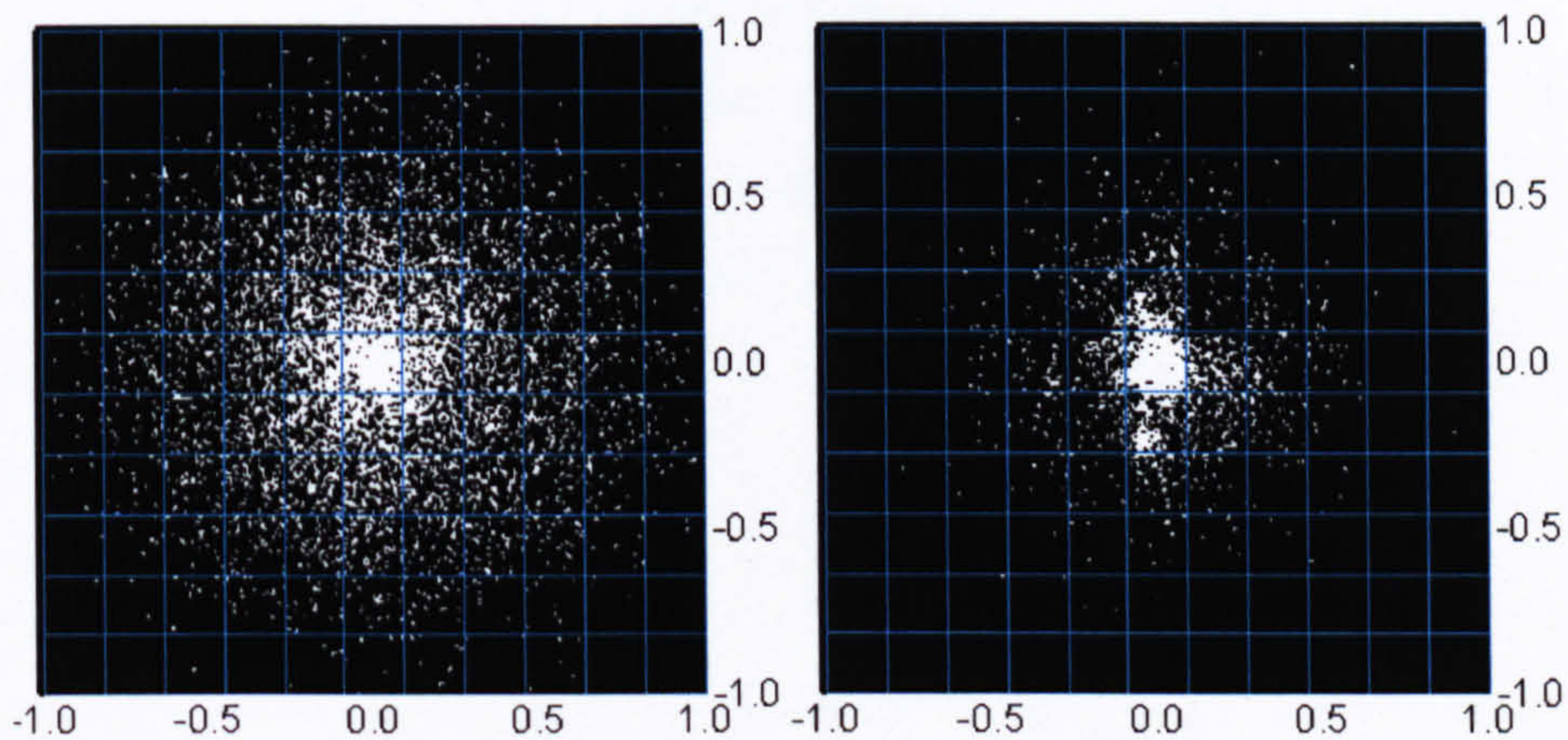


Fig. 5.6 Top view of the predicted spray shapes for the new model (left) and O'Rourke's model (right).

To avoid the influence of gas flow, the aerodynamic drag is turned off in the simulations. The breakup model is also switched off, and instead the injected droplet sizes are assumed to follow χ^2 -distribution with a SMR of $10 \mu m$. The top view of predicted spray shapes is shown in Fig.5.6. For the cases of even mesh, spays are injected close to the central vertex. An apparent shape of a "clover leaf" is predicted by O'Rourke's model. This is attributed to the

assumption that all droplets in a cell collide with each other, which renders the outward velocity component of droplets in the cells situated on the injection point follow along the diagonal lines through the injection point, as the outward velocity components are averaged in the cells as the outcome of collisions. For the case of odd mesh, sprays are injected in the centre of a cell. The sprays are tended to be prohibited to move outward, as the outward velocity components are averaged out. Most of spray droplets are clustered around the spray injection line. The predicted sprays by the new model do not show any artifacts for both the even and odd meshes, and the spray droplets are distributed uniformly around the injection line.

5.2.2.2 Realistic spray test cases

It is well-known that O'Rourke's model cannot achieve grid-convergent results of spray penetration depth and SMR in Cartesian meshes. Realistic spray test cases are used to investigate the grid-dependency of the predicted penetration depth and SMR from the two models. The parameters of the test cases are listed in Table 5.2.

Table 5.2 Computational data of the realistic spray test cases

Cases	Case 1	Case 2	Case 3	Case 4
Computed domain	$2 \times 2 \times 4 \text{ cm}$			
Mesh	Non-uniform even meshes: Fine: $40 \times 40 \times 50$ Medium: $30 \times 30 \times 40$ Coarse: $20 \times 20 \times 30$		Non-uniform odd meshes: Fine: $41 \times 41 \times 50$ Medium: $31 \times 31 \times 40$ Coarse: $21 \times 21 \times 30$	
Collision model	O'Rourke	New	O'Rourke	New
Breakup model	Switched off			
Drag	Turned on			
Turbulence model	LES one-equation SGS model			
Gas velocity interpolation	Turned on			
SGS velocity	Switched off			
Inject flow rate	5g/s			
Initial size distribution	χ^2 -distribution; SMR=10 μm			
Initial inject velocity	50 m/s			
Particle number rate	$1 \times 10^7 \text{ s}^{-1}$			
Spray angle	Solid 25 degree			
Ambient pressure	5 MPa			
Ambient temperature	293 K			
Computed time	1ms			

The breakup model is switched off, and the injected droplet sizes are assumed to follow χ^2 -distribution with a SMR of $10 \mu m$. Gas drag is considered in the test cases and the one-equation SGS model is used to close the NS equations. SGS velocity is neglected in the simulations. To alleviate the grid-dependence of the predicted results, gas velocity is interpolated at the particle positions. Both even mesh and odd meshes are used and three different grid-resolutions are used for each kind of mesh. All the meshes are clustered around the injection point as shown in Fig. 5.7.

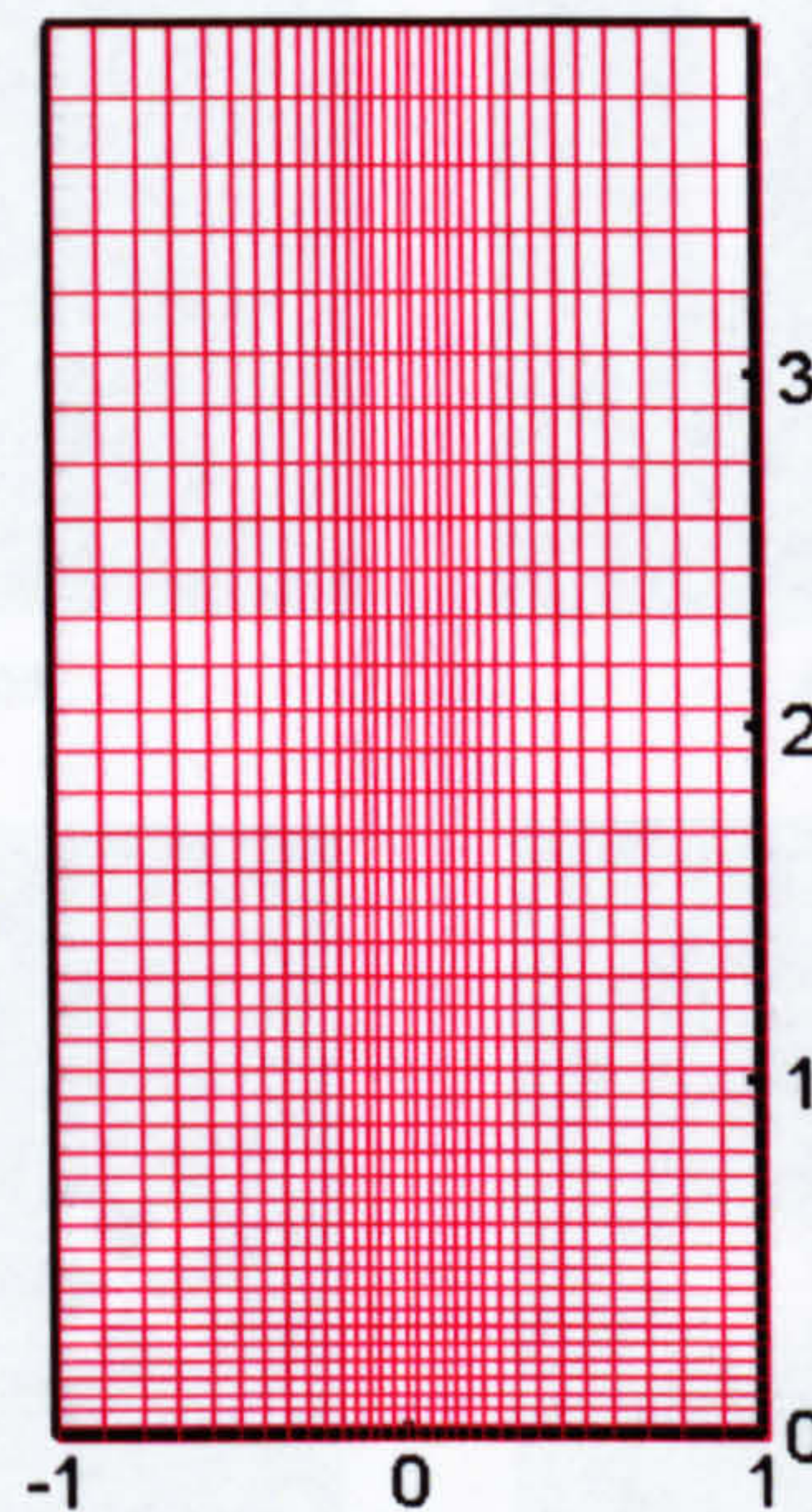


Fig. 5.7 Computational mesh.

The overview of the predicted sprays is shown in Fig. 5.8. The predicted sprays by O'Rourke's model still show the artifacts as explained in the last section, and the new model correctly reproduces the dispersion of the sprays. The predicted sprays travel faster in the odd mesh than in the even mesh, since the injected droplets are initially distributed into four cells for the even mesh.

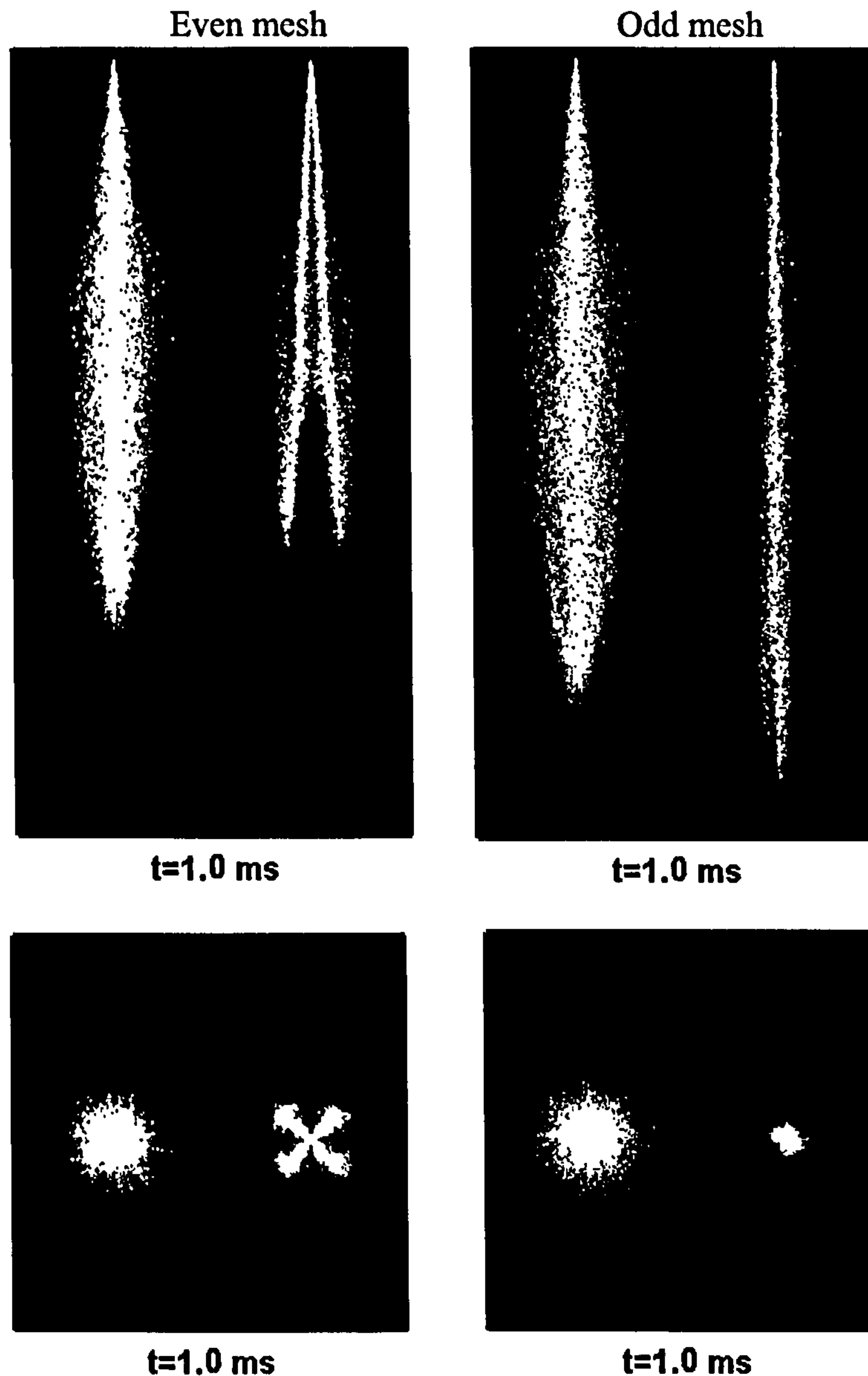


Fig. 5.8 The predicted spray shapes for the new model (left) and O'Rourke's model (right).

The computed penetration depths are shown in Fig. 5.9. The results show that the predicted penetration depths by O'Rourke's model are highly grid-dependent, while the grid-dependence can be significantly reduced by the new collision model. The maximum discrepancy between two adjacent curves is only in an order of 1mm for the new collision model. Total grid-convergent result is difficult

to achieve for a numerical prediction of fuel spray using a Lagrangian method to track particle due to the insufficient resolution for the momentum exchange between the two phases.

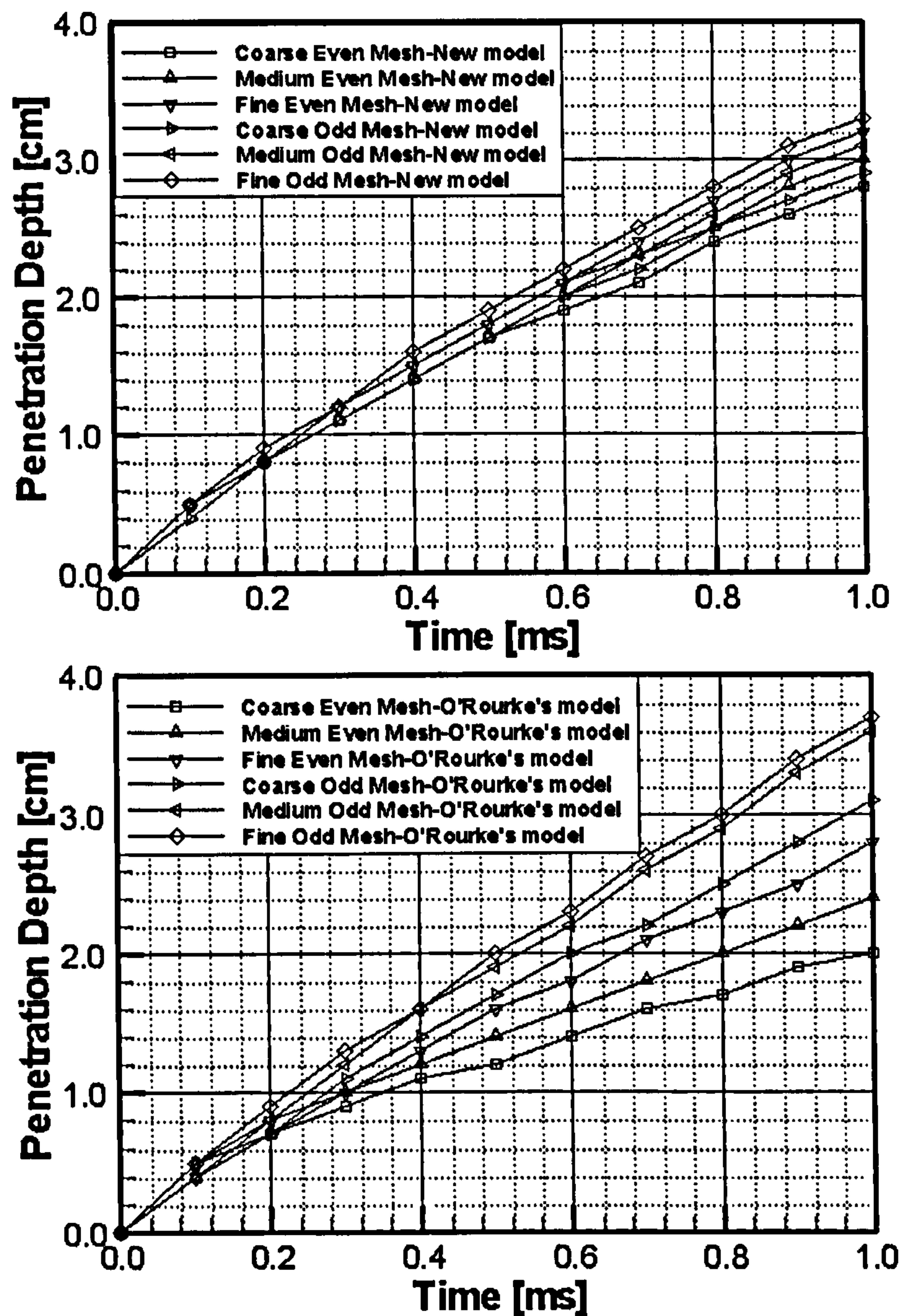


Fig. 5.9 The curves of predicted penetration depth.

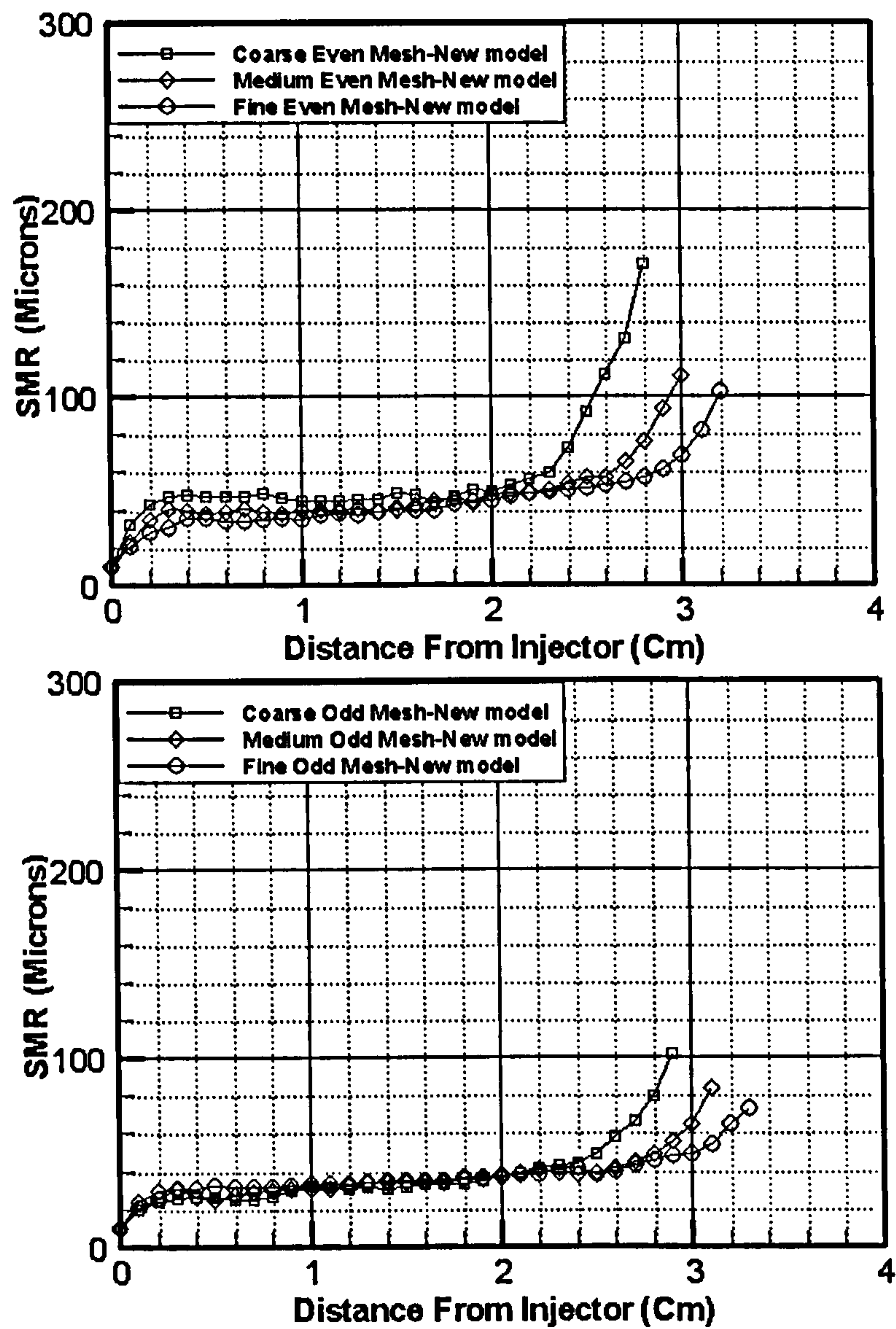


Fig. 5.10 The curves of the predicted SMR.

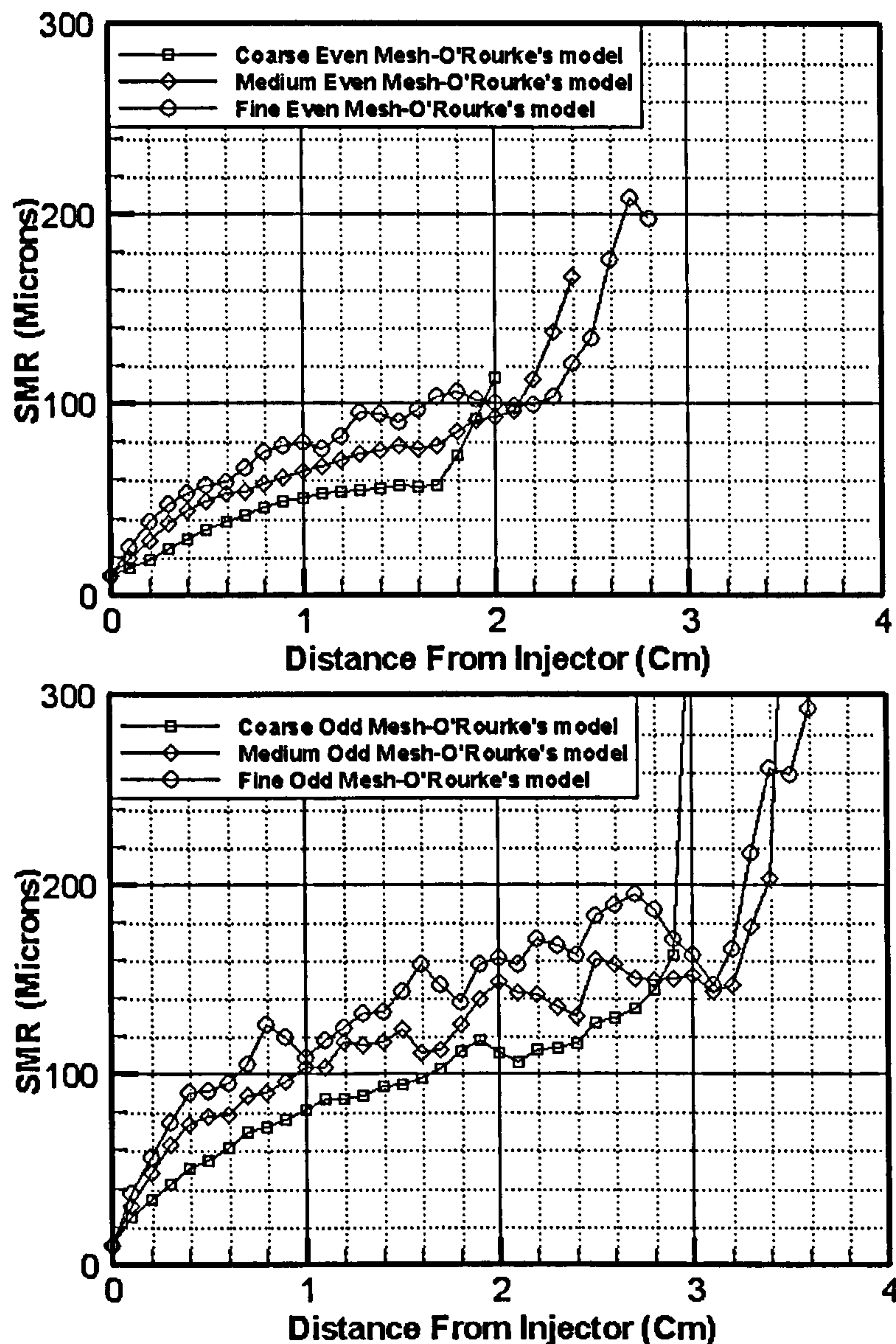


Fig. 5.10 (continued) The curves of the predicted SMR.

The computed SMRs are shown in Fig. 5.10. The results show that the computed SMRs by O'Rourke's model are also highly grid-dependent, while the results by the new model show little grid-dependence. There is a big discrepancy at the tips of the spray, since it is very dense due to the accumulation of large droplets. The results of the even mesh by the new model show an excellent grid-convergence except for the tip. The predicted SMRs by the new model show a substantial increase in the dense region. In the dilute region, the predicted SMRs increase

slowly, since the frequency of collision is small. The results by the O'Rourke's model show little difference of the increasing rate of SMR between the dense and the dilute regions. Moreover, because of the artifacts of the O'Rourke's model, the predicted droplets cluster in few cells. This makes the sprays very dense in these cells, hence the model significantly over-predict the SMR values.

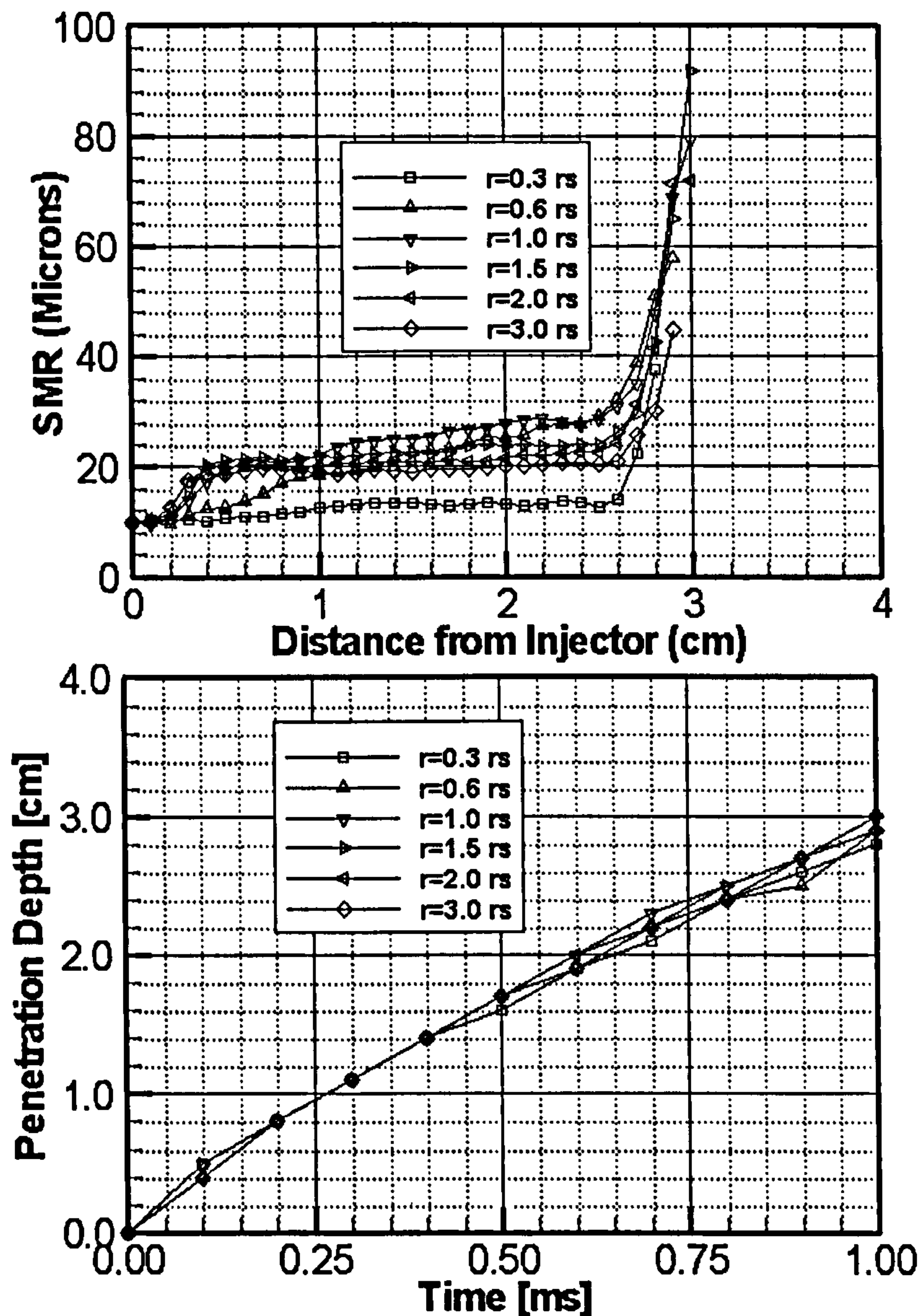


Fig. 5.11 Predicted SMR and penetration depth for the cases with the fixed particle number and different particle could radii.

5.2.2.3 Effect of the parameter of particle cloud radius

In this section, the effect of the parameter of particle cloud radius on a real spray is tested against varied cloud radii and particle numbers. The test cases use the fine odd mesh of the test cases in section 5.2.2.2, and other parameters are kept unchanged. The injected particle rates of $1 \times 10^7 s^{-1}$, corresponding to total injected particle number of 10,000 during the computed time, is used. In this test, droplet collisions are only considered for the particles 2mm away from the injector. The particles very close to the injector nearly cluster to a point. Collisions between these particles can not be treated nicely by collision models. For a real spray case, there is a breakup length. Injected fuel blobs start to breakup after the length which is normally greater than several millimeters. To more accurately investigate the effect of the particle cloud radius, the collisions close to the injector are omitted.

The predicted SMRs and penetration depths for the particle injection rate of $10^7 s^{-1}$ are shown in Fig. 5.11. The cloud radius has an apparent influence on the SMR. Although for the test case of the uniformly distributed droplets in Section 5.2.1 $r = 0.3r_c$ is the optimum cloud radius, the SMR is substantially under-predicted with the radius. This is because that the spray is poorly resolved in the cells close to the injector and the particles are non-uniformly distributed due to the discontinuous injection of particles limited by the discrete time step. This under-prediction can be alleviated by increasing the radius. The maximum SMR is predicted by using $r = r_c$. When $r > r_c$, the predicted SMR slightly decreases with increase in the radius due to the underestimation of collision frequency. Although the predicted SMRs show a dependence on the radius, the predicted penetration depth is nearly independent on the radius.

5.3 Conclusions

The new collision model based on the assumption of particle clouds has been validated in this chapter. The main reason why the existing O'Rourke's model is grid-dependant is due to the assumption that only droplets from two particles sharing the same cell have a chance to collide. In the new model, a particle is assumed to have a dimension, and the droplets in a particle occupy a fictitious cloud sphere. With this assumption, droplets in two particles tend to collide with each other when their spherical volumes are overlapped.

The new collision scheme is faster than O'Rourke's scheme since it abandons the sampling procedure to compute the collision number. The new model delivers sufficient accuracy in calculating the collision number of the case with uniformly distributed droplets, although O'Rourke's model seems to perform better. However, for the prediction of a real spray in Cartesian mesh, the new model has delivered much improved results. The predictions of the new model do not show any grid-dependent artefacts, and less grid-dependent results are achieved. Finally, when the cloud radius is between r_c and $2r_c$, the predicted SMRs and penetration depths show little dependence on the radius.

Chapter 6

LES of Non-Evaporating and Evaporating Diesel Fuel Sprays

6.1 Introduction

Diesel fuel spray plays a key role for research of spray combustion in direction injection (DI) diesel engines as it is responsible for providing the desired mixture distribution for the combustion process. Spray penetration and fuel vapour distribution have dominant effects on the combustion characteristics such as ignition delay, flame position and lift-off, heat release rate and emissions formation, etc. Generation of harmful combustion products in the exhaust of diesel engines, such as nitrogen oxide and soot, is affected by uneven distribution of temperature and equivalence ratio in the flame. This uneven distribution originates from the uneven distribution of fuel droplets, which is induced by the motion of large-scale vortices formed in diesel spray. “Branch-like” heterogeneous spray structure was discovered by Azetsu [10] and Takagishi [121] in their optical measurements.

The primary problems in analysing and modelling the spray behaviour lie in the incomplete understanding of the important physical processes and the lack of relevant experimental data. These processes lead to cavitation in the nozzle, atomisation, break-up, inter-droplet collision and coalescence, inter-phase transfer of mass, momentum and energy, and spray interaction with the chamber. Most previous numerical studies of fuel spray focus on atomisation, droplet break-up, inter-droplet collision and coalescence. Detailed information on the previous numerical modelling of fuel spray has been introduced in §1.4

Most researchers used RANS code for spray modelling [85,89,107,116,122]. Since fuel spray is a highly transient process, the time-averaged RANS approach

Chapter 6 LES of Non-Evaporating and Evaporating Diesel Fuel Sprays

is too dissipative for such cases while large eddy simulation appears to be more suitable. As mentioned in the beginning, the fuel spray induces large scale vortices in the gas flow field. These vortices affect the distribution of droplets in the spray. Large scale vortices are smeared out by the large numerical viscosity in RANS methods, while they are explicitly resolved in LES. Subramaniam and O'Rourke [116] obtained an unrealistic decreasing penetration length for the finest grid using KIVA-3V, implying that the RANS approach is not suitable for numerical simulation of fuel spray jet. They also concluded that the computed penetration length of a spray was dependent on the grid resolution and that the results did not show a trend towards grid-independence. Although LES sounds like a very promising approach, rare attempts have been made. The only attempt found in the literature was made by Apte et al. [7]. They employed LES to validate a secondary break-up model based on Kolmogorov's discrete break-up model rewritten in the form of differential Fokker-Planck equation for the PDF of droplet radii. They found that LES led to more accurate predictions of turbulent transport in spray jets. In their study, droplet collision/coalescence and the effect of SGS velocity were neglected. There is a great velocity gradient in the region close to the injector. In this region, the unresolved SGS energy can not be omitted. The effect of SGS velocity should be considered in LES of fuel spray.

In this chapter, KIVA-LES is used to study and validated against non-evaporating and evaporating diesel fuel sprays. The predictions are compared with the experiments by Hiroyasu and Kadota [55] and by Naber and Siebers [81] and also with the predictions of the original KIVA-3V.

6.2 Problem description

The experiments of Hiroyasu and Kadota [55], and Naber and Siebers [81] were frequently used as benchmark cases for validating numerical spray models in the literature [7,89,122]. In the experiments, tip penetration, droplets size and spray angles were measured under different gas back pressures. The computed cases and the input data are tabulated in Table 6.1-6.3.

Table 6.1 Computational data for cases of Hiroyasu and Kadota [55]

PARAMETERS	CASE 1	CASE 2	CASE 3
Gas species	N_2		
Gas pressure p_g [MPa]	1.1	3.0	5.0
Gas temperature K	293	293	293
Exit velocity u_e [m/s]	102.0	90.3	86.4
Fuel flow rate G_f [g/s]	4.72	4.18	4.00
Initial droplet radii r_0 [mm]	0.15	0.15	0.15
Initial spray angle θ_0 [°]	10	12	14
Injection time t_i [ms]	4.25	5	5

Table 6.2 Computational data for non-evaporating cases of Naber and Siebers [81]

PARAMETERS	CASE 1	CASE 2	CASE 3	CASE 4
Gas species	N_2			
Gas pressure p_g [MPa]	0.48	1.98	4.04	16.61
Gas temperature K	455	452	452	452
Gas density ρ_g [kg/m ³]	3.6	14.8	30.2	124.0
Injection pressure [MPa]	138	140	140	155
Exit velocity u_e [m/s]	478	479	475	479
Fuel flow rate G_f [g/s]	10.26	10.85	10.76	10.85
Initial droplet radii r_0 [mm]	0.129	0.129	0.129	0.129
Initial spray angle θ_0 [°]	10	10	10	10
Injection time t_i [ms]	0.6	1.5	2.0	2.0

Table 6.3 Computational data for evaporating cases of Naber and Siebers [81]

PARAMETERS	CASE 1	CASE 2	CASE 3
Gas species	N_2 (90.33%), CO_2 (6.11%), H_2O (3.56%)		
Gas pressure p_g [MPa]	0.95	4.04	17.1
Gas temperature K	995	1001	1005
Gas density ρ_g [kg/m ³]	3.3	13.9	58.6
Injection pressure [MPa]	138	142	157
Exit velocity u_e [m/s]	478	475	479
Fuel flow rate G_f [g/s]	10.26	10.76	10.85
Initial droplet radii r_0 [mm]	0.129	0.129	0.129
Initial spray angle θ_0 [°]	10	10	10
Injection time t_i [ms]	0.8	1.5	1.5

Table 6.4 Data for the Computational meshes

GRID	NX	NY	NZ	DX MM	DY MM	DZ MM
Fine LES	51	51	120	0.4	0.4	0.9
Medium LES	41	41	110	0.6	0.6	1.0
Coarse LES	31	31	100	0.9	0.9	1.2
Fine KIVA3V	40	40	100	0.5	1.0	1.0
Medium KIVA3V	30	30	90	0.6	0.6	1.2
Coarse KIVA3V	20	20	80	1.2	1.2	1.4

The experimental domains of the above experiments are enclosed cylinders. Since the influence of walls on the spray is negligible, the computational domain, as shown in Fig. 6.1, is an enclosed box of $4 \times 4 \times 13.8(cm)$. A Cartesian grid is adopted. The mesh is clustered near the nozzle exit. Three different grid sizes, as detailed in Table 6.4, were tested for grid sensitivity studies.

Each spray originates in the centre of the upper boundary, with the centreline of the spray aligned with the gravitational vector. The size of the computational domain was defined to be sufficiently large enough to minimize the effect of the walls on the spray development. All the calculations are performed in three dimensions. Three levels of refinement have been used to investigate the grid-dependence of the predicted results. To be consistent with the experimental sprays, the fluid in each spray simulation begins at rest.

The evaporation model was turned off for all non-evaporating spray test cases. For the purposes of comparison with experimental data, the predicted liquid fuel penetration is defined as the distance from the nozzle to the particle furthest from the nozzle in the domain.

6.3 Computational results and analysis

6.3.1 Overview of the predicted spray

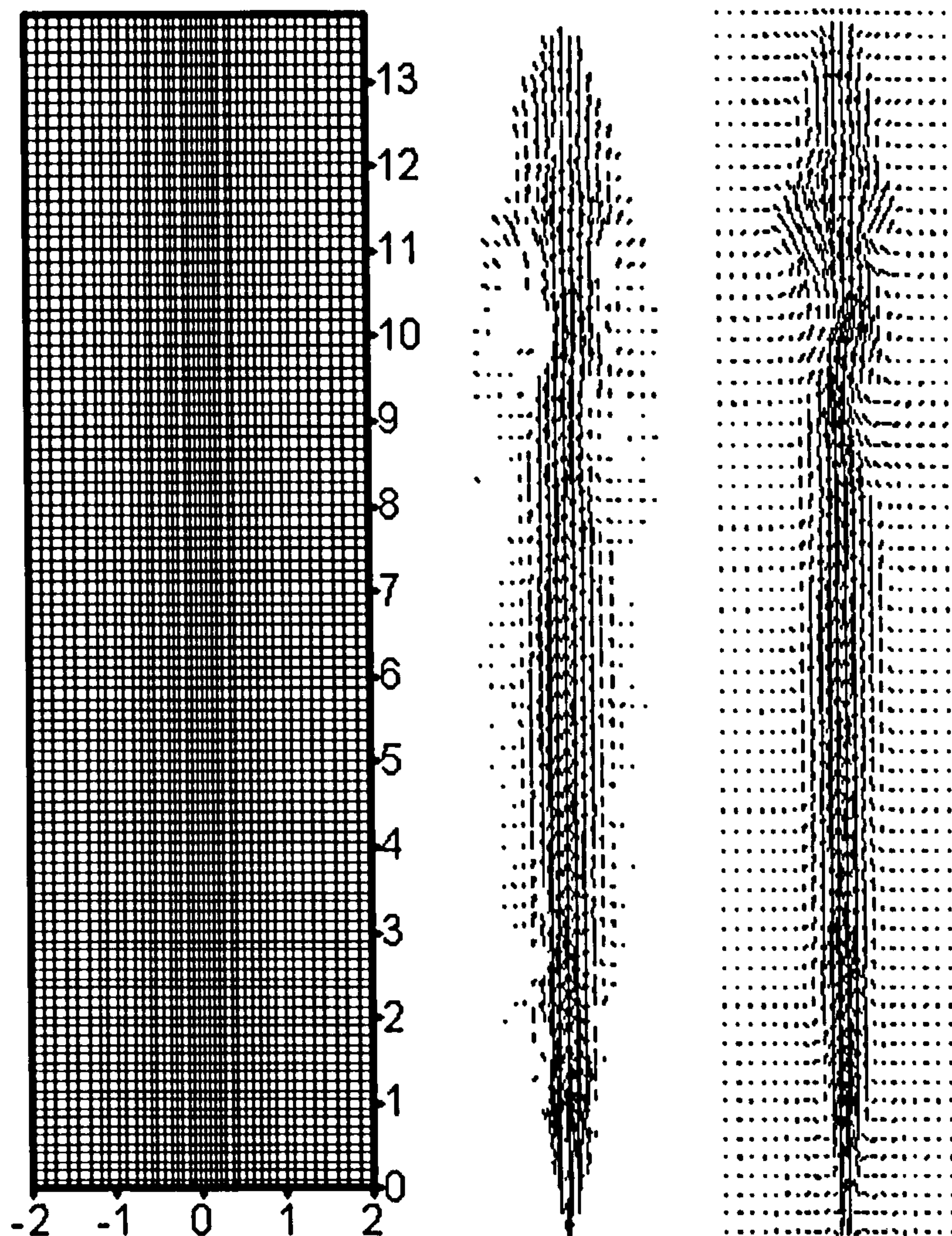


Fig. 6.1 Computational mesh (left), vector of cell averaged droplet velocity (middle), and vector of gas velocity (right)

Vectors of droplet and gas velocity for Hiroyasu' Case 2 are plotted in Fig. 6.1 with the former averaged within each cell. As the gas flow is induced by the spray, their velocities follow similar distribution patterns. Downstream of the nozzle, the gas velocity starts to flap and large-scale vortical structures emerge at the boundary of the spray, caused by large scale eddies due to the Kelvin-Helmholz instability of the shear layer, similar to a free gas jet. The large scale vortical

structures are vital to the spray, which not only distort the spray into “branch-like” shape [10,121] but also distribute spray droplets unevenly inside the spray as droplets tend to follow the gas flow. The spray induced large scale vortical structure is more evident in Fig. 6.2 by the instantaneous velocity vector and the iso-surface of total vorticity of non-evaporating Case 3 of Naber and Siebers.

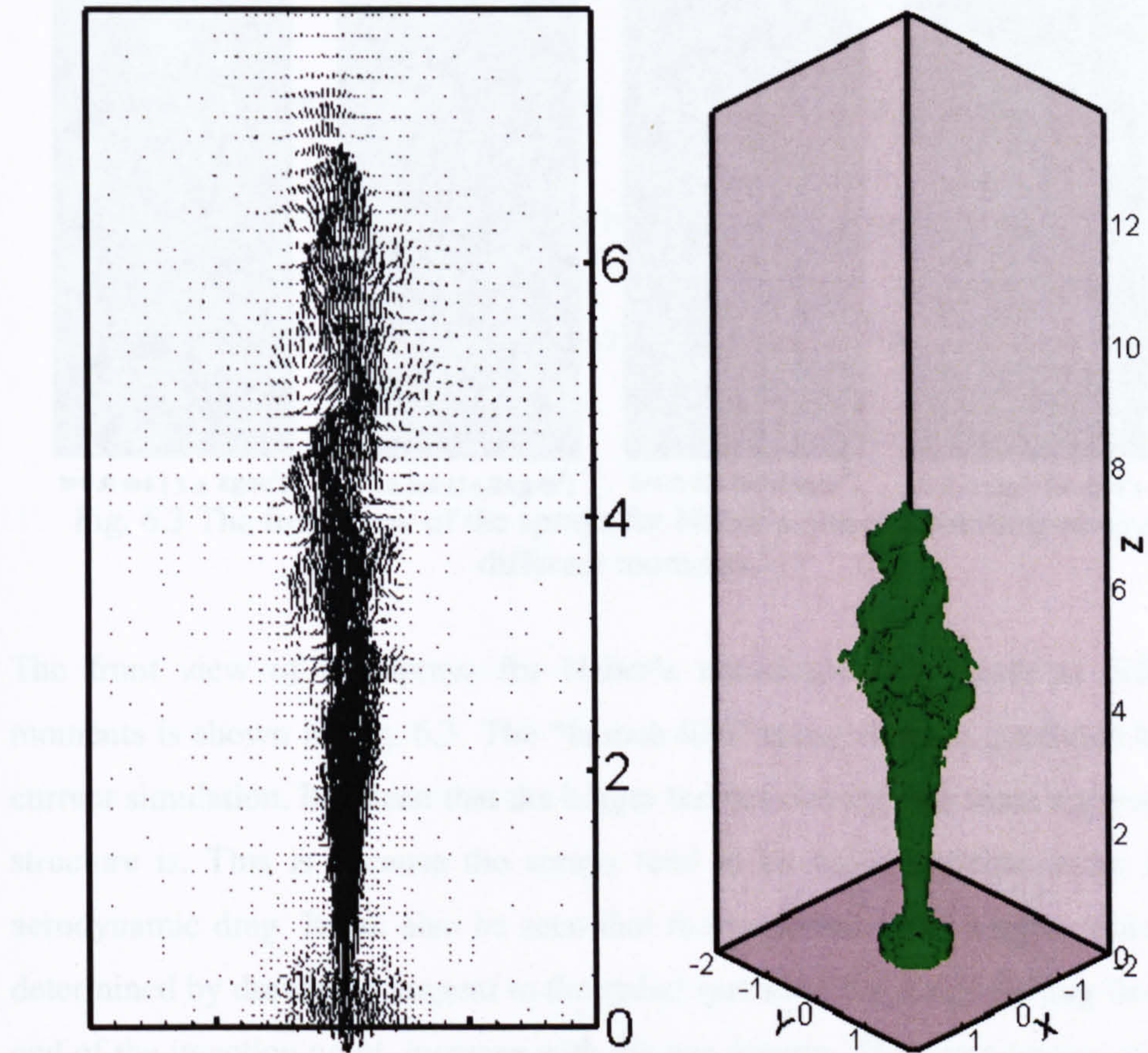


Fig. 6.2 The instantaneous velocity vector and the iso-surface of total vorticity of non-evaporating Case 3 of Naber and Siebers at 1.5ms.

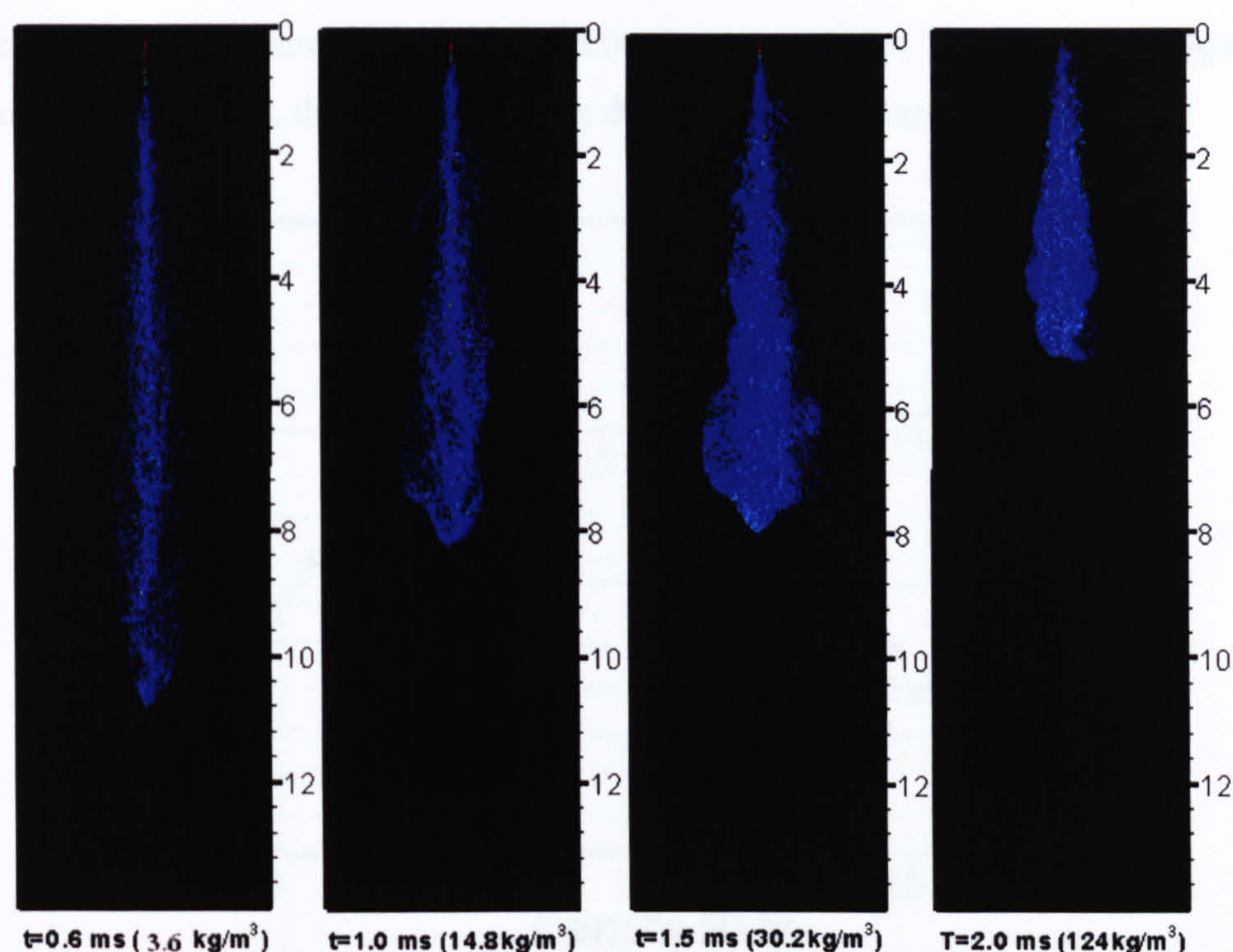


Fig. 6.3 The front view of the sprays for Naber’s non-evaporating cases at different moments.

The front view of the sprays for Naber’s non-evaporating cases at different moments is shown in Fig. 6.3. The “branch-like” spray shape is predicted by the current simulation. It is seen that the bigger the gas density, the more apparent the structure is. This is because the sprays tend to be more unstable under larger aerodynamic drag. It can also be seen that the predicted spray angles, which are determined by drawing a tangent to the radial spread of the spray starting from the end of the injection point, increase with the gas density. The computation of spray angle assures inclusion of 99% of the liquid mass in the whole domain. The comparison of the predicted spray angle with the data is shown in Fig 6.4. The predicted angles are in very close agreement with the measurement.

The injected blobs do not break up immediately upon leaving the nozzle. There exists a break-up length [122]. After this length, the blobs start to break-up. As seen in the Fig. 6.2, the break-up length is getting smaller as the gas density

increases. Aerodynamic drag is proportional to gas density. The bigger drag spray droplets experience, the more easily the droplets tend to break-up.

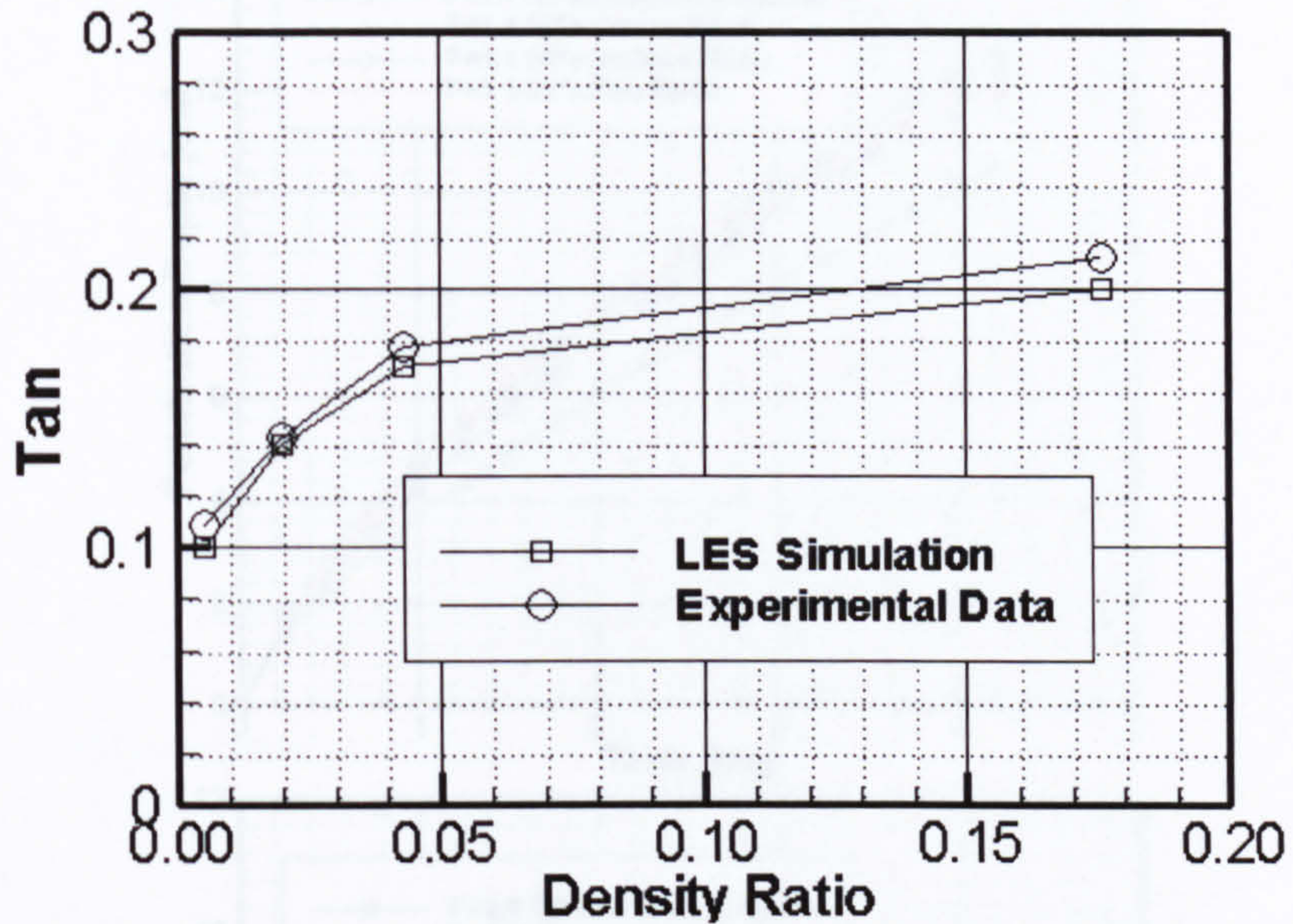


Fig. 6.4 The comparison of predicted angle with the experimental data of Naber’s non-evaporating cases [81]

A top view of the predicted spray is presented in Fig. 6.5. The droplets distribute evenly around the axis of the spray. It displays no trace of the “clover-leaf” artefact [34] described in Chapter 5.

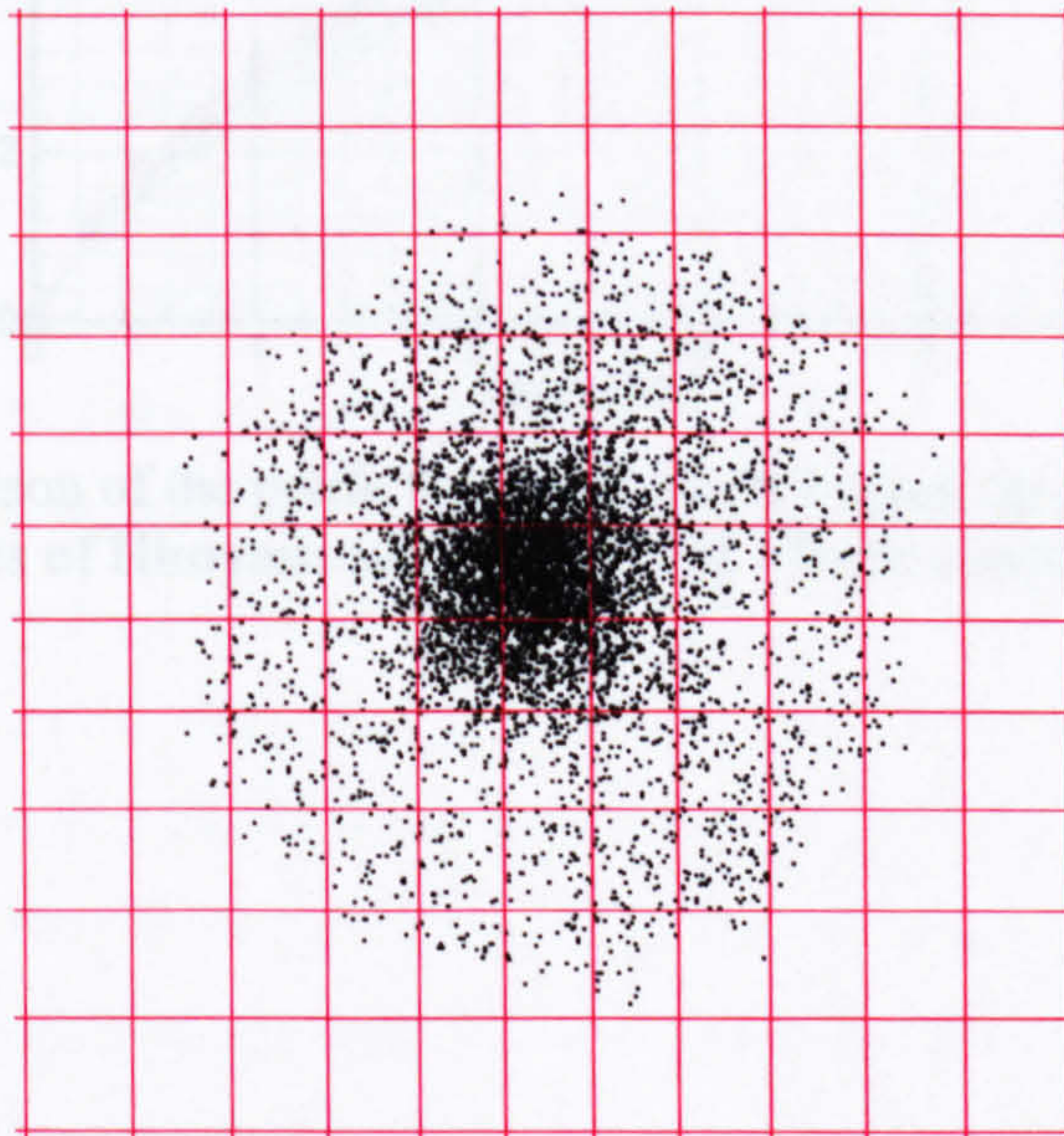


Fig. 6.5 Top view of CASE 2 of Hiroyasu and Kadota [55] at $t = 1.0ms$ (CASE 2)

6.3.2 The predicted spray tip penetration

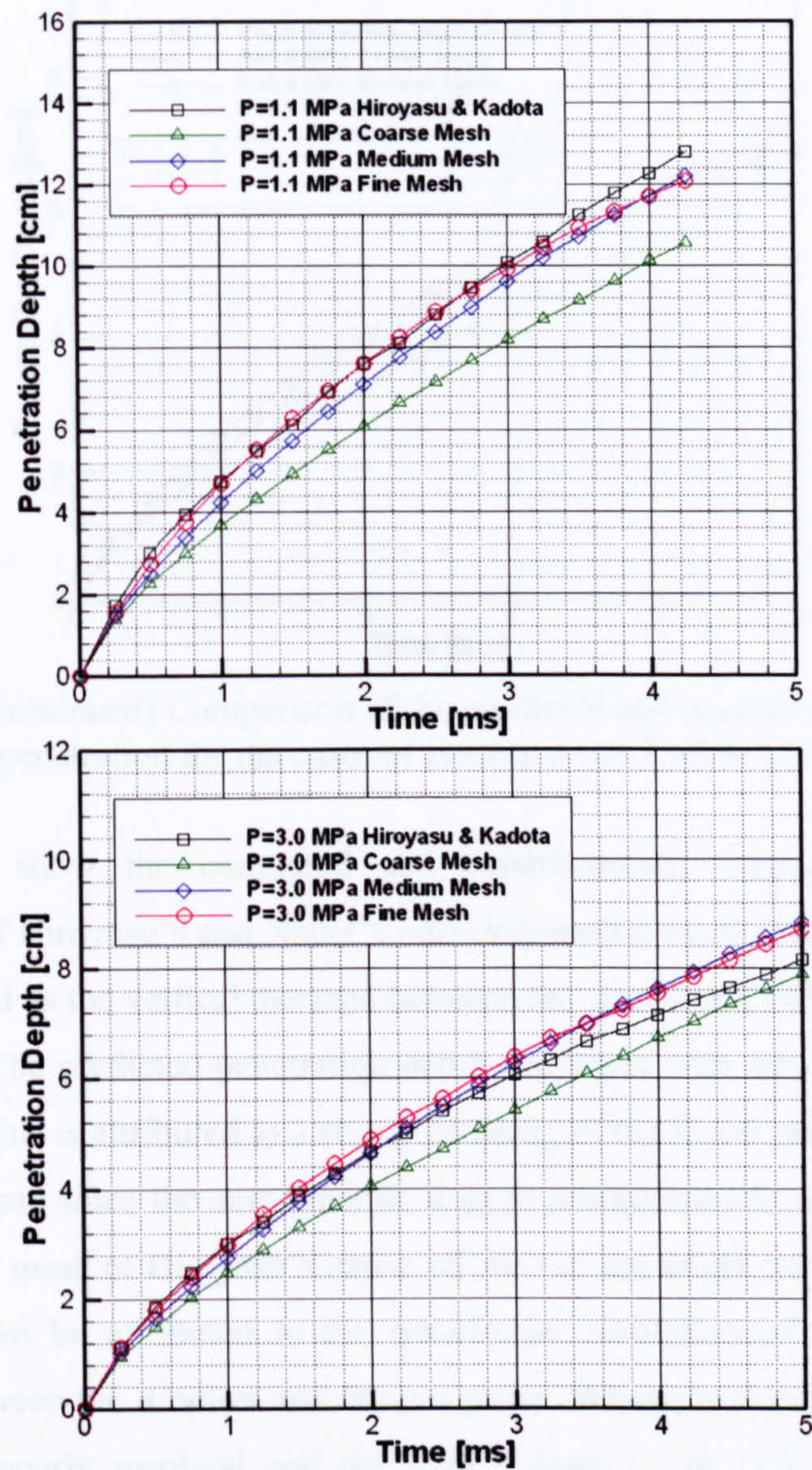


Fig. 6.6 Comparison of the predicted and measured spray tip penetration for the cases of Hiroyasu and Kadota [55]. (To be continued)

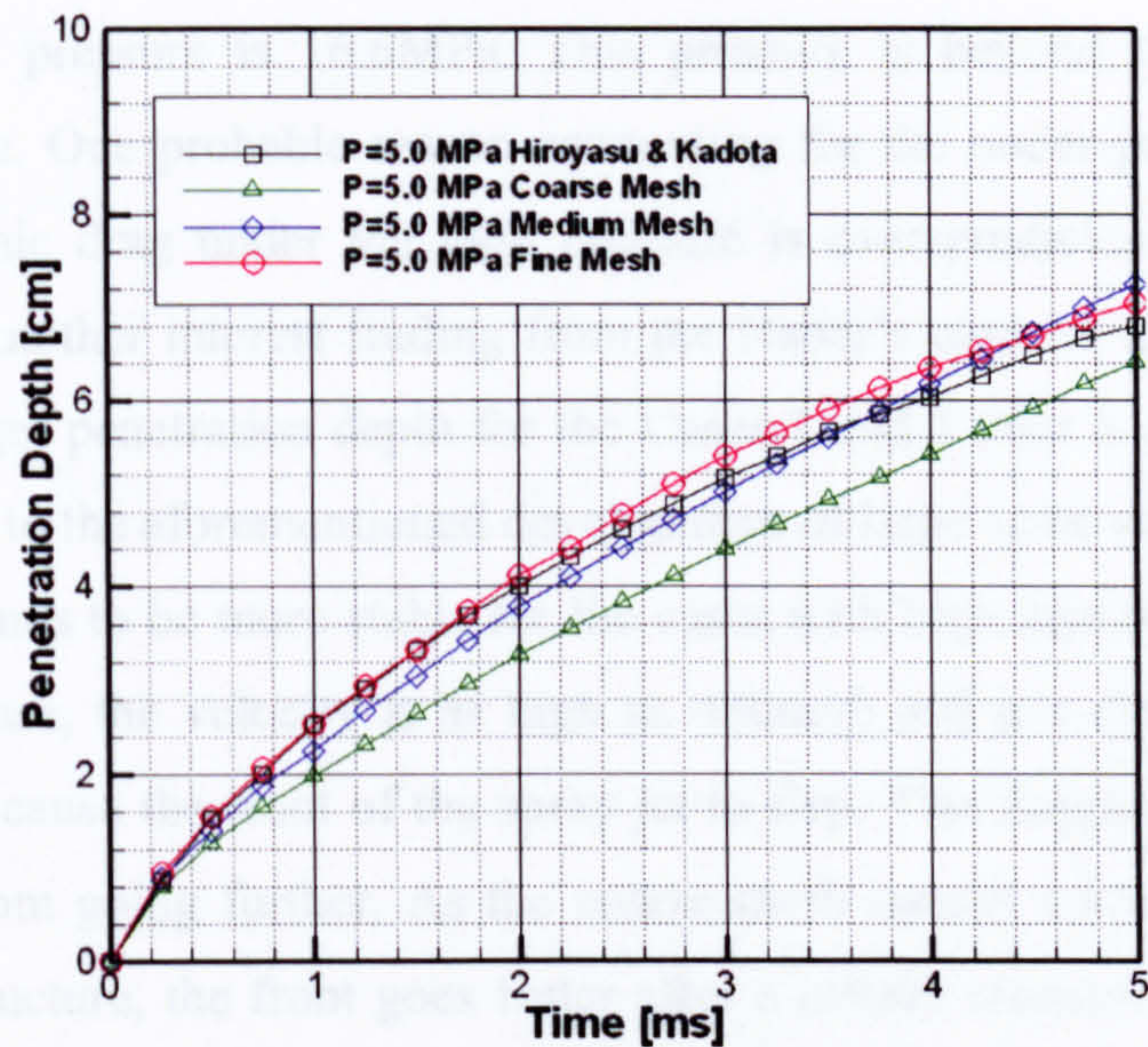


Fig. 6.6 (continued) Comparison of the predicted and measured spray tip penetration for the cases of Hiroyasu and Kadota [55]

Figs. 6.6-6.7 show the computed and experimentally measured spray tip penetrations of Hiroyasu's and Naber's non-evaporating cases [55]. The predicted tip was defined as the vertical distance between the nozzle and the utmost particle in the spray. The predicted penetration depth decreases with increase in pressure (or density). This is attributed to a strong damping of the liquid momentum by the denser gas phase since the aerodynamic drag is proportional to ambient density. For the coarse mesh of Hiroyasu's cases, all the tips are under-predicted in all the cases. This can be attributed to the insufficient resolution of the momentum exchange between the droplets and the gas phase. When the coarse mesh is used, the spray is poorly resolved and the total volume of all cells which contain droplets is much larger than the actual spray volume. The result is that the spray has to accelerate more gas. This leads to a lower gas velocity in a coarse mesh. Excellent agreement is obtained for all the cases using the medium and fine meshes. This proves that the momentum exchange is correctly resolved by the two mesh resolutions. For the Naber's cases, the predicted penetration depths are also in reasonably good agreement with the experimental data and grid independent except for the highest gas density case. The penetration is under-predicted for the

Chapter 6 LES of Non-Evaporating and Evaporating Diesel Fuel Sprays

case. The gas pressure is 16.6MPa. This pressure is beyond the limit of the modern engine. One probable reason accounting for the under-prediction is that the aerodynamic drag under the high pressure is over-predicted by the current drag model. Another interest finding from the Naber's cases is that coarse mesh presents a larger penetration depth for the Cases 2 and 3 after a certain moment. This is related to the aforementioned development of large scale vertical structures. The fuel jet tends to be more stable for the cases with high injection velocity (for the Naber's case, the velocity is as high as 480m/s) and gas density. The large scale vortices cause the front of the spray jet to flap. This flapping will defer the spray front from going further. As the coarse mesh cannot correctly capture the large scale structure, the front goes faster after a certain moment. In general, the grid-convergent prediction for the tip which could not be achieved by KIVA-3V, has been obtained in the current study.

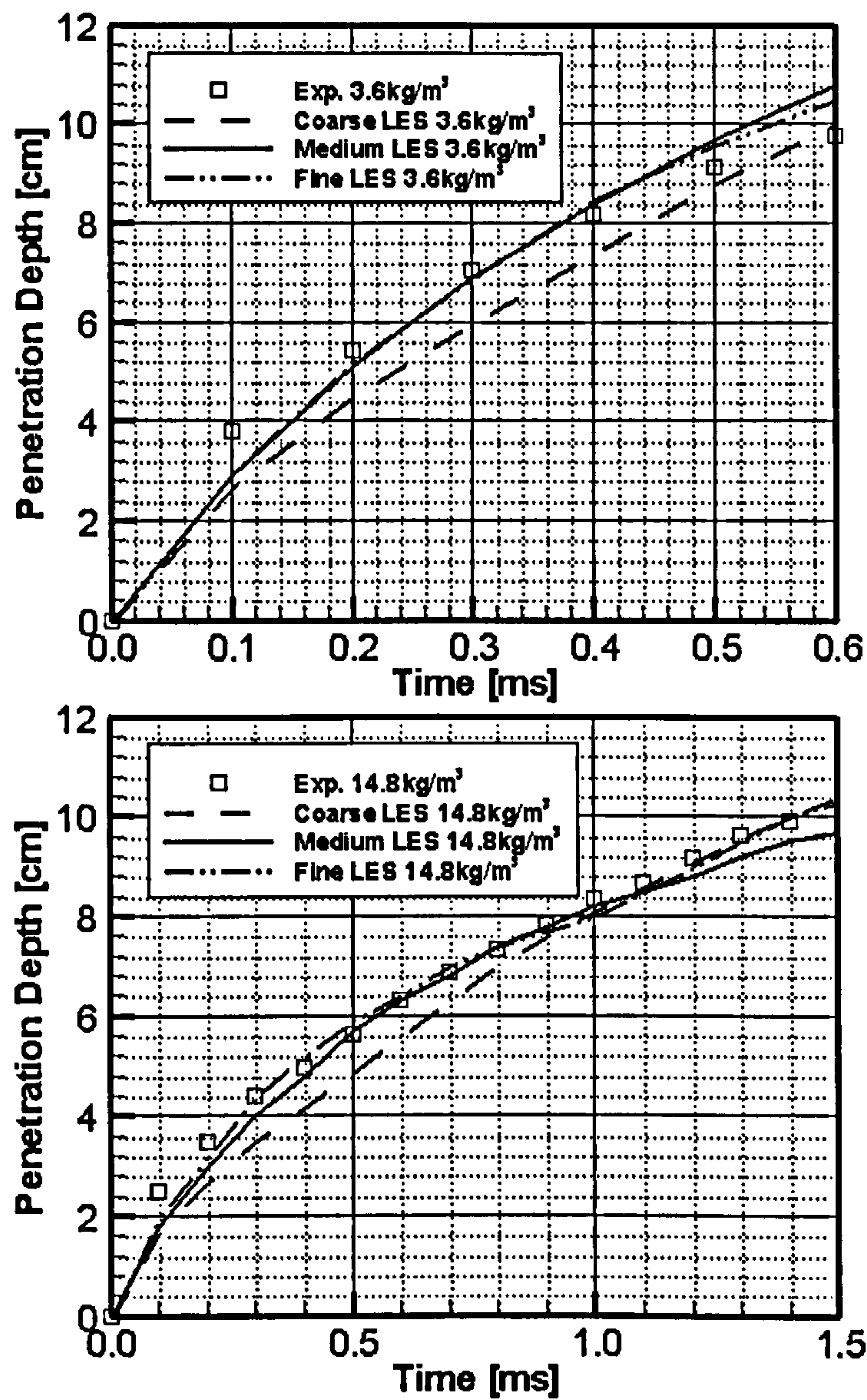


Fig. 6.7 Comparison of the predicted and measured spray tip penetration for the non-evaporating cases of Naber and Siebers [55]. (To be continued)

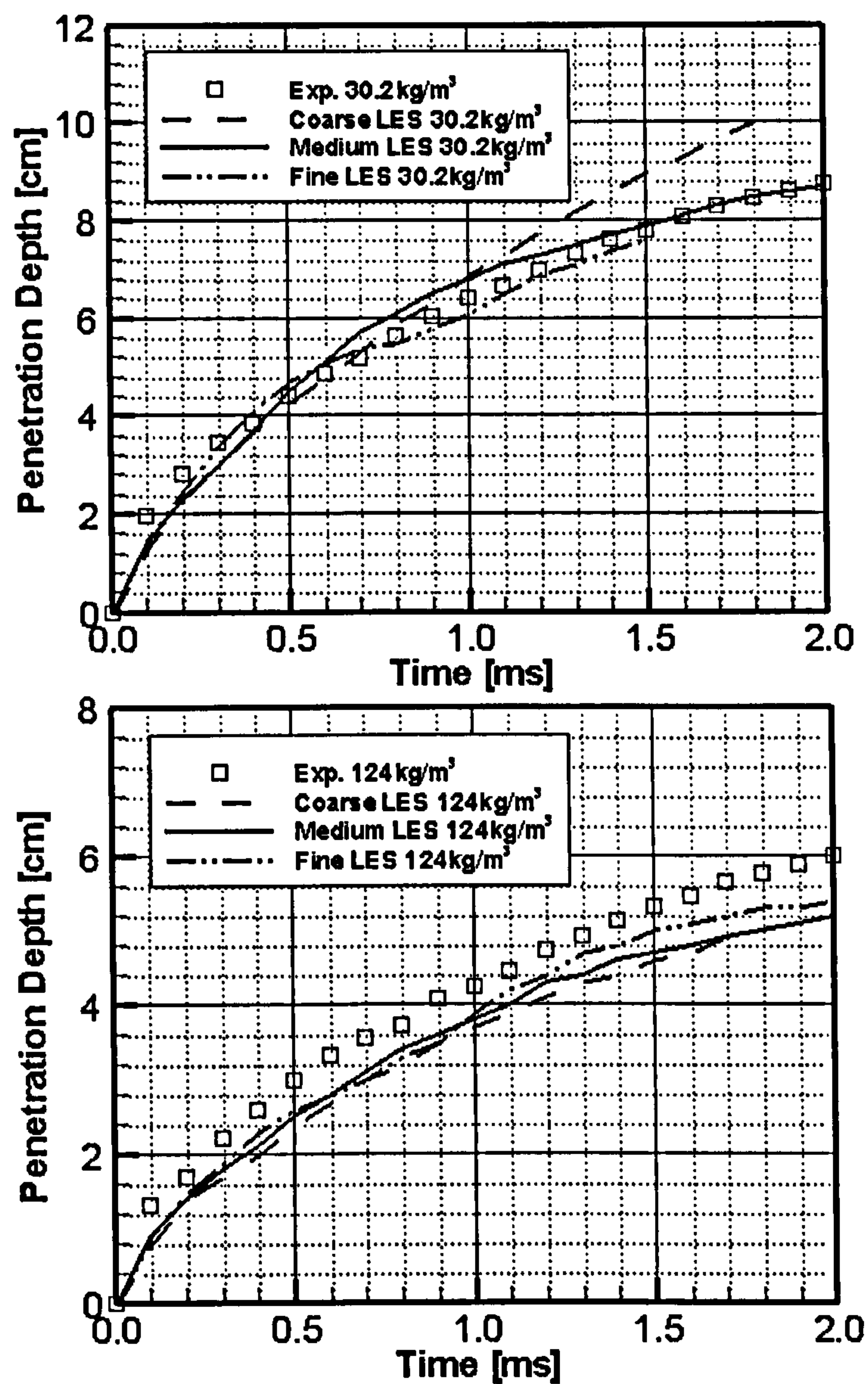
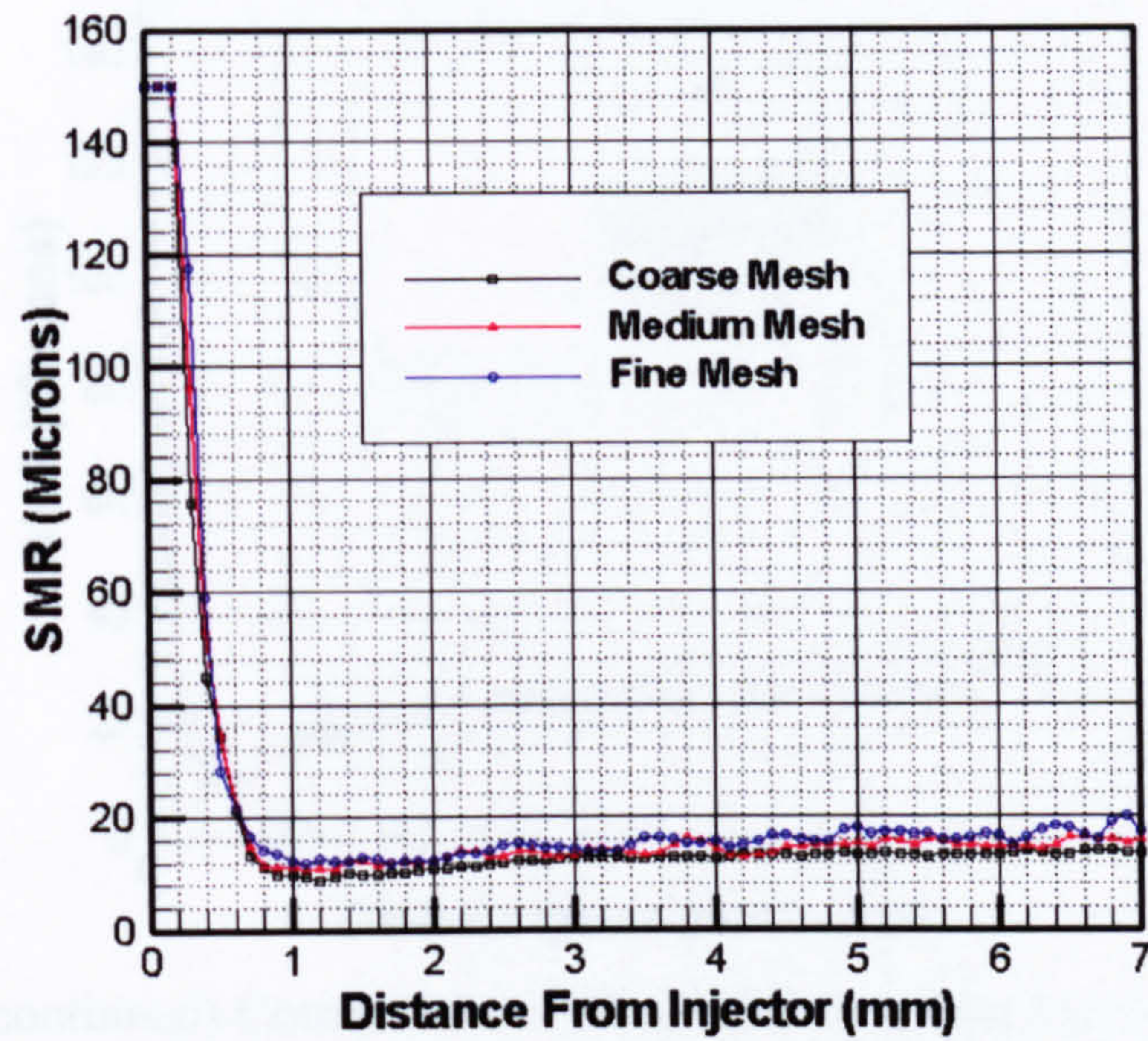


Fig. 6.7 (continued) Comparison of the predicted and measured spray tip penetration for the non-evaporating cases of Naber and Siebers [55].

6.3.3 The Predicted SMR

(Case1)



(Case2)

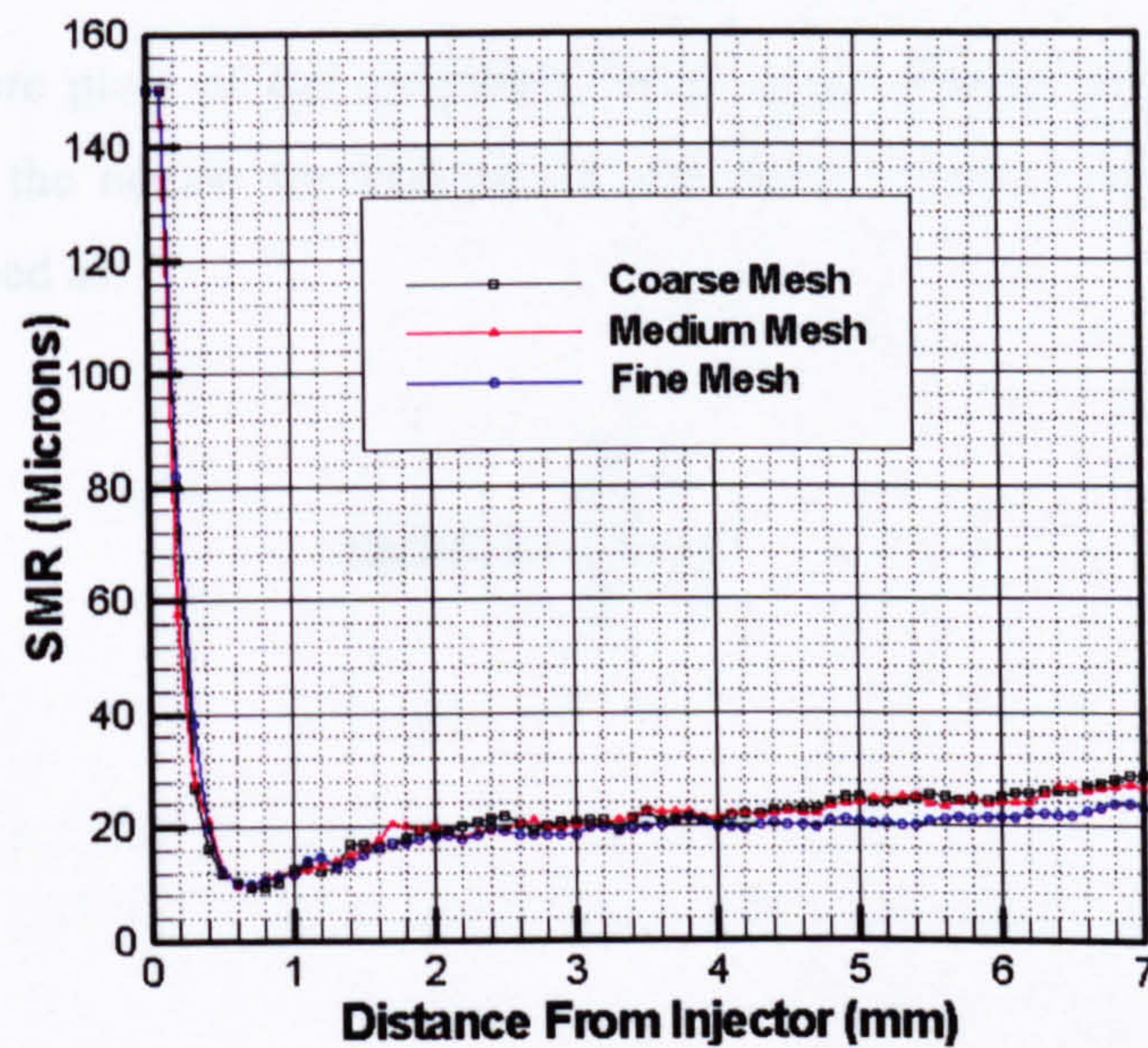


Fig. 6.8 Comparison of the predicted and measured spray tip penetration for the cases of Hiroyasu and Kadota [55]. (To be continued)

(Case3)

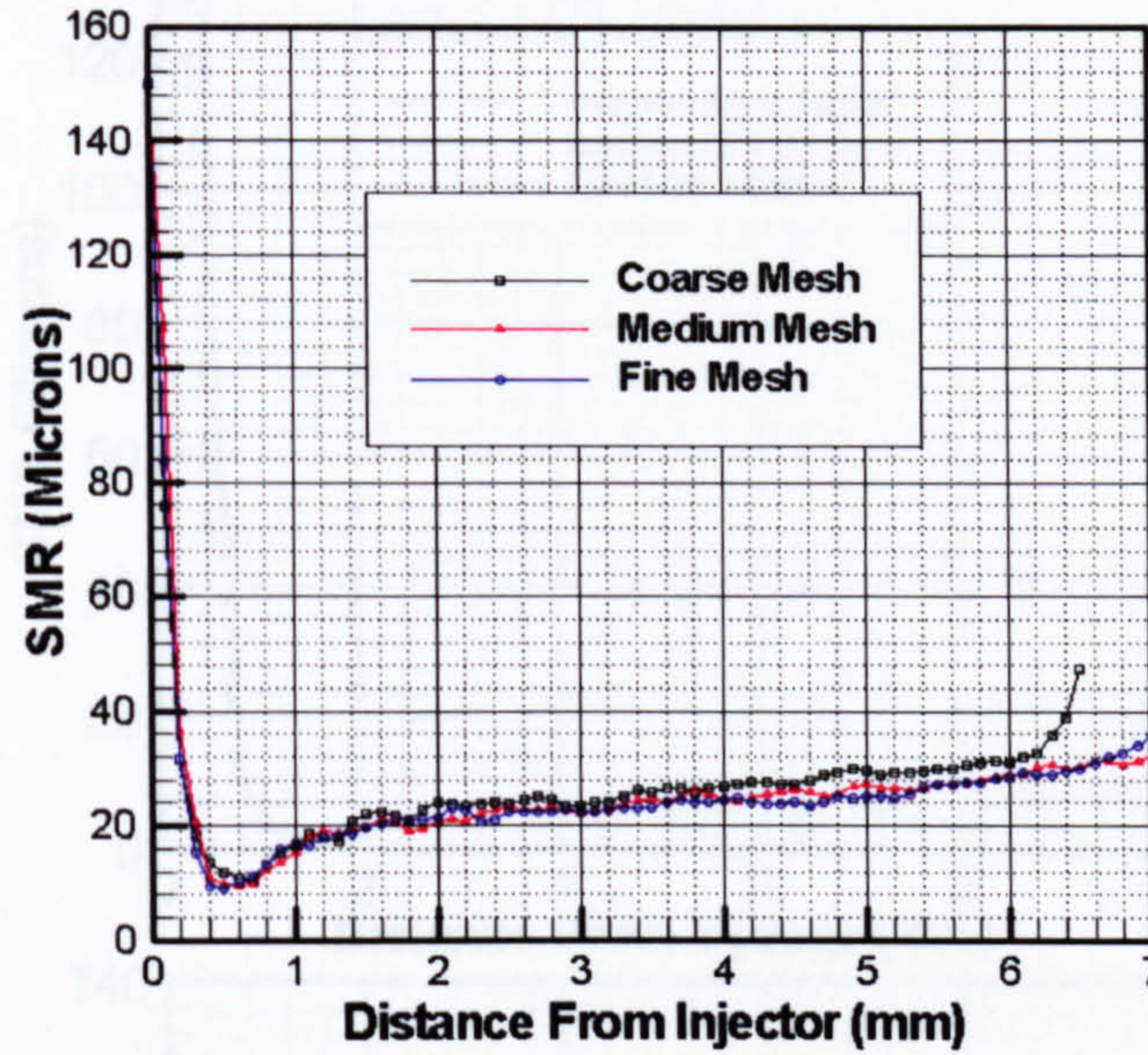


Fig. 6.8 (continued) Comparison of the predicted and measured spray tip penetration for the cases of Hiroyasu and Kadota [55].

Figs. 6.8-6.9 are plots of the computed Sauter Mean Radius (SMR) versus the distance from the nozzle for Hiroyasu's and Naber's cases. The Sauter Mean Radius is defined as:

$$SMR(z) = \frac{\sum_{r_i \in D} r_i^3}{\sum_{r_i \in D} r_i^2}, \quad (6.1)$$

Fig. 6.9 Comparison of the predicted and measured spray tip penetration for the non-evaporating cases of Kadota and Naber's spray cases [55].

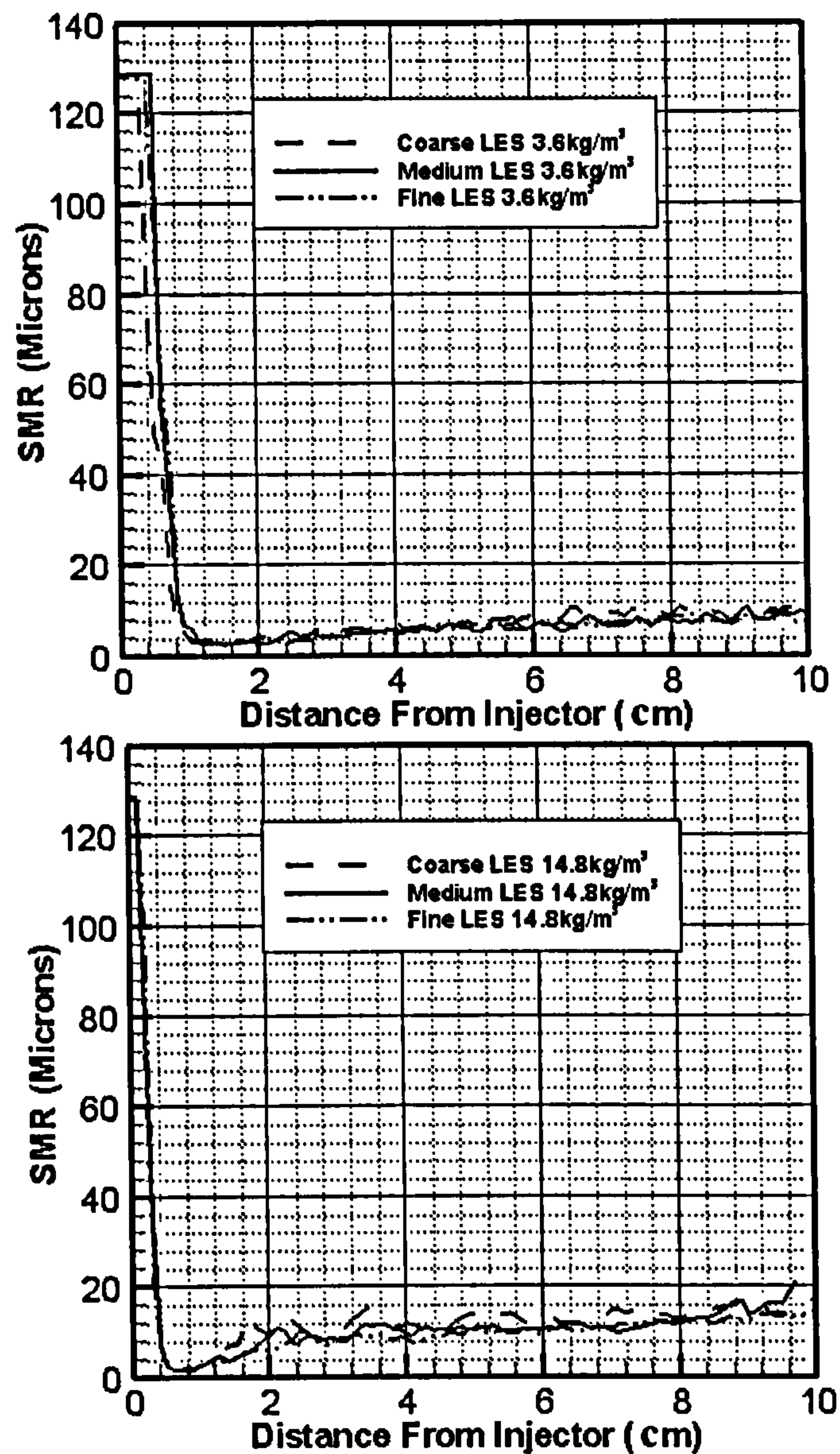


Fig. 6.9 Comparison of the predicted and measured spray tip penetration for the non-evaporating cases of Naber and Siebers [55]. (To be continued)

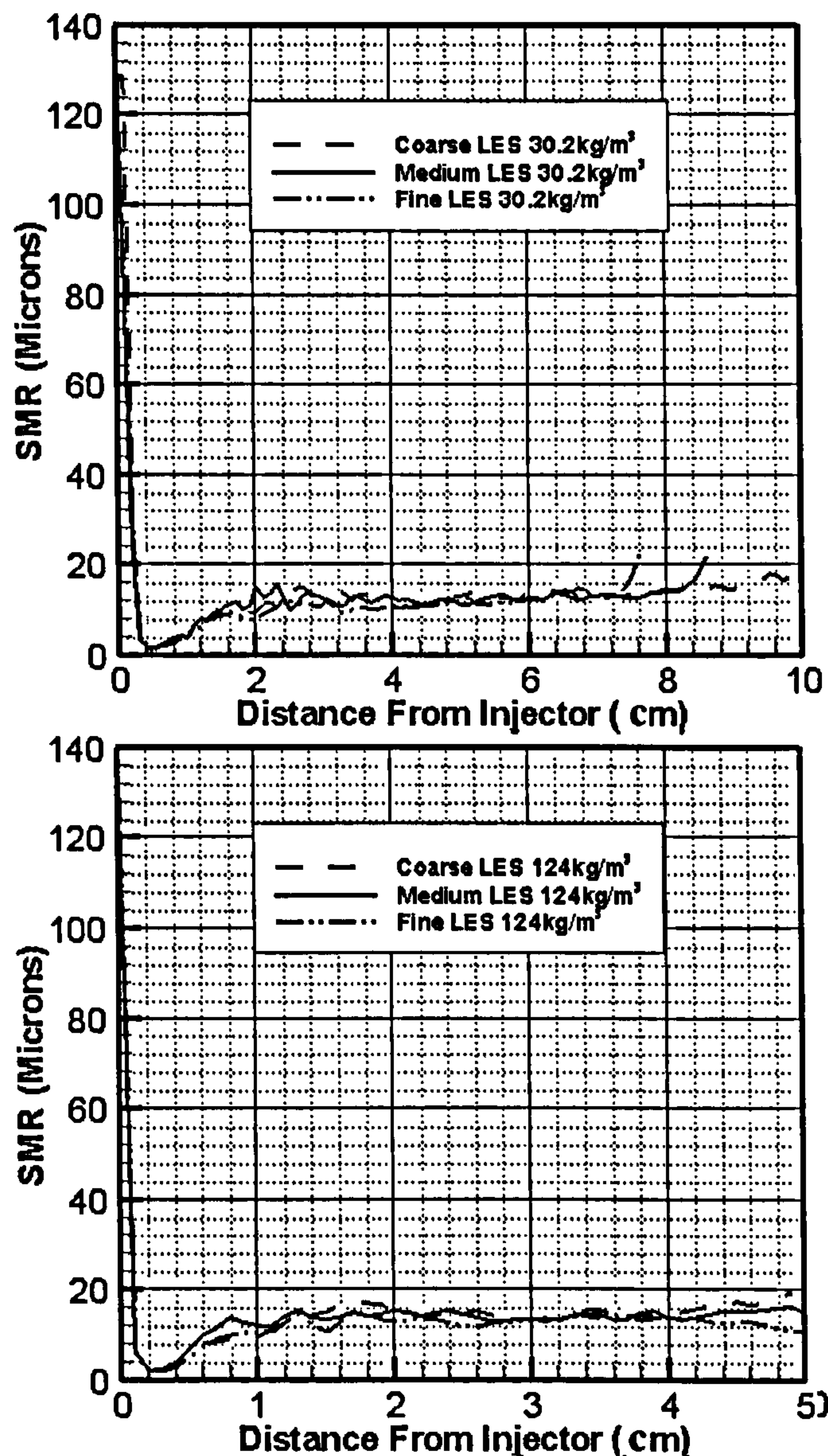


Fig. 6.9 (continued) Comparison of the predicted and measured spray tip penetration for the non-evaporating cases of Naber and Siebers [55].

where $D(z) = \{(x, y, \zeta) | z - \Delta z \leq \zeta \leq z + \Delta z\}$, $\Delta z = 1mm$. Only one measured result (at the position $z = 6.5cm$) is available for each of Hiroyasu's cases. They were respectively 21 microns, 24 microns and 29 microns [55]. The computed SMR curves show little grid dependence in all the cases. For the Hiroyasu's cases, the predicted values agree well with the experimental data at $z = 6.5cm$, except a little bit under-prediction for CASE 1. This may be caused by the ETAB break-up

model, which produces too small droplets. The comparison of the predictions of Hiroyasu's and Naber's cases shows that high injection velocity can produce finer spray droplets.

In Figs. 6.8-6.9 where the Sauter mean radius versus distance from the nozzle exit is plotted, the atomization, dense and dilute regions can be clearly distinguished. Droplet break-up is dominant in the atomization region where the SMR reduces sharply to a very low level. After the SMR reaches the minimum at the end of the atomization region, it starts to increase again in the dense region, where the droplet collision frequency is very high and collision/coalescence plays a more important role. Subsequently in the dilute region, where the droplet collision frequency is relatively low, the increase of SMR slows down. These results show that KIVA-LES with the new model is capable of distinguishing between the dense and the dilute regions while the original collision model in KIVA-3V failed to capture such differences as will be given in the next section.

6.3.4 The predicted results by KIVA-3V with O'Rourke's model

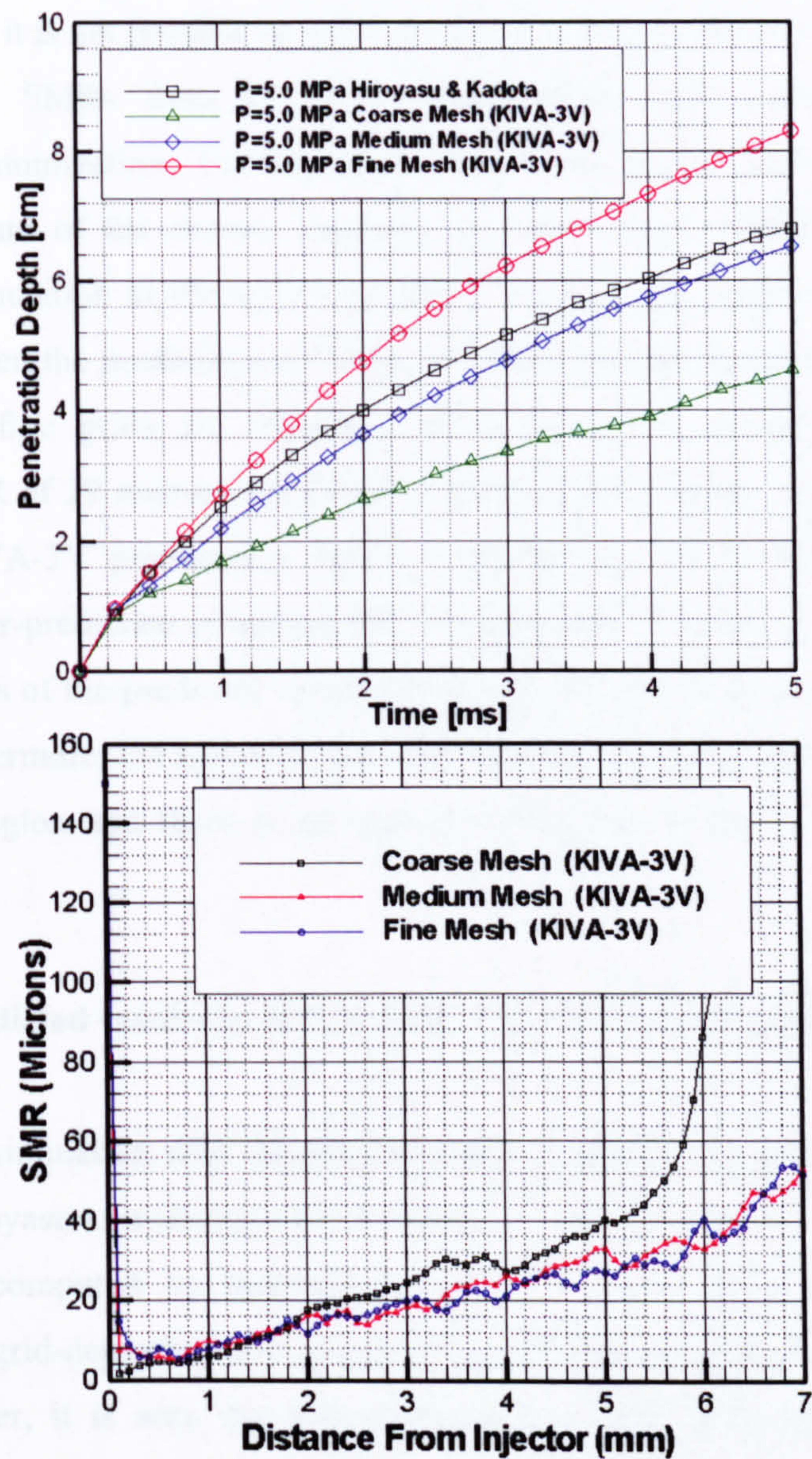


Fig. 6.10 The computed (KIVA-3V) and measured spray tip penetration for Case 3 of Hiroyasu and Kadota [55]

For comparison, the predictions using the original KIVA-3V with O'Rourke's collision model for Case 3 of Hiroyasu are shown in Fig. 6.10. It is seen that the predictions are very sensitive to grid density. The penetration length was over-predicted by the fine mesh while it was under-predicted by the coarse mesh. The

predictions of the medium size grid seem to be the closest to the data. However, the fact that the predictions continued to change with the change of grid density has shown that it is not possible to achieve grid-convergent results with the model. The predicted SMRs from all three computational grids increase steadily following the atomization. For the coarse mesh, there is even a sharp increase in SMR at the end of the curves, implying that the model predicted unrealistic droplets accumulation at the tip of the spray. Furthermore, there are significant changes between the predictions of different grids although the predictions of the medium and fine grids are relatively close. Moreover, comparing with the measured SMR of 29 microns for CASE 3 at $z=6.5\text{cm}$ [55], the original collision model in KIVA-3V predicted a value of 48 microns. It is thought that this significant over-prediction of around 60% by O'Rourke's model is mainly caused by the artefacts of the predicted spray, which artificially increases droplet density in cells. Furthermore, the increase rate of SMR remains almost constant after the atomization region and there is no apparent difference between the dense and dilute regions.

6.3.5 The predicted results by KIVA-LES with O'Rourke's model

A large eddy simulation with the original collision model was also conducted for Case 3 of Hiroyasu to investigate the influence of the LES solver on the computed results. The computed tip penetrations and SMRs are shown in Figs. 6.11. Although the grid-dependence of the predictions can be significantly alleviated by the LES solver, it is seen that the predictions are still quite sensitive to grid resolutions. Since the original collision model in KIVA-3V over-predicts the droplet size, the predicted tip penetration is greater than that of the experimental data. Moreover, it still cannot capture the differences between the dense and dilute regions even after being combined with the LES solver.

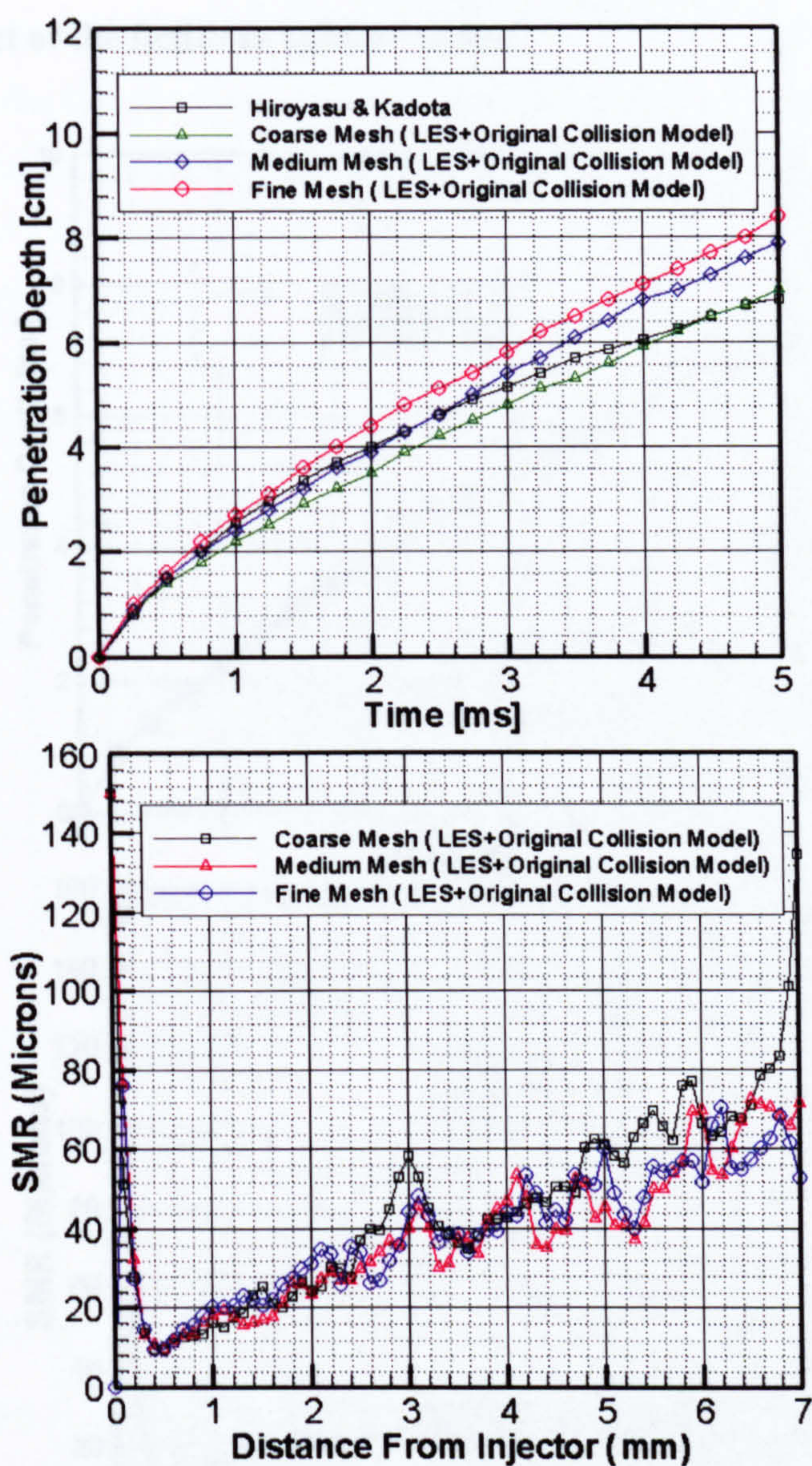


Fig. 6.11 LES predictions with the O'Rourke model for Case 3 of Hiroyasu and Kadota [55]

6.3.6 The effect of the fictitious sphere volume

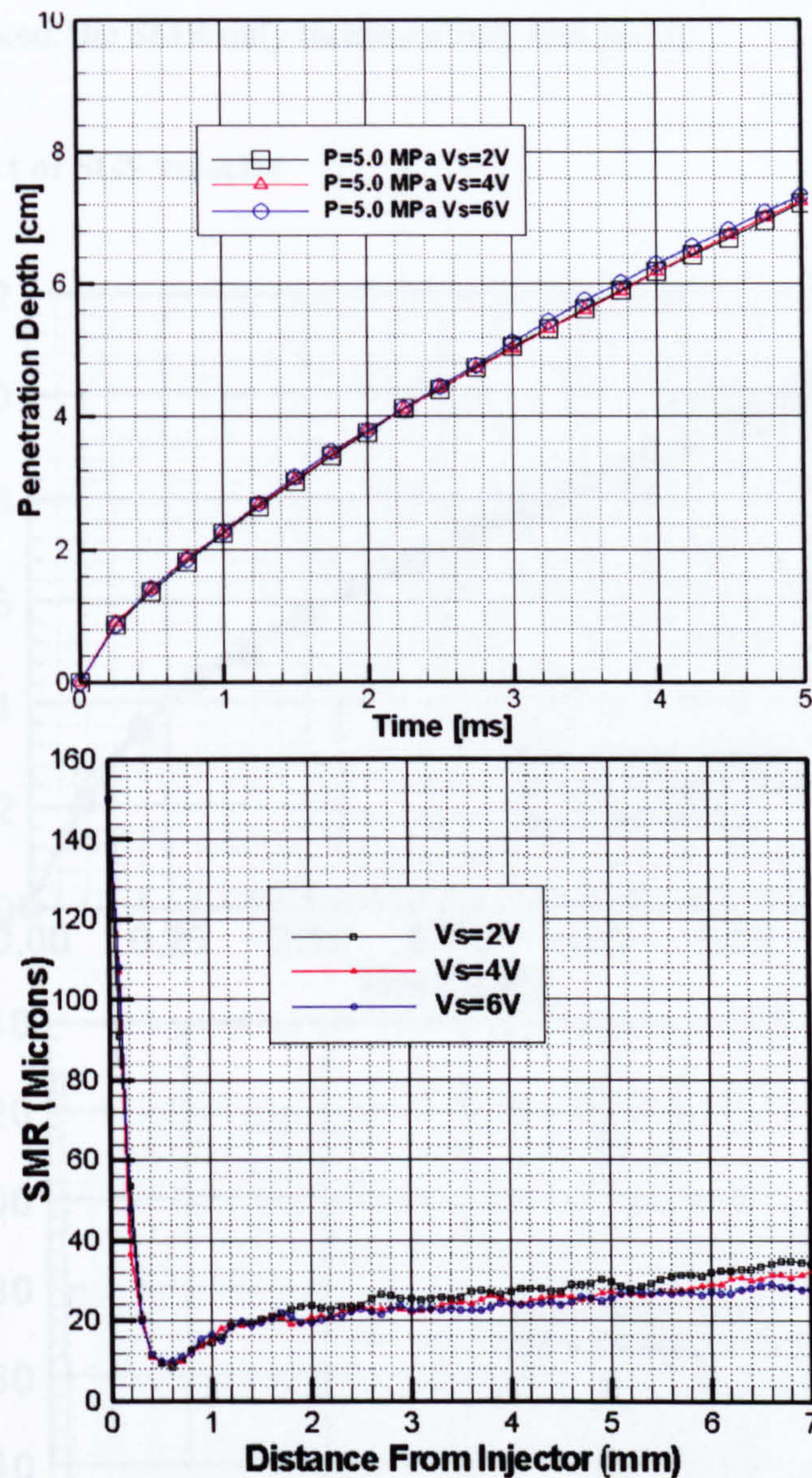


Fig. 6.12 The computed spray tip penetrations and SMRs in terms of different volumes of the fictitious parcel cloud for Case 3 of Hiroyasu and Kadota [55].

The fictitious sphere volume (or radius) of a parcel affects the collision frequency. The simulations for Case 3 of Hiroyasu and Kadota with three different fictitious sphere volumes (2V, 4V, 6V, and V is defined in 2.6.4) are carried out to investigate the effect of the sphere volume on the predictions. The computed

results are presented in Fig. 6.12. The tip penetration and predicted SMR show insensitivity to the sphere volumes as expected in analysis of section 2.6.4. As the volume is reduced, the SMR only increases very marginally.

6.3.7 The effect of SGS velocity

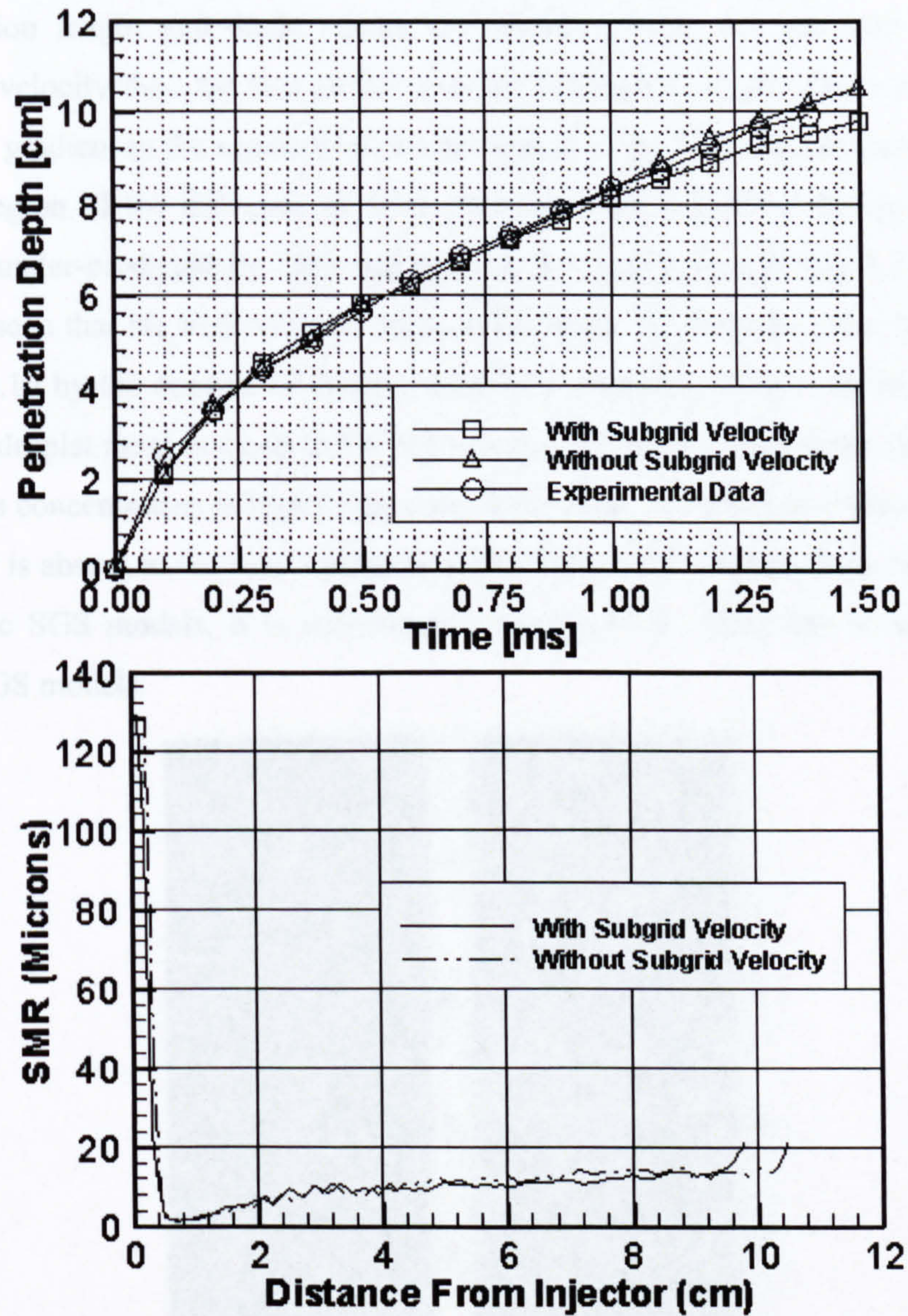


Fig. 6.13 The computed spray tip penetrations and SMR in terms of with and without SGS velocity for Case 3 of Naber and Siebers [81]

The influence of subgrid velocity on the results is shown in Figs. 6.13 where the results with and without subgrid velocity are compared for Case 3 of Naber and Siebers [81]. For this test case, a finer mesh ($61 \times 61 \times 130$) is used to reduce the error of the SGS model. The results show that the subgrid velocity contributes little to the tip penetration and the SMR in the current simulation of the fuel jet. However, since the subgrid velocity disperses more uniform. The computed penetration length and SMR values are slightly greater for the case without subgrid velocity than for that of the case with subgrid velocity. There is a great velocity gradient in the region close to the injector. The SGS velocity is also high in the region. If the influence of SGS velocity is not modelled, the spray angle will be under-predicted by 28% and this can be clearly seen in Fig 6.14. It can also be seen that the SGS velocity helps to distribute the droplets more uniformly in Fig 6.15 by the contour of droplet mass concentration which is defined as the ratio of droplet mass in a cell to the cell volume. It is also visible in the figure that the mass concentration is high in the core of the spray. As the information of SGS velocity is absent in the most common used SGS models such as Smagrinisky and Dynamic SGS models, it is inconvenient to take SGS effect into account with these SGS models.

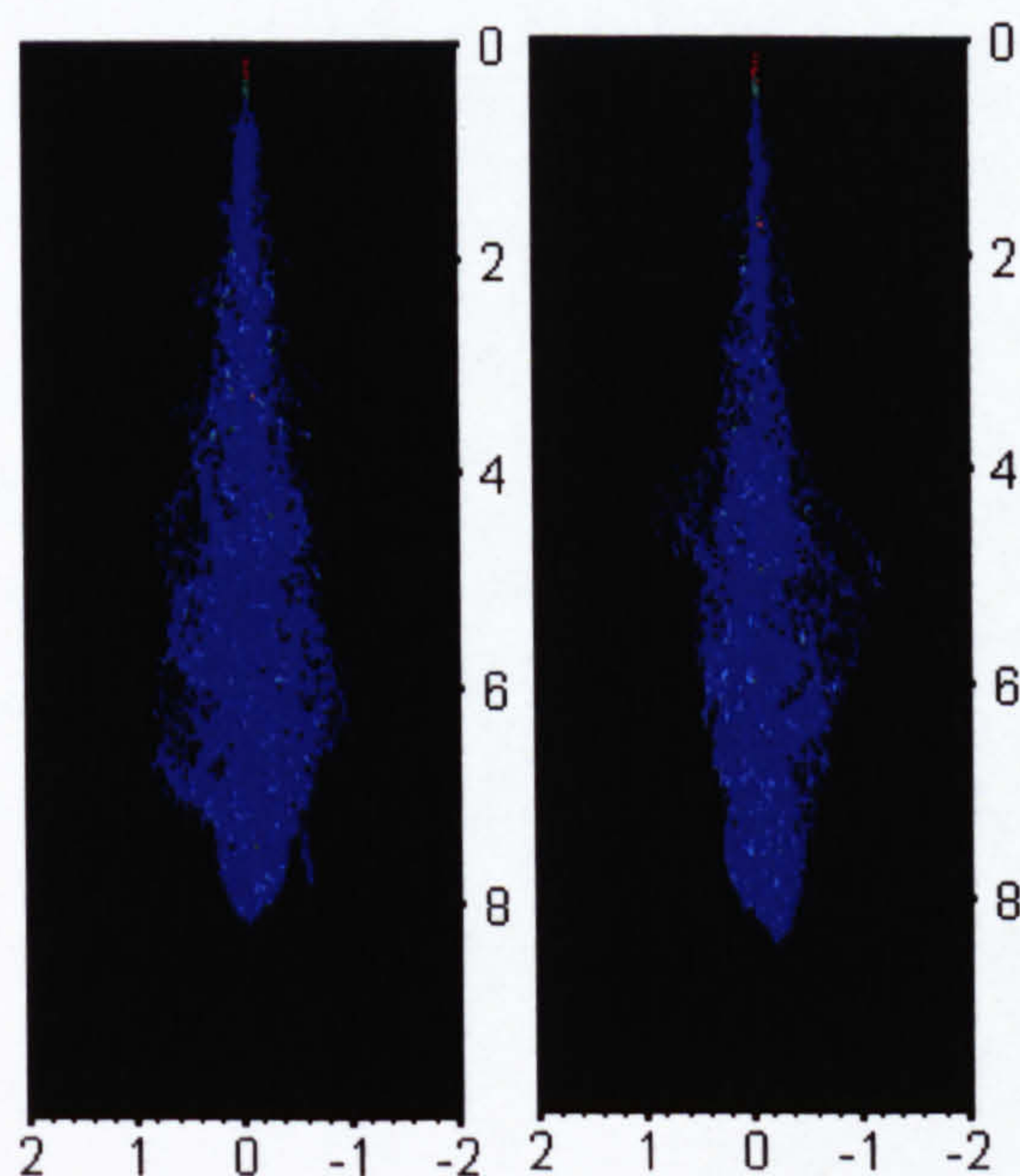


Fig. 6.14 Front view of the predicted spray with and without SGS velocity for Naber's non-evaporating Case 3 at $t=1.0$ ms

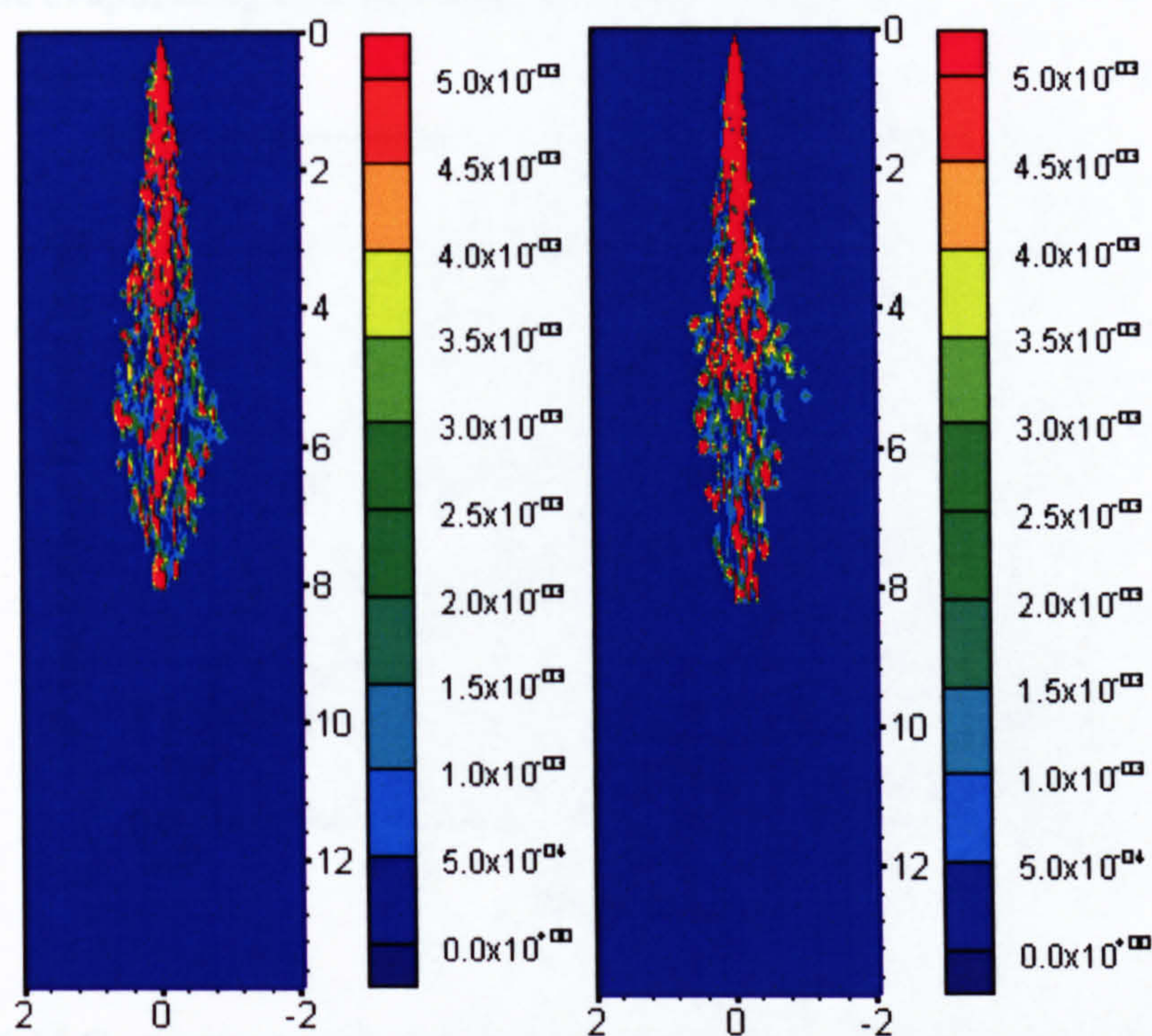


Fig. 6.15 Contour of the droplet mass concentration in g/cm^3 for Naber's non-evaporating Case 3 with (left) and without (right) SGS velocity at $t=1.0$ ms

4.3.8 The evaporating case of Naber and Siebers [81]

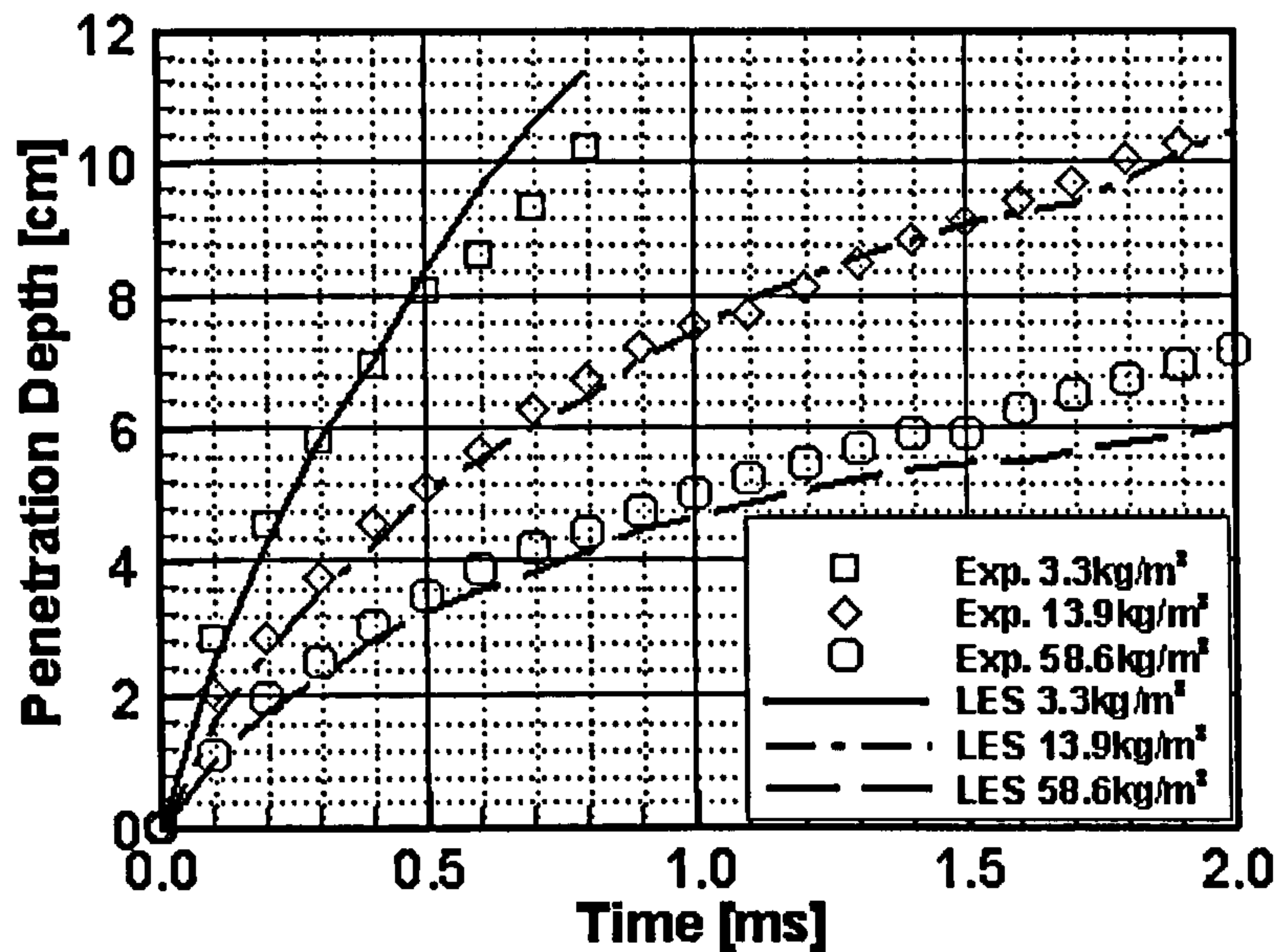


Fig. 6.16 Comparison of the predicted and measured spray tip penetration for evaporating cases of Naber and Siebers [81]

The predicted spray tip penetration for the evaporating test cases of Naber and Siebers is shown in Fig. 6.16. The predicted results agree reasonably well with the experimental data although the predicted penetration depth is a little bit over-predicted for the low gas density case and slightly under-predicted for the high gas density case. Grid sensitivity study of the evaporating cases is only conducted for Case 1 of Naber and Siebers and the results are shown in Fig. 6.17. The predictions show that the medium and fine meshes produce very similar results. The resolution of the fine mesh is therefore considered as sufficient to provide grid-convergent result. The good agreement with the data shows that the evaporating model works fine with KIVA-LES.

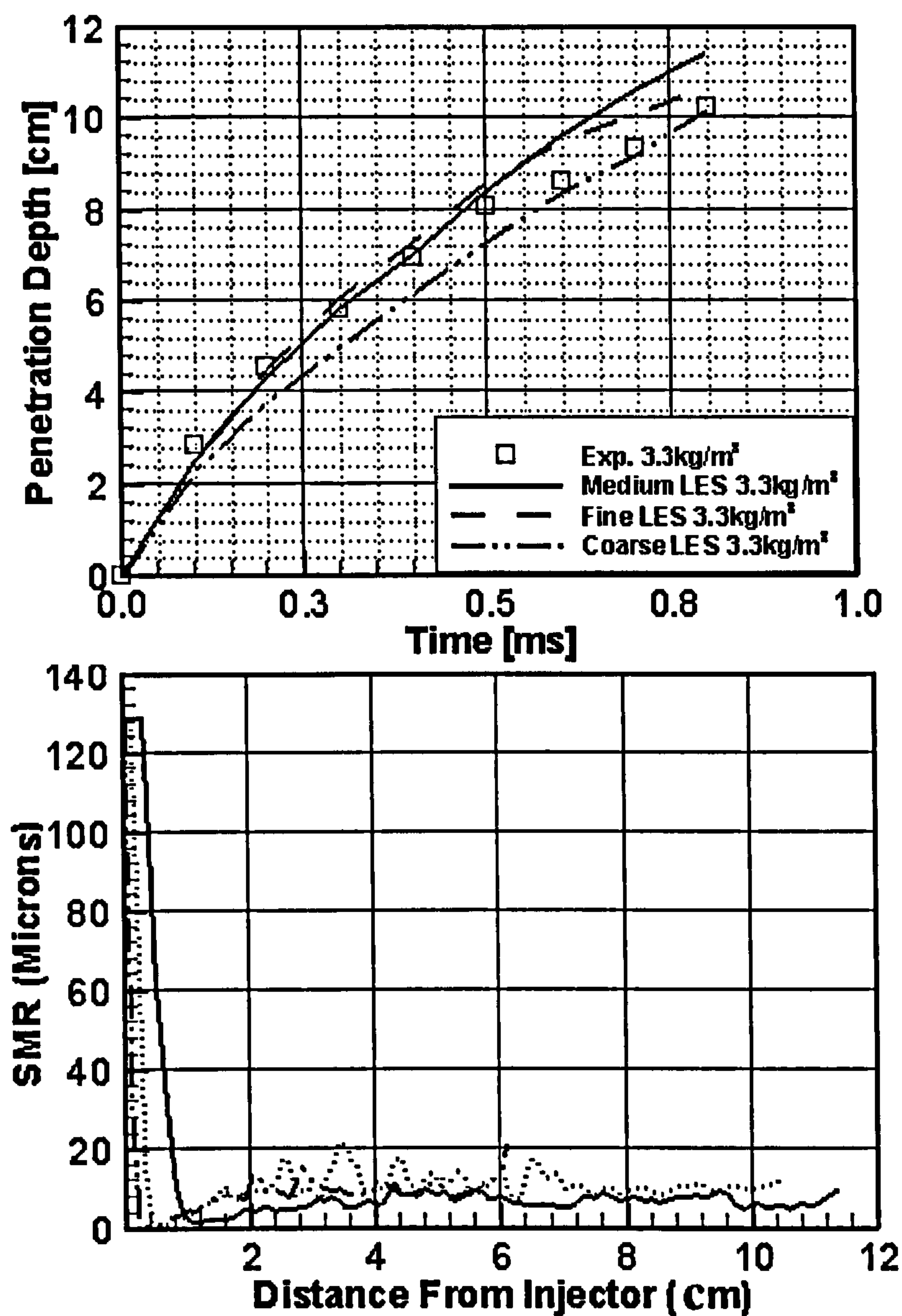


Fig. 6.17 Grid sensitivity study for evaporating Case 1 of Naber and Siebers [81]

6.4 Summary

KIVA-LES has been validated against published experimental data for non-evaporating and evaporating diesel fuel sprays under varied gas densities. The new collision model is less grid-independent, accurate, and insensitive to the chosen fictitious sphere volume. It offers considerable advantages over the original collision model in KIVA-LES.

The predictions are in good agreement with the experimental data. The large scale vortical structures are reproduced by the LES simulations. These structures cause “branch-like” spray shape and influence the spray penetration depth. The predictions have also captured the differences between the dense and dilute regions. The LES of diesel spray also proves that the SGS velocity has a significant influence on the predicted spray angle. Without the SGS velocity, the spray angle will be under-predicted. Grid-convergent results, which were difficult to obtain with the original KIVA-3V, have been obtained in the current simulations. This is thought to be due to a combination of the LES solver and the new collision model.

Chapter 7

LES of a Coaxial Gas Turbine Model Combustor

7.1 Introduction

The importance of fuel/air unmixedness in combustion performance has been experimentally demonstrated for liquid-fueled direct and prevaporised systems as well as for gaseous-fueled premixed systems [47,120]. Fric [39] also experimentally found that it is not sufficient to consider only spatial non-uniformities in fuel mixture, temporal unmixedness or concentration fluctuations also contribute significantly to higher NO_x emissions. In addition to fuel distribution, droplet size and velocity both play critical roles in the combustion processes. The nature of the aerodynamic flow is also of importance. For example, the size and extent of the recirculation zone can result in various residence times that may play as much a role as fuel distribution in combustion performance.

Both numerical modelling and optic diagnostics have been widely used in the study of the actual combustion processes in gas turbines. While optical diagnostics has been frequently used with success in the study of fuel injection and mixture formation [38,52,79,141], much less has been carried out using complimentary numerical modelling techniques to characterize the actual fuel distribution prior to combustion [1,23,96,101]. The limited modelling work found in the literature also suffers from the use of steady state boundary conditions while the actual fuel injection and the subsequent mixing processes are intrinsically fully transient. Apart from Caraeni et al. [20], most previous studies were based on RANS based CFD. On the other hand, the aforementioned recirculating nature of the mixture flow has in fact rendered the traditional

Reynolds Averaged Navier-Stokes (RANS) CFD techniques to be unsuitable. LES techniques, being intermediate between DNS and RANS based CFD, are ideally placed to capture the complex transient flows categorized by non-stationary vortices. The LES technique has been convincingly shown to be superior to RANS in accurately predicting turbulent mixing and combustion dynamics [70] in simpler combustor geometries. In LES, all turbulent length-scales larger than a specified cut-off are resolved in both space and time while modelling is employed for those small, unresolved scales (referred to as subgrid scale or SGS). Larger eddies, those on the order of the geometric length-scale, are highly-anisotropic and energetic and their dynamics is strongly dependent on the geometry of the system. Small eddies are more isotropic and less energetic, and easy to be modelled.

In order to simulate these critical processes prior to combustion, the numerical model will need to correctly predict the evaporating fuel spray - the size and quantity of the droplets, droplet dispersion in the mixture, droplet evaporation characteristics and the non-linear interactions of these different physical processes. The work of Caraeni et al. [20] has brought important advance in LES applications to fuel air mixing. But it has involved simplified assumptions on the temperature field and suffers from the lack of validation. Their attempt to combine the simulation of fuel flow in the swirlers, the injection nozzle and the combustion chamber also makes it difficult to judge the accuracy of the individual components of the model.

Sommerfeld et al. [113] conducted experimental studies of spray evaporation in a coaxial gas turbine model combustor. The flow configuration was a pipe expansion with an expansion ratio of three, where heated air entered through an annulus with a hollow cone spray nozzle being mounted in the centre. In the experiments isopropyl-alcohol was used as a liquid due to its high evaporation rates. Phase-Doppler anemometry (PDA) was applied to obtain the spatial change of the droplet size spectrum in the flow field and to measure droplet size-velocity

Chapter 7 LES of a Coaxial Gas Turbine Model Combustor

correlations. From these local measurements of droplet mean velocities, velocity fluctuations and droplet mean diameters were obtained by averaging over all size classes. The droplet mass flux and the global evaporation rate were also measured in their study.

In this chapter, LES approach is used to simulate spray evaporation in the coaxial gas turbine model combustor. The predictions are compared with Sommerfeld's experimental data. This study is a first step towards a more comprehensive numerical analysis of practical industrial combustors where multiple inlets and more complex combustor geometry are encountered.

7.2 Problem description

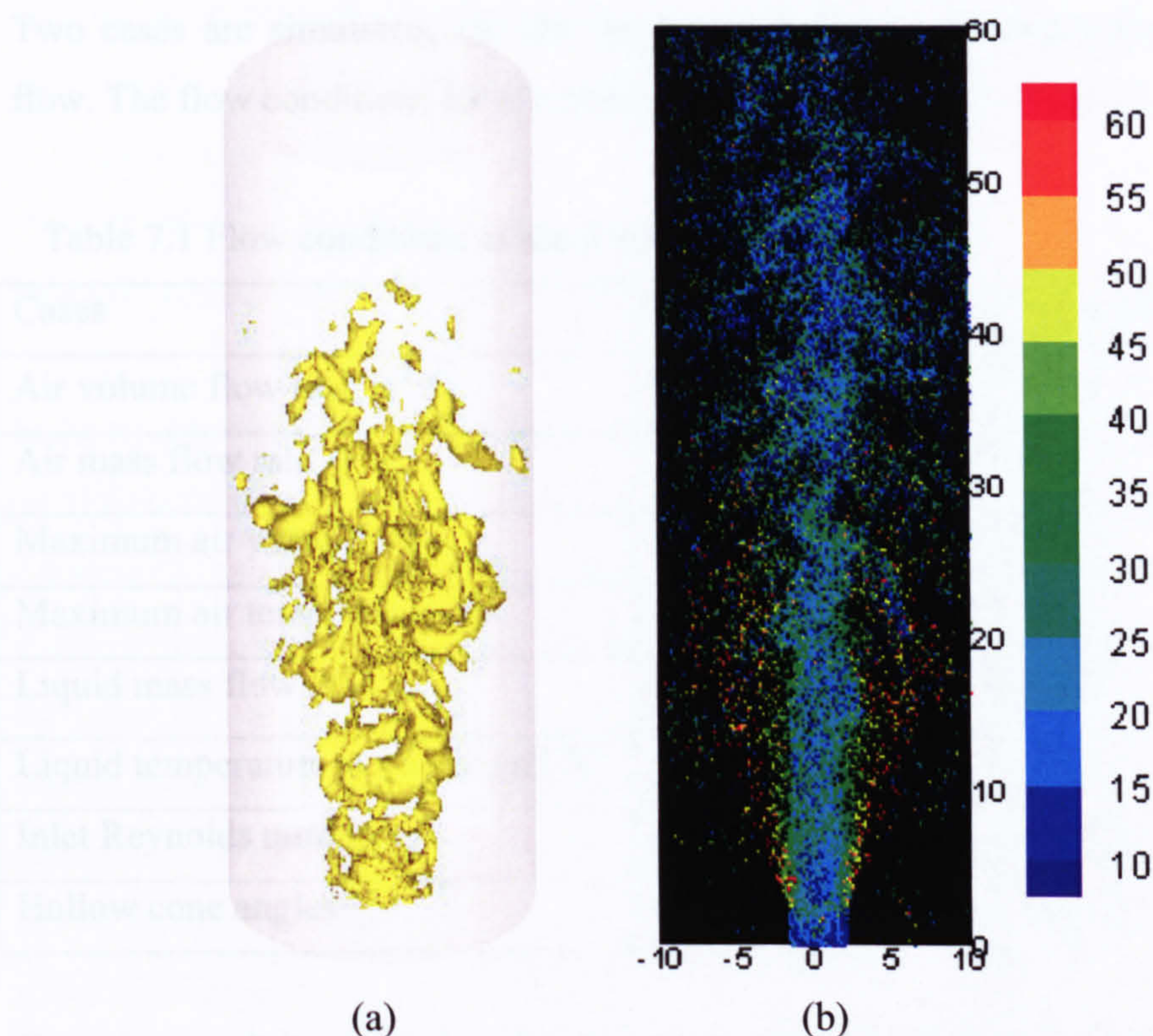


Fig. 7.1 Computational geometry overlapped by a snapshot of iso-surface of pressure fluctuation (a) and coloured spray particle distribution according to droplet sizes (b).

In Sommerfeld's experiment, the heated air was blown from an annular injection tube into the test section which had an inner diameter of 200 mm and a length of 1.5m. With a 64 mm outer diameter and a 40 mm inner diameter of the annulus, an expansion ratio of about 3 was established. A hollow-cone pressure atomizer was mounted in the cylindrical centre-body of the inlet tube. Isopropyl-alcohol was used as a spray liquid, and the thermodynamic properties of isopropyl vapor and liquid is taken from [127] and implemented into the KIVA-LES. Fig.7.1 shows the computational geometry. The computational domain is a cylinder with a length of 0.6m. The available experimental data for comparison is up to 0.4m. Simulations with different length were carried out to investigate its influence. The results showed that the length of 0.6m was sufficient to minimize the influence of the downstream outflow boundary on the predictions. The Reynolds number

R_e based on the outer diameter of the annulus and the bulk velocity is 46,000. Two cases are simulated, i.e. the single phase flow and evaporating two-phase flow. The flow conditions for the computed cases are listed in Table 7.1.

Table 7.1 Flow conditions of the computed cases

Cases	Single phase flow	Two phase flow
Air volume flow rate m^3 / s	0.032	0.031
Air mass flow rate g / s	29.0	28.3
Maximum air velocity m / s	18.0	18.0
Maximum air temperature $^{\circ}C$	100	100
Liquid mass flow rate g / s	-	0.44
Liquid temperature at nozzle exit $^{\circ}C$	-	34
Inlet Reynolds number	46,000	46,000
Hollow cone angles $^{\circ}$	-	60 (15)

Cartesian mesh is adopted in the current simulations although cylindrical mesh is a natural choice for the cylindrical geometry. Attempts were made to use cylindrical meshes, but some preliminary calculations revealed that cylindrical meshes were not suitable for the current cases. It is thought that LES will suffer from two aspects by using a cylindrical mesh. One is the commutation errors due to its highly uneven grids around the axis. Another is the extremely small time steps constricted by the small grid size in the azimuthal direction around the axis. Since the predicted flow field of LES is highly unstable, the azimuthal velocity component is substantial. To ensure the numerical accuracy of simulations, a very small time step must be used. The computational mesh is clustered in the axial direction. To minimize the filter commutation errors arising from the uniform grids, the transition of grid size in the neighbouring grids is limited by less than 5%. In the current implementation of LES, the filter size is equal to the grid size. This results in more small scales being resolved with the increase of the grid resolution. In fact, LES will converge to DNS when all scales of motion are

resolved. To verify that the grid resolution is fine enough to resolve those eddies that are large enough to contain information about the geometry and dynamics of the specific problem under investigation, grid sensitivity is investigated by comparing a high resolution case ($100 \times 100 \times 100$) and a lower resolution case ($80 \times 80 \times 80$) for the single phase flow case. For the case of two phase flow, the fine grid resolution of $100 \times 100 \times 100$ is adopted.

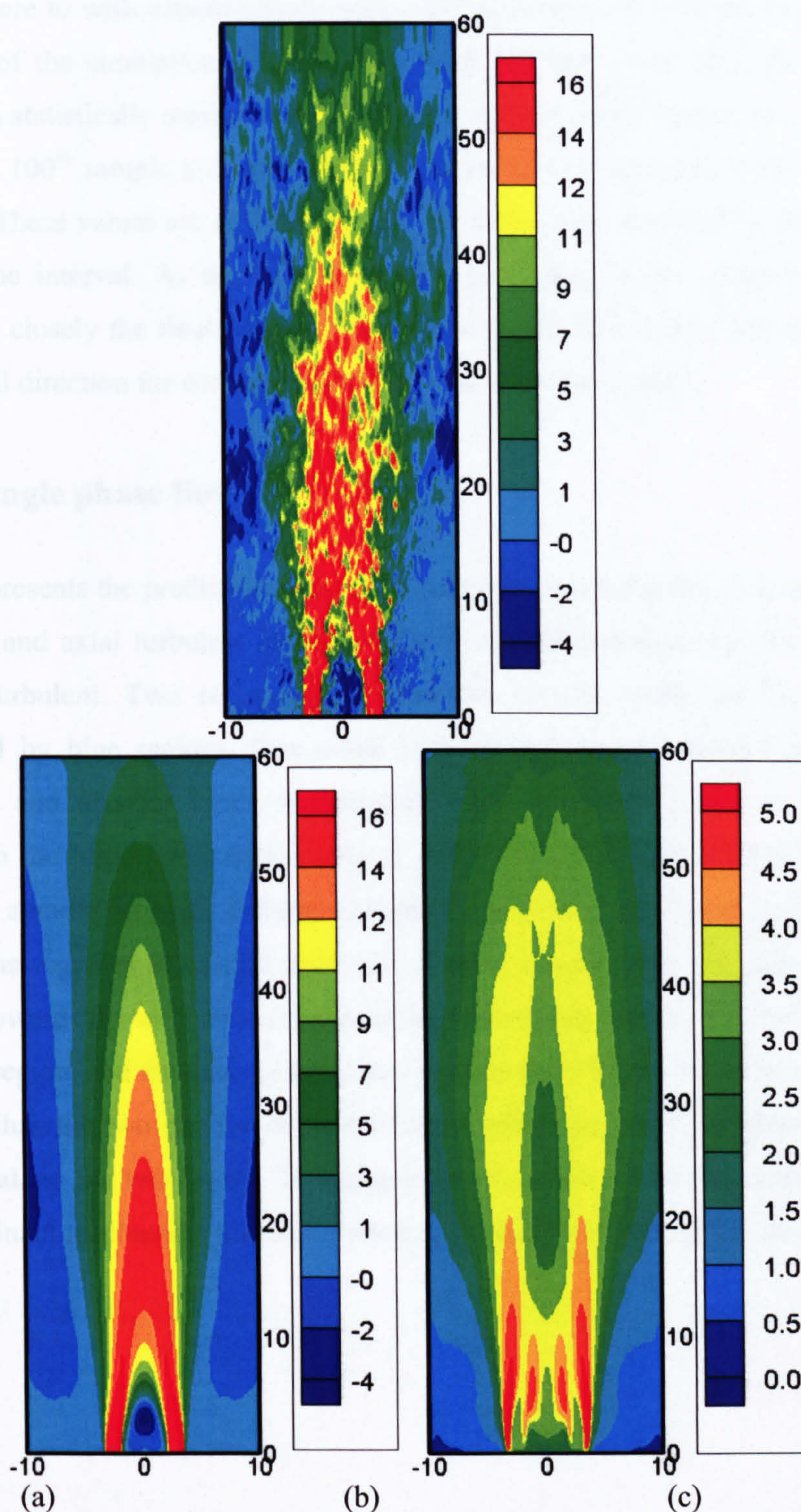
Inflow boundary condition is applied on the inlet annular plane. The specification of inflow boundary condition is an important factor for LES as discussed in Chapter 2. In the experiment, detailed inflow boundary conditions of gas and spray phases were measured. In this study, a random noise with the same turbulent intensity as the experimental data is imposed on the inflow boundary to mimic the turbulent inflow condition. Although some researchers tend to use a separate LES calculation to define the inflow boundary condition, Wang et al. [130] found that there was little difference between the two inflow boundary conditions except that the deterministic inflow boundary condition can predict a more physical energy spectrum. A continuative outflow boundary condition (zero gradient) is applied on the outlet plane. Wang et al. [130] concluded that there was little difference between the continuative outflow boundary condition and the frequently used convective outflow boundary condition in their LES of a confined turbulent swirling flow. No-slip wall condition is applied on the solid walls even though the walls are not resolved in the simulations. The wall boundary layer is weakly coupled with the core region flow. The predictions show that the wall boundary layer has little influence on the flow in the core region. Both the simulations start from still.

The inflow conditions for the spray phase are adjusted according to the experimental data of Sommerfeld [113]. The injected droplet size is sampled from the experimental discrete PDF (Probability Density Function). Firstly, the discrete cumulative distribution $h(r)$ is computed according to the discrete PDF. Then the

cumulative distribution is interpolated and stored in increments of $0.04r_{32}$ between $r = 0$ and $r = 4r_{32}$, r_{32} is the SMR. To determine the injected droplet size, a random number XX is needed to be selected. With the random number, value of n can be found in

$$h[0.04r_{32}(n-1)] \leq XX \leq h[0.04r_{32}n]. \quad (7.1)$$

Then the injected droplet radius is $r = 0.04r_{32}n$. Using a hollow spray cone angel of 60 (15) degree, a satisfactory representation of the experimental data is achieved. After being injected into the computational domain, each particle is traced in the simulation and subject to breakup. Two-way coupling is applied between the gas and spray phases, and the effect of SGS velocity is also included. The particle injection rate is taken as 15 millions per second. This yields around 1 million particles in the domain when the simulation reaches a statistically stable condition. In the conventional RANS simulation, the typical particle number is around 1,000-10,000. This is not sufficient for LES, since a large number of particles are needed to represent the dynamic disperse phase and ensure a sufficient particle number in a cell for the calculation of statistics. The effect of collision/coalescence is neglected in the current simulation since the spray is dilute except in the nozzle region.



187

To compare to with experimental results, the predictions are averaged during the running of the simulations by sampling every ten time steps after the solution reaches a statistically steady condition. The averaged values start to be calculated from the 100th sample and the turbulent variances are computed from the 200th sample. These values are calculated every sampling time step and monitored at a fixed time interval. As the sample number increases, the so computed values resemble closely the final results. The predictions are also space averaged in the azimuthal direction for comparison with the experimental results.

7.3.1 Single phase flow

Fig.7.2 presents the predicted contours of instantaneous axial velocity, mean axial velocity and axial turbulent intensity. The predicted instantaneous flow field is highly turbulent. Two recirculation zones are clearly visible in Fig. 7.2 (b) indicated by blue regions. One small recirculation zone is located inside the annulus, and another large recirculation zone is located close to the wall. Although the large recirculation zone is rather weak, it extends to almost $z=50$ cm. The annular jet tends to bend towards the axis after leaving the annulus and then joins together at around $z=10$ cm. Further downstream, the flow starts to spread towards the wall due to the momentum exchange with the core region. The outside region, and the axial velocity also decays accordingly. When the jet leaves the annulus, the two circular boundary layers induce two high turbulent intensity regions along the two layers. The generation of turbulence in the shear layers is the dominant mechanism for the turbulence production in the present simulation.

Fig. 7.3 Comparison of the predicted and experimental results for the axial velocity, mean axial velocity and axial turbulent intensity.

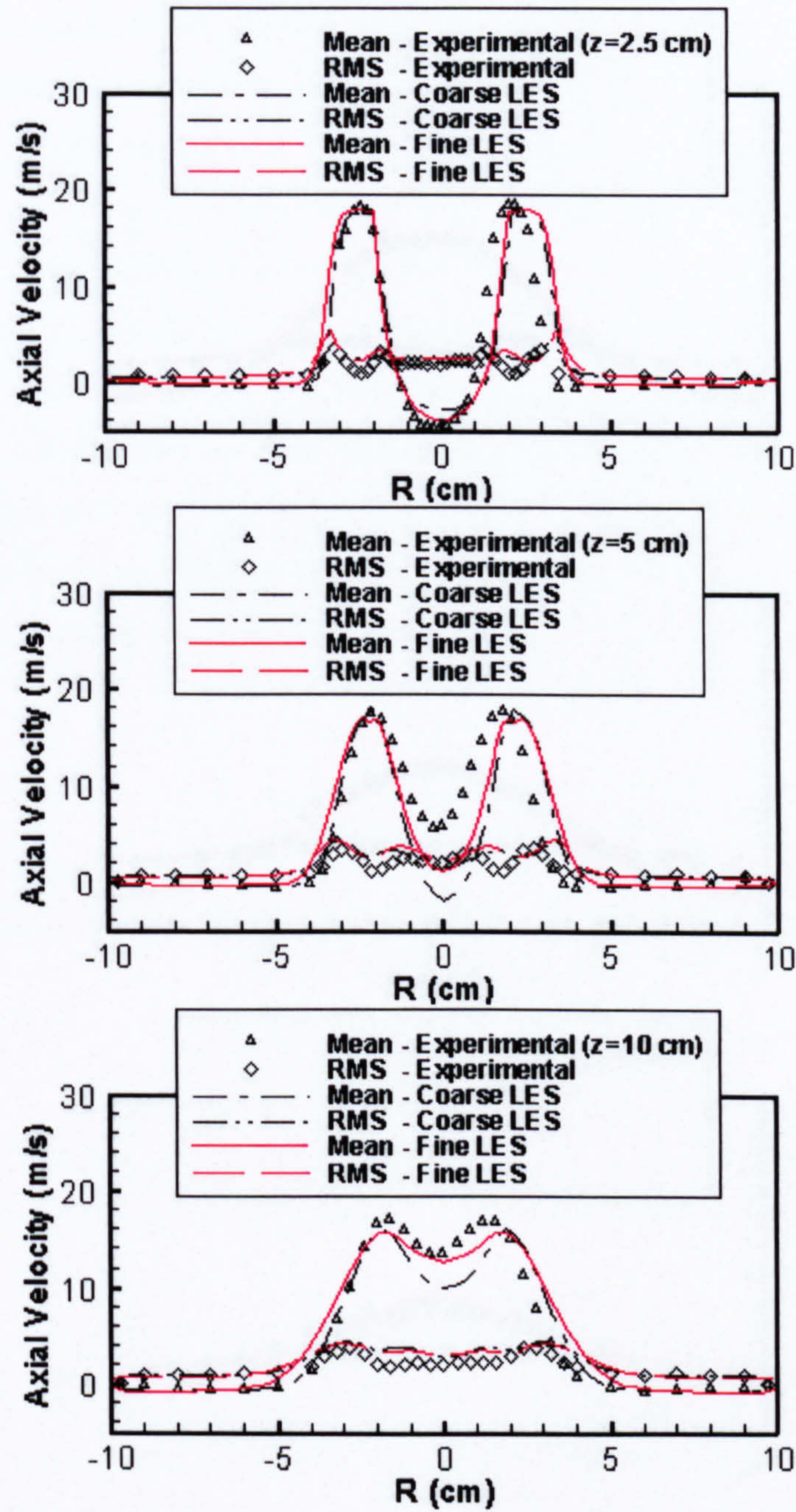


Fig. 7.3 Comparison of the predicted axial mean velocity and the axial turbulent intensity with experiment. (To be continued)

The predicted axial mean velocity and axial turbulent intensity at various downstream locations are compared with the experimental data in the Fig. 7.3. To test the grid sensitivity of the results, the results of 6.5 cm and 6 cm grid

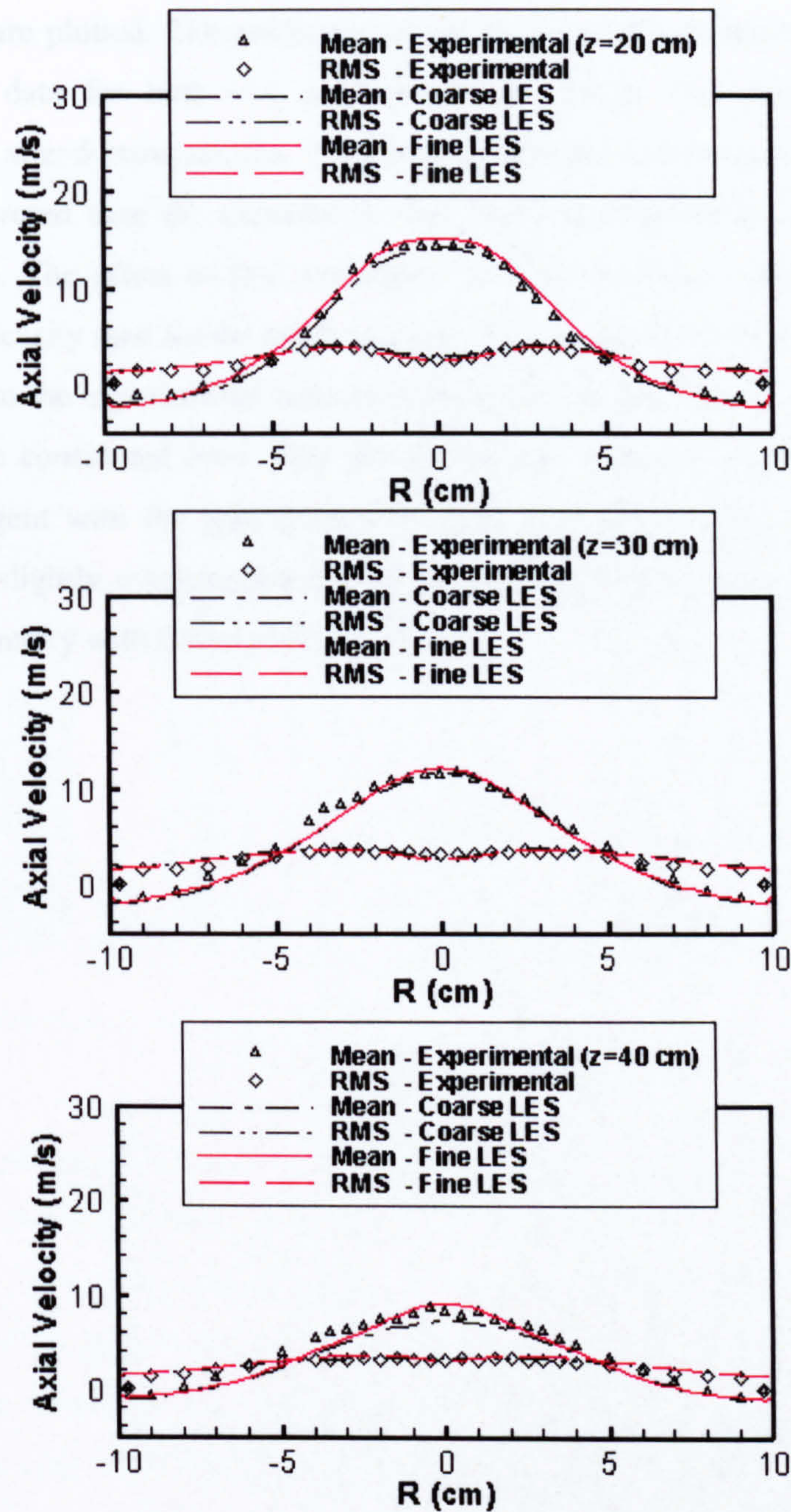


Fig. 7.3 (continued) Comparison of the predicted axial mean velocity and the axial turbulent intensity with experiment.

The predicted axial mean velocity and axial turbulent intensity at various downstream locations are compared with the experimental data in the Fig. 7.3. To test the grid sensitivity of the results, the results of both coarse and fine grid

resolutions are plotted. The predicted results are in excellent agreement with the experiment data for both two grid resolution, except that there is a slight discrepancy at $z=5$ cross section. The predicted central recirculation zone is more slowly recovered than the experiment. This has improved when fine resolution grid is used. The effect of grid resolution is found to be less profound for the turbulent intensity than for the mean velocity. The results of the fine resolution are quite close to the experimental data indicating that this resolution is sufficient for the test case considered here. This proves that the current simulation is reliable and convergent with the grid resolution. Prior to $z=20$ cm, the axial turbulent intensity is slightly over-predicted. This may be due to the approximation of the circular geometry with Cartesian cells.

Fig. 7.4 Comparison of the results using coarse and fine grid resolution for the mean velocity and turbulent intensity at $z=5$ cm cross section.

The predicted results of the mean axial gas velocity (U_{ax}) and the turbulent intensity are compared with the experimental data at the axial plane $z=5$ cm, shown in the same figure. The spray plane separates the two phases, the gas and the liquid, and the exchange of momentum between the two phases. The predicted mean axial recirculation zone in the gas flow field, but the recirculation zone in the spray recirculation zone has become smaller due to the over-prediction of the spray. There even appears to be a positive axial velocity region behind the spray at $z=5$ cm inside the recirculation zone. The off-axis point marked by (2.02, 0.02) is the coaxial jet for the two phase case moves farther downstream by 10% of the length of the spray. The point p_{max} , as shown in Fig. 7.4, is defined by the point on the axis with the maximum axial velocity.

7.3.2 Evaporating two phase flow

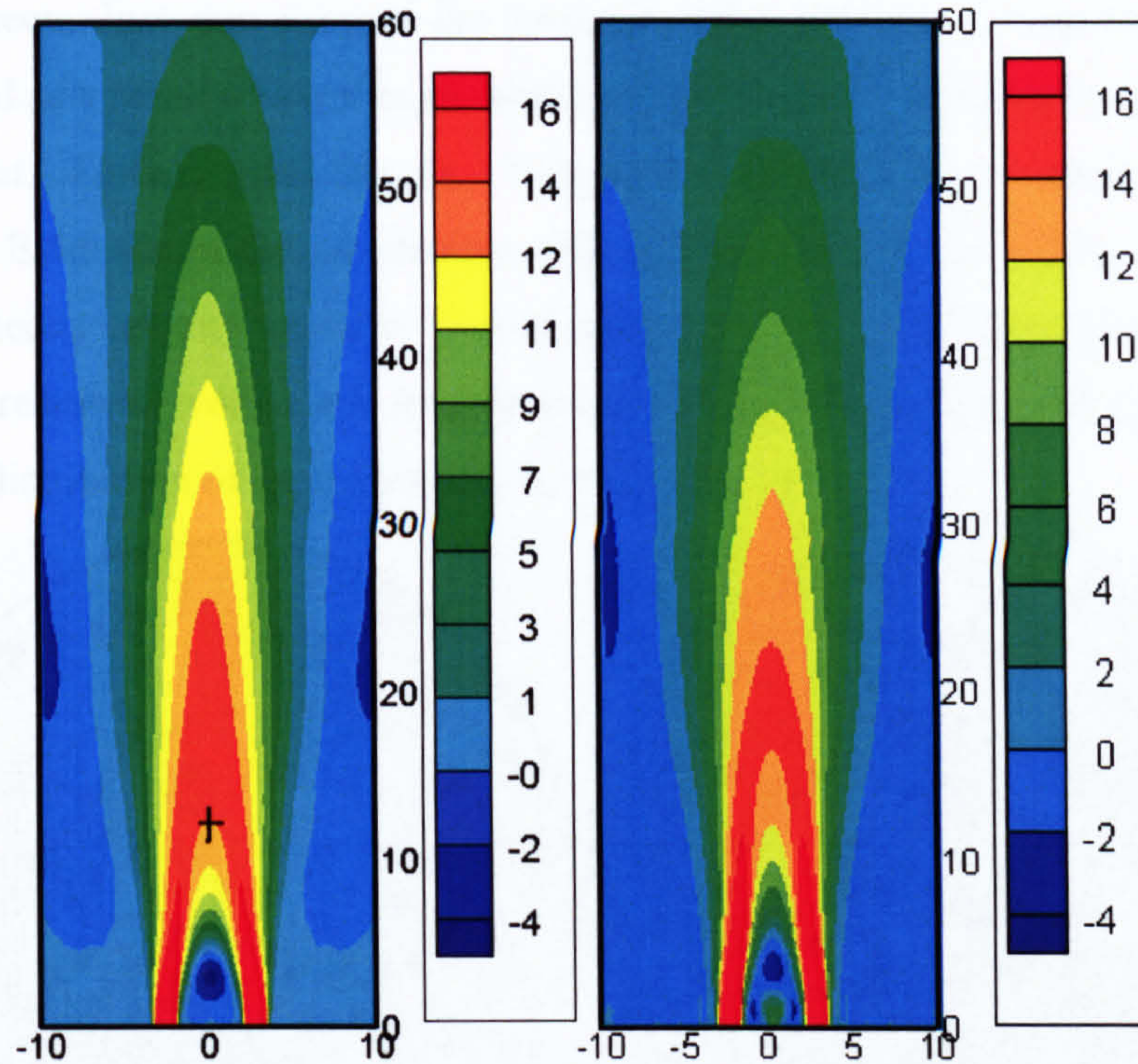


Fig. 7.4 Contours of the mean axial gas velocity for the single phase case (left) and the two-phase case (right)

The predicted contour of the mean axial gas velocity is shown in Fig. 7.4. For comparison the predicted contour of the single phase case is also shown in the same figure. The spray phase influences the gas phase flow field through the exchange of momentum between the two phases. There still exist two recirculation zones in the gas flow field, but the intensity of the central recirculation zone has become smaller due to the counteraction of the spray. There even appears to be a positive axial velocity region induced by the spray injection inside the recirculation zone. The on-axis join point (marked by black cross) of the coaxial jet for the two phase case moves further downstream by the deflection of the spray. The join point, as shown in Fig. 7.4, is defined by the point on the axis with the maximum axial velocity.

A snapshot of the iso-surface of pressure fluctuation is displayed in Fig. 7.1. The predicted flow field is quite turbulent. Some coherent vortical structures can be clearly seen. Just downstream the annulus, there are some “ring-like” vortex generated as a result of shear layer instability of the Kelvin-helmholtz type as in a round jet. Further downstream, “worm-like” streamwise vortical structure appears. Evidence of the streamwise vortex can also be found in Fig. 7.5 by the instantaneous velocity vector at various downstream cross-sections. The existence of the streamwise vortex can greatly enhance the mixing process of fuel vapour and the distribution of spray droplets by rolling up the fluid.

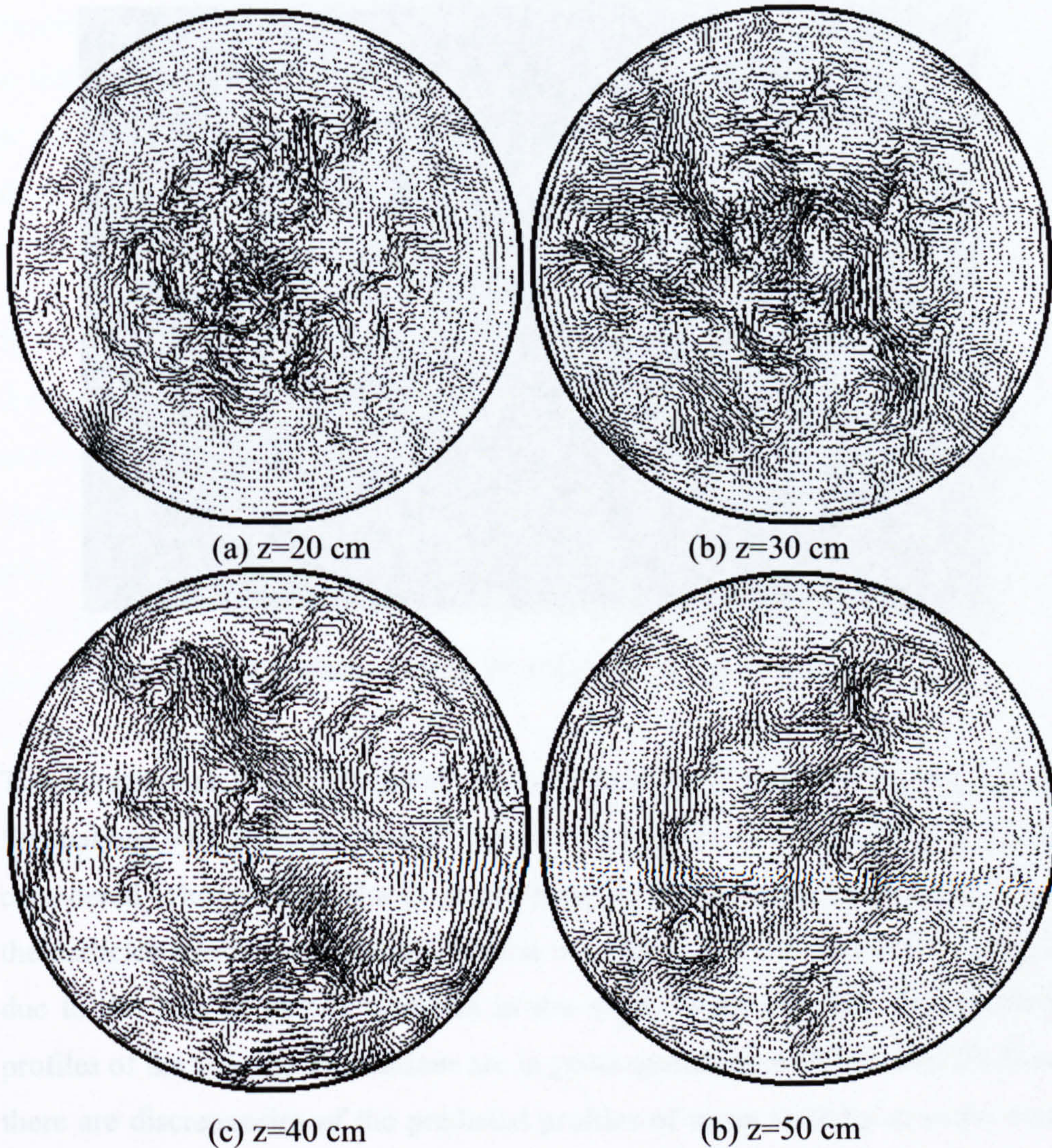


Fig. 7.5 Instantaneous velocity vectors on the various downstream cross-sections.

The predicted distributions of spray droplets on the plane through the axis and on the six different cross-sections are shown in Fig. 7.1 and Fig. 7.6, respectively. At the beginning, the spray droplets concentrate around the centreline. Some small size droplets are trapped inside the central recirculation zone. These small droplets have small inertia and easily follow the gas flow. Some of the large droplets with more inertia can penetrate through the coaxial flow and move further outside. Moving further downstream, the droplets tend to spread towards the wall by the spreading gas flow. Due to evaporation, the droplet sizes are getting smaller.

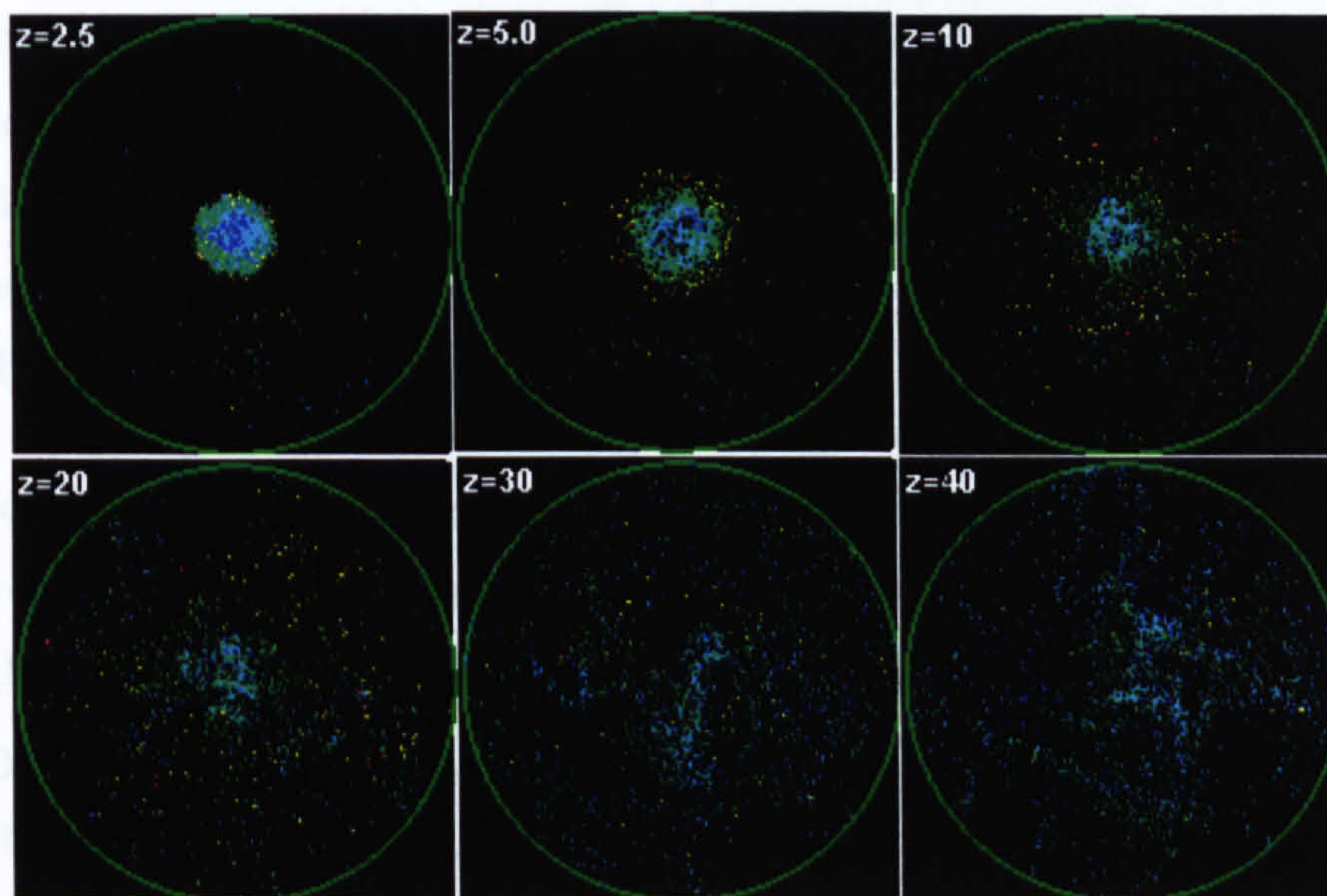


Fig. 7.6 Distribution of spray droplets on six various cross sections.

The comparison of the predicted mean axial droplet velocity and its velocity fluctuations with the experimental data is shown in Fig. 7.7. Six cross-sections are considered. The droplet velocity is computed by mass ensemble averaging of all the particles residing in a control volume cell. There is a second peak at $z=2.5$ cm due to the lack of particle samples in the second peak position. The predicted profiles of the velocity fluctuations are in good agreement with the data. However, there are discrepancies of the predicted profiles of mean velocity at some cross-sections. The predicted mean profiles show a good agreement at the cross-sections

of $z=2.5$ cm and $z=40$ cm. But the mean axial velocity is under-predicted close to the centreline at $z=5$ cm and over-predicted at the other cross-sections. The under-prediction could probably be attributed to the under-estimate of the restoration velocity in the centreline as the single phase flow. As the experimental data is not available for the gas phase, the over-predictions are not so sure. Two possible reasons may be accounted for it. One is that the gas flow is possibly over-predicted, hence the over-predictions of the droplet velocity. However, the single phase flow of the combustor was accurately simulated in the last section. This may lead to the existence of another reason, i.e. the slip velocity between the two phases is perhaps under-estimated. The predicted droplet velocity behaves easily to follow the gas flow as will be shown in the next paragraph. At the cross-section of $z=40$ cm, the droplets are small due to the evaporation, and they easily follow the gas flow because of the small inertia. The predicted profile agrees well again with the experiment at this location.

The comparison of the mean axial velocity and its velocity fluctuation between the two phases are examined in Fig. 7.8. Since droplet sizes are small around the centreline caused by the hollow spray, the axial velocity of the small droplets closely follows the gas flow due to their small inertia. Away from the centreline prior to $z=20$ cm, the droplet velocity is lower than the gas phase velocity, so there is an acceleration of the droplet velocity. At $z=10$ cm, since large droplets penetrate though the coaxial flow, there exists a region in which the droplet velocity is greater than that of the gas phase. Downstream at $z=20$ cm, the predicted droplets follow well with the gas phase and there is little difference between the two phase velocities.

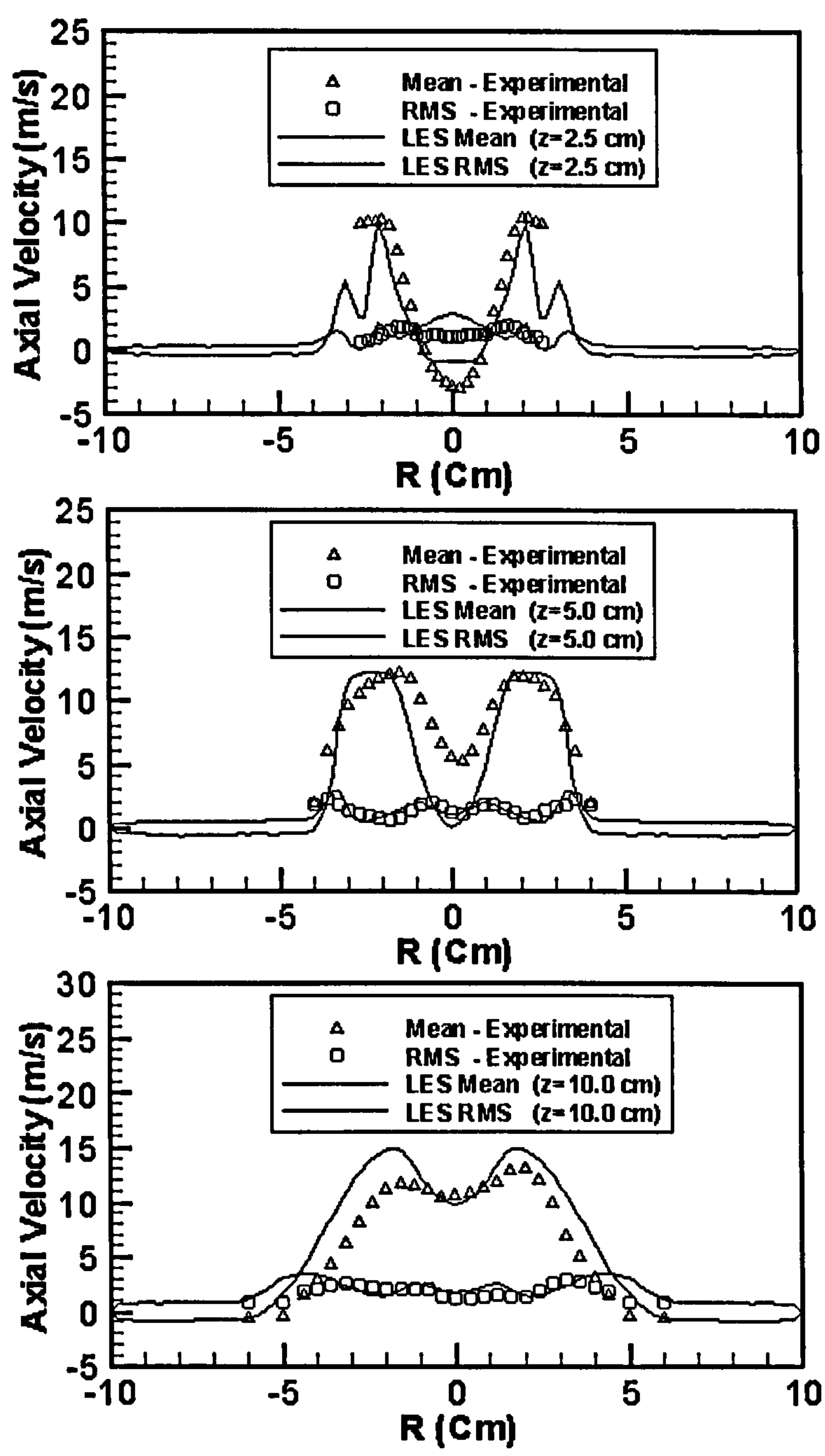


Fig. 7.7 Comparison of the predicted mean axial droplet velocity and its velocity fluctuation with the experimental data. (To be continued)

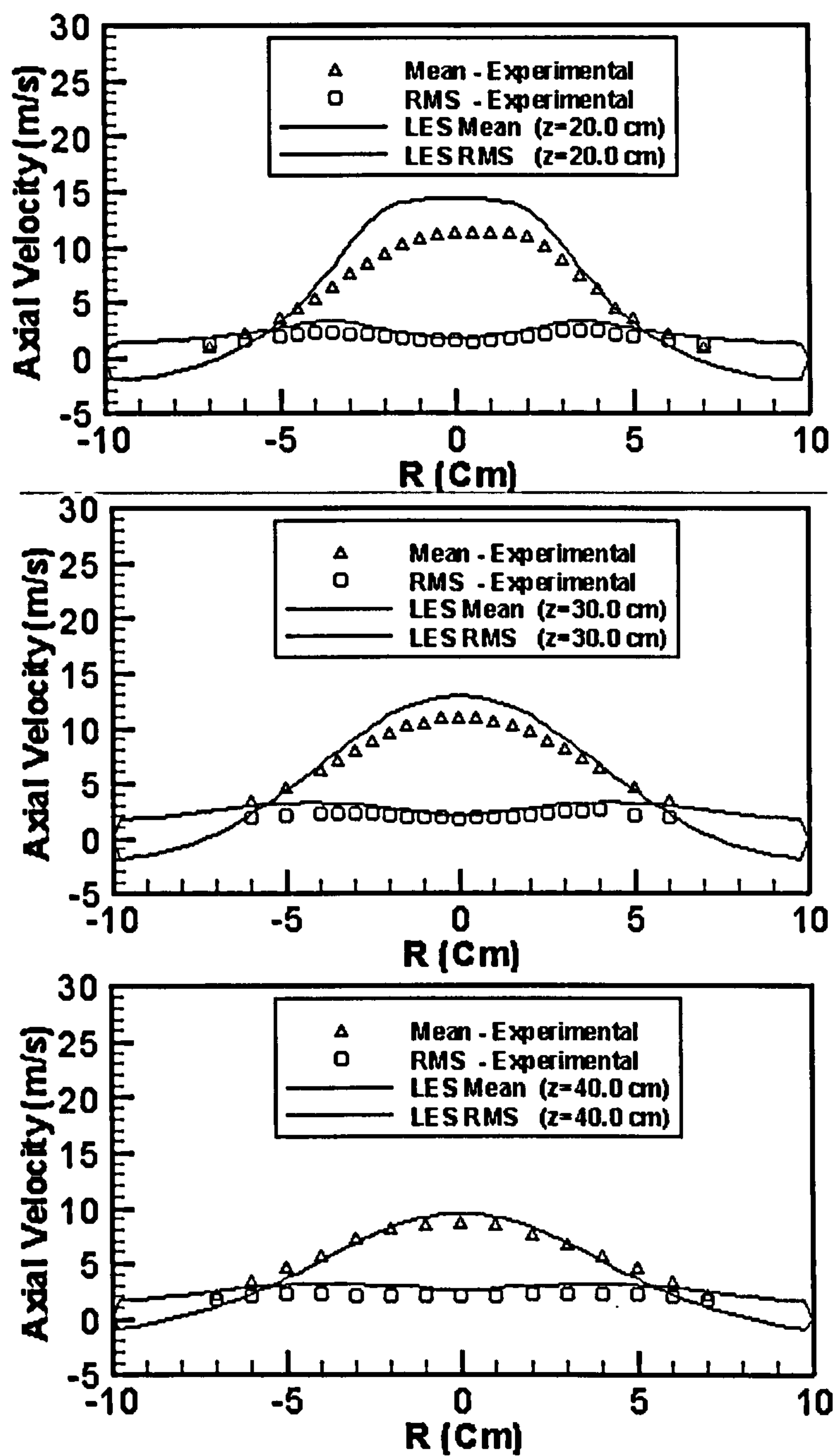


Fig. 7.7 (continued) Comparison of the predicted mean axial droplet velocity and its velocity fluctuation with the experimental data

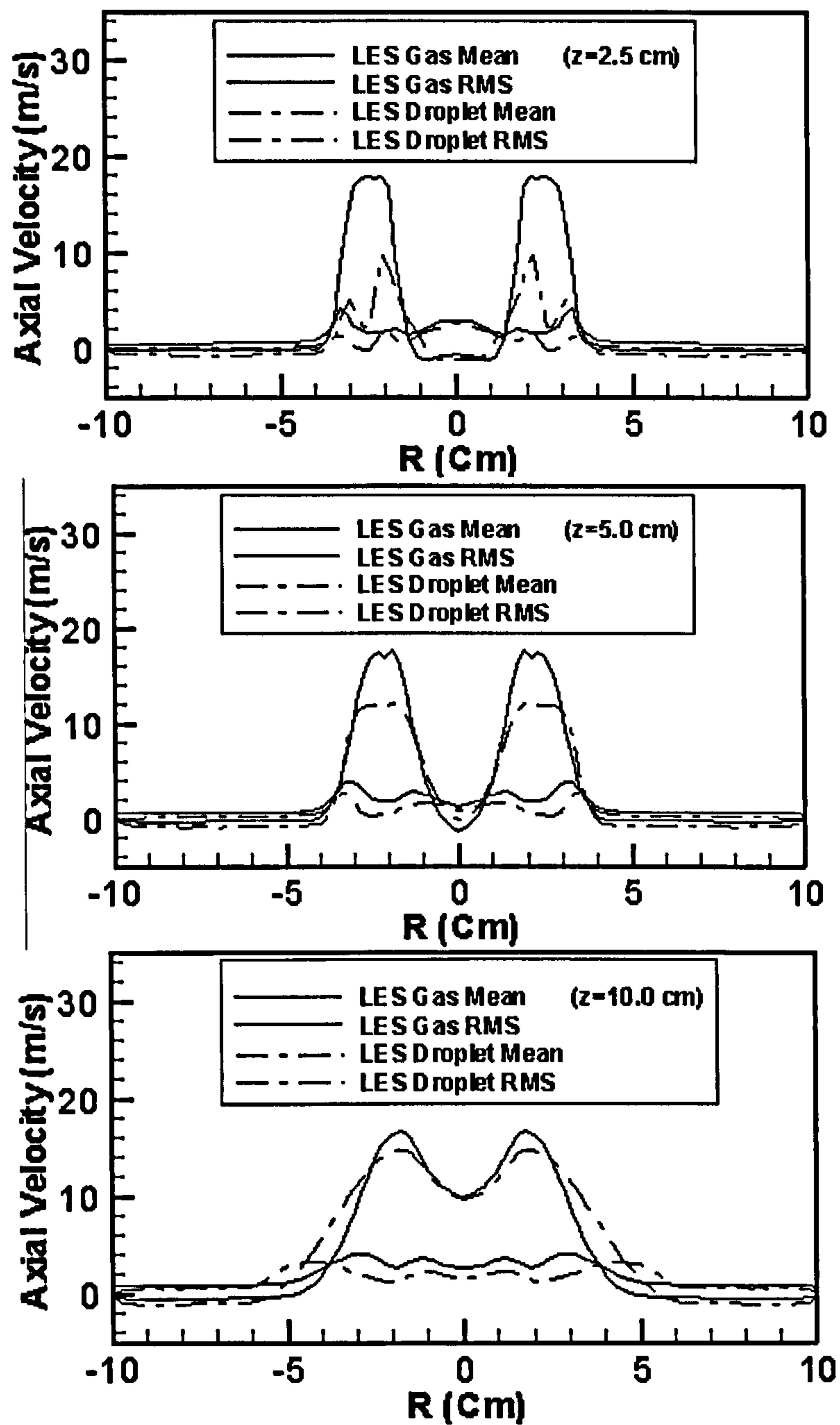


Fig. 7.8 Comparison of the predicted mean axial droplet velocity and its velocity fluctuations with the counterparts of gas phase. (To be continued)

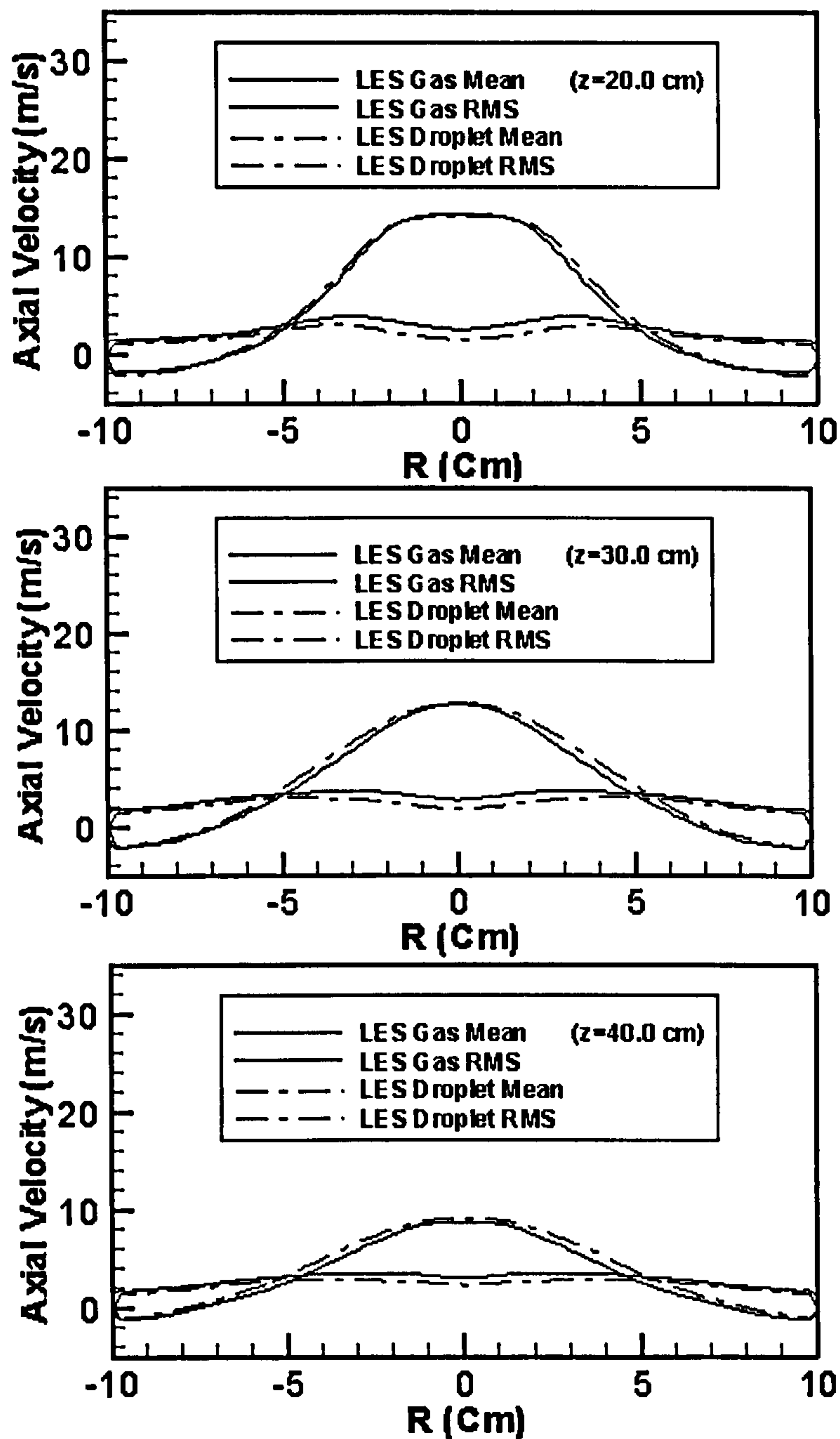


Fig. 7.8 (continued) Comparison of the predicted mean axial droplet velocity and its velocity fluctuations with the counterparts of gas phase

Fig. 7.9 shows the comparison of the predicted mean radial droplet velocity with the data. The predicted sparks at large radius position are caused by the lack of particle samples. The predicted mean radial velocity agrees reasonably well with

the experimental data. Within the spray cone, the largest radial velocities are found indicating the outward radial spread of the spray. Prior to $z=10$ cm, the maximum radial velocity continuously decreases and downstream of $z=10$ cm the radial spread increases again slightly. This trend implies that initially air from the annular jet is entrained into the spray causing a reduction in the radial spread. Moving further downstream, the flow continuously expands due to the reduced dimensions of the recirculation region in the edge of the pipe expansion.

The comparison of the predicted Sauter Mean Diameter (SMD) with the data is displayed in Fig. 7.10. The predicted sparks at large radius position are also caused by the lack of particle samples. The comparison of the predicted SMD with the experimental data is rather well except a little under-prediction after $z=30$ cm. A simulation with an assumption that the injected droplet size follows χ^2 -distribution was performed. Less satisfactory results were obtained due to more large droplets produced by the distribution. The predicted profiles of SMD show the typical result expected from a hollow-cone atomizer where smaller droplets are found in the core region and larger droplets near the edge of the spray. At the position of $z=5$ cm, an increase in the predicted SMD is observed near the edge of the spray. This is due to the quick evaporation of the small droplets. With increasing distance from the inlet, the droplet mean diameter becomes more and more uniform over the pipe cross-sections due to evaporation, turbulent dispersion and entrainment from the outer region of the spray. Downstream of $z=30$ cm, the SMD is almost constant in the cross-section and slowly decreases with downstream distance as a result of evaporation. The largest changes of the SMD are observed at the edge of the spray where the highest evaporation rates are expected due to the high relative velocity between the two phases.

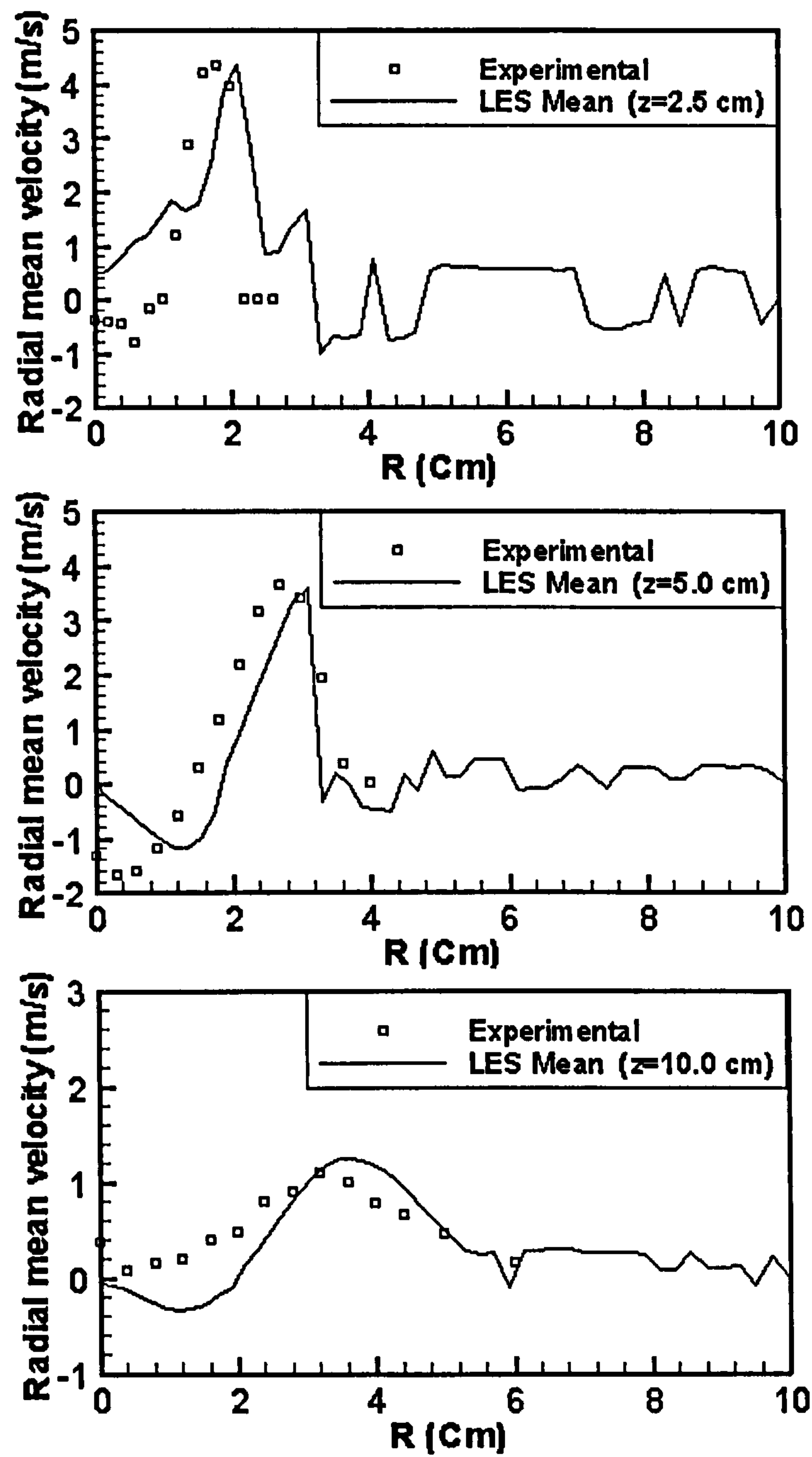


Fig. 7.9 Comparison of the predicted mean radial droplet velocity with the experimental data. (To be continued)

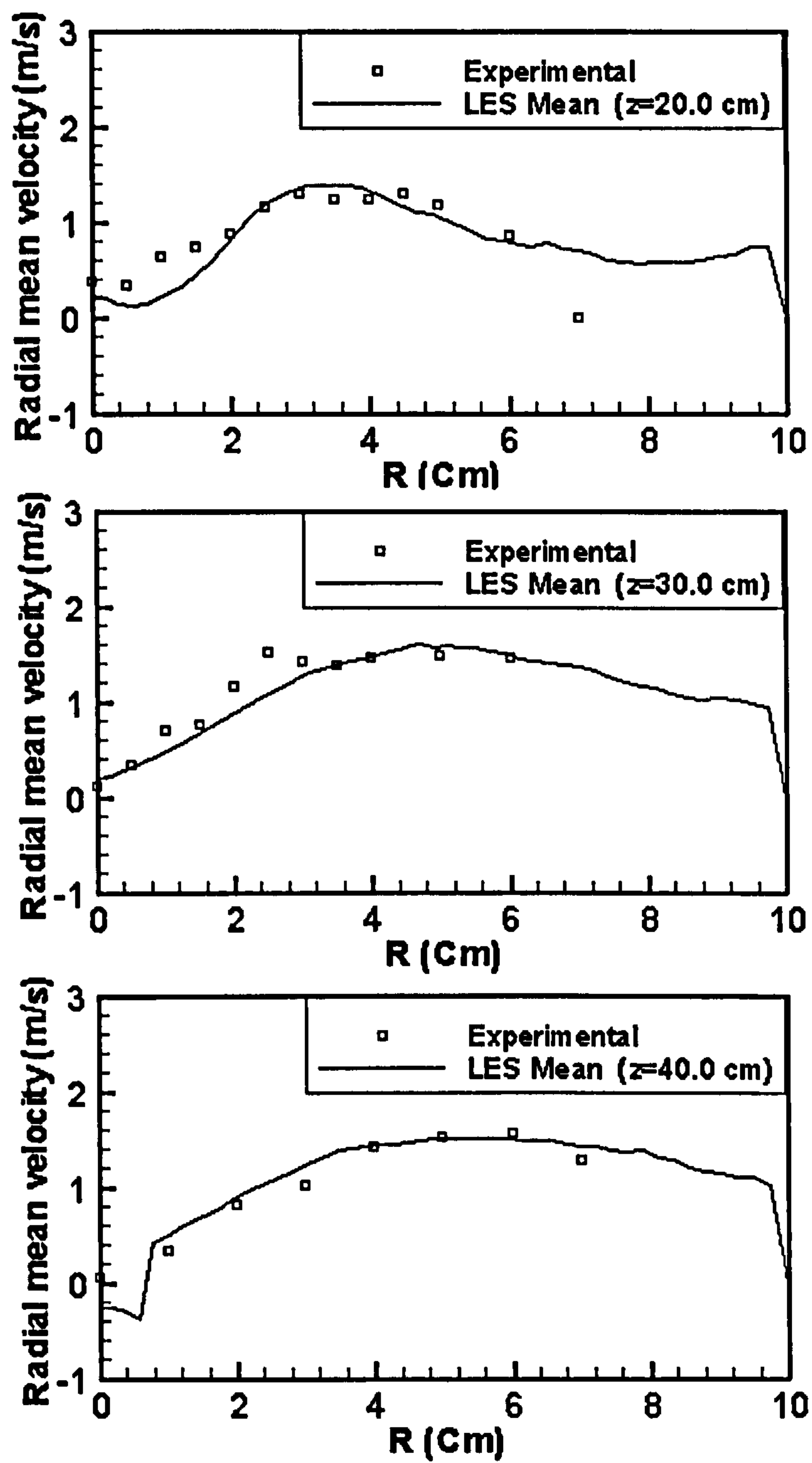


Fig. 7.9 (continued) Comparison of the predicted mean radial droplet velocity with the experimental data

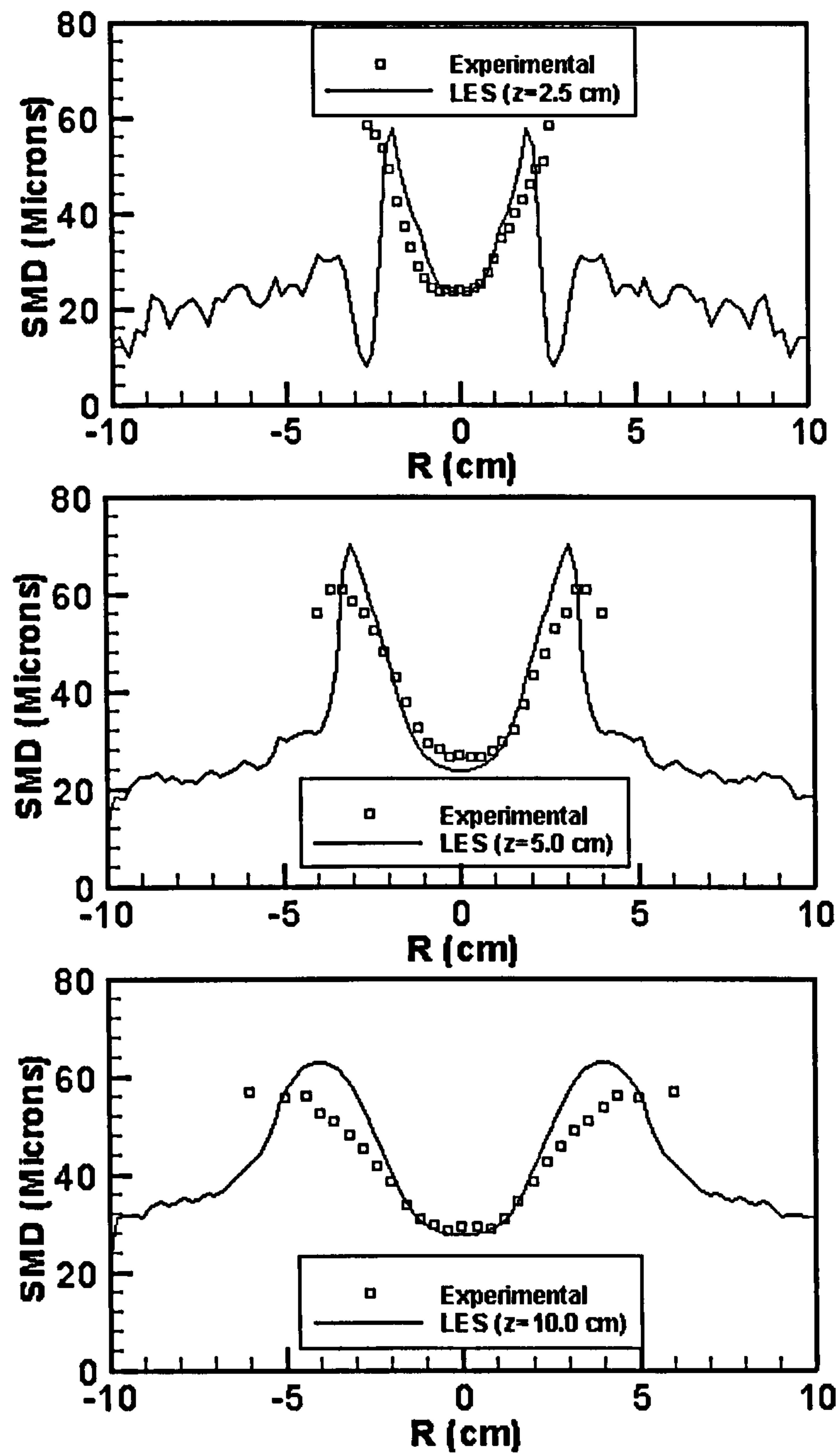


Fig. 7.10 Comparison of the predicted Sauter Mean Diameter (SMD) with the experimental data. (To be continued)

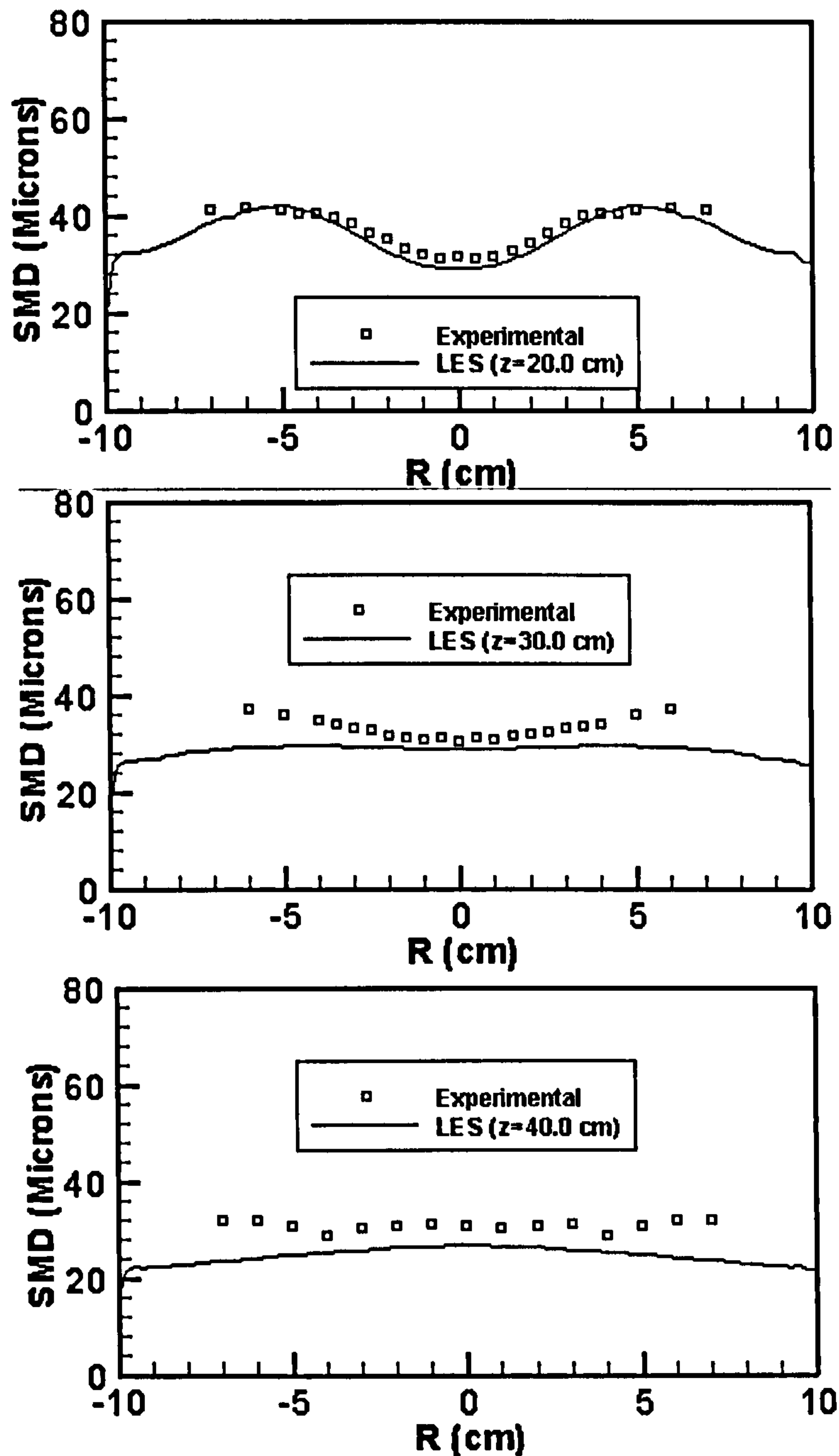


Fig. 7.10 (continued) Comparison of the predicted Sauter Mean Diameter (SMD) with the experimental data

Fig. 7.11 shows the comparison of the predicted axial droplet mass flux with the experimental data. The axial droplet mass flux is computed by the product of the mean axial velocity and the droplet cell volume density, while the latter is defined

by the mass of droplets residing in a cell divided by the cell volume. The predicted axial droplet mass flux agrees very well with the data, except an under-prediction observed near the centreline at $z=5$ cm which is probably due to the under-prediction of the axial velocity of the gas phase. The predicted profiles of the droplet mass flux show the two peaks associated with the hollow-cone spreading spray prior to $z=5$ cm. Due to the central recirculation zone, a negative predicted droplet mass flux is observed near the centreline at $z=2.5$ cm. Further downstream the spreading of the spray is hindered due to the entrainment of the annular air jet and the maximum of the droplet mass flux moves towards the centreline. Downstream of $z=5$ cm, the droplet mass flux is continuously decreasing. Most of the liquid has evaporated at $z=40$ cm.

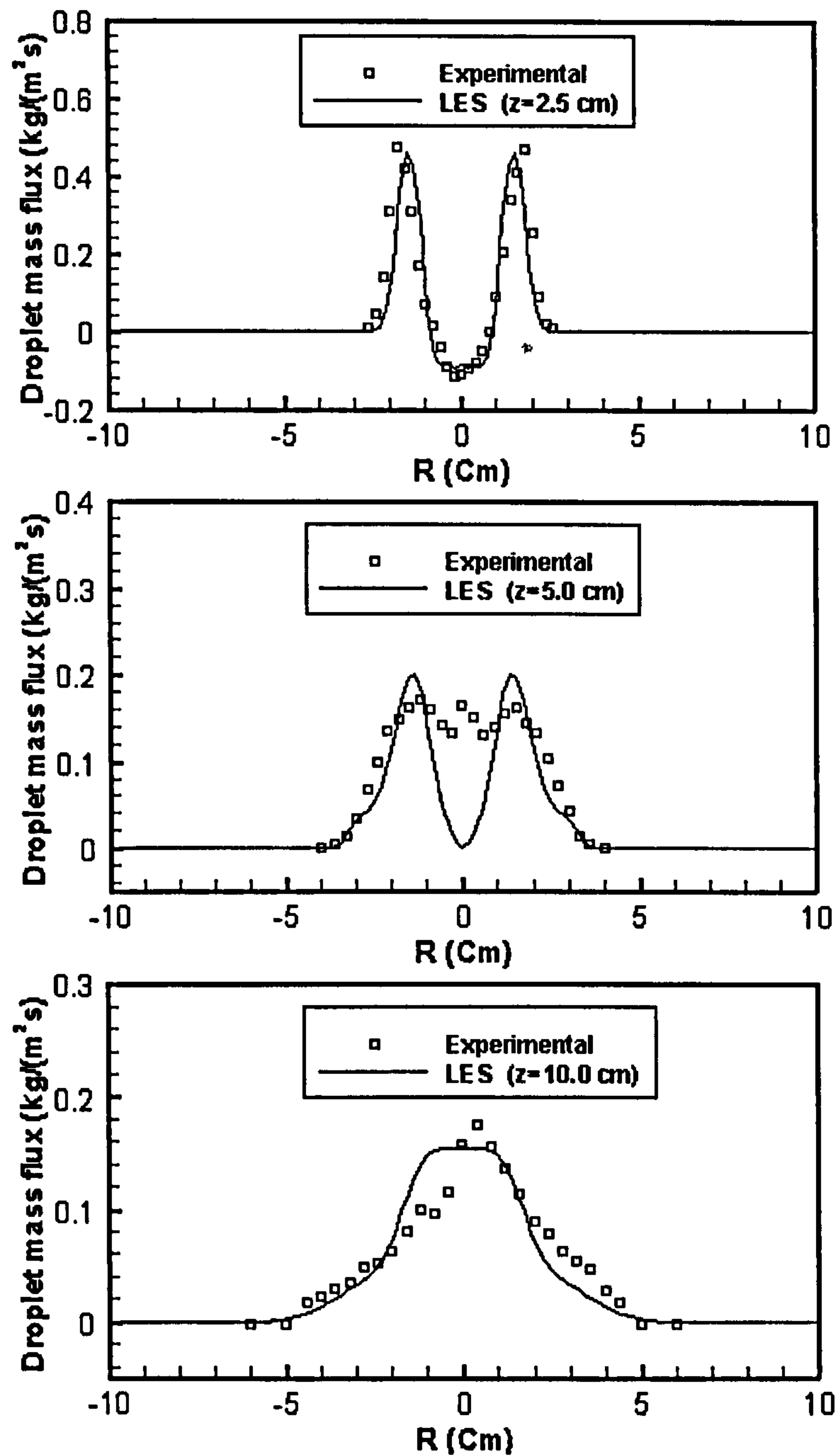


Fig. 7.11 Comparison of the predicted axial droplet mass flux with the experimental data. (To be continued)

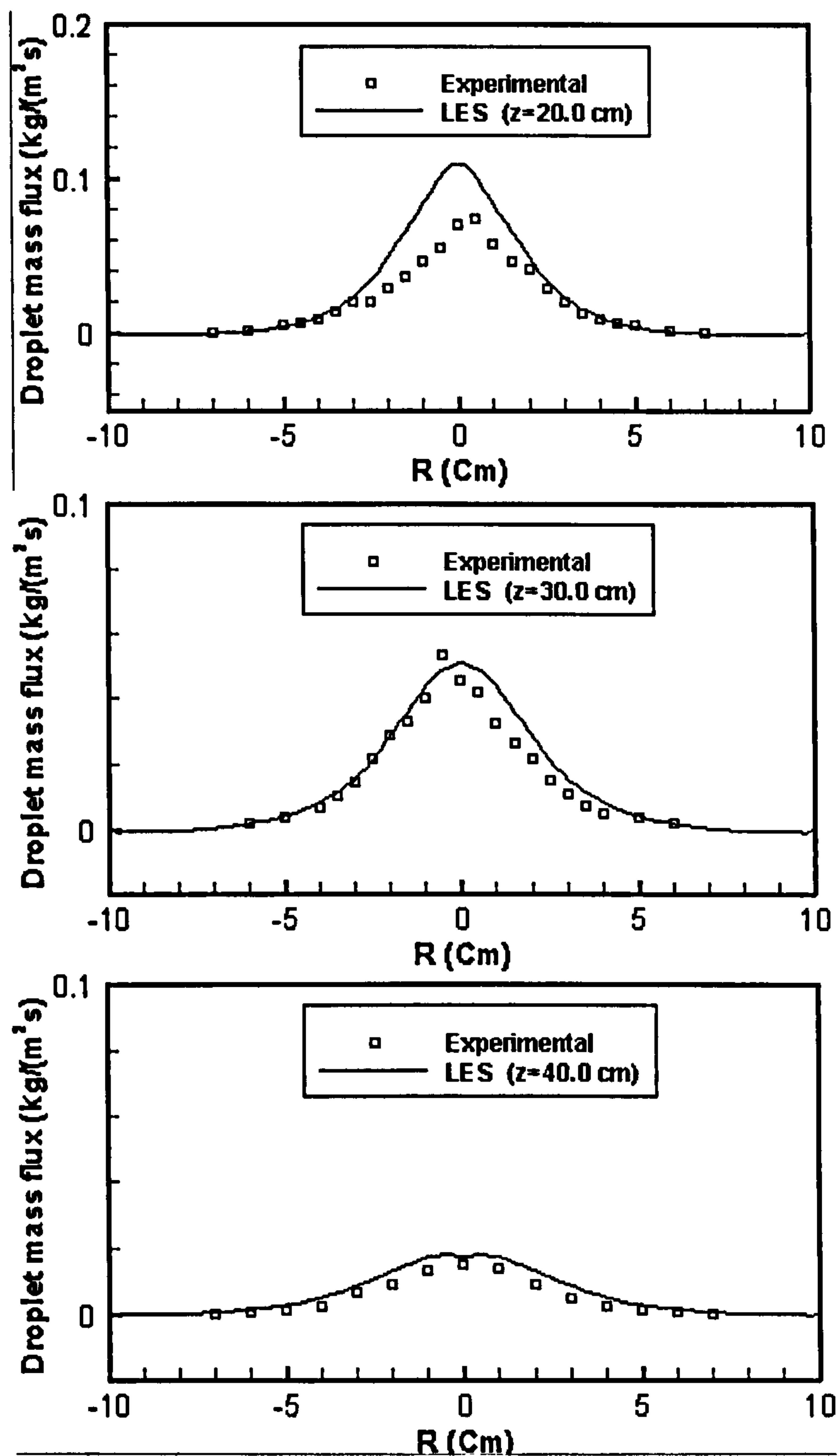


Fig. 7.11 (continued) Comparison of the predicted axial droplet mass flux with the experimental data.

7.4 Summary

Large eddy simulations of single phase flow and evaporating two phase flow in a coaxial gas turbine model combustor have been carried out under conditions corresponding to the experiments of Sommerfeld and Qiu [113]. Two grid resolutions are used for the single phase flow to test the grid sensitivity of the predicted results. A hollow-cone pressure atomizer is employed and isopropyl-alcohol is used as a spray liquid. Two-way coupling is applied between the gas and spray phases, and the SGS velocity is also considered. One million particles are traced in the simulation to represent the dynamic disperse phase.

Good agreements with the data have been achieved for both the single phase and evaporating two phase flows. Grid independence is tested achieved for the single phase flow. The predictions have captured the “Ring-like” vortices just downstream the annulus and “worm-like” streamwise vortical structure further downstream. The axial droplet mass flux and SMD are also well predicted. In general, this study demonstrates the accuracy and reliability of KIVA-LES and its capability to handle evaporating two phase flows in coaxial gas turbine combustors.

Chapter 8

Conclusions and Recommendations for Future Work

8.1 Conclusions

The time accuracy of the KIVA-3V code has been made fully second order by implementing a combination of a semi-implicit Crank-Nicolson method in Phase B and a two stage MacCormack method in Phase C. Spatial accuracy has also been improved by using central differencing for momentum equations and QSOU for the species density and energy question to stabilize the numerical solution. The adoption of the One-equation SGS model makes relative coarse mesh possible in a LES and also makes it possible to include the effect of SGS velocity on the dispersed phase.

Validations show that the current numerical methods have sufficient accuracy to simulate complex turbulent flows such as plane impinging jets. The dissipative error of the numerical methods was found to be minor, and the effect of the SGS model was evidently not masked out by the numerical errors. The SGS model successfully models the small scales and plays a significant role in stabilizing the numerical solutions. The results with explicit SGS model are much closer to the experimental data than the implicit SGS model (MILES approach).

KIVA-LES is superior to the original RANS based KIVA-3V code not only in providing more accurate turbulent statistic results, but also in providing more insight into the dynamics of turbulent flow. Most turbulent flows are dominated by large scale, coherent vortices which are responsible for turbulent mixing and major flow properties. High quality numerical simulations can not be achieved if these vortices are not resolved. However, these eddy structures are smeared out in a RANS simulation by adoption of a large numerical viscosity. In the present

Chapter 8 Conclusions and Recommendations for Future work

study, large scale vortices have been successfully captured. The reproduction of spanwise rollers, successive ribs, cross ribs and wall ribs of the forced plane impinging jet have been achieved, which were only reported in experiments and to our best knowledge never wholly reported in numerical simulations. The “branch-like” fuel spray shape caused by large scale vortices has also been reproduced in the current LES. Furthermore, the predicted “ring-like” and “worm-like” vortices play an important role in turbulent mixing of the coaxial gas turbine combustor.

Grid-convergent results of a fuel spray jet can not be achieved by KIVA-3V. By combining the new collision model with the LES solver, the predictions are much less dependent on the grid resolutions and a trend of grid-convergence has been achieved. Moreover, the predicted spray shapes do not show any artifacts in a Cartesian mesh. The dense and dilute spray regions are also distinguished by the current LES with the new model.

Finally, large eddy simulation of single phase flow and evaporating two phase flows in a coaxial gas turbine model combustor has been conducted. The predictions have achieved reasonably good agreement with the experimental data, demonstrating that KIVA-LES with the newly developed collision model can deliver reasonably accurate predictions for evaporating two phase flows in coaxial gas turbine combustors.

8.2 Recommendations for future work

The following recommendations can be considered for future work:

- Parallelization of KIVA-LES code. It takes about 360 CPU hours to finish a LES of the model combustor with 1 million grid points and 1 million particles. Several millions grid points are required for a realistic modern gas turbine combustor. To make it feasible for KIVA-LES code to handle a realistic combustor, the code needs to be parallelized.
- Implementation of a dynamic one-equation SGS model. In the current LES code, only one SGS model, i.e. the one-equation model was implemented. There are two constants in the SGS model. To prevent the dependence on the two constants, it will be desirable to implement a dynamic one-equation model.
- Implementation of a high order less dissipative scalar advection scheme. In the current LES code, the QSOU scheme is retained for the scalar advection, which is quasi-second order. To reduce the dissipative error of the scheme, a high order less dissipative scalar advection scheme should be considered.
- Implementation of SGS combustion models. The current study focus on fuel vapor formation and mixing, no combustion is included. To reach the final goal of the study to simulate combustion in a realistic gas turbine combustor, SGS combustion models should be included.

References

- [1] M.A. AAMIR AND A.P. WATKINS. *Int. J Heat and Fluid Flow*, 21:420-431, 2000.
- [2] A.A. AMSDEN, P.J. O'ROURKE, AND T.D. BUTLER. KIVA-II: A computer program for chemically reactive flows with sprays. *Technical report LA-11560-MS, Los Alamos National Laboratory*, 1989.
- [3] A.A. AMSDEN. KIVA-3: A KIVA Program with Block-Structured Mesh for Complex Geometries. *Los Alamos National Laboratory report LA-12503-MS*, 1993.
- [4] A.A. AMSDEN. KIVA-3V: A Block-Structured KIVA Program for Engines with Vertical or Canted Valves. *Los Alamos National Laboratory report LA-13313-MS*, 1997.
- [5] A.A. AMSDEN, J.D. RAMSHAW, L.D. CLOUTMAN, AND P.J. O'ROURKE. Improvements and extensions to the KIVA Computer Program. *Los Alamos National Laboratory Report LA-10534-MS*, 1985.
- [6] C. ANGELBERGER, F. EGOLFOPOULOS, AND D. VEYNANTE. *Flow Turb. Combust.* 65 pp. 205-222, 2000.
- [7] S.V. APTE, M. GOROKHOVSKI, P. MOIN. LES of atomizing spray with stochastic modelling of secondary break-up. *Int. J. of Multiphase flow* 29, pp. 1503-1522, 2003.
- [8] S.V. APTE, K. MAHESH, P. MOIN, AND J.C. OEFELEIN. Large eddy simulation of swirling particle-laden flows in a coaxial-jet combustor. *Int. J. of Multiphase flow*, 29 pp. 1311-1331, 2003.
- [9] E. ARAD. Analysis of boundary layer separation over a bump using large eddy simulation. *AIAA Paper 2001-2558*, 2001.
- [10] A. AZETSU, S. DODO, T. SOMEA, AND C. OIKAWA. A study on the structure of diesel spray (2-D visualization of the non-evaporating spray). *COMODIA 90*, pp.199-204, 1990.

- [11] F. BEAUBERT AND S.VIAZZO. Large eddy simulation of plane turbulent impinging jets at moderate Reynolds numbers. *Int. J. Heat and Fluid flow* 24 pp.512-519, 2003.
- [12] R. BEAUBERT AND S. VIAZZO. Large eddy simulations of plane turbulent impinging jets. *In: 14th Australasian Fluid Mechanics Conference. Adelaide University, Australia*, pp. 425-428, 2001.
- [13] S. BELTAOS AND N. RAJARATNAM. Plane turbulent impinging jets. *J.Hydr. Res.* 11, pp.29-45, 1973.
- [14] A. BERLEMONT, M.S. GRANCHER, AND G. GOUESBET. Heat and mass transfer coupling between vaporizing droplets and turbulence using a Lagrangian approach. *Int. J. Heat Mass Transfer*, 38 (16), 3023-3034, 1995.
- [15] L.P. BERNAL AND A. ROSHKO. Streamwise vortex structure in plane mixing layers. *J. Fluid Mech.*, 170, pp.499-526, 1986.
- [16] R.B. BIRD, E.W. STEWART, AND E.N. LIGHTFOOT. Transport phenomena. *J. Willey*, 1960.
- [17] J.P. BONNET, J. DELVILLE, P. DRUAULT, P. SAGAUT, AND R. GROHENS. Linear stochastic estimation of LES inflow conditions. *Advances in DNS/LES*, C. Liu, Z.Liu eds, Greyden Press, 341-348, 1997.
- [18] F.V. BRACCO. Modeling of engine sprays. *SAE Paper No.850394*, 1995.
- [19] P.R. BRAZIER- SMITH, S.G. JENNINGS, AND J. LATHAM. The interaction of falling water drop; coalescence. *Prog. Roy. Soc., London*, A326, 393-408, 1972.
- [20] D. CARAENI, C. BERGSTROM AND L. FUCHS. Modelling of liquid fuel injection, evaporation and mixing in a gas turbine burner using large eddy simulations. *Turbulence and combustion*, 65 pp. 223-244, 2000.
- [21] V.K. CHAKRAVARTHY AND S. MENON. Large eddy simulations of turbulent premixed flames in the flamelet regime. *Comb. Sci. and Tech.*, 162:175-222, 2001.
- [22] D.R. CHAPMAN AND G.D. KUHN. The limiting behavior of turbulence near a wall. *J. Fluid Mech.*, 70, pp. 265-92, 1986.

- [23] J.L. CHEN, M. WELL AND J. CREEHAN. *Trans. ASME, J of Eng. For Gas Turbines and Power*, 120, 1988.
- [24] S.H. CHUANG AND C.Y. WE. Computations for a jet impinging obliquely on a flat surface. *Int. J. Numer. Methods Fluids* 12, p.637, 1991.
- [25] C. CLINE, D. MICHAEL, J. MICKLOW, J. GERALD, S.L. YANG, AND H.L. NGUYEN. Numerical analysis of the flow fields in a staged gas turbine combustor. *J. of Propulsion and Power*, Vol.11 No. 5 pp. 894-898, 1995.
- [26] J.M. COHEN AND T.J. ANDERSON. Experimental investigation of near-blowout instabilities in a lean, premixed step combustor. *34th Aerospace Sciences Meeting & Exhibit, AIAA 96-0819*, January 15-18. Reno, NV: AIAA, 1996.
- [27] S.M. CORREA AND M.D. SMOOKE. NO_x in parametrically varied methane flames. *Twenty-Third Symposium (International) on Combustion*. Pittsburgh, PA: *The Combustion Institute*, pp. 289-95, 1990.
- [28] S.M. CORREA. Lean premixed combustion for gas-turbines: review and acquired research. In: Ruiz R, editor, *Energy-sources technology conference and exhibition*, PD-Vol. 33, *Fossil Fuel Combustion*, January 20-23. Houston, TX: ASME, pp. 1-9, 1991.
- [29] S.M. CORREA. *Comb Sci Tech*. 87:329-62, 1992.
- [30] T. CRAFT, L. GRAHAM, AND B. LAUNDER. Impinging jet studies for turbulence model assessment, an examination of the performance of four turbulence models. *Int. J. Heat Mass Transfer* 366, pp.2685-2697, 1993.
- [31] C.T. CROWE. A computational model for the gas-droplet flow-field in the vicinity of an atomiser. In *11th JANAF Symposium*, No. 74-23, *The Combustion Institute*, 1974.
- [32] T. CZIESLA, G. BISWAS, H. CHATTOPADHYAY, AND N.K. MITRA. Large eddy simulation of flow and heat transfer in an impinging slot jet. *Int. J. Heat Fluid Flow* 22, pp.500-508, 2001.
- [33] J.W. DEARDORFF. *J. Fluid Mech*, 41,453, 1970.
- [34] J.M. DEUR, K.P. KUNDU, D.D. DARLING, M.C. CLINE, G.J. MICKLOW, M.R. HARPER, AND T.A. SIMONS. Analysis of lean

- premixed / prevaporized combustion with KIVA-II. *29th Intersociety Energy Conversion Engineering Conference, AIAA 94-3895*, August 7-12. Monterey, CA: AIAA, 1994.
- [35] J.K. DUKOWICZ. A particle-fluid numerical model for liquid sprays. *J. of Computational Physics* 35, 229-253, 1980.
- [36] M.E. ESSAM AND D. REITZ. An experimental and numerical study of injector behavior for Diesel Engines. *SAE World Congress & Exhibition*, 2003.
- [37] G.M. FAETH. *Prog. Energy Combust. Sci.* 3, 191, 1977.
- [38] N. FARRUGIA, R.D. LOCKETT RD, S.C. HARDING AND D.A. GREENHALGH. LIF imaging of fuel distribution in gas turbine combustors. *Proc. ILASS-Europe, Florence, Italy*, 1997.
- [39] T.J. FRIC. *Prop. Power* 9: pp.708-713, 1993.
- [40] R. FRIEDRICH AND M. ARNAL. Analyzing turbulent backward-facing step flow with the lowpass-filtered Navier-Stokes equations. *J. Wind Eng. Ind. Aerodyn.* 35, 101-128, 1990.
- [41] M. GAVAISES. Modelling of diesel fuel injection processes, Ph.D. Thesis. *Imperial college of science and technology and medicine, department of mechanical engineering, university of London*, 1997
- [42] M. GAVAISES, A. THEODORAKAKOS, G. BERGELES, AND G. BREEN. Evaluation of the effect of droplet collisions on spray mixing. *Proceedings of the Institution of Mechanical Engineers* 210, pp.465-475, 1996.
- [43] A. GEL. PhD thesis, A Distributed-memory implementation of KIVA-3 with refinements for large eddy simulation. *College of Engineering and Mineral Resources at West Virginia University*, 1999.
- [44] S. GHOSAL. Mathematical and physical constraints on large-eddy simulation of turbulence. *AIAA J.* 37, pp.425-433, 1999.
- [45] S. GHOSAL, P. MOIN. The basic equations for the large-eddy simulation of turbulent flows in complex geometry. *J. Comput. Phys.* 118, 24-37, 1995.

- [46] I.R. GRAN, I.S. ERTESVAG, AND B.F. MAGNUSSEN. Influence of Turbulence Modelling of Predictions of Turbulent Combustion. *AIAA J.*, Vol. 35, No. 1, pp. 106-110, 1997.
- [47] D.A. GREENHALGH. Laser imaging of fuel injection systems and combustors. *Proc. Instn Mech Engrs*, Vol 214, Part A, 1991.
- [48] G. GROTZBACH. *Encyclopedia of Fluid Mechanics*, edited by N. P. Cheremisinoff, Gulf, West Orange, NJ, Vol.6, 1987.
- [49] A.K. GUPTA AND D.G. LILLEY. *Journal of the Institute of Energy*. 65:106-17, 1992.
- [50] E. GUTMARK, M. WOLFSHTEIN AND I. WYGNANSKI. The plane turbulent impinging jet. *J. Fluid Mech.*, 88, pp.737-756, 1978.
- [51] Z. HAN AND R.D. REITZ. Turbulence Modeling of Internal Combustion Engines Using RNG $k - \epsilon$ Models. *Comb. Sci. Tech.* 106, 207, 1995.
- [52] S.C. HARDING AND D.A. GREENHALGH. Fuel-air mixing and combustion in an optical, lean, premixed, prevaporised gas turbine combustor. *ASME paper 98-GT-553*, 1998.
- [53] Y. A. HASSAN AND H.R. BARSAMIAN. New-wall modelling for complex flows using the large eddy simulation technique in curvilinear coordinates. *Int. J. of Heat and Mass Transfer*, Vol. 44, pp.4009-4026, 2001.
- [54] T. HERBERT. Secondary instability of boundary layers. *Ann. Rev. Fluid Mech.*, 20, pp.487-526, 1988.
- [55] H. HIROYASU AND T. KADOTA. Fuel droplet size distribution in diesel combustion chamber. *SAE Technical Paper 740715*, 1974.
- [56] C. HIRSCH. Numerical computation of internal and external flows. *Wiley: Chichester*, 1990.
- [57] C.W. HIRT, A.A. AMSDEN, AND J.L. COOK. *J. Comput. Phys.* 14,227, 1974.
- [58] Y. HUANG, H.G. SUNG, S.Y. HSIEH, AND V. YANG. Large eddy simulation of combustion dynamics of lean-premixed swirl-stabilized combustor. *J. of Propulsion and Power*, vol. 19, No. 5, pp. 782-794, 2003.

- [59] V. HUIJNEN, L.M.T. SOMERS, R.S.G. BAERT AND L.P.H. DE GOEY. Validation of the LES approach in Kiva-3V on a square duct geometry. *Int. J. Numer. Meth. Engng*; 00:1-12, 2005.
- [60] A.K.M.F HUSSAIN. Coherent structures and turbulence. *J. Fluid Mech.*, 173, pp.303-356, 1986.
- [61] P. JOHANSSON, A. SJUNNESSON AND S. OLOVSSON. Development of an experimental LPP gas turbine combustor. *International Gas turbine and Aeroengine Congress and Exposition*. 94-GT-284, June 13-16. The Hague, Netherlands: ASME, 1994.
- [62] A.R. KERSTEIN. Linear-eddy model of turbulent transport II. *Combustion and Flame*, Vol. 75, pp. 397-413, 1989
- [63] K. KNOWLES. Computational studies of impinging jets using k- ϵ turbulence models. *Int. J. Numer. Methods Fluids* 22, p.799, 1996.
- [64] B.L. KOFF. Aircraft gas turbine emissions challenge. *J. of Eng. for Gas Turbines and Power*. Vol. 116, No. 3, pp. 474-477, 1994
- [65] S. LEE, S.K. LELE, AND P. MOIN. Simulation of spatially evolving turbulence and the application of Taylor's hypothesis in compressible flow. *Phys. Fluids A* 4(7), pp.1521-1530, 1992,.
- [66] D. LEE, E. POMRANING, AND C. J. RUTLAND. LES Modeling of Diesel Engines. *SAE 2002-01-2779*, 2002
- [67] A.B. LIU AND R.D. REITZ. Mechanism of air-assisted liquid atomization. *Atomization and Spray*, vol.3:pp.55-75, 1993
- [68] S.C. LO AND H.J. SUNG. Large-scale turbulent vortical structures inside a sudden expansion cylinder chamber. *Flow, Turbulence and Combustion* 68:269-287, 2002.
- [69] R.W. MACCORMACK. The effect of viscosity in hypervelocity impact cratering. *AIAA paper* 69-354, 1969.
- [70] K. MAHESH, G. CONSTANTINESCU, AND P. MOIN. A numerical method for large eddy simulations in complex geometries. *J. Comput. Phys.*, 197, pp. 215-240, 2004.

- [71] F. MARE, W.P. JONES, AND K.R.MENZIES. Large eddy simulation of a model gas turbine combustor. *Combustion and Flame*. Vol. 137, pp. 278-294, 2004
- [72] S. MAUREL, M. PAVAGEAU, AND C. SOLIEC. Parametric analysis of impinging plane air jet on variable scaled-down models. *In: ASME Fluids Engineering Conference, Boston, 2000.*
- [73] S. MENON, C. STONE AND N. PATEL. Multi-scale modelling for LES of engineering designs of large-scale combustors, *AIAA 204-0157*, 2003.
- [74] S. MENON, AND W.-W. KIM. High Reynolds number flow simulations using the localized dynamic subgrid-scale model. *AIAA-96-0425*, 1996.
- [75] S. MENON, P.-K. YEUNG, AND W.-W. KIM. Effect of sub-grid models on the computed interscale energy transfer in isotropic turbulence. *Computers and Fluids*, 25(2):165-180, 1996.
- [76] G.J. MICKLOW, S. ROYCHOUDHURY, H.L. NGUYEN, AND M.C. CLINE. Emissions Reduction by Varying the Swirler Air Flow Split in Advance Gas Turbine Combustors. *J. of Eng. For Gas Turbines, and Power*, Vol. 115, No. 3, pp 563-569, 1993.
- [77] R. MITTAL AND P. MOIN. Suitability of upwind-biased finite difference schemes for large eddy simulation of turbulent flows. *AIAA J.* 35, pp.1415-1417, 1997.
- [78] P. MOIN AND J. KIM. Large eddy simulation of turbulent channel flow. *J. Fluid Mech.*, 118 p. 341, 1982.
- [79] R.K. MONGIA. *Proc. Combustion Institute*, 26, 1996.
- [80] I. NAMER AND M.V. OTUGEN. Velocity measurements in a plane turbulent air jet at moderate Reynolds numbers. *Exp. Fluids* 6, pp.387-399,1988.
- [81] J. NABER AND D.L. SIEBERS. Effects of gas density and vaporization on penetration and dispersion of diesel sprays. *SAE960034*, pp. 59-90, 1996.
- [82] S.P. NANDULA, R.W. PITZ, R.S. BARLOW, AND G.J. FIECHTNER. Rayleigh/Raman/LIF measurements in a turbulent lean premixed combustor.

- 34 Aerospace Sciences Meeting & Exhibit, AIAA-96-0937*. January 15-18. Reno, NV: AIDD, 1996.
- [83] D.G. NICOL, P.C. MALTE, AND R.C. STEELE. Simplified models for NO_x production rates in lean-premixed combustion. *International Gas Turbine and Aeroengine Congress and Exposition*. 94-GT-432, June 13-16. The Hague, Netherlands: ASME, 1994.
- [84] F. NICOUD AND F. DUCROS. *Flow Turb. Combust.* 62 pp. 183-200, 1999.
- [85] N. NORDIN. Complex chemistry modelling of diesel spray combustion, Ph.D. thesis. *Chalmers university of technology, Sweden*, 2000
- [86] P.J. O'ROURKE. The KIVA Computer Program for Multidimensional Chemically Reactive Fluid Flows with Fuel Sprays. *Numerical Simulation of Combustion Phenomena*, Eds, R. Glowinski, B. Larrouturou, and R. Temam, Springer Verlag, New York, 1985.
- [87] P.J. O'ROURKE. Collective drop effect on vaporizing liquid sprays. Ph.D. thesis, *department of mechanical and aerospace engineering, Princeton University*, 1981.
- [88] P.J. O'ROURKE, AND A.A. AMSDEN. Implementation of a conjugate residual iteration in the KIVA computer program. *Los Alamos National Laboratory report LA-10849-MS*, 1986.
- [89] P.J. O'ROURKE, AND A.A. AMSDEN. The TAB method for numerical calculations of spray droplet break-up. *SAE Technical paper 87-2089*, 1987.
- [90] P.J. O'ROURKE AND F. BRACCO. Modelling of drop interactions in thick sprays and a comparison with experiments. *Proceedings of the Institution of Mechanical Engineers* 9, pp.101-106, 1980.
- [91] M. OLSSON AND L. FUCHS. Large eddy simulation of the proximal region of a spatially developing circular jet. *Phys. Fluids* 8,2125, 1996..
- [92] S.V. PATANKAR. *Numerical Heat Transfer and Fluid Flow*, Hemisphere Publishing Corporation, Washington D.C., 1980.
- [93] A.E. PERRY AND T.T. LIM. Coherent structures in coflowing jets and wakes. *J. Fluid Mech.*, 88, pp. 451-463, 1978.

- [94] U. PIOMELLI, J.H. FERZIGER, P. MOIN, AND J. KIM. New approximate boundary conditions for large eddy simulations of wall-bounded flows. *Phys. Fluids A* 1, p. 1061, 1989.
- [95] M. RACHNER. *Proc. Combustion Institute*, vol. 26, 1996.
- [96] M.K. RAZDAN, J.T. MCLEROY, AND W.E. WEAVER. Retrofittable dry low emissions combustor for 501-K industrial gas turbine engines. *International Gas Turbine and Aeroengine Congress and Exposition*. 94-GT-439, June 13-16. The Hague, Netherlands: ASME, 1994
- [97] R.D. REITZ. Modelling atomization processes in high-pressure vaporizing sprays. *Atomization Spray Tech.* 3, 307, 1987.
- [98] H.L. RELATION, J.L. BATTAGLIOLI, AND W.F. NG. Numerical simulations of non-reacting flows for industrial gas turbine combustor geometries. *J. of Eng. For Gas Turbines and Power*, Vol. 120. No. 1, pp. 460-467, 1998.
- [99] W.C. REYNOLDS, J.J. ALONSO, AND M. FATICA. Aircraft gas turbine engine simulations. *AIAA 2003-3698, 16th AIAA Computational Fluid Dynamics Conference*, 2003.
- [100] C.M. RHIE, AND W.L. CHOW. *AIAA J.* 31 1525-1533, 1983.
- [101] N.K. RIZK, J.S. CHIN, M.K. RAZDAN. *Trans. ASME, J of Eng. For Gas Turbines and Power*, 119, 1997.
- [102] P. SAGAUT. Large eddy simulation for incompressible flows, second Edition. *Springer*, 2002
- [103] J. SAKAKIBARA, K. HISHIDA AND R.C. PHILLIPS. On the vortical structure in a plane impinging jet. *J. Fluid Mech.* 434, pp.273-300, 2001.
- [104] S. SARKAR, G. ERLEBACHER, M.Y. HUSSAINI, AND H.O. KREISS. The analysis and modelling of dilatational terms in compressible turbulence. *J. Fluid Mech.*, 227:473-393, 1991.
- [105] J. SAKAKIBARA, K. HISHIDA AND M. MAEDA. Three-dimensional vortex structure in the stagnation region of a forced plane impinging jet. *Bull. Amer. Phys. Soc.*, 40, p.1933, 1995.

- [106] J. SAKAKIBARA, K. HISHIDA AND M. MAEDA. Vortex structure and heat transfer in the stagnation region of an impinging plane jet (Simultaneous measurements of velocity and temperature fields by digital particle image velocimetry and laser-induced fluorescence). *Int. J. Heat Mass Trans.*, 40, pp.3163-3176, 1997.
- [107] D.P. SCHMIDT, AND C.J. RUTLAND. A new droplet collision algorithm. *J. Comput. Phys.* 164,62-80, 2000.
- [108] U. SCHUMANN. *J. Comput. Phys.* 18, 376, 1975.
- [109] B. SCHNEIDER. Experimental investigation of diesel sprays. *CRFD and Laser Diagnostic Workshop, 21st CIMAC Congress, Interlaken*, 1995.
- [110] L. SELLE, G. LARTIGUE, T. POINSOT, R. KOCH, AND K.-U. SCHILDMACHER, W. KREBS, B. PRADE, P. KAUFMANN, AND D. VEYNATE. Compressible large eddy simulation of turbulent combustion in complex geometry on unstructured meshes. *Combustion and Flame* 137 pp. 489-505, 2004.
- [111] D.G. SLOAN, P.J. SMITH, AND L.D. SMOOTH. Modelling of swirl in turbulent flow systems. *Progress in Energy and Combustion Science*. Vol. 12, pp. 103-250, 1986.
- [112] A. SMIRNOV, S. SHI, AND I. CELIK. Random flow generation technique for large eddy simulations and particle dynamics modelling. *J. Fluids Engng.* 123, pp. 359-371, 2001.
- [113] M. SOMMERFEL AND H. H. QIU. Experimental studies of spray evaporation in turbulent flow. *Int. J. Heat and Fluids Flows*, 19: 10-22, 1997.
- [114] K. SONE. AND S. MENON. KIVALES: Large-Eddy Simulations of Internal Combustion Engines. Part I: Theory and Formulation. *Georgic Tech, CCL Technical Report CCL-00-008*, 2000
- [115] K. SONE, N. PATEL, AND S. MENON. Large eddy simulation of fuel-air in an internal combustion engine. *Aerospace sciences meeting and exhibit, 39th, Reno, NV.*, 2001.

- [116] S. SUBRAMANIAM AND P.J. O'ROURKE. Numerical convergence of the KIVA-3 code and its implications for modelling. *Los Alamos Unclassified Report LAUR 98—5465*, 1998.
- [117] R.C. SWANSON, AND E. TURKEL. One central difference and upwind schemes. *Journal of Computational Physics*, Vol. 101, pp. 292-306, 1992.
- [118] P. SWEBY, AND SIAM. *J. Numer. Anal.* 21 (5) 995-1011, 1984.
- [119] D. TACINA, AND R. ROBERT. Sector tests of a low-NO_x, lean, direct-injection, multipoint integrated module combustor concept conducted. research & technology. *NASA/TM--2002-211333*, p. 116, 2002
- [120] N.P. TAIT AND D.A. GREENHALGH. 2D Laser induced fluorescence imaging o parent fuel fraction in nonpremixed combustion. *Proc. Combustion Institute*, vol. 24, 1992.
- [121] TAKAGISHI. Analysis of flow field in diesel fuel sprays by particle-image velocimety. *Trans JSME 65B*, (631), pp.1128-1133, 1990
- [122] F.X. TANNER. Liquid jet atomization and droplet break-up modelling of non-evaporating diesel fuel sprays. *SAE transactions: J. Engines*. 106, 127-140, 1998.
- [123] G.I. TAYLOR. The shape and acceleration of a drop in a high speed air stream. *The Scientific Papers of G. I. Taylor, Ed. G. K. Batchelor*. Vol. III *University Press, Cambridge, England*, 1963.
- [124] D.J. TORRES, P.J. O'ROURKE, A.A. AMSDEN. A discrete multicomponent fuel model. *Atomization and sprays*, 2003.
- [125] C. TRUESDELL. A first course in rational continuum mechanics. Vol.1, *Academic Press*, 1977.
- [126] M. TSUBOKURA, T. KOBAYASHI, N. TANIGUCHI, AND W.P. JONES. A numerical study on the eddy structures of impinging jets excited at the inlet. *Int. J. Heat and Fluid flow* 24, pp.500-511, 2003.
- [127] VARGAFTIK. Handbook of Physical Properties of Liquids and Gases, 2nd Edition, 1983

- [128] P.R. VOKE, S. GAO AND D. LESLIE. Large eddy simulation of plane impinging jets. *Exp. Thermal Fluid Sci.* 13, pp.364-373, 1995.
- [129] P.R. VOKE AND S.G. POTAMITIS. Numerical simulation of a low-Reynolds number turbulent wake behind a flat plate. *Int. J. Numer. Meth. Fluids* 19, 377-393, 1994.
- [130] P.WANG AND X.S. BAI, M.WESSMAN AND J. KLINGMANN. Large eddy simulation and experimental studies of a confined turbulent swirling flow. *Phys. of Fluids*, Vol. 16, No 9, pp. 3306-3324, 2004.
- [131] W. WANG. AND K.D. SQUIRES. Transport of heavy particles in a three-dimensional mixing layer. *J. of fluids engineering*, Vol. 120, pp.613-620, 1998.
- [132] H. WERNER AND H. WENGLE. Large eddy simulation of turbulent flow over and around a cube in a plate channel. *Turbulent Shear Flows*, Springer, Berlin, pp.155-168, 1991.
- [133] D.C. WILCOX. Turbulent modelling. *Griffin Printing, Glendale, California*, 1993.
- [134] A. WILLIAMS. Combustion of sprays of liquid fuels. *Elek Science*, London, 1976.
- [135] F.A. WILIAMS. *Phys. Fluids*, 1, 541, 1958
- [136] S. L. YANG, R. CHEN, M. C. CLINE, H. L. NGUYEN, AND G. J. MICKLOW. Numerical simulation of a low emission gas turbine combustor using KIVA--II. *Intl. J. for Numer. Methods in Fluids*, 15(8):865—881, 1992
- [137] S.L. YANG, B.D. PESCHE, AND K. HANKALIC. Second moment closure model for IC engine flow simulation using KIVA Code. *ASME J. of Engineering for Gas Turbine and Power*, Vol. 122, No.2, pp.357-365, 2000.
- [138] F W. YAO AND N.D. SANDHAM. DNS of turbulent flow over a bump with shock/boundary-layer interactions. *Proceedings of the Fifth Engineering Turbulence Modelling and Measurements*, Rodi, and Fueyo eds, 2002.

- [139] S. YOKOBORI, N. KASAGI AND M. HIRATA. Characteristic behavior of turbulence in the stagnation region of a two-dimensional submerged jet impinging normally on a flat plate. *Proc. Symp. Turbulent Shear Flows, Penn State*, 3.17-3.25, 1977.
- [140] S. YOKOBORI, N. KASAGI AND M. HIRATA. Transport phenomena at the stagnation region of a two-dimensional impinging jet. *Trans. JSME ser. B* 49 (441), pp. 1029-1039, 1983.
- [141] Q.P. ZHENG, A.K. JASUJA, AND A.H. LEFEBVRE. *Proc. Combustion Institute*, vol. 26, 1996.